



HAL
open science

Photonic integrated circuits on InP for high power signals generation in the millimeter wave range

Andrzej Jankowski

► **To cite this version:**

Andrzej Jankowski. Photonic integrated circuits on InP for high power signals generation in the millimeter wave range. Optics / Photonics. Université Grenoble Alpes, 2019. English. NNT: 2019GREAT126 . tel-03130034

HAL Id: tel-03130034

<https://theses.hal.science/tel-03130034>

Submitted on 3 Feb 2021

HAL is a multi-disciplinary open access archive for the deposit and dissemination of scientific research documents, whether they are published or not. The documents may come from teaching and research institutions in France or abroad, or from public or private research centers.

L'archive ouverte pluridisciplinaire **HAL**, est destinée au dépôt et à la diffusion de documents scientifiques de niveau recherche, publiés ou non, émanant des établissements d'enseignement et de recherche français ou étrangers, des laboratoires publics ou privés.

THÈSE

Pour obtenir le grade de

DOCTEUR DE L'UNIVERSITÉ GRENOBLE ALPES

Spécialité : OPTIQUE ET RADIOFREQUENCES

Arrêté ministériel : 25 mai 2016

Présentée par

Andrzej JANKOWSKI

Thèse dirigée par **Jean-François ROUX**

et **Frédéric VAN DIJK**

préparée au sein du **Laboratoire Institut de Microélectronique, Electromagnétisme et Photonique - Laboratoire d'hyperfréquences et de caractérisation** dans l'**École Doctorale Electronique, Electrotechnique, Automatique, Traitement du Signal (EEATS)**

Circuits intégrés photoniques sur InP pour la génération de signaux de puissance dans la gamme des ondes millimétriques

Photonic integrated circuits on InP for high power signals generation in the millimeter wave range

Thèse soutenue publiquement le **13 décembre 2019**, devant le jury composé de :

Monsieur Jean-François ROUX

Maître de Conférences, Université Savoie Mont Blanc, Directeur de thèse

Monsieur François BONDU

Directeur de Recherche, CNRS, Rapporteur

Monsieur Jean-François LAMPIN

Directeur de Recherche, CNRS, Rapporteur

Monsieur Ronan SAULEAU

Professeur, Université de Rennes 1, Président du jury

Monsieur Guillermo CARPINTERO DEL BARRIO

Professeur, Université Carlos III de Madrid, Examineur

Monsieur Frédéric VAN DIJK

Ingénieur de Recherche, III-V Lab, Co-directeur de thèse



TABLE OF CONTENTS

ACKNOWLEDGEMENTS.....	I
TERMS AND ABBREVIATIONS.....	II
LIST OF FIGURES	V
CHAPTER 1	1
INTRODUCTION	1
1.1 Dissertation organization	4
References	5
CHAPTER 2	6
MILLIMETER WAVE ELECTRONICS.....	6
2.1 Oscillators at mm-waves	7
2.2 Diode-based oscillators	9
2.2.1 Gunn diodes	9
2.2.2 SLEDs (Superlattice Electronic Devices)	10
2.2.3 IMPATT and TUNNET diodes	10
2.2.4 RTDs (Resonant Tunneling Diodes).....	10
2.2.5 Summary of diode-based oscillators	11
2.3 Transistor-based oscillators	13
2.3.1 LC-tank oscillators	14
2.3.1.1 Colpitts and Hartley oscillators.....	15
2.3.1.2 Cross-coupled and Push-push oscillators	16
2.3.2 Summary of transistor-based oscillators.....	17
2.4 Frequency multipliers	20
2.5 LNAs and PAs in mm-waves.....	20
MILLIMETER WAVE PHOTONICS	23
2.6 Optical generation of mm-waves signals.....	24
2.6.1 Laser sources for optical generation of mm-wave signals	24
2.6.2 Optical heterodyning.....	25
2.6.3 Phase noise reduction techniques.....	28
2.7 Photodetectors	31
2.7.1 p-i-n and UTC photodiodes	33
2.7.2 Summary of p-i-n and UTC photodiodes.....	35
2.8 Photoconductive switch.....	37
2.9 Millimeter wave electronics and photonics - summary	38

References	41
CHAPTER 3.....	50
DESIGN AND RF SOLUTIONS TO INCREASE OUTPUT POWER	50
3.1 UTC photodiode - limitations.....	51
3.2 Photodiodes - topologies	54
3.2.1 Distributed photodetectors.....	56
3.3 Antenna Arrays and power combined photodetectors.....	59
3.4 Design and RF solutions to increase output power – conclusions.....	63
References	65
CHAPTER 4.....	68
RF AND OPTICAL DESIGN AND SIMULATIONS	68
4.1 Transmission line and waveguides	69
4.1.1 S-parameters.....	72
4.1.2 Impedance matching.....	73
4.2 UTC PDs with CPW output - design	74
4.2.1 UTC PD with CPW – simulation results and summary	78
4.3 Wilkinson power combiner.....	83
4.3.1 2-way Wilkinson power combiner - design.....	84
4.3.2 2-way Wilkinson power combiner - simulation results	87
4.3.3 4-way Wilkinson power combiner - design.....	93
4.3.4 4-way Wilkinson power combiner - simulation results	95
4.3.5 Wilkinson power combiners - summary	102
4.4 Antenna integrated UTC PDs	105
4.4.1 3x folded-dipole antenna-integrated UTC PD - design	111
4.4.2 3x folded-dipole antenna-integrated UTC PD – simulation results	113
4.4.3 Bow-tie antenna-integrated UTC PDs – design.....	118
4.4.3.1 3x bow-tie antenna-integrated UTC PDs – simulation results	121
4.4.3.2 2x bow-tie and separated 1x bow-tie antenna-integrated UTC PD – simulation results	126
4.4.3.3 Separated and connected 2x bow-tie antenna-integrated UTC PD – simulation results	129
4.4.4 Antenna-integrated UTC PDs – summary.....	135
4.5 Optical design and simulations.....	139
4.5.1 Passive optical waveguides – introduction	139
4.5.2 Ridge optical waveguides and S-bends – design and simulation results.....	142
4.5.3 MMI - introduction.....	153
4.5.4 MMIs – design and simulation results.....	154
4.5.5 Optical design and simulations - summary.....	155

References	158
CHAPTER 5	161
PIC FABRICATION	161
5.1 Cleanroom processing - steps.....	162
5.2 Cleanroom processing – results and summary	168
CHAPTER 6	176
MEASUREMENTS AND RESULTS	176
6.1 Measured devices - description	177
6.2 Electrical parameters – Fiwin5G – measurements and discussion	178
6.2.1 Electrical parameters – previous fabrication run (iPHOS)	184
6.2.2 Wilkinson power combiners – measurements with VNA up to 65 GHz	187
6.3 Bandwidth and saturation measurements.....	200
6.3.1 Propagation losses of optical waveguides	207
6.3.2 Bandwidth measurements – iPHOS fabrication run	209
6.3.3 Bandwidth measurements - antenna-integrated devices.....	213
6.3.4 Bandwidth measurements - antenna-integrated devices – previous fabrication run (iPHOS)	218
6.4 LPT antenna-integrated UTC PD – measurements with Mode-locked Laser	224
6.5 Photonic integrated circuit – measurements	227
6.6 Measurements and results - summary.....	233
References	234
GENERAL CONCLUSIONS	235
ANNEX 1	238

ACKNOWLEDGEMENTS

In the beginning, I would like to express my gratitude to my supervisor Frédéric Van Dijk. His support, guidance and motivation during my PhD thesis were essential for the completion of this work. I would also like to thank Jean-François Roux, my academic co-supervisor, for his valuable discussions and support.

I would like to thank prof. François Bondu and prof. Jean-François Lampin for reviewing my manuscript and all their appreciated comments that helped me improve it. I would also like to thank my examiners prof. Ronan Sauleau and prof. Guillermo Carpintero del Barrio for valuable discussions during my defence.

I would like to thank all my colleagues from FiWiN5G Marie Skłodowska-Curie European Union's Horizon 2020 Research and Innovation Programme under Grant 642355, for the great time during the summer and winter schools.

Moreover, I want to thank all III-V Lab members, in particular the cleanroom staff, for their support during my PhD thesis. Special thanks to Alexandre Larrue, Michel Garcia and Frederic Pommereau for their help during the cleanroom processing.

Furthermore, I would like to thank all my colleagues and fellow PhD students from III-V Lab for the great atmosphere and support. Special thanks to my room-mates: Roberto, Peppino, Sylvain, Gil and Barbara.

Finally, I would like to thank my family and friends for their love and understanding while working on this project.

TERMS AND ABBREVIATIONS

BCB	Benzocyclobutene
BiCMOS	Bipolar Complementary Metal–Oxide–Semiconductor
BJT	Bipolar Junction Transistor
CBCPW	Conductor-Backed Coplanar Waveguide
CDMA	Code Division Multiple Access
CMOS	Complementary Metal–Oxide–Semiconductor
CPW	Coplanar Waveguide
CW	Continuous-Wave
DBR	Distributed Bragg Reflector
DFB	Distributed-Feedback
EDGE	Enhanced Data rates for GSM Evolution
ErAs	Erbium Arsenide
EVM	Error Vector Magnitude
FBG	Fiber Bragg Grating
FCC	Federal Communications Commission
FET	Field Effect Transistor
GaAs	Gallium Arsenide
GaN	Gallium Nitride
GCPW	Grounded Coplanar Waveguide
GSG	Ground Signal Ground
GS-MBE	Gas Source - Molecular-Beam Epitaxy
HBT	Heterojunction-Bipolar Transistor
HBV	Hetero-Barrier Varactors
HEMT	High Electron Mobility Transistor
IBE	Ion Beam Etching
ICP	Inductively Coupled Plasma
ICPCVD	Inductively Coupled Plasma Chemical Vapour Deposition
IMPATT	Impact Ionization Avalanche Transit Time
IMWP	Integrated Microwave Photonics
InAlAs	Indium Aluminium Arsenide
InGaAs	Indium Gallium Arsenide
InGaAsP	Indium Gallium Arsenide Phosphide
InP	Indium Phosphide
IoT	Internet of Things
ITU	International Telecommunication Union

LD	Laser Diode
LTE	Long-Term Evolution
LNA	Low Noise Amplifier
LT-GaAs	Low-Temperature Gallium Arsenide
MLA	Micro-Lens Array
MLL	Mode-locked Laser
MMI	Multi-Mode Interference
MMIC	Monolithic Microwave Integrated Circuit
MOS	Metal–Oxide–Semiconductor
MOSFET	Metal–Oxide–Semiconductor Field-Effect Transistor
MWP	Microwave Photonics
MZM	Mach-Zehnder Modulator
NDC	Negative Differential Conductance
NDR	Negative Differential Resistance
OEO	Optoelectronic Oscillator
OFCG	Optical Frequency Comb Generation
OIL	Optical Injection Locking
OPLL	Optical Phase Lock Loop
PA	Power Amplifier
PECVD	Plasma-Enhanced Chemical Vapor Deposition
QPSK	Quadrature Phase Shift Keying
RF	Radio Frequency
RIE	Reactive Ion Etching
RSPG	Radio Spectrum Policy Group
RTA	Rapid Thermal Annealing
RTD	Resonant Tunneling Diodes
SBD	Schottky Barrier Diode
SiGe	Silicon-Germanium
SLED	Superlattice Electronic Device
SOLT	Short Open Load Thru
TD-SCDMA	Time Division Synchronous Code Division Multiple Access
TED	Transferred Electron Device
TEM	Transverse Electromagnetic Mode
TTD	True Time Delay
TUNNETT	Tunnel-Injection Transit Time
TWPD	Travelling Wave Photodetector
UDN	Ultra Dense Network

UTC	Uni-Travelling Carrier
VCO	Voltage-Controlled Oscillator
VMPD	Velocity-Matched Photodetector
VNA	Vector Network Analyzer
WCDMA	Wideband Code Division Multiple Access
WG-PD	Waveguide Photodiode

LIST OF FIGURES

FIG. 1. 1 ERICSSON GLOBAL MOBILE SUBSCRIPTIONS FORECAST BY TECHNOLOGY (A) AND MOBILE DATA TRAFFIC BY APPLICATION CATEGORY (B) [1].	1
FIG. 1. 2 ATMOSPHERIC ATTENUATION OF MM-WAVES FREQUENCIES. BAND CANDIDATES FOR FUTURE 5G APPLICATIONS ARE HIGHLIGHTED.	3
FIG. 1. 3 HETEROGENEOUS NETWORK WITH INDOOR, STREET LEVEL AND DIRECT DEVICE TO DEVICE MODE.	3
FIG. 2. 1 GENERIC RF TRANSCEIVER [8].	7
FIG. 2. 2 PLL-BASED FREQUENCY SYNTHESIZER WITH FREQUENCY DIVIDER IN THE FEEDBACK PATH [37].	7
FIG. 2. 3 (A) SCHEMATIC MODEL OF LINEAR LC RESONATOR CIRCUIT AND (B) ITS OUTPUT SIGNAL ATTENUATION OVER TIME DUE TO LOSSES.	8
FIG. 2. 4 SCHEMATIC MODEL OF (A) DIODE/TRANSISTOR-BASED OSCILLATOR MODEL WITH NEGATIVE RESISTANCE AND (B) TRANSISTOR-BASED OSCILLATOR WITH POSITIVE FEEDBACK.	8
FIG. 2. 5 CROSS SECTION OF PACKAGED INP GUNN DIODE [18].	9
FIG. 2. 6 PLANAR GUNN DIODE COPLANAR LAYOUT FOR S-PARAMETER MEASUREMENTS WITH AIR BRIDGE INTERCONNECTION [19].	9
FIG. 2. 7 (A) CONDUCTION BAND DIAGRAM OF DOUBLE HETEROJUNCTION BARRIER RTD UNDER BIAS VOLTAGE. WITH INCREASING BIAS VOLTAGE, QUANTUM LEVELS INSIDE QW MOVE BELOW THE EC BAND RESULTING IN SUDDEN CURRENT DROP IN THE I-V CHARACTERISTICS (B).	11
FIG. 2. 8 THE OVERVIEW OF DIODE-BASED OSCILLATOR IN THE MM-WAVE AND THZ FREQUENCY RANGE. DATA POINT BASED ON [13], [15], [18], [21], [24], [25], [26], [27],[28], [29],[30], [31], [33], [34].	12
FIG. 2. 9 AN OSCILLATOR MODEL WITH POSITIVE FEEDBACK LOOP AND FREQUENCY-SELECTIVE CIRCUIT.	13
FIG. 2. 10 OSCILLATION MECHANISM PERIODS, FROM (A) INITIAL, (B) AMPLIFIED, (C) FEEDBACK, AND (D) THE STABLE STATE [37].	14
FIG. 2. 11 THE AC EQUIVALENT CIRCUIT AND SMALL-SIGNAL MODEL OF COLPITTS MOSFET OSCILLATOR [39].	15
FIG. 2. 12 CROSS-COUPLED OSCILLATOR (A), (B) MERGED LOAD TANKS, (C) EQUIVALENT CIRCUIT OF CROSS-COUPLED PAIR [8].	16
FIG. 2. 13 CROSS-COUPLED AND COLPITTS VCO SCHEMATICS WITH NODES (RED DOT) WHERE THE SECOND HARMONIC SIGNAL CAN BE COLLECTED [10].	17
FIG. 2. 14 FREQUENCY, OUTPUT POWER AND PHASE NOISE OF (A) COLPITTS AND (B) CROSS-COUPLED VCO [42].	18
FIG. 2. 15 AN OVERVIEW OF OUTPUT POWERS AT MM-WAVES OF DIFFERENT OSCILLATORS' CONFIGURATIONS WITH RESPECT TO THE FABRICATION TECHNOLOGY. DATA POINTS BASED ON [38][43][45][46][47][48][49].	19
FIG. 2. 16 AN OVERVIEW OF PHASE NOISE FIGURES AT MM-WAVES OF DIFFERENT OSCILLATORS' CONFIGURATIONS WITH RESPECT TO THE FABRICATION TECHNOLOGY. DATA POINTS BASED ON [38][43][45][46][47][48][49].	19
FIG. 2. 17 SEM MICROGRAPH OF A DOUBLER GAAs SCHOTTKY CIRCUIT [52].	20
FIG. 2. 18 MM-WAVE PLL FREQUENCY MULTIPLIER AT 60 GHz [53].	20
FIG. 2. 19 GENERAL MODEL OF LNA [55].	21
FIG. 2. 20 AN OVERVIEW OF POWER ADDED EFFICIENCY AT MM-WAVES OF DIFFERENT POWER AMPLIFIERS' TOPOLOGIES WITH RESPECT TO THE FABRICATION TECHNOLOGY. DATA POINTS BASED ON [45][58][59][60].	22
FIG. 2. 21 AN OVERVIEW OF SATURATED OUTPUT POWER AT MM-WAVES OF DIFFERENT POWER AMPLIFIERS' TOPOLOGIES WITH RESPECT TO THE FABRICATION TECHNOLOGY. DATA POINTS BASED ON [45][58][59][60].	22

FIG. 2. 22 SCHEMATIC OF MICROWAVE PHOTONIC LINK. THE RF INPUT SIGNAL IS CONVERTED INTO OPTICAL DOMAIN AND TRANSMITTED VIA OPTICAL FIBER. THE OUTPUT RF SIGNAL IS CONVERTED BACK INTO ELECTRICAL DOMAIN.	23
FIG. 2. 23 SCHEMATICS OF THE FABRY-PEROT CONVENTIONAL CAVITY LASER (LEFT) AND IMPROVED GAIN-GUIDED STRIPE LASER (RIGHT). DUE TO STRIPE-SHAPE ELECTRODE, LASING IS TAKING PLACE ONLY IN THE CENTRAL REGION OF THE STRUCTURE, EFFECTIVELY SUPPRESSING HIGHER-ORDER TRANSVERSAL MODES.	25
FIG. 2. 24 SIMPLIFIED SCHEMATIC OF THE OPTICAL HETERODYNING WITH TWO OPTICAL WAVES TO GENERATE MMW OR THZ SIGNAL. IRF IS A PHOTODETECTOR OUTPUT CURRENT, A IS A CONSTANT WHICH IS DETERMINED BY $E01$, $E02$ AND THE RESPONSIVITY OF THE PHOTODETECTOR [77].	25
FIG. 2. 25 SIMPLIFIED SCHEMATIC OF OFCG FOR MM-WAVE SIGNAL GENERATION.	27
FIG. 2. 26 SIMPLIFIED SETUP OF MLL USED TO GENERATE FREQUENCY COMBS.	28
FIG. 2. 27 SCHEMATIC OF THE OPTICAL FIELD AMPLITUDES FOR (A) A TIME-DOMAIN SINUSOID AND (B) A TIME-DOMAIN	28
FIG. 2. 28 SETUP WITH MZM BIASED AT MAXIMUM TRANSFER POINT FOR FREQUENCY QUADRUPLING.	28
FIG. 2. 29 SETUP FOR OIL OF THE SLAVE LASERS AT $\pm 2^{ND}$ SIDE BANDS.	29
FIG. 2. 30 SETUP FOR THE OPLL WITH HARMONIC GENERATOR.	30
FIG. 2. 31 SCHEMATIC OF A SINGLE LOOP OEO.	30
FIG. 2. 32 SIMPLIFIED DIAGRAMS OF PHOTOGENERATION OF ELECTRON-HOLE PAIR IN A (A) SEMICONDUCTOR, (B) PHOTOCONDUCTOR, (C) PN PHOTODIODE AND (D) PIN PHOTODIODE.	31
FIG. 2. 33 TYPICAL PHOTODIODE I-V CHARACTERISTIC.	32
FIG. 2. 34 BAND STRUCTURE OF CONVENTIONAL P-I-N PHOTODIODE (A) AND MODIFIED BAND DIAGRAM (B) AT HIGH OPTICAL INPUT [93].	34
FIG. 2. 35 BAND STRUCTURE OF CONVENTIONAL UTC PHOTODIODE (A) AND MODIFIED BAND DIAGRAM (B) AT HIGH OPTICAL INPUT [93].	34
FIG. 2. 36 STATE-OF-THE-ART OF P-I-N AND UTC PHOTODIODES WITH HIGHEST OUTPUT POWERS [97]- [104].	35
FIG. 2. 37 STATE-OF-THE-ART OF ANTENNA-INTEGRATED PHOTODIODES WITH HIGHEST OUTPUT POWERS [105]-[109].	36
FIG. 2. 38 TOP VIEW AND CROSS-SECTIONAL VIEW OF A PHOTOMIXER WITH PLANAR DIPOLE ANTENNA. BOTTOM SIDE COUPLING OF MM-WAVE/THZ RADIATION VIA DIELECTRIC LENS TO FREE SPACE. ADAPTED FROM [111].	37
FIG. 2. 39 OUTPUT POWER LEVELS OF ELECTRONICS-BASED AND PHONICS-BASED SOLUTIONS FROM 30 GHz TO 300 GHz. DATA POINTS ARE BASED ON REPORTED RESULTS PRESENTED IN PREVIOUS SUB-CHAPTERS.	39
FIG. 2. 40 AVERAGE PHASE NOISE LEVELS OF ELECTRONICS-BASED AND PHOTONICS-BASED SOLUTIONS FROM 30 GHz TO 300 GHz. DATA POINTS ARE BASED ON REPORTED RESULTS PRESENTED IN PREVIOUS SUB-CHAPTERS.	39
FIG. 3. 1 TYPICAL CURVE OF -1 dB COMPRESSION POINT OF PHOTODIODE.	50
FIG. 3. 2 BAND STRUCTURE OF CONVENTIONAL UTC PHOTODIODE AT HIGH OPTICAL INPUT.	51
FIG. 3. 3 RELATIONSHIP BETWEEN 3-DB BANDWIDTH FOR INP/INGaAs UTC-PDs AND P-I-N PDs [2].	52
FIG. 3. 4 EQUIVALENT CIRCUIT OF LUMPED ELEMENT PHOTODETECTOR.	53
FIG. 3. 5 TOP (A) AND BACK (B) ILLUMINATED P-I-N PHOTODIODES.	55
FIG. 3. 6 WAVEGUIDE (A), EVANESCENTLY-COUPLED (B) AND WITH REFRACTIVE FACET (C) P-I-N PD.	56
FIG. 3. 7 SIMPLIFIED DISTRIBUTED STRUCTURES OF A TRAVELLING-WAVE PD (A) AND (B) A VELOCITY-MATCHED PDs.	56
FIG. 3. 8 MICROGRAPH OF THE TWPD (P-I-N PDs) CHIP WITH $d = 90$ NM. THE INPUT SIGNAL IS FED FROM THE LEFT VIA MODE CONVERTER AND RIB WAVEGUIDE INTO MMI SPLITTER [23].	57
FIG. 3. 9 MUTC CHIP WITH FOUR DIODES AND ALN SUBMOUNT WITH TRANSMISSION LINE [24].	57
FIG. 3. 10 DIAGRAM OF THE EVANESCENTLY-COUPLED P-I-N PHOTODIODE ARRAYS (LEFT) AND RF POWER AT 105 GHz VS. OPTICAL INPUT POWER (RIGHT) AT DIFFERENT BIAS VOLTAGE [26].	59

FIG. 3. 11 SCHEMATIC ILLUSTRATION OF THE MICROSTRIP ANTENNA ARRAY (LEFT) AND ANTENNA ELEMENT (RIGHT) [27].	60
FIG. 3. 12 OVERALL STRUCTURE OF AN ANTENNA MODULE FOR 60 GHz APPLICATIONS [29].	60
FIG. 3. 13 RECEIVED RF POWERS AND SNR VALUES FOR THE QPSK SIGNAL AS A FUNCTION OF THE RF PROPAGATION DISTANCE [29].	60
FIG. 3. 14 OVERVIEW OF THE SETUP WITH ARRAY OF BOW-TIE ANTENNA INTEGRATED UTC PDs, OPTICAL DELAY LINES (DL) AND SCHOTTKY BARRIER DIODE AS A POWER DETECTOR (SBD)[30].	61
FIG. 3. 15 OUTPUT POWER OF THE SYSTEM WITH DELAY LINES [30].	61
FIG. 3. 16 TOP VIEW (LEFT) OF FABRICATED UTC PDs WITH T-JUNCTION POWER COMBINER AND SCHEMATIC OF THE PACKAGE MODULE (RIGHT) [31].	62
FIG. 3. 17 TWO-WAY (TOP) AND FOUR-WAY (BOTTOM) WILKINSON POWER COMBINER WITH BACK-ILLUMINATED PHOTODIODES [34][35].	62
FIG. 3. 18 SCHEMATIC EXAMPLE OF PROPOSED PICs WITH 2-WAY WILKINSON POWER COMBINER (TOP) AND 2X ANTENNA-INTEGRATED PHOTODIODES ARRAY (BOTTOM).	63
FIG. 4. 1 SCHEMATIC EXAMPLE OF PROPOSED PICs WITH 2-WAY WILKINSON POWER COMBINER (TOP) AND 2X ANTENNA-INTEGRATED PHOTODIODES ARRAY (BOTTOM).	68
FIG. 4. 2 TRANSMISSION LINE EQUIVALENT CIRCUIT [5].	69
FIG. 4. 3 TERMINATED TRANSMISSION LINE WITH CHARACTERISTIC IMPEDANCE Z_0 CONNECTED TO A LOAD Z_L .	70
FIG. 4. 4 CROSS-SECTIONS OF MICROSTRIP, COPLANAR/GROUNDED COPLANAR WAVEGUIDE AND SCHEMATIC OF GCPW WITH METAL ELECTRODES (GSG). THE GCPW CAN BE ALSO REFERRED AS CBCPW (CONDUCTOR-BACKED COPLANAR WAVEGUIDE).	71
FIG. 4. 5 ELECTRIC FIELD DISTRIBUTION OF A GCPW WITH (A) DOMINANT COPLANAR MODE AND (B) THE MICROSTRIP MODE.	71
FIG. 4. 6 S-PARAMETERS OF THE TWO-PORT NETWORK.	73
FIG. 4. 7 SINGLE SECTION QUARTER-WAVE TRANSFORMER WITH $l = \lambda/4$ AND ELECTRICAL LENGTH $\pi/2$ AT THE DESIGN FREQUENCY f_0 .	74
FIG. 4. 8 UTC PDs DIMENSIONS AND ABBREVIATIONS.	75
FIG. 4. 9 UTC PD STRUCTURE WITH CPW OUTPUT DIMENSIONS OPTIMIZED DURING SIMULATIONS TO OBTAIN LOW LOSS PROPERTIES.	76
FIG. 4. 10 THEORETICAL UTC PD CAPACITANCE VS. UTC PD DIMENSION.	76
FIG. 4. 11 CLOSE UP VIEW OF A UTC PD STRUCTURE SIMULATED AS A LUMP ELEMENT WITH ADAPTED VALUES OF R AND C.	77
FIG. 4. 12 UTC PD (L2W3) WITH ADAPTED CPW OUTPUT DIMENSIONS.	77
FIG. 4. 13 S-PARAMETERS FOR L1W1, L2W1 AND L3W1 AT FREQUENCY SWEEP FROM 1 GHz UP TO 110 GHz. SOURCE (PORT) IMPEDANCE: 50 Ω .	78
FIG. 4. 14 S-PARAMETERS FOR L1W2, L2W2 AND L3W2 AT FREQUENCY SWEEP FROM 1 GHz UP TO 110 GHz. SOURCE (PORT) IMPEDANCE: 50 Ω .	79
FIG. 4. 15 S-PARAMETERS FOR L1W3, L2W3 AND L3W3 AT FREQUENCY SWEEP FROM 1 GHz UP TO 110 GHz. SOURCE (PORT) IMPEDANCE: 50 Ω .	79
FIG. 4. 16 S-PARAMETERS FOR L1W4, L2W4 AND L3W4 AT FREQUENCY SWEEP FROM 1 GHz UP TO 110 GHz. SOURCE (PORT) IMPEDANCE: 50 Ω .	80
FIG. 4. 17 FAMILY OF S_{21} CHARACTERISTICS FOR ALL UTC PD DIMENSIONS FROM 1 GHz TO 110GHz.	80
FIG. 4. 18 BANDWIDTH OF THE UTC PD L2W3 FROM 1 GHz TO 300 GHz.	81

FIG. 4. 19 E-FIELD DISTRIBUTION IN UTC PD L2W3 AT 60 GHz.	81
FIG. 4. 20 S-PARAMETERS FOR UTC PD WITH ADAPTED CPW OUTPUT DIMENSIONS FROM FIG. 4. 12 AT FREQUENCY SWEEP FROM 1 GHz UP TO 110 GHz. SOURCE (PORT) IMPEDANCE: 50 Ω	82
FIG. 4. 21 SCHEMATIC OF WILKINSON POWER COMBINER.....	83
FIG. 4. 22 THE OVERVIEW OF THE 2-WAY WILKINSON POWER COMBINER WITH ISOLATION RESISTORS.	85
FIG. 4. 23 DESIGN DETAILS OF INPUT Z_0 CPW (TOP VIEW).	86
FIG. 4. 24 THE BACKSIDE OVERVIEW OF THE 2-WAY WILKINSON WITH ISOLATION RESISTORS WITH SIMPLIFIED CROSS-SECTIONS OF UNDER-BRIDGE CONNECTIONS AND CONNECTIONS TO THE RESISTORS.....	86
FIG. 4. 25 THE OVERVIEW OF THE 2-WAY WILKINSON POWER COMBINER WITHOUT ISOLATION RESISTORS.....	87
FIG. 4. 26 S-PARAMETERS OF THE 2-WAY WILKINSON POWER COMBINER FROM 1 GHz TO 110 GHz (TOP) AND FROM 30 GHz TO 40 GHz (BOTTOM). PORT IMPEDANCE: 50 Ω	88
FIG. 4. 27 S-PARAMETERS FOR 2-WAY WILKINSON POWER COMBINER WITH ISOLATION RESISTORS FROM 60 GHz TO 80 GHz. SOURCE (PORT) IMPEDANCE: 50 Ω	88
FIG. 4. 28 S-PARAMETERS OF THE 2-WAY WILKINSON POWER COMBINER WITHOUT ISOLATION RESISTORS FROM 1 GHz TO 110 GHz (TOP) AND FROM 30 GHz TO 40 GHz (BOTTOM). SOURCE (PORT) IMPEDANCE: 50 Ω	89
FIG. 4. 29 S-PARAMETERS FOR 2-WAY WILKINSON POWER COMBINER WITHOUT ISOLATION RESISTORS FROM 60 GHz TO 80 GHz. SOURCE (PORT) IMPEDANCE: 50 Ω	90
FIG. 4. 30 THE PHASE OF THE COMBINED SIGNALS S_{21} AND S_{31} FOR THE 2-WAY WILKINSON POWER COMBINER WITH ISOLATION RESISTORS.	91
FIG. 4. 31 THE PHASE OF THE COMBINED SIGNALS S_{21} AND S_{31} FOR THE 2-WAY WILKINSON POWER COMBINER WITHOUT ISOLATION RESISTORS.	91
FIG. 4. 32 EXAMPLE OF THE E-FIELD DISTRIBUTION FOR THE 2-WAY WILKINSON POWER COMBINER WITH ISOLATION RESISTOR AT 68 GHz.	92
FIG. 4. 33 EXAMPLE OF THE E-FIELD DISTRIBUTION FOR THE 2-WAY WILKINSON POWER COMBINER WITH ISOLATION RESISTOR AT 68 GHz.	92
FIG. 4. 34 THE OVERVIEW OF THE 4-WAY WILKINSON POWER COMBINER WITH ISOLATION RESISTORS AND PORT ASSIGNMENTS.	93
FIG. 4. 35 THE BACKSIDE OVERVIEW OF THE 4-WAY WILKINSON WITH ISOLATION RESISTORS.	94
FIG. 4. 36 TOP VIEW OF 4-WAY WILKINSON POWER COMBINER AND CASCADE DESIGN PRINCIPLE.....	94
FIG. 4. 37 S-PARAMETERS OF THE 4-WAY WILKINSON POWER COMBINER FROM 10 GHz TO 110 GHz (TOP) AND FROM 40 GHz TO 70 GHz (BOTTOM). SOURCE (PORT) IMPEDANCE: 50 Ω	95
FIG. 4. 38 S-PARAMETERS (TRANSMISSION) OF THE 4-WAY WILKINSON POWER COMBINER FROM 10 GHz TO 110 GHz (TOP) AND FROM 40 GHz TO 70 GHz (BOTTOM). SOURCE (PORT) IMPEDANCE: 50 Ω	96
FIG. 4. 39 S-PARAMETERS (ISOLATION) OF THE 4-WAY WILKINSON POWER COMBINER FROM 10 GHz TO 110 GHz (TOP) AND FROM 40 GHz TO 70 GHz (BOTTOM). SOURCE (PORT) IMPEDANCE: 50 Ω	96
FIG. 4. 40 S-PARAMETERS OF THE 4-WAY WILKINSON POWER COMBINER WITHOUT ISOLATION RESISTOR FROM 10 GHz TO 110 GHz (TOP) AND FROM 40 GHz TO 70 GHz (BOTTOM). SOURCE (PORT) IMPEDANCE: 50 Ω	97
FIG. 4. 41 S-PARAMETERS (TRANSMISSION) OF THE 4-WAY WILKINSON POWER COMBINER WITHOUT ISOLATION RESISTOR FROM 10 GHz TO 110 GHz (TOP) AND FROM 40 GHz TO 70 GHz (BOTTOM). SOURCE (PORT) IMPEDANCE: 50 Ω	98
FIG. 4. 42 S-PARAMETERS (ISOLATION) OF THE 4-WAY WILKINSON POWER COMBINER WITHOUT ISOLATION RESISTOR FROM 10 GHz TO 110 GHz (TOP) AND FROM 40 GHz TO 70 GHz (BOTTOM). SOURCE (PORT) IMPEDANCE: 50 Ω	98
FIG. 4. 43 S-PARAMETERS (PHASE) OF THE 4-WAY WILKINSON POWER COMBINER FROM 10 GHz TO 110 GHz (TOP) AND AROUND OPTIMUM VALUE OF 47 GHz AND 63 GHz (BOTTOM). SOURCE (PORT) IMPEDANCE: 50 Ω	99

FIG. 4. 44 S-PARAMETERS (PHASE) OF THE 4-WAY WILKINSON POWER COMBINER WITHOUT ISOLATION RESISTOR FROM 10 GHz TO 110 GHz (TOP) AND AROUND OPTIMUM VALUE OF 47 GHz AND 63 GHz (BOTTOM). SOURCE (PORT) IMPEDANCE: 50 Ω .	99
FIG. 4. 45 TOP VIEW OF E-FIELD DISTRIBUTION FOR THE 4-WAY WILKINSON POWER COMBINER WITH ISOLATION RESISTORS AT 63 GHz.	100
FIG. 4. 46 TOP VIEW OF E-FIELD DISTRIBUTION FOR THE 4-WAY WILKINSON POWER COMBINER WITHOUT ISOLATION RESISTORS AT 63 GHz.	100
FIG. 4. 47 BACKSIDE VIEW OF E-FIELD DISTRIBUTION FOR THE 4-WAY WILKINSON POWER COMBINER WITH ISOLATION RESISTORS AT 63 GHz.	101
FIG. 4. 48 BACKSIDE VIEW OF E-FIELD DISTRIBUTION FOR THE 4-WAY WILKINSON POWER COMBINER WITHOUT ISOLATION RESISTORS AT 63 GHz.	101
FIG. 4. 49 TOP VIEW OF E-FIELD DISTRIBUTION FOR THE 4-WAY WILKINSON POWER COMBINER WITH ISOLATION RESISTORS AT 63 GHz AT PORT 1 AND PORT 2, AND FOR THE DEVICE WITHOUT ISOLATION RESISTORS (BOTTOM FIGURE).	102
FIG. 4. 50 SUMMARY OF THE S-PARAMETERS FOR THE 2-WAY WILKINSON POWER COMBINER WITH AND WITHOUT ISOLATION RESISTORS.	103
FIG. 4. 51 SUMMARY OF THE S-PARAMETERS FOR THE 4-WAY WILKINSON POWER COMBINER WITH AND WITHOUT ISOLATION RESISTORS.	103
FIG. 4. 52 COORDINATE SYSTEM FOR ANTENNA ANALYSIS AND RADIATION PATTERN WITH MAJOR AND MINOR LOBES [17].	105
FIG. 4. 53 EXAMPLE OF LOG-PERIODIC TOOTHED PLANAR ANTENNA [18].	107
FIG. 4. 54 EXAMPLE OF BOW-TIE ANTENNA.	107
FIG. 4. 55 EXAMPLE OF DIPOLE ANTENNA.	108
FIG. 4. 56 EXAMPLE OF A MICROSTRIP BIAS T NETWORK WITH A BANDSTOP FILTER FOR RF CHOKE [25] (A) AND (B) AN EXAMPLE OF A COMMERCIALY AVAILABLE BIAS T FROM 0.1 MHz TO 50 GHz [26].	109
FIG. 4. 57 MAXIMUM ELEMENT SPACING (D) TO MAINTAIN ONE OR TWO AMPLITUDE MAXIMA OF A LINEAR ARRAY [17].	110
FIG. 4. 58 EXAMPLE OF THE AMPLITUDE PATTERNS FOR BROADSIDE (MAXIMA $\theta_0 = 90^\circ$) AND BROADSIDE/END-FIRE FOR 10-ELEMENT ARRAY (MAXIMA $\theta_0 = 0^\circ, 90^\circ$ AND 180°). [17].	111
FIG. 4. 59 OVERVIEW OF THE 3X FOLDED-DIPOLE ANTENNA-INTEGRATED UTC PDS WITH BIAS T CIRCUIT AND PORTS ASSIGNMENT.	113
FIG. 4. 60 DIMENSIONS OF A SINGLE FOLDED-DIPOLE ANTENNA-INTEGRATED UTC PD.	113
FIG. 4. 61 S-PARAMETERS OF INPUT REFLECTIONS FOR THE 3X FOLDED-DIPOLE ANTENNA-INTEGRATED UTC PD FROM 30 GHz TO 300 GHz AND 95 GHz TO 130 GHz. SOURCE (PORT) IMPEDANCE: 50 Ω .	114
FIG. 4. 62 S-PARAMETERS OF INPUT REFLECTIONS FOR THE 3X FOLDED-DIPOLE ANTENNA-INTEGRATED UTC PD FROM 180 GHz TO 300 GHz. SOURCE (PORT) IMPEDANCE: 50 Ω .	114
FIG. 4. 63 Z-PARAMETERS OF INPUT REFLECTIONS FOR THE 3X FOLDED-DIPOLE ANTENNA-INTEGRATED UTC PD FROM 30 GHz TO 300 GHz AND 95 GHz TO 130 GHz. SOURCE (PORT) IMPEDANCE: 50 Ω .	115
FIG. 4. 64 Z-PARAMETERS OF INPUT REFLECTIONS FOR THE 3X FOLDED-DIPOLE ANTENNA-INTEGRATED UTC PD FROM 180 GHz TO 220 GHz. SOURCE (PORT) IMPEDANCE: 50 Ω .	115
FIG. 4. 65 THE 3X FOLDED-DIPOLE ANTENNA INTEGRATED UTC PD WITH OPTICAL WAVEGUIDES, THE BEAM POINTING DIRECTION WITH THE STEERING ANGLE AND CALCULATION OF THE TIME DELAY. EQUATIONS BASED ON [17][34].	116

FIG. 4. 66 THREE-DIMENSIONAL RADIATION PATTERN (SCALE: 0.5) OF THE 3X FOLDED-DIPOLE ANTENNA-INTEGRATED UTC PD AT 100 GHz AND THE E-PLANE AND H-PLANE GAIN PATTERNS.....	117
FIG. 4. 67 E-PLANE AND H-PLANE GAIN PATTERN AT 95 GHz (A) AND (B) EVOLUTION OF E-PLANE GAIN PATTERN FROM 95 GHz UP TO 190 GHz OF THE 3X FOLDED-DIPOLE ANTENNA-INTEGRATED UTC PD.	117
FIG. 4. 68 E-PLANE AND H-PLANE GAIN PATTERN AT 95 GHz (A) AND (B) EVOLUTION OF E-PLANE GAIN PATTERN FROM 95 GHz UP TO 190 GHz OF THE 3X FOLDED-DIPOLE ANTENNA-INTEGRATED UTC PD WITH A TIME DELAY COMPENSATION.....	118
FIG. 4. 69 OVERVIEW OF THE 3X BOW-TIE ANTENNA-INTEGRATED UTC PDs WITH BIAS CIRCUIT AND PORTS ASSIGNMENT.	119
FIG. 4. 70 DIMENSIONS OF A SINGLE BOW-TIE ANTENNA-INTEGRATED UTC PD.	119
FIG. 4. 71 OVERVIEW OF THE 2X BOW-TIE AND SEPARATED 1X BOW-TIE ANTENNA-INTEGRATED UTC PDs WITH BIAS CIRCUIT AND PORTS ASSIGNMENT.	120
FIG. 4. 72 OVERVIEW OF THE SEPARATED 2X BOW-TIE ANTENNA-INTEGRATED UTC PDs WITH BIAS CIRCUIT AND PORTS ASSIGNMENT.	120
FIG. 4. 73 OVERVIEW OF THE CONNECTED 2X BOW-TIE ANTENNA-INTEGRATED UTC PDs WITH BIAS CIRCUIT AND PORTS ASSIGNMENT.	121
FIG. 4. 74 S-PARAMETERS OF INPUT REFLECTIONS FOR THE 3X BOW-TIE ANTENNA-INTEGRATED UTC PD FROM 30 GHz TO 300 GHz AND 80 GHz TO 160 GHz. SOURCE (PORT) IMPEDANCE: 50 Ω	122
FIG. 4. 75 S-PARAMETERS OF INPUT REFLECTIONS FOR THE 3X BOW-TIE ANTENNA-INTEGRATED UTC PD FROM 180 GHz TO 280 GHz. SOURCE (PORT) IMPEDANCE: 50 Ω	122
FIG. 4. 76 Z-PARAMETERS OF INPUT REFLECTIONS FOR THE 3X BOW-TIE ANTENNA-INTEGRATED UTC PD FROM 30 GHz TO 300 GHz AND 80 GHz TO 160 GHz. SOURCE (PORT) IMPEDANCE: 50 Ω	123
FIG. 4. 77 Z-PARAMETERS OF INPUT REFLECTIONS FOR THE 3X BOW-TIE ANTENNA-INTEGRATED UTC PD FROM 180 GHz TO 280 GHz. SOURCE (PORT) IMPEDANCE: 50 Ω	123
FIG. 4. 78 E-PLANE AND H-PLANE GAIN PATTERN OF THE 3X BOW-TIE ANTENNA-INTEGRATED UTC PD AT 110 GHz. .	124
FIG. 4. 79 E-PLANE AND H-PLANE GAIN PATTERN OF THE 3X BOW-TIE ANTENNA-INTEGRATED UTC PD AT 150 GHz. .	124
FIG. 4. 80 E-PLANE AND H-PLANE GAIN PATTERN OF THE 3X BOW-TIE ANTENNA-INTEGRATED UTC PD AT 250 GHz. .	125
FIG. 4. 81 S-PARAMETERS OF INPUT REFLECTIONS FOR THE 2X BOW-TIE AND SEPARATED 1X BOW-TIE ANTENNA-INTEGRATED UTC PD FROM 30 GHz TO 300 GHz AND 80 GHz TO 260 GHz. SOURCE (PORT) IMPEDANCE: 50 Ω	126
FIG. 4. 82 Z-PARAMETERS OF INPUT REFLECTIONS FOR THE 2X BOW-TIE AND SEPARATED 1X BOW-TIE ANTENNA-INTEGRATED UTC PD FROM 30 GHz TO 300 GHz AND 80 GHz TO 260 GHz. SOURCE (PORT) IMPEDANCE: 50 Ω	127
FIG. 4. 83 E-PLANE AND H-PLANE GAIN PATTERN OF THE 2X BOW-TIE AND 1X SEPARATED BOW-TIE ANTENNA-INTEGRATED UTC PD AT 110 GHz.	127
FIG. 4. 84 E-PLANE AND H-PLANE GAIN PATTERN OF THE 2X BOW-TIE AND 1X SEPARATED BOW-TIE ANTENNA-INTEGRATED UTC PD AT 150 GHz.	128
FIG. 4. 85 E-PLANE AND H-PLANE GAIN PATTERN OF THE 2X BOW-TIE AND 1X SEPARATED BOW-TIE ANTENNA-INTEGRATED UTC PD AT 250 GHz.	128
FIG. 4. 86 S-PARAMETERS OF INPUT REFLECTIONS FOR THE SEPARATED 2X BOW-TIE ANTENNA-INTEGRATED UTC PD FROM 30 GHz TO 300 GHz AND FROM 60 GHz TO 280 GHz. SOURCE (PORT) IMPEDANCE: 50 Ω	129
FIG. 4. 87 S-PARAMETERS OF INPUT REFLECTIONS FOR THE CONNECTED 2X BOW-TIE ANTENNA-INTEGRATED UTC PD FROM 30 GHz TO 300 GHz AND FROM 70 GHz TO 280 GHz. SOURCE (PORT) IMPEDANCE: 50 Ω	130

FIG. 4. 88 Z-PARAMETERS OF INPUT REFLECTIONS FOR THE SEPARATED 2X BOW-TIE ANTENNA-INTEGRATED UTC PD FROM 30 GHz TO 300 GHz AND 60 GHz TO 280 GHz. SOURCE (PORT) IMPEDANCE: 50 Ω	130
FIG. 4. 89 Z-PARAMETERS OF INPUT REFLECTIONS FOR THE CONNECTED 2X BOW-TIE ANTENNA-INTEGRATED UTC PD FROM 30 GHz TO 300 GHz AND 70 GHz TO 280 GHz. SOURCE (PORT) IMPEDANCE: 50 Ω	131
FIG. 4. 90 E-PLANE AND H-PLANE GAIN PATTERN OF THE SEPARATED 2X BOW-TIE ANTENNA-INTEGRATED UTC PD AT 130 GHz.....	132
FIG. 4. 91 E-PLANE AND H-PLANE GAIN PATTERN OF THE CONNECTED 2X BOW-TIE ANTENNA-INTEGRATED UTC PD AT 130 GHz.....	132
FIG. 4. 92 E-PLANE AND H-PLANE GAIN PATTERN OF THE SEPARATED 2X BOW-TIE ANTENNA-INTEGRATED UTC PD AT 150 GHz.....	133
FIG. 4. 93 E-PLANE AND H-PLANE GAIN PATTERN OF THE CONNECTED 2X BOW-TIE ANTENNA-INTEGRATED UTC PD AT 150 GHz.....	133
FIG. 4. 94 E-PLANE AND H-PLANE GAIN PATTERN OF THE SEPARATED 2X BOW-TIE ANTENNA-INTEGRATED UTC PD AT 250 GHz.....	134
FIG. 4. 95 E-PLANE AND H-PLANE GAIN PATTERN OF THE CONNECTED 2X BOW-TIE ANTENNA-INTEGRATED UTC PD AT 250 GHz.....	134
FIG. 4. 96 COMPARISON BETWEEN THE SIMULATED PARAMETERS OF 3X FOLDED-DIPOLE, 3X BOW-TIE AND 2X BOW-TIE SEPARATED 1X BOW-TIE ANTENNA-INTEGRATED UTC PDS STRUCTURES.....	136
FIG. 4. 97 COMPARISON BETWEEN THE SIMULATED PARAMETERS OF SEPARATED AND CONNECTED 2X BOW-TIE ANTENNA-INTEGRATED UTC PDS STRUCTURES.....	137
FIG. 4. 98 ASYMMETRIC PLANAR WAVEGUIDE (A) AND (B) ZIG-ZAG TRAJECTORY OF A RAY INSIDE THE FILM LAYER.....	139
FIG. 4. 99 TYPES OF THE MOST COMMON DIELECTRIC WAVEGUIDES: (A) THIN FILM WAVEGUIDE, (B) RAISED STRIP OR CHANNEL WAVEGUIDE, (C) RIDGE OR RIB WAVEGUIDE, (D) STRIP-LOADED WAVEGUIDE, (E) BURIED OR EMBEDDED STRIP WAVEGUIDE [38].	141
FIG. 4. 100 EXAMPLE MODEL USED FOR ANALYSIS OF (A) A RECTANGULAR WAVEGUIDE, (B) WAVEGUIDE H, AND (C) WAVEGUIDE W [38].	141
FIG. 4. 101 SIMPLIFIED RIDGE AND DEEP RIDGE PASSIVE OPTICAL WAVEGUIDE STRUCTURE WITH MATERIAL AND THICKNESS PARAMETERS USED FOR THE SIMULATIONS.	143
FIG. 4. 102 TOP VIEW OF THE UTC PD WITH A STRAIGHT OPTICAL WAVEGUIDE STRUCTURE.....	143
FIG. 4. 103 EXAMPLE OF THE DEEP RIDGE OPTICAL WAVEGUIDE DEFINITION USED IN FIMMWAVE AND OVERVIEW OF PROPAGATED MODE INSIDE THE STRUCTURE.....	143
FIG. 4. 104 EXAMPLE OF DEEP RIDGE OPTICAL WAVEGUIDE DEFINITION USED IN BEAMPROP AND OVERVIEW OF PROPAGATED MODE INSIDE THE STRUCTURE.....	144
FIG. 4. 105 COMPARISON BETWEEN SIMULATION RESULTS FOR THE RIDGE (LEFT) AND THE DEEP RIDGE (RIGHT) OPTICAL WAVEGUIDES WITH 2000 MM.....	144
FIG. 4. 106 EXAMPLE OF LIGHT PROPAGATION INSIDE RIDGE OPTICAL WAVEGUIDE OF 100 MM LENGTH TO UTC PD (L2W3) ABSORBER LAYER.....	145
FIG. 4. 107 CROSS SECTIONS CONTOUR PLOTS OF MODE PROPAGATION AT THE EDGE AND INSIDE OF UTC PD L2W3 STRUCTURE.....	145
FIG. 4. 108 CONFINEMENT FACTOR FOR UTC PD INGaAs ABSORBER LAYER.....	146
FIG. 4. 109 S-BEND PARAMETER DEFINITION.....	146
FIG. 4. 110 DATA OF SIMULATED S-BEND RIDGE WAVEGUIDES STRUCTURES.....	147
FIG. 4. 111 EXAMPLE COMPARISON OF DIFFERENT RIDGE OPTICAL WAVEGUIDE S-BENDS.....	147

FIG. 4. 112 OVERVIEW OF OPTICAL WAVEGUIDES AND MMI FOR A 3X FOLDED-DIPOLE ANTENNA INTEGRATED UTC PD STRUCTURE.	148
FIG. 4. 113 COMPARISON BETWEEN SIMULATION RESULTS FOR A RIDGE AND DEEP RIDGE S-BEND STRUCTURE (MIDDLE S-BEND) APPLIED IN 3X FOLDED-DIPOLE ANTENNA-INTEGRATED UTC PD.	149
FIG. 4. 114 OVERVIEW OF OPTICAL WAVEGUIDES AND MMI FOR A 3X BOW-TIE ANTENNA-INTEGRATED UTC PD STRUCTURE.	149
FIG. 4. 115 COMPARISON BETWEEN SIMULATION RESULTS FOR A RIDGE AND DEEP RIDGE S-BEND STRUCTURE (MIDDLE S-BEND) APPLIED IN 3X BOW-TIE ANTENNA-INTEGRATED UTC PD.	150
FIG. 4. 116 4-WAY AND 2-WAY WILKINSON POWER COMBINER WITH OPTICAL WAVEGUIDES AND 1X2 MMIs.	150
FIG. 4. 117 SIMULATION RESULTS OF SHORTER (LEFT) AND LONGER (RIGHT) RIDGE S-BEND OF 4-WAY WILKINSON POWER COMBINER.	151
FIG. 4. 118 COMPARISON BETWEEN SIMULATION RESULTS FOR A RIDGE AND DEEP RIDGE S-BEND STRUCTURE OF 2-WAY WILKINSON POWER COMBINER.	151
FIG. 4. 119 OVERVIEW OF 2X BOW-TIE AND SEPARATED 1X BOW-TIE ANTENNA-INTEGRATED UTC PDS STRUCTURES. ...	152
FIG. 4. 120 UTC PDS WITH ADAPTED CPW OUTPUT AND S-BENDS.	152
FIG. 4. 121 COMPARISON BETWEEN SIMULATION RESULTS FOR A RIDGE AND DEEP RIDGE S-BEND STRUCTURE OF THE UTC PD WITH ADAPTED OUTPUT.	153
FIG. 4. 122 SCHEMATIC STRUCTURE OF A 1 X 2 MMI DEVICE.	153
FIG. 4. 123 CONTOUR PLOTS AND DIMENSIONS OF 1X2 MMI (TOP) AND 1X3 MMI (BOTTOM) FOR RIDGE TYPE STRUCTURES.	154
FIG. 4. 124 MODES PROPAGATION IN 1X2 MMI (LEFT) AND 1X3 MMI (RIGHT) RIDGE TYPE STRUCTURES.	155
FIG. 4. 125 DATA OF SIMULATED S-BEND STRUCTURES APPLIED IN THE OPTICAL DESIGN OF INTEGRATED CIRCUITS.	156
FIG. 4. 126 SIMULATION RESULTS OF 1X2 AND 1X3 MMIs WITH RIDGE AND DEEP RIDGE STRUCTURE TYPE.	156
FIG. 5. 1 FINAL CHIP LAYOUT OVERVIEW.	161
FIG. 5. 2 SUBSTRATE LAYER STACK LAYOUT BEFORE AND AFTER EPITAXIAL RE-GROWTH. (SI: SEMI-INSULATING).	162
FIG. 5. 3 SIMPLIFIED DIAGRAM OF THE MESA ETCHING STEP TO SEPARATE UTC PD AND OPTICAL WAVEGUIDE LAYERS.	163
FIG. 5. 4 SIMPLIFIED SCHEMATIC OF THE EPITAXIAL RE-GROWTH.	163
FIG. 5. 5 SIMPLIFIED DIAGRAM OF THE UTC PD AND OPTICAL WAVEGUIDE ETCHING.	164
FIG. 5. 6 SIMPLIFIED DIAGRAM OF (A) THE ETCHING STEP TILL SI-INP AND (B) PASSIVATION PROCESS.	165
FIG. 5. 7 SCHEMATIC OVERVIEW OF THE 2-WAY WILKINSON POWER COMBINER AND THE POSITION OF THE NiCr RESISTORS.	166
FIG. 5. 8 SIMPLIFIED DIAGRAM OF THE N-CONTACT DEPOSITION.	166
FIG. 5. 9 SCHEMATIC OVERVIEW OF THE BOTTOM SIDE OF THE 2-WAY WILKINSON POWER COMBINER WITH THE N-CONTACTS AND METAL CONNECTIONS POSITION.	167
FIG. 5. 10 SIMPLIFIED DIAGRAM OF THE BCB PLANARIZATION AND ETCHING STEP.	167
FIG. 5. 11 SIMPLIFIED DIAGRAM OF THE TOP METALLIZATION STEP.	168
FIG. 5. 12 BROKEN PART OF THE SUBSTRATE DURING THE PROCESSING.	169
FIG. 5. 13 OPTICAL MICROSCOPE PHOTOGRAPH OF A UTC PDS AFTER THE FABRICATION PROCESS.	170
FIG. 5. 14 OPTICAL MICROSCOPE PHOTOGRAPH OF THE FABRICATED 2-WAY WILKINSON POWER COMBINER WITH ISOLATION RESISTORS AND A CLOSE-UP ON UTC PD AND NiCr RESISTOR.	170
FIG. 5. 15 OPTICAL MICROSCOPE PHOTOGRAPH OF THE FABRICATED 4-WAY WILKINSON POWER COMBINER (A) WITHOUT ISOLATION RESISTORS AND (B) WITH ISOLATION RESISTORS.	171

FIG. 5. 16 OPTICAL MICROSCOPE PHOTOGRAPH OF THE UNDER-BRIDGE CONNECTION OF THE 4-WAY WILKINSON POWER COMBINER WITH THE OPTICAL FOCUS ON THE (A) TOP METAL LAYER AND (B) BOTTOM METAL LAYER.	171
FIG. 5. 17 OPTICAL WAVEGUIDES AND MMIS OF THE 2-WAY AND 4-WAY WILKINSON POWER COMBINER AFTER CHIP CLEAVING.....	172
FIG. 5. 18 FOLDED-DIPOLE ANTENNA-INTEGRATED UTC PD STRUCTURE WITH OPTICAL WAVEGUIDES AFTER FABRICATION AND CLEAVING.	173
FIG. 5. 19 3X BOW-TIE ANTENNA-INTEGRATED UTC PD STRUCTURE WITH OPTICAL WAVEGUIDES AFTER FABRICATION AND CLEAVING.	173
FIG. 5. 20 2X BOW-TIE AND 1X BOW-TIE SEPARATED ANTENNA-INTEGRATED UTC PD STRUCTURE WITH OPTICAL WAVEGUIDES AFTER FABRICATION AND CLEAVING.	174
FIG. 5. 21 CONNECTED 2X BOW-TIE ANTENNA-INTEGRATED UTC PD STRUCTURE WITH OPTICAL WAVEGUIDES AFTER FABRICATION AND CLEAVING.	174
FIG. 6. 1 AN OVERVIEW OF CHARACTERIZED DEVICES FABRICATED WITHIN THE FIWIN5G PROJECT.	177
FIG. 6. 2 AN OVERVIEW OF CHARACTERIZED DEVICES FABRICATED WITHIN THE IPHOS PROJECT.....	178
FIG. 6. 3 DARK CURRENT VERSUS BIAS VOLTAGE FOR SINGLE UTC PDs FOR ALL OF THE DIMENSIONS.	179
FIG. 6. 4 DARK CURRENT VERSUS BIAS VOLTAGE FOR SINGLE UTC PDs FOR DIFFERENT DIMENSIONS GROUP.....	179
FIG. 6. 5 THE I-V CHARACTERISTICS OF SINGLE UTC PDs FOR ALL OF DIMENSIONS.....	180
FIG. 6. 6 COMPARISON OF THE SERIES RESISTANCE VALUES BETWEEN DIFFERENT DIMENSIONS OF THE UTC PDs.....	180
FIG. 6. 7 THE CURRENT DENSITY CHARACTERISTICS OF SINGLE UTC PDs FOR ALL DIMENSIONS.....	181
FIG. 6. 8 I-V CHARACTERISTICS OF WILKINSON POWER COMBINERS AND ANTENNA-INTEGRATED DEVICES.	182
FIG. 6. 9 COMPARISON OF THE R_s VALUES BETWEEN DIFFERENT DEVICES BASED ON I-V CHARACTERISTICS.....	182
FIG. 6. 10 ELECTRICAL INSPECTION OF THE UNDER-BRIDGE CONNECTION (A) FROM SIDE-TO-SIDE AND (B) SIDE-TO-MIDDLE OF 2-WAY WILKINSON POWER COMBINER.....	183
FIG. 6. 11 ESTIMATED VALUES OF R_s FOR UNDER-BRIDGE CONNECTIONS IN THE 2-WAY AND 4-WAY WILKINSON POWER COMBINER STRUCTURE IN COMPARISON TO THEORETICAL VALUES.....	183
FIG. 6. 12 DARK CURRENT VERSUS BIAS VOLTAGE FOR SINGLE UTC PDs FROM IPHOS FABRICATION RUN.....	185
FIG. 6. 13 THE I-V CHARACTERISTICS OF SINGLE UTC PDs FROM IPHOS FABRICATION RUN.....	185
FIG. 6. 14 COMPARISON OF THE R_s VALUES BETWEEN IPHOS UTC PDs BASED ON I-V CHARACTERISTICS.....	186
FIG. 6. 15 MEASUREMENT SETUP USED FOR S-PARAMETERS MEASUREMENTS OF THE 2-WAY AND 4-WAY WILKINSON POWER COMBINERS WITH UTC PDs.....	187
FIG. 6. 16 THE 2-WAY WILKINSON POWER COMBINER WITH GSG PROBES USED FOR THE S-PARAMETERS MEASUREMENTS.	188
FIG. 6. 17 SCHEMATIC OF THE GSG PROBES POSITION IN A CONFIGURATION (A) FOR A TRANSMISSION (NO. 1) AND (B) FOR THE ISOLATION (NO. 2) MEASUREMENTS OF THE S-PARAMETERS OF THE 2-WAY WILKINSON POWER COMBINER. THE SAME CONFIGURATIONS ARE USED IN THE HFSS SIMULATIONS.....	188
FIG. 6. 18 TRANSMISSION MEASUREMENT AND HFSS SIMULATION OF THE S-PARAMETERS OF THE 2-WAY WILKINSON POWER COMBINER WITHOUT ISOLATION RESISTOR (CONFIGURATION NO. 1).	189
FIG. 6. 19 TRANSMISSION MEASUREMENT AND HFSS SIMULATION OF THE S-PARAMETERS OF THE 2-WAY WILKINSON POWER COMBINER (CONFIGURATION NO. 1).	190
FIG. 6. 20 ISOLATION MEASUREMENT AND HFSS SIMULATION OF THE S-PARAMETERS OF THE 2-WAY WILKINSON POWER COMBINER WITHOUT ISOLATION RESISTORS (CONFIGURATION NO. 2).....	191
FIG. 6. 21 ISOLATION MEASUREMENT AND HFSS SIMULATION OF THE S-PARAMETERS OF THE 2-WAY WILKINSON POWER COMBINER (CONFIGURATION NO. 2).....	191

FIG. 6. 22 THE 4-WAY WILKINSON POWER COMBINER WITH GSG PROBES USED FOR THE S-PARAMETERS MEASUREMENTS.	192
FIG. 6. 23 SCHEMATIC OF THE GSG PROBES POSITION IN CONFIGURATION FOR A TRANSMISSION MEASUREMENTS (A) NO. 1 AND (B) NO. 2 OF THE S-PARAMETERS OF THE 4-WAY WILKINSON POWER COMBINER. THE SAME CONFIGURATIONS ARE USED IN THE HFSS SIMULATIONS.	192
FIG. 6. 24 TRANSMISSION MEASUREMENT AND HFSS SIMULATION OF THE S-PARAMETERS OF THE 4-WAY WILKINSON POWER COMBINER WITHOUT ISOLATION RESISTORS (CONFIGURATION NO. 1).	193
FIG. 6. 25 TRANSMISSION MEASUREMENT AND HFSS SIMULATION OF THE S-PARAMETERS OF THE 4-WAY WILKINSON POWER COMBINER (CONFIGURATION NO. 1).	193
FIG. 6. 26 TRANSMISSION MEASUREMENT AND HFSS SIMULATION OF THE S-PARAMETERS OF THE 4-WAY WILKINSON POWER COMBINER WITHOUT ISOLATION RESISTORS (CONFIGURATION NO. 2).	194
FIG. 6. 27 TRANSMISSION MEASUREMENT AND HFSS SIMULATION OF THE S-PARAMETERS OF THE 4-WAY WILKINSON POWER COMBINER (CONFIGURATION NO. 2).	194
FIG. 6. 28 SCHEMATIC OF THE GSG PROBES POSITION IN CONFIGURATION FOR AN ISOLATION MEASUREMENT IN CONFIGURATION (A) NO. 3 AND (B) NO. 4 OF THE S-PARAMETERS OF THE 4-WAY WILKINSON POWER COMBINER. THE SAME CONFIGURATIONS ARE USED FOR THE HFSS SIMULATIONS.	195
FIG. 6. 29 ISOLATION MEASUREMENT AND HFSS SIMULATION OF THE S-PARAMETERS OF THE 4-WAY WILKINSON POWER COMBINER WITHOUT ISOLATION RESISTORS (CONFIGURATION NO. 3).	196
FIG. 6. 30 ISOLATION MEASUREMENT AND HFSS SIMULATION OF THE S-PARAMETERS OF THE 4-WAY WILKINSON POWER COMBINER (CONFIGURATION NO. 3).	196
FIG. 6. 31 ISOLATION MEASUREMENT AND HFSS SIMULATION OF THE S-PARAMETERS OF THE 4-WAY WILKINSON POWER COMBINER WITHOUT ISOLATION RESISTORS (CONFIGURATION NO. 4).	197
FIG. 6. 32 ISOLATION MEASUREMENT AND HFSS SIMULATION OF THE S-PARAMETERS OF THE 4-WAY WILKINSON POWER COMBINER (CONFIGURATION NO. 4).	197
FIG. 6. 33 COMPARISON OF MEASURED S-PARAMETERS FOR THE 2-WAY WILKINSON POWER COMBINER IN THE TRANSMISSION CONFIGURATION (NO. 1).	198
FIG. 6. 34 COMPARISON OF MEASURED S-PARAMETERS FOR THE 4-WAY WILKINSON POWER COMBINER IN THE TRANSMISSION CONFIGURATION (NO.1 AND NO. 2).	198
FIG. 6. 35 OPTICAL HETERODYNE SETUP FOR THE BANDWIDTH MEASUREMENT UP TO 40 GHz.	200
FIG. 6. 36 OPTICAL PART OF THE HETERODYNE SETUP USED FOR THE BANDWIDTH AND SATURATION CURRENT MEASUREMENTS; (OSA, PD, EDFs NOT SHOWN).	201
FIG. 6. 37 FIBER-TO-CHIP COUPLNG TEST BENCH USED IN THE OPTICAL HETERODYNE SETUP.	201
FIG. 6. 38 FREQUENCY RESPONSE MEASUREMENTS UP TO 40 GHz WITH NORMALIZED OUTPUT POWER TO 1 mA OF PHOTOCURRENT.	202
FIG. 6. 39 THE 3-DB BANDWIDTH BASED ON THE MEASUREMENTS RESULTS UP TO 40 GHz.	203
FIG. 6. 40 SIMULATED S-PARAMETERS OF UTC PD L2W3 WITH R_s FROM 1.5 k Ω TO 6 k Ω .	203
FIG. 6. 41 SIMULATED S-PARAMETERS OF 2-WAY WILKINSON W/O ISOLATION RESISTORS WITH $R_s = 2000 \Omega$.	204
FIG. 6. 42 SIMULATED S-PARAMETERS OF 4-WAY WILKINSON W/O ISOLATION RESISTORS WITH $R_s = 2000 \Omega$.	205
FIG. 6. 43 THE -1-DB COMPRESSION POINT MEASUREMENT AT 20 GHz AND -4.7 V BIAS.	206
FIG. 6. 44 OUTPUT POWER AND POWER DISSIPATION BASED ON 1-DB COMPRESSION POINT MEASUREMENTS.	206
FIG. 6. 45 MEASURED PHOTOCURRENT VALUES VS. THE OPTICAL LENGTH FOR A DIFFERENT STRUCTURE FROM FIWIN5G FABRICATION RUN.	208
FIG. 6. 46 OPTICAL HETERODYNE SETUP FOR THE BANDWIDTH MEASUREMENT FROM 77 GHz – 110 GHz OF THE UTC PDS FROM IPHOS FABRICATION RUN.	209

FIG. 6. 47 FREQUENCY RESPONSE MEASUREMENTS FROM 77 GHz TO 110 GHz FOR UTC PD D3x10.....	210
FIG. 6. 48 FREQUENCY RESPONSE MEASUREMENTS FROM 77 GHz TO 110 GHz FOR UTC PD D3x15 01.....	210
FIG. 6. 49 FREQUENCY RESPONSE MEASUREMENTS FROM 77 GHz TO 110 GHz FOR UTC PD D4x15 01.....	210
FIG. 6. 50 FREQUENCY RESPONSE MEASUREMENTS FROM 77 GHz TO 110 GHz FOR UTC PD D2x15.....	211
FIG. 6. 51 FREQUENCY RESPONSE MEASUREMENTS FROM 77 GHz TO 110 GHz FOR UTC PD D3x15.....	211
FIG. 6. 52 FREQUENCY RESPONSE MEASUREMENTS FROM 77 GHz TO 110 GHz FOR UTC PD D4x15.....	211
FIG. 6. 53 COMPARISON OF UTC PD OUTPUT POWER FROM 77 GHz – 110 GHz FROM IPHOS FABRICATION RUN.	212
FIG. 6. 54 DOWN-CONVERSION PRINCIPLE USED IN THE MEASUREMENT SETUP.....	213
FIG. 6. 55 MEASUREMENT SETUP FOR CHARACTERIZATION OF THE ANTENNA-INTEGRATED DEVICES AT 50 GHz.....	214
FIG. 6. 56 PART OF THE MEASUREMENT SETUP WITH HR Si LENS USED IN THE ANTENNA-INTEGRATED DEVICES CHARACTERIZATION.....	214
FIG. 6. 57 FREQUENCY RESPONSE MEASUREMENTS OF 3X BOW-TIE ANTENNA INTEGRATED UTC PDs AT 50 GHz.....	215
FIG. 6. 58 FREQUENCY RESPONSE MEASUREMENTS OF 2X BOW-TIE AND SEPARATED 1X BOW-TIE ANTENNA-INTEGRATED UTC PD AT 50 GHz (RESULTS FOR 2X BOW-TIE ONLY).....	215
FIG. 6. 59 FREQUENCY RESPONSE MEASUREMENTS OF CONNECTED 2X BOW-TIE ANTENNA INTEGRATED UTC PDs AT 50 GHz.....	216
FIG. 6. 60 FREQUENCY RESPONSE MEASUREMENTS OF SEPARATED 2X BOW-TIE ANTENNA INTEGRATED UTC PDs AT 50 GHz.....	216
FIG. 6. 61 COMPARISON OF THE RF OUTPUT POWER AT 50 GHz BETWEEN BOW-TIE ANTENNA INTEGRATED UTC PD DEVICES.....	217
FIG. 6. 62 MEASUREMENT SETUP FOR CHARACTERIZATION OF THE ANTENNA-INTEGRATED DEVICES FROM 77 GHz – 110 GHz.....	218
FIG. 6. 63 POSITION OF THE HORN ANTENNAS IN THE MEASUREMENT SETUP FOR ANTENNA-INTEGRATED DEVICES CHARACTERIZATION FROM 77 GHz – 110 GHz.....	219
FIG. 6. 64 TOP VIEW OF (A) BOW-TIE AND (B) LPT ANTENNA-INTEGRATED UTC PD STRUCTURE FROM PREVIOUS FABRICATION RUN WITH DIMENSIONS.....	219
FIG. 6. 65 FREQUENCY RESPONSE MEASUREMENTS FROM 77 GHz – 110 GHz FOR BOW-TIE ANTENNA-INTEGRATED UTC PD FROM PREVIOUS FABRICATION RUN AT 0° AND 90° POSITION OF HORN ANTENNA.....	220
FIG. 6. 66 FREQUENCY RESPONSE MEASUREMENTS FROM 77 GHz – 110 GHz FOR LPT ANTENNA-INTEGRATED UTC PD FROM PREVIOUS FABRICATION RUN AT 0° AND 90° POSITION OF HORN ANTENNA.....	221
FIG. 6. 67 SIMULATION RESULTS OF THE S-PARAMETER FOR THE BOW-TIE ANTENNA-INTEGRATED UTC PD STRUCTURE FROM PREVIOUS FABRICATION RUN. SOURCE (PORT) IMPEDANCE WAS SET TO 50 Ω AND 100 Ω.....	222
FIG. 6. 68 SIMULATION RESULTS OF THE S-PARAMETER FOR THE LPT ANTENNA-INTEGRATED UTC PD STRUCTURE FROM PREVIOUS FABRICATION RUN. SOURCE (PORT) IMPEDANCE WAS SET TO 50 Ω AND 100 Ω.....	222
FIG. 6. 69 COMPARISON BETWEEN THE BOW-TIE AND LPT ANTENNA-INTEGRATED UTC PD OUTPUT POWER FROM 77 GHz – 110 GHz.....	223
FIG. 6. 70 MEASUREMENT SETUP FOR CHARACTERIZATION OF THE ANTENNA-INTEGRATED DEVICES FROM 77 GHz – 110 GHz WITH MODE-LOCKED LASER.....	224
FIG. 6. 71 EXAMPLE OF THE OPTICAL FREQUENCY COMB OF QD MLL LASER AT DIFFERENT CURRENT SUPPLY POINTS....	225
FIG. 6. 72 MEASUREMENT OF THE LPT ANTENNA-INTEGRATED UTC PD AT 80 GHz VS. THE OPTICAL FIBER LENGTH. .	226
FIG. 6. 73 MEASUREMENT OF THE LPT ANTENNA-INTEGRATED UTC PD AT 85 GHz, 96 GHz AND 107 GHz OUTPUT POWER IN COMPARISON TO STANDARD HETERODYNE SETUP.....	226
FIG. 6. 74 MICROSCOPE VIEW OF THE INTEGRATED PHOTONIC CHIP.....	228

FIG. 6. 75 MEASUREMENT SETUP USED FOR PIC CHARACTERIZATION AND WITH CONFIGURATION FOR OPTICAL FREQUENCY COMB GENERATION (RED AND BLUE SQUARES).....	228
FIG. 6. 76 PART OF THE MEASUREMENT SETUP WITH CLOSE UP VIEW ON THE PIC ON ALN SUBMOUNT.....	229
FIG. 6. 77 OPTICAL FREQUENCY COMB AT DIFFERENT BIAS CONDITION OF SOAs AT 1 GHz (TOP) AND 2 GHz (BOTTOM) FOR GENERATOR SIGNAL.	230
FIG. 6. 78 COMPARISON OF OPTICAL FREQUENCY COMBS AT DIFFERENT FREQUENCIES FOR 200 mA OF BIAS CURRENT. ..	230
FIG. 6. 79 OPTICAL (A) AND (B) ELECTRICAL SPECTRUM FOR CROSS INJECTION LOCKING WITH SUB-HARMONIC INJECTION LOCKED WITH 20 dBm OF ELECTRICAL INJECTION.....	231
FIG. 6. 80 ELECTRICAL SPECTRUM OF THE BEAT-NOTE FOR LOCK-IN CONDITION AT 33.5 GHz.....	232
FIG. 6. 81 COMPARISON BETWEEN THE SYNTHESIZER AND THE SELF-INJECTED BEAT-NOTE PHASE NOISE.....	232

CHAPTER 1

INTRODUCTION

Rapid year-on-year growth of new mobile subscriptions, reaching 95 million just in the third quarter of 2017, will push to the limit current telecommunication solutions based on the 3rd and the 4th generations of wireless networks (Fig. 1. 1a) [1][2]. Ongoing research and increasing potential of new possible applications of telecommunication technologies will have a strong economic impact on global industry, manufacturing, healthcare, security, and media [3][4]. According to the forecasts, most of the mobile data traffic will come from smartphones, significantly overcoming PCs and tablets. Recent mobile data traffic measurements place video streaming in the first place of the overall traffic, and it is predicted to keep the position in the upcoming years (Fig. 1. 1b). Moreover, huge investment in self-driving cars solutions, massive machine type communications and IoT (Internet of Things) are strictly connected with the development of new 5th telecommunication standard [5][6].

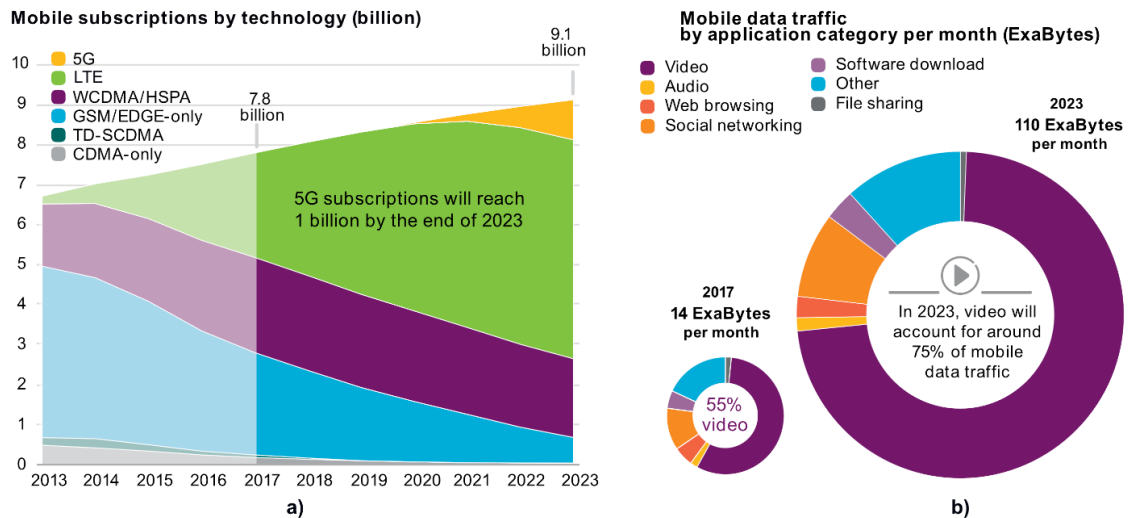


Fig. 1. 1 Ericsson global mobile subscriptions forecast by technology (a) and mobile data traffic by application category (b) [1].

In order to fulfil market needs and keep the rapid growth of the possible new market applications, much higher transmission rates are necessary and bands at higher frequencies with wider spectral bands must be exploited. International allocation of electromagnetic spectrum place mm-waves between 30 GHz and 300 GHz, the wavelength of which is between 10 mm to 1 mm. Since 2012, there are ongoing legislation and standardization work on the band allocations agreements for 5G. This long-term procedure involves several institutions

such as International Telecommunication Union (ITU), Federal Communications Commission (FCC) and the Radio Spectrum Policy Group (RSPG) of the European Commission to work on comprehensive wireless strategy to facilitate the launch of the 5G deployment. In the EU region, the RSPG considers 700 MHz and 3.4 – 3.6 GHz band to be the primary bands suitable for the introduction of 5G-based services, and 24.25 – 27.5 GHz band as a pioneer band at higher frequencies (Fig. 1. 2)[7]. Additional to that, bands between 31.8 – 33.4 GHz and 40.5 – 43.5 GHz are considered to be soon available for entry tests. Moreover, unlicensed bands for services in 66 - 71 GHz, 71 - 76 GHz and 81 - 86 GHz attract a lot of attention for possible usage for 5G telecommunication systems. Final decisions concerning future 5G bands allocations are to be taken during World Radiocommunication Conference in 2019 (WRC-19).

Practical applications of mm-waves in the future 5th generation wireless networks have to address several challenges. High atmospheric attenuation and a cost of a new infrastructure adapted for mm-waves frequencies makes the development and commercial implementation of such systems very demanding [8]. Fortunately, already performed demonstration of existing systems at mm-wave frequencies can provide potential solutions for capacity limits of the current telecommunication systems. The outdoor channel measurements in heavy urban environment of New York city area [9][10][11] at 28, 38 and 73 GHz concluded that even at the comparable level of cell density, the mm-wave systems could offer an order of magnitude increase in capacity. Nevertheless, the design of system cells needs meaningful changes, due to limited range of mm-waves, to fully exploit the potential of 5th generation mobile systems. Study of deployment models performed by several research groups [12][13][14] also ascertained that new heterogeneous model of ultra-dense network (UDN) has to be applied instead of standard homogeneous approach. The realization of UDN concept is based on dense deployment of small cells, and consequently the end user is as close as possible to access nodes, as illustrated in Fig. 1. 3. In other words, UDN requires much bigger cell density, than the number of active users, which also introduce additional challenges to confront by 5G. Case study performed in [14], indicated as well, that micro cells and indoor deployments are necessary to meet not only customer expectations, but also to increase the network capacity. Although, future communication systems for the 5G wireless networks have to address several obstacles, application of high frequencies enables design and production of complex compact systems based on **microwave photonics**. The physical sizes of elements at high frequencies permit to integrate antenna elements within a single chip, significantly reducing production cost and greatly improve compactness. What is more, **photonic integrated circuits** can meet various requirements of modern communication systems, including wide frequency tuning capabilities, high data rate transmissions and low phase noise signals. Nevertheless, high

output power signal is necessary and for many years numerous solutions based on electronics and photonics have been under intensive research and development. This is the aim of this work to investigate possible ways of increasing the power of RF signals generated around 100 GHz by microwave photonics means. The motivation of my dissertation is to develop high-power photonic integrated circuits that can fulfil the requirements of modern telecommunication systems. The first approach to increase output power levels is based on the power combining technique. This solution target E-band frequencies (60 GHz – 90 GHz). Second approach is based on the antenna-array devices to be applied in the W-band (75 GHz – 110 GHz) with the possibility of application at higher frequencies.

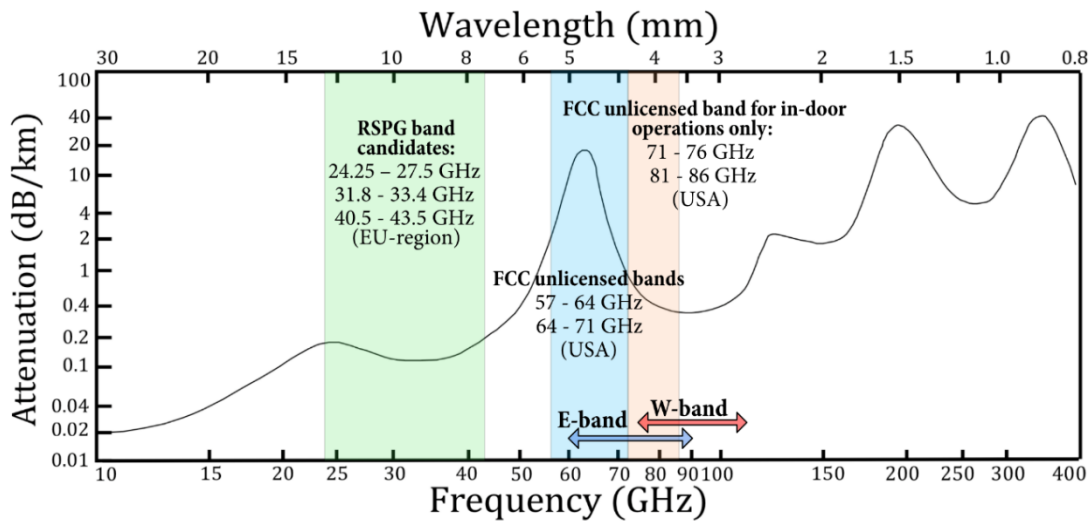


Fig. 1. 2 Atmospheric attenuation of mm-waves frequencies. Band candidates for future 5G applications are highlighted.

Heterogeneous networks

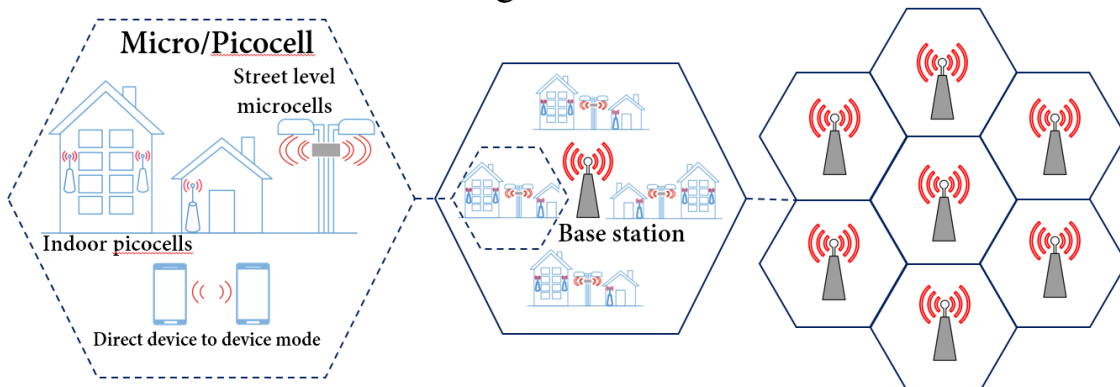


Fig. 1. 3 Heterogeneous network with indoor, street level and direct device to device mode.

1.1 DISSERTATION ORGANIZATION

Chapter 2 is dedicated to compare electronic-based and photonic-based solutions in the mm-W frequencies. Detailed state of the art of the existing solutions to generate millimetre wave signals are discussed. Chapter 3 presents the limitations and the most promising solutions to generate high-output power levels. Chapter 4 describes the design and simulation results of novel PICs with integrated power combiners and antenna-arrays. Chapter 5 presents the fabrication process of the designed circuits. Chapter 6 is dedicated to present the measurements and the results of the characterized circuits. Final conclusions are given in the last chapter.

REFERENCES

- [1] P. Jonsson, S. Carson, J. Singh Sethi, M. Arvedson, R. Svenningsson, P. Lindberg, Kati Ö., P. Hedlund, Ericsson Mobility Report, 2017.
- [2] Cisco Visual Networking Index, “Forecast and Methodology”, 2017.
- [3] Arthur D. Little, “Creating a Gigabit Society – The role of 5G”, Vodafone Group PLC, 2017.
- [4] J. Restrepo, “World Radio 5G roadmap: challenges and opportunities ahead Conferences, WRC”, ITU Regional Radiocommunication Seminar, 2017.
- [5] L. Li, W. L. Huang, Y. Liu, N. N. Zheng and F. Y. Wang, "Intelligence Testing for Autonomous Vehicles: A New Approach," *IEEE Transactions on Intelligent Vehicles*, vol. 1, no. 2, pp. 158-166, 2016.
- [6] Z. Dawy, W. Saad, A. Ghosh, J. G. Andrews and E. Yaacoub, "Toward Massive Machine Type Cellular Communications," in *IEEE Wireless Communications*, vol. 24, no. 1, pp. 120-128, 2017.
- [7] 5G Americas White Paper on 5G Spectrum Recommendations, 2017.
- [8] Morgado, K. M. Saidul Huq, S. Mumtaz, J. Rodriguez, A survey of 5G technologies: Regulatory, standardization and industrial perspectives, Digital Communications and Networks, 2017.
- [9] T. S. Rappaport *et al.*, "Millimeter Wave Mobile Communications for 5G Cellular: It Will Work!," *IEEE Access*, vol. 1, pp. 335-349, 2013.
- [10] MacCartney and T. S. Rappaport, "73 GHz millimeter wave propagation measurements for outdoor urban mobile and backhaul communications in New York City," 2014 IEEE International Conference on Communications (ICC), Sydney, NSW, 2014, pp. 4862-4867
- [11] M. R. Akdeniz *et al.*, ‘Millimeter Wave Channel Modeling and Cellular Capacity Evaluation’, *IEEE Journal on Selected Areas in Communications*, vol. 32, no. 6, pp. 1164–1179, 2014.
- [12] S. Rangan, T. S. Rappaport, and E. Erkip, ‘Millimeter-Wave Cellular Wireless Networks: Potentials and Challenges’, *Proceedings of the IEEE*, vol. 102, no. 3, pp. 366–385, 2014.
- [13] P. Philip and David Britz, “Millimeter Wave and Terahertz Communications: Feasibility and Challenges”, vol.10, no.4, p. 3-12, 2012.
- [14] Ultra Dense Network (UDN) White Paper, Nokia.

CHAPTER 2

MILLIMETER WAVE ELECTRONICS

Along with the introduction of CMOS technology in 1963 by Frank Wanlass [1] and monolithic microwave integrated circuits (MMICs) development in early 1970s [2], electrical based solutions to generate mm-wave frequency signals have attracted a lot of attention of many research groups. Before abovementioned technologies, signal generation at these frequency ranges were mostly achieved by the klystron vacuum-tube sources, invented by Varian brothers but they were expensive and unreliable for mass scale applications in the telecommunication systems for trunk traffic [3]. Gunn diodes, impact ionization avalanche transit time diodes (IMPATT) or tunnel-injection transit time devices (TUNNETT) have been the successors, used as a microwave sources for a few decades as the silicon and GaAs technology advanced [4]. Nowadays, the transistor-based oscillators have overtaken the research and development at mm-wave frequencies. Moreover, due to constant progress in the epitaxial and lithography processing, the design and production of highly integrated III-V semiconductor-based devices with very competitive figure of merits to CMOS technology has been possible [5]. Novel oscillators and amplifiers are based-on various transistor architectures including mostly field effect transistors (FETs), bipolar junction transistors (BJTs), heterojunction-bipolar transistors (HBTs) and high electron mobility transistors (HEMTs). Some of the novel oscillators are able to deliver low noise signals at very high frequencies of oscillations exceeding 1 THz [5]-[7]. Nevertheless, electrical solutions require several building blocks, and the higher the target frequency, the circuit design becomes more challenging and more limited by fabrication capabilities or semiconductor material properties. Moreover, cooling to cryogenic temperatures greatly improves the performance of the electronic sources, but this cannot be applied in the majority of consumer applications.

Following sub-chapter describes briefly fundamental principles of mm-wave signal generation by electronic means and design principles of the most relevant diode-based and transistor-based oscillators in the millimeter frequencies at room-temperature operation. Low noise amplifiers and power amplifiers are briefly presented as well.

2.1 OSCILLATORS AT MM-WAVES

An oscillator is the fundamental building block in the wireless transceiver (Fig. 2. 1) that delivers tuneable mm-wave frequency signal within subsystem called frequency synthesizer (Fig. 2. 2) [8]. Low noise amplifier (LNA) and power amplifier (PAs) are other crucial components in the transceiver design.

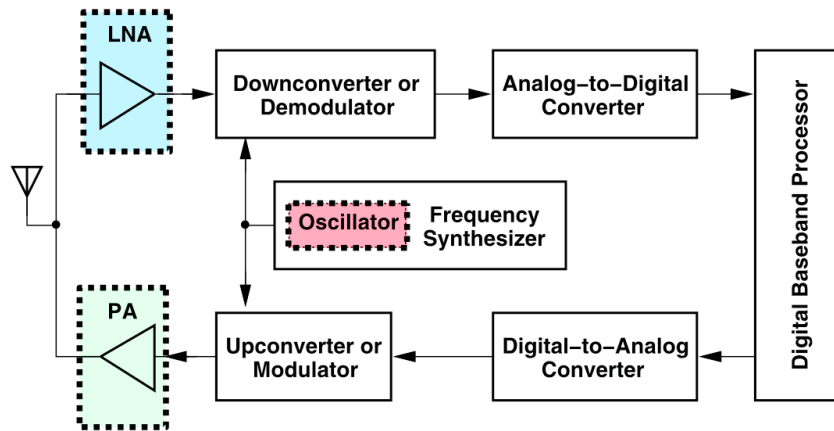


Fig. 2. 1 Generic RF transceiver [8].

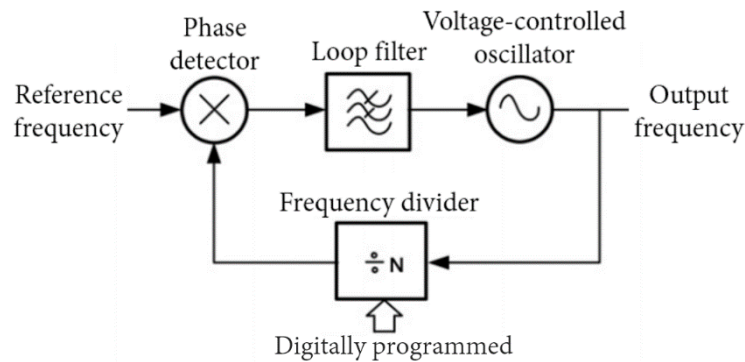


Fig. 2. 2 PLL-based frequency synthesizer with frequency divider in the feedback path [37].

There are several different oscillator topologies based on diode and transistor employment. The working principle in the majority of the oscillators is based on a resonant LC circuit, also called a harmonic oscillator [9]. It generates the near-sinusoidal signal after dc voltage is applied at the frequency close to circuit resonance. Signal decays over time due to losses in capacitor (C) and in inductor (L), represented as a resistor (R) in Fig. 2. 3.

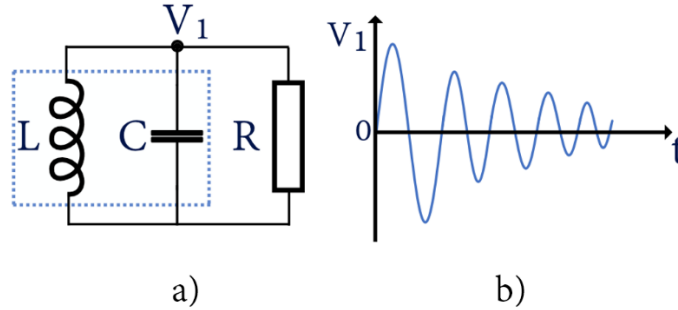


Fig. 2. 3 (a) Schematic model of linear LC resonator circuit and (b) its output signal attenuation over time due to losses.

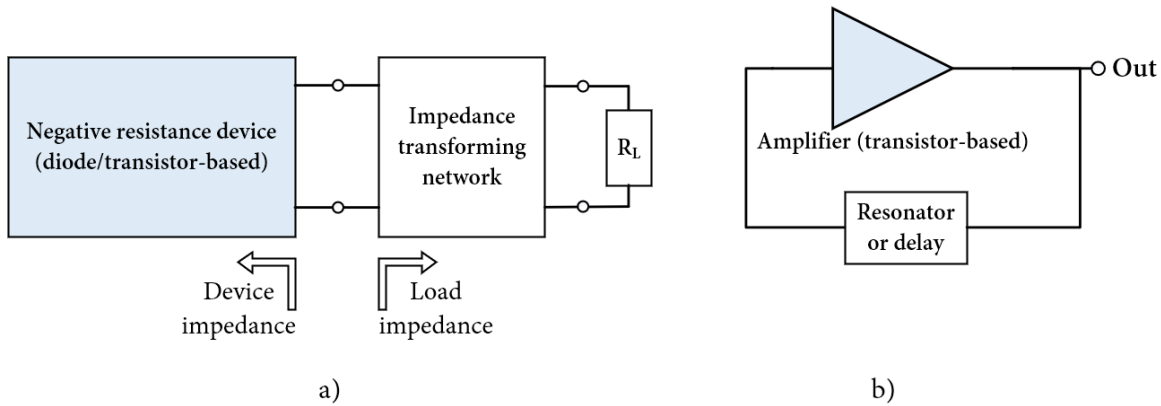


Fig. 2. 4 Schematic model of (a) diode/transistor-based oscillator model with negative resistance and (b) transistor-based oscillator with positive feedback.

In order to maintain and reach stable oscillation conditions and overcome the losses, implementation of an active device is necessary. There are two main methods to design and analyze an oscillator in the circuit design:

1. One-port model, oscillator with negative resistance, in which diodes and transistors can be applied (Fig. 2. 4a).
2. Two-port model, transistor-based oscillator with positive feedback (Fig. 2. 4b).

2.2 DIODE-BASED OSCILLATORS

In this oscillator design approach, semiconductor devices such as Gunn, IMPATT, TUNNETT, resonant tunneling diodes (RTDs), superlattice electronic devices (SLEDs) are utilized, although a transistor fed back with a suitable passive network can be applied as well in this configuration [10]. Negative resistance in diode devices is obtained due to layers' properties of the semiconductor structure, usually based upon GaAs and InP. The physical mechanisms behind negative resistance occurrence differs between the diodes. Moreover, Gunn and RTDs current-voltage characteristics have a common N-shaped curvature, where a negative differential conductance (NDC) or in other words, negative differential resistance (NDR) region is present (Fig. 2. 7b), whereas for the transit-time devices this region is not present.

2.2.1 Gunn diodes

In the Gunn diodes, commonly labelled as Transferred Electron Devices (TEDs), the Gunn-effect [11] is exploited to acquire negative resistance. This effect, firstly observed by J.B. Gunn in 1962 [12], originates from transfer of electrons between the main valley (Γ) and the satellite valley in the GaAs and InP band structure, after external bias of adequately high value is applied. This process causes average electron mobility degradation as more electrons are transferred to low-mobility satellite valley and as a result a negative differential resistance appears across the device. Dimensions of the device and doping levels play a crucial role in oscillation frequency, as well as the resonant circuit terminating the device electrodes. InP and GaAs are the most commonly used semiconductor materials for Gunn diode fabrication, although there are more than 10 semiconductor materials known for transferred-electron effect [13]. Moreover, there are reported results of planar Gunn diodes that unlike the vertical structures can be fabricated as a part of MMIC chip and used as a frequency source [17].

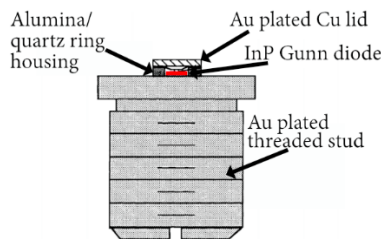


Fig. 2. 5 Cross section of packaged InP Gunn diode [18].

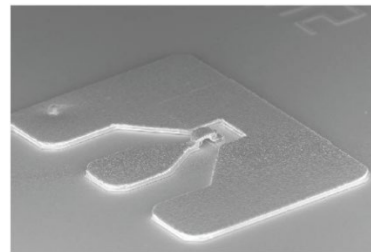


Fig. 2. 6 Planar Gunn diode coplanar layout for S-parameter measurements with air bridge interconnection [19].

2.2.2 SLEDs (Superlattice Electronic Devices)

SLEDs structures were proposed in 1970 by Esaki and Tsu [20]. NDR occurrence is due to the Bragg reflections of minibands electrons in a semiconductor superlattice. As a result, a creation of regions of negative differential velocity, similar to travelling domains in Gunn devices appears causing negative differential resistance between the device terminals to form. The physical mechanism behind NDR is based on Bloch effect, and the relevant time constants are much shorter than those in the transfer-electron effect devices [21].

2.2.3 IMPATT and TUNNET diodes

The IMPATT diodes deliver negative resistance due to phase shift greater than 90° between the current and the applied voltage [4], and there is no negative slope in the I-V characteristic. The device comprises reversed biased, highly doped P-N junction and a low doped drift zone next to it. The most common semiconductor materials used are Si and GaAs. After high bias voltage application, close to the breakdown in PN junction due to avalanche multiplication, carriers are injected into the drift zone at saturated velocity. Thanks to constant value of this velocity it is possible to establish a linear relationship between the device length and the current delay, which as a result can be used by the designers to fix the device length for negative resistance at dedicated frequency band. The TUNNET devices are another kind of transit-time diodes, where the tunneling effect is used for the current generation instead of avalanche effect, and as a result, a lower noise operation at higher frequency of oscillations can be obtained. There are several other types of transit-time diodes [22], but the above described are found in the most mm-wave applications.

2.2.4 RTDs (Resonant Tunneling Diodes)

RTDs [23] are another type of diodes where tunneling effect is exploited. These devices are usually composed of two heterobarriers with a quantum well in between. In Fig. 2. 7a typical RTD band diagram is presented. With the bias voltage increase, the discrete energy levels inside the quantum well (resonant states) starts to be in alignment with the adjacent energy levels of the emitter region. At a certain bias point, the resonant tunneling occurs, and the maximum peak in the I-V characteristic can be observed followed by a sudden drop. It is caused due to misalignment of the discrete quantum well energy levels. With increasing bias voltage, they shift below the conduction-band bottom on the emitter side and no more electron tunneling occurs. Moreover, the oscillation frequency is defined by the resonant frequency of the loaded circuit of an RTD, which in most applications act as an antenna.

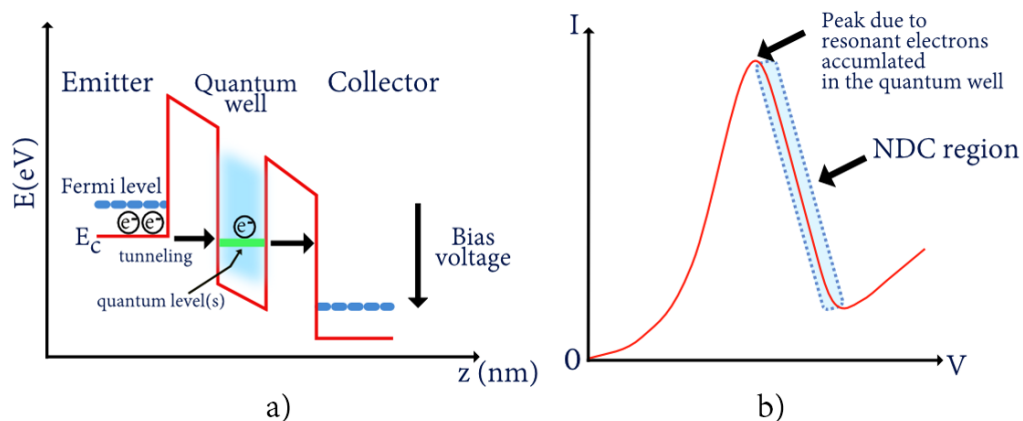


Fig. 2. 7 (a) Conduction band diagram of double heterojunction barrier RTD under bias voltage. With increasing bias voltage, quantum levels inside QW move below the E_c band resulting in sudden current drop in the I-V characteristics (b).

2.2.5 Summary of diode-based oscillators

There are several reports comparing output powers between Gunn, IMPATT, TUNNET, RTDs and SLED devices [13], [18], [21], [24], [27]. Based on reported results, Gunn and IMPATT diodes can deliver the highest output powers at mm-wave frequencies in fundamental mode of operation, reaching 27 dBm at 35 GHz and 63 GHz, respectively. It is possible to generate signals above 300 GHz in 2nd and 3rd harmonic mode, but it requires application of waveguide transitions [25]. The maximum reported frequency can reach up to 479 GHz with -10 dBm of output power for Gunn diode in the 3rd harmonic mode of operation. For the SLEDs in fundamental mode of operation, output powers of 19 dBm at 63 GHz, and 0 dBm at 155 GHz are reported [26]. At higher frequencies, the second-harmonic power extraction is applied, up to 317 GHz with -10 dBm of measured output power [26]. Furthermore, phase noise performance differs between diode-based sources. InP Gunn diodes noise levels are generally below -110 dBc/Hz up to 150 GHz, with 500 kHz off-carrier frequency, and are considered to have better noise performance in comparison to IMPATT diodes [13]. Tuning range of Gunn devices is achieved mechanically, and is generally reduced to few GHz [13], whereas IMPATT diodes are tuned with a bias current with tuning ranges of 10 GHz [14]. TUNNET devices operate at higher frequencies and at lower noise levels in comparison to IMPATT diodes and are able to deliver high output powers at frequencies above 200 GHz with reduced bias-tuning capabilities [16][21]. Moreover, development of GaN-based devices and simulation results shows potential increase in the output power levels in fundamental mode of operation, up to 20 dBm at 200 GHz and 13 dBm at 300 GHz are expected. IMPATT diodes find application as transmitters in radar applications. The highest frequencies of oscillations are reported for RTD diodes up to 1.92 THz with -34 dBm of output

power [32]. Other results at 1.1 THz and 1.46 THz are reported, with -34 dBm and -40 dBm of output power, respectively [33],[34]. RTDs are promising candidate for frequencies in the THz range, but in comparison to Gunn or IMPATT diodes at lower frequencies, the RTDs output powers are relatively lower. Nevertheless, RTDs due to low noise performance find applications as receivers and dominate at higher frequencies above 300 GHz in comparison to other diode-based sources.

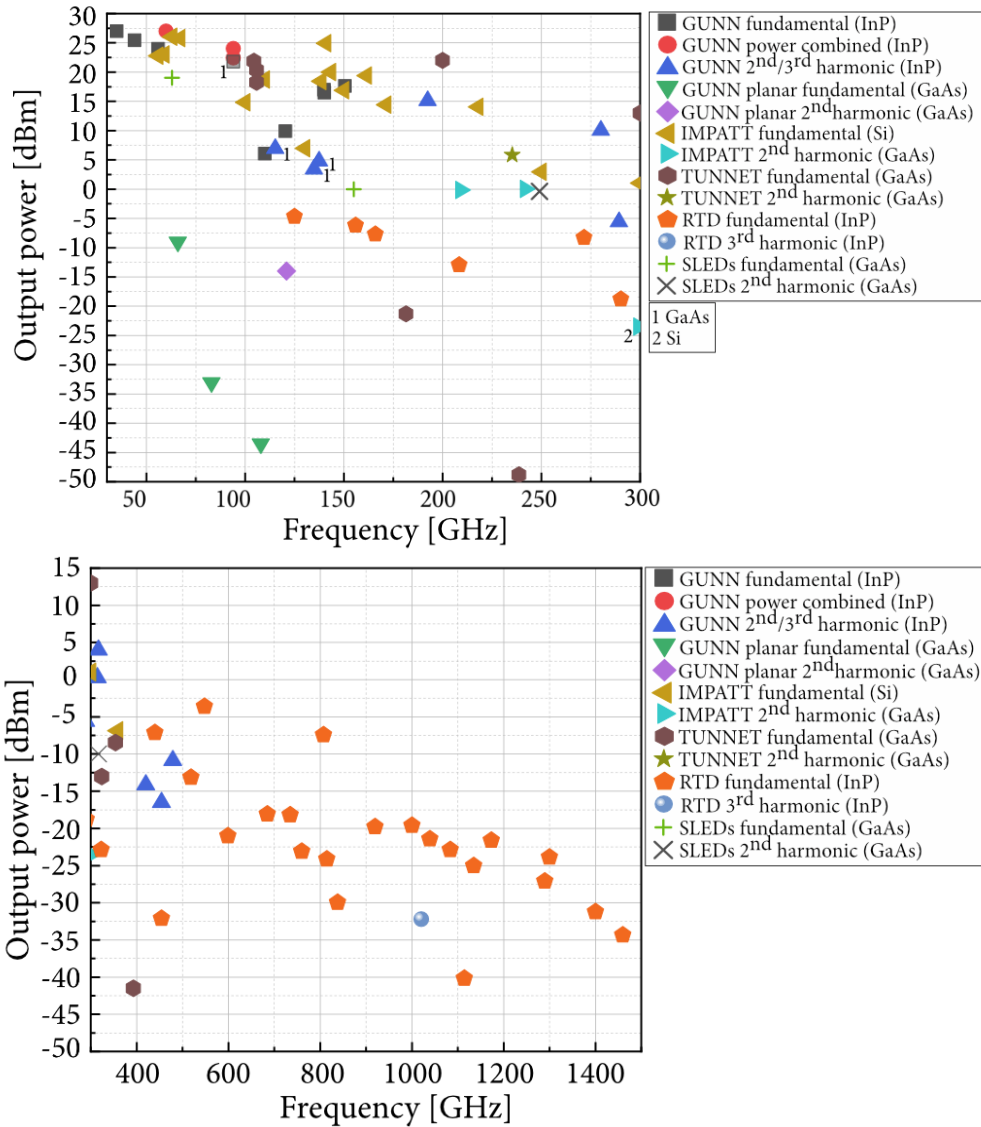


Fig. 2. 8 The overview of diode-based oscillator in the mm-wave and THz frequency range. Data point based on [13], [15], [18], [21], [24], [25], [26], [27],[28], [29],[30], [31], [33], [34].

2.3 TRANSISTOR-BASED OSCILLATORS

Transistor-based oscillators find application in the majority of the integrated circuits used for telecommunication systems nowadays. It is due to the fact, that other circuit elements, implemented to overcome the losses of the oscillating signal, such as power amplifiers, can be easily integrated on the same circuit. Moreover, along with the technology and lithography processing improvement, several transistor types can be applied in the circuit topology. The choice between them, and the semiconductor materials depends on the desired oscillating frequency and oscillator application. Transistor-based oscillators can be divided in three different topology categories: ring oscillators, relaxation oscillators and tuned oscillators [8]. The first two categories are generally less favourable in mm-wave design as the tuned oscillators have better frequency stability and spectral purity. Moreover, as in the case of diode-based oscillators, passive LC resonators are mostly employed. Basic model of an oscillator is presented in Fig. 2. 9. It can be analyzed as an amplifier with a positive feedback loop and a frequency-selective network (LC circuit) [36].

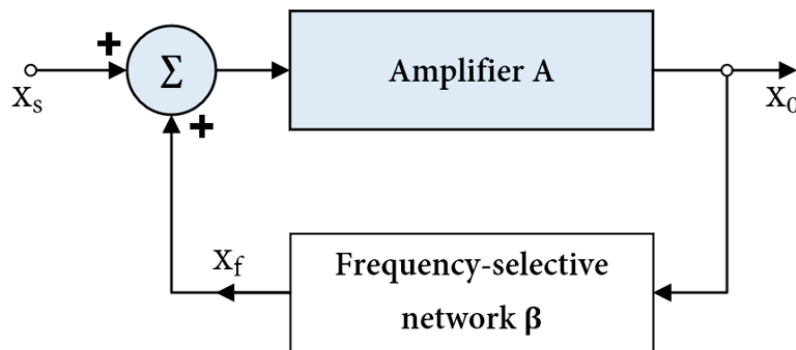


Fig. 2. 9 An oscillator model with positive feedback loop and frequency-selective circuit.

The oscillator is designed in the way, that at the zero input (only noise present in the circuit), the output signal is produced. The gain with a positive-feedback loop is given by:

$$A_f(s) = \frac{A(s)}{1 - A(s)\beta(s)} \quad (2.1)$$

The loop gain, can be determined by:

$$L_g(s) \equiv A(s)\beta(s) \quad (2.2)$$

The characteristic equation leading to oscillations is:

$$1 - L_g(s) = 0 \quad (2.3)$$

For the loop gain $A\beta=1$, at specific frequency f_0 , the A_f will be infinite. It is a definition of an oscillator where for the zero input signal the circuit will have finite output. The condition for the feedback loop to provide sinusoidal signal at frequency ω_0 is based on Barkhausen criterion given by:

$$L(j\omega_0) \equiv A(j\omega_0)\beta(j\omega_0) = 1 \quad (2.4)$$

where at ω_0 , the phase shift of the loop gain should be zero or an integer multiple of 2π , and the magnitude of the loop gain should be unity. For the feedback loop from Fig. 2. 9, in order to produce and sustain an output x_0 , with no input applied ($x_s = 0$), the feedback signal $x_f = \beta x_0$, and $x_0 = Ax_f$, which results in $A\beta x_0 = x_0$, for $A\beta = 1$. It is worth to mention, that the Barkhausen criterion is a necessary condition for oscillation, but it is not a sufficient condition [35].

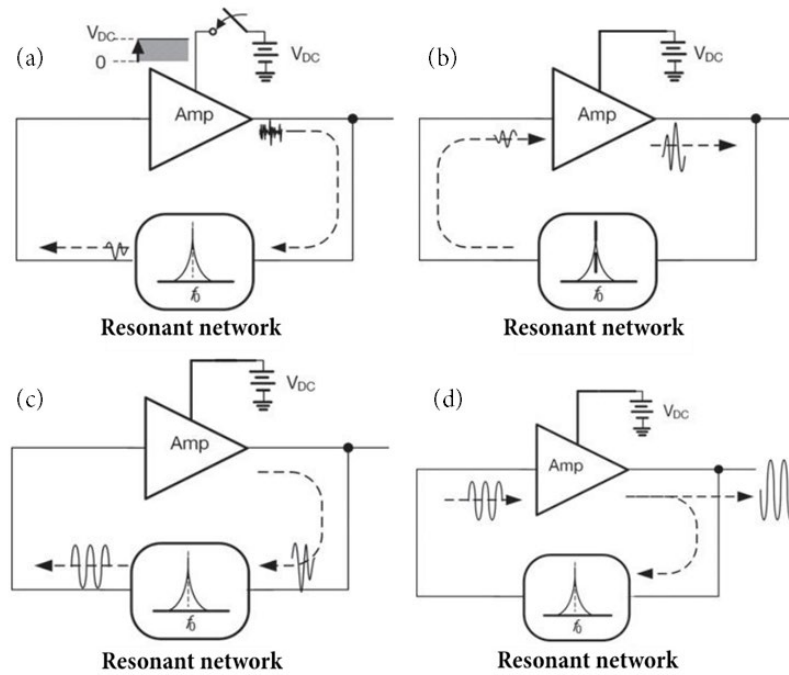


Fig. 2. 10 Oscillation mechanism periods, from (a) initial, (b) amplified, (c) feedback, and (d) the stable state [37].

2.3.1 LC-tank oscillators

There are several topologies of LC oscillators, among which Colpitts, cross-coupled and push-push are the most commonly applied in high-speed low-voltage applications. Moreover, in modern oscillators, a frequency-tuning possibility is needed. For this reason, a varactor is

used instead of the capacitor in the LC resonator, and frequency tuning is achieved by varying varactor bias-voltage. PN-junctions used as varactors are less preferable in the circuit design and are commonly replaced with MOS varactors [10]. Furthermore, regardless the topology, all oscillators need to have negative input resistance in order to cancel resistive losses in the circuit [10].

2.3.1.1 Colpitts and Hartley oscillators

In the Colpitts configuration presented in Fig. 2. 11, a capacitive voltage divider is employed to obtain the positive feedback [39]. The small-signal equivalent circuit is used for circuit analysis to find condition for oscillation and oscillation frequency.

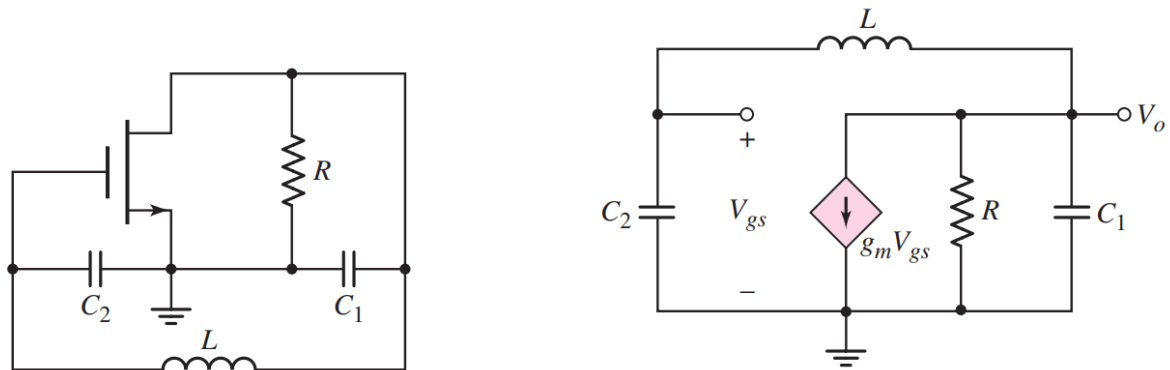


Fig. 2. 11 The AC equivalent circuit and small-signal model of Colpitts MOSFET oscillator [39].

The oscillation frequency is given by:

$$\omega_0 = \frac{1}{\sqrt{L \left(\frac{C_1 C_2}{C_1 + C_2} \right)}}, \quad (2.5)$$

which is the resonant frequency of the LC circuit. The ratio $\frac{C_1}{C_2}$ determines the feedback factor and in order to ensure the start of the oscillations, this must be adapted with the transistor gain.

In the Hartley oscillator, the inductive voltage divider is used to obtain the positive feedback. Similarly, to Colpitts topology, a parallel resonator is used to tune the frequency. The frequency of oscillations is defined as:

$$\omega_0 = \frac{1}{\sqrt{C(L_1 + L_2)}} \quad (2.6)$$

The ratio $\frac{L_1}{L_2}$, is the feedback factor adapted with the transistor gain.

2.3.1.2 Cross-coupled and Push-push oscillators

This type of LC-tank oscillator widely used in the integrated circuits is presented in Fig. 2. 12[8][40]. It consists of a pair of MOSFET transistors in a differential amplifier configuration with an LC tank. The drain of each of the transistor is connected to the gate and the circuit is commonly referred as cross-coupled differential oscillator. Moreover, due to cross-coupled connection and positive feedback, the negative resistance occurs between the transistor drains.

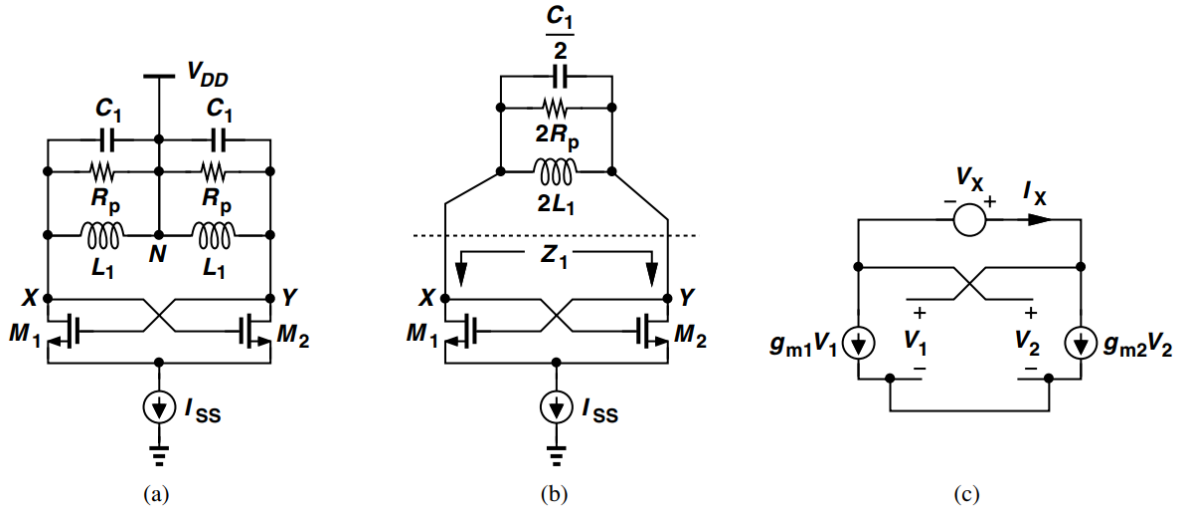


Fig. 2. 12 Cross-coupled oscillator (a), (b) merged load tanks, (c) equivalent circuit of cross-coupled pair [8].

As mentioned in the introduction, oscillators with frequency tunability are realized mainly with MOS varactors. This type of oscillator is commonly referred as voltage-controlled oscillator (VCO), for which frequency of oscillation is given as:

$$\omega_0 = \frac{1}{\sqrt{L_1(C_1 + C_{VAR})}}, \quad (2.7)$$

where C_{VAR} is the average value of respective varactor capacitance.

Push-push VCO topologies are other types of VCO oscillators finding application in high frequency systems. In this topology (Fig. 2. 13), higher-order harmonics of the fundamental frequency can be utilized giving the possibility to use the oscillator at higher frequencies [10]. N-push oscillators are possible, but with higher harmonic the output power level is decreasing. Moreover, in comparison to solutions using frequency multiplications [41], push-push oscillators can offer lower phase noise level and require smaller chip areas.

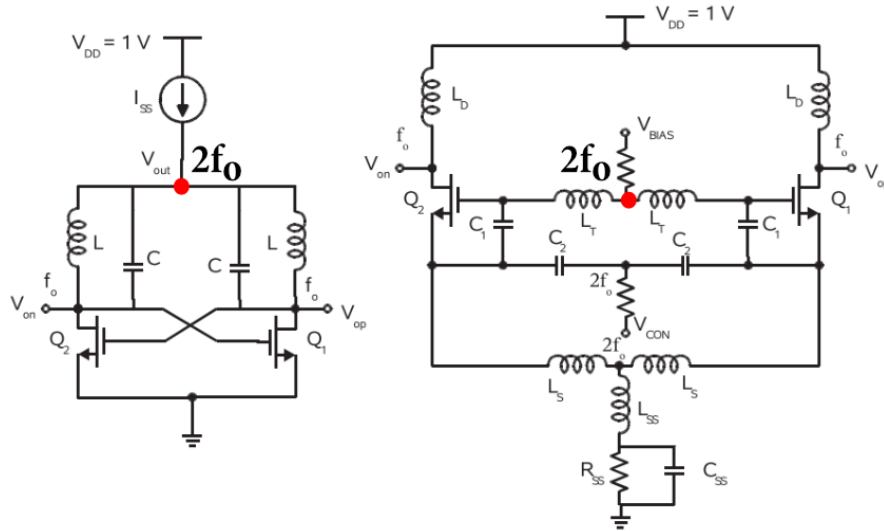


Fig. 2. 13 Cross-coupled and Colpitts VCO schematics with nodes (red dot) where the second harmonic signal can be collected [10].

2.3.2 Summary of transistor-based oscillators

A practical example of realization and design methodology of CMOS Colpitts VCO and cross-coupled VCO at 77 GHz, as well as frequency scaling technique is presented in [42]. Based on the results, Colpitts configuration achieved better tuning range of 8.1%, and lower phase noise level of -100 dBc/Hz (at 1 MHz offset), in comparison to 2.6% and -84 dBc/Hz for cross-coupled configuration. The output powers of -13.8 dBm (Colpitts VCO) and -13.4 dBm (cross-coupled VCO) were measured. In the cross-coupled VCO, the tuning range is limited by the transistor size. It is due to transistors' parasitic capacitance directly lumped to the tank capacitance. Moreover, in the cross-coupled configuration a presence of the output buffer is necessary to match the VCO output impedance, which further degrades the tuning range.

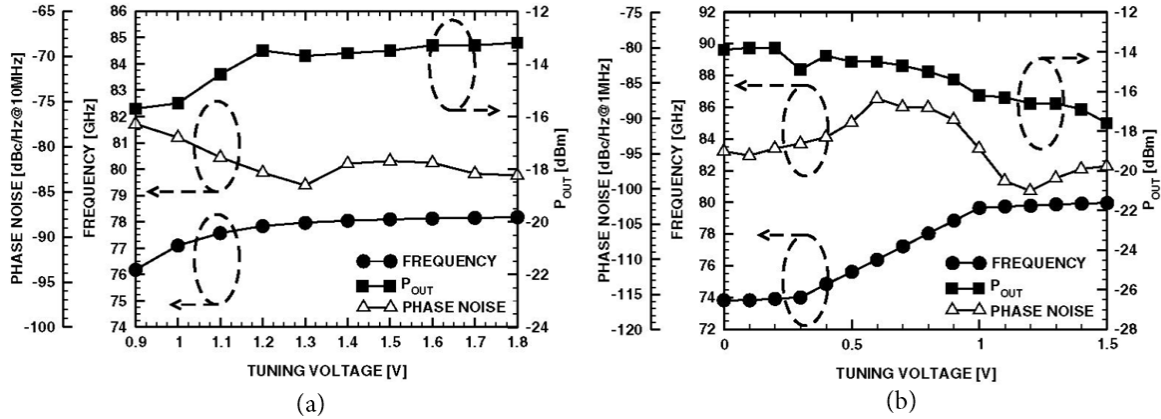


Fig. 2. 14 Frequency, output power and phase noise of (a) Colpitts and (b) cross-coupled VCO [42].

A good comparison of monolithically integrated SiGe push-push oscillators based on Hartley topology at 75 GHz and 278 GHz are presented in [43][44]. The output frequency in [43] of the oscillator was varactor tuned from 71.3 GHz to 75.8 GHz. In the reported tuning range, the output power was 3.5 dBm and the measured single sideband phase noise was less than -105 dBc/Hz at 1 MHz offset frequency. The frequency of the output signal in [44] was tuned between 275.5 GHz and 279.6 GHz, with output power of -20 dBm. Moreover, in the oscillator presented in Fig. 2. 14b, the inductors are replaced by microstrip lines to obtain higher Q-values. There are several reports of transistor-based solutions for high-data rate and sensor application systems at mm-wave frequencies with dedicated scaling solutions and technology comparison [21][38][43][45][46][47]. The majority of the reported VCOs configurations are based on Colpitts, cross-coupled and push-push topologies. The overviews of the output powers and phase noise levels are presented in Fig. 2. 15 and Fig. 2. 16 respectively. As can be noticed, majority of the output powers are below 0 dBm, with phase noise figures in the range of -90 dBc/Hz to -100 dBc/Hz at 1 MHz frequency offset. It also confirms that in order to increase the output power signal, implementation of an amplifier circuit is necessary.

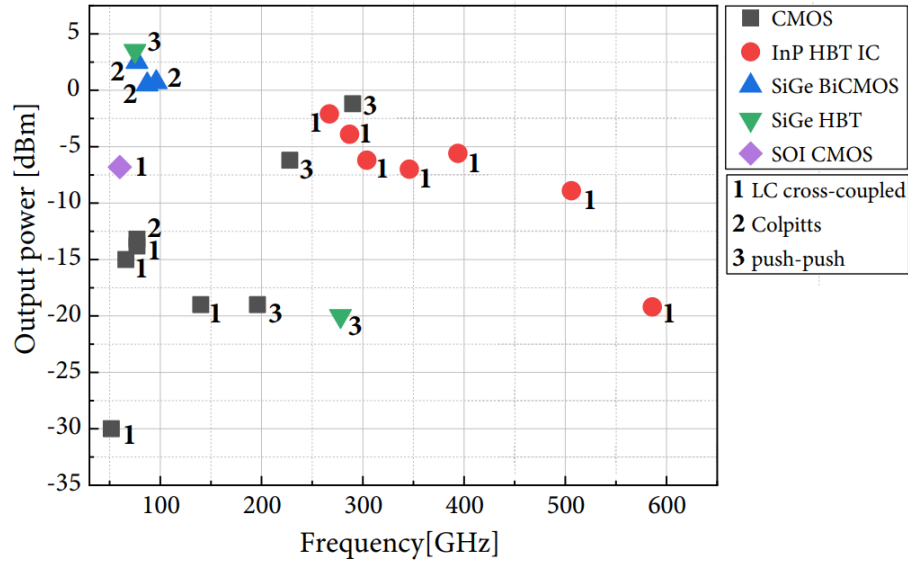


Fig. 2. 15 An overview of output powers at mm-waves of different oscillators' configurations with respect to the fabrication technology. Data points based on [38][43][45][46][47][48][49].

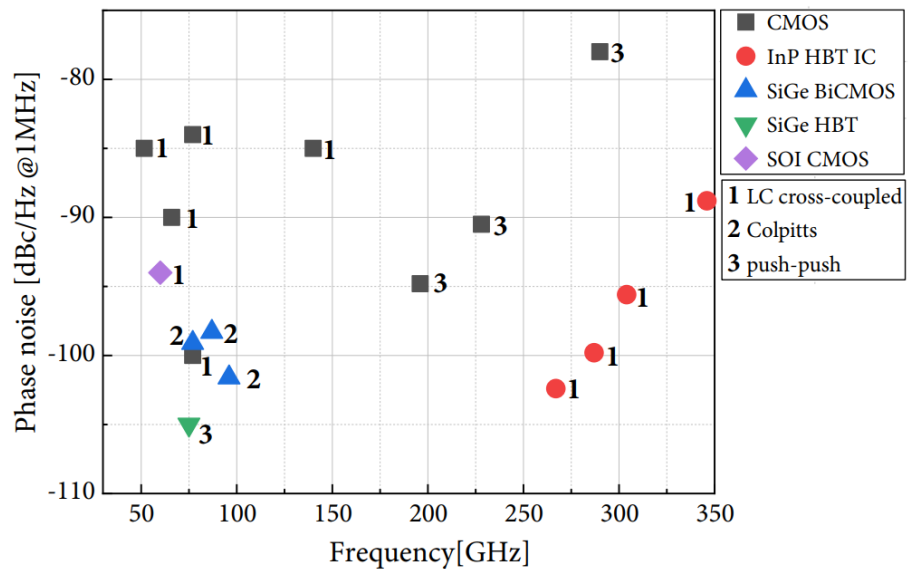


Fig. 2. 16 An overview of phase noise figures at mm-waves of different oscillators' configurations with respect to the fabrication technology. Data points based on [38][43][45][46][47][48][49].

2.4 FREQUENCY MULTIPLIERS

Frequency multiplication is another technique that can be applied to generate specific harmonic of an input signal at millimeter and THz frequency range [7]. Schottky diodes and Hetero-Barrier Varactors (HBVs) have found application in many multiplier designs for narrow band and broadband operation [21]. Nonlinear capacitance or varactor is applied to generate harmonics, and these devices are in form of doublers (Fig. 2. 17) or triplers to obtain higher multiplication factor [7]. Unfortunately, these devices suffer from the output power degradation and phase noise level with each multiplication step. The conversion efficiency lowers as well at higher frequencies. Some current results of HBVs can be found in [50]. Values of 22 dBm of output power at 100 GHz for 29 dBm of input power have been obtained. Recent results of commercially available Schottky based devices have been reported in [51]. Up to 22 dBm of output power with 26 dBm of input power from 130 GHz to 160 GHz have been stated.

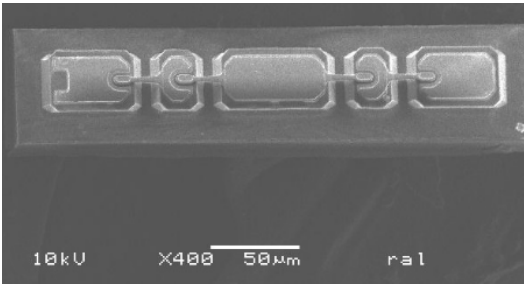


Fig. 2. 17 SEM micrograph of a doubler GaAs Schottky circuit [52].

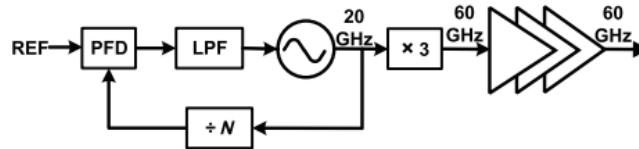


Fig. 2. 18 mm-wave PLL frequency multiplier at 60 GHz [53].

Frequency multiplication is also applied in frequency synthesizers as a possibility to improve phase noise performance and power efficiency (

Fig. 2. 18). Good example with a 20 GHz signal multiplied to 60 GHz, based on third-harmonic extraction, is reported in [53]. The phase noise level of -100 dBc/Hz at 1 MHz offset have been achieved. Current results of frequency multipliers application can be found in [53] and [54]. For the majority of the reported results with frequency multiplication schemes, phase noise levels at 1 MHz frequency offset are from -91 dBc/Hz to -95 dBc/Hz.

2.5 LNAs AND PAs IN MM-WAVES

As presented in the previous sub-chapter, signal output powers from majority of the mm-wave sources based on transistor solutions require amplification. There are two main types of amplifiers used in the mm-wave systems:

Low noise amplifiers (LNAs) – employed in the receiver circuitry, where as low as possible level of additional noise is introduced during signal amplification. It consists of at least one

active device (transistor), which is responsible for the gain of LNA, but also noise and nonlinearities. Moreover, a number of passive components such as inductors, capacitors and resistors are also required in the amplifier design. The LNA needs to provide enough gain at low noise figure to overcome the losses, as well as noise, of the next blocks in the receiver topology. Furthermore, the LNA should meet system requirements in terms of power consumption, linearity, input and output impedance matching and bandwidth (narrow band and wide band configuration are possible) [10][55]. A general model of an LNA is presented in Fig. 2. 19. The transistor is biased with the conduction angle ($2\theta = 360^\circ$), where conduction angle refers to the portion of the waveform period cycle during which the transistor conducts (for 2θ transistor conducts all the time) [55]. Input matching network and output matching network are used for input and output RF signals, respectively. Feedback part depends on the LNA configuration and can be omitted. Moreover, multi-stage LNAs are very often designed in order to reach required gains, which also requires interstage matching.

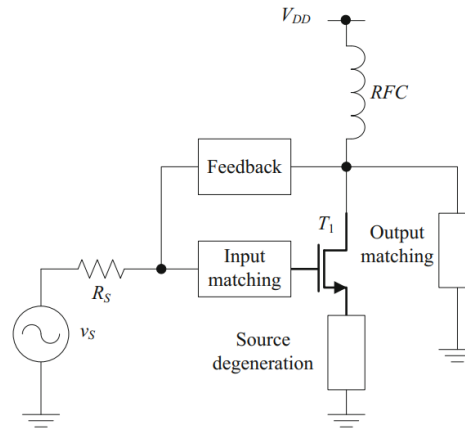


Fig. 2. 19 General model of LNA [55].

Power amplifiers – utilized in the transmitter circuitry, an ideal PA converts the DC power (bias) into output signal power under linear control of an RF input [56]. PAs are the most power consuming building blocks in the wireless systems, which is another challenging task in the mm-wave range for long battery life solutions. Similar to LNAs, they can be characterized by series of parameters such as linearity, suitable for chosen modulation scheme, output power levels, bandwidth, power efficiency and power added efficiency [38]. Moreover, power combing techniques are very often employed in the amplifiers design, either by on-chip power combining or spatial power combining with antenna arrays [38][58]. Power combining has several advantages over impedance transformation in increasing output power, including improved reliability and robustness, as well as, possibility to generate different power levels. This can be used to control power and amplitude modulation [58]. Majority of the recent results published in several reports comparing performance of PAs in the mm-range are based

on CMOS and BiCMOS technology [45][58][59][60]. Some of the recent results of InP HBT, InP HEMT and GaN HEMT are presented in [61][62]. Comparison of the published results are shown in Fig. 2. 20 and Fig. 2. 21.

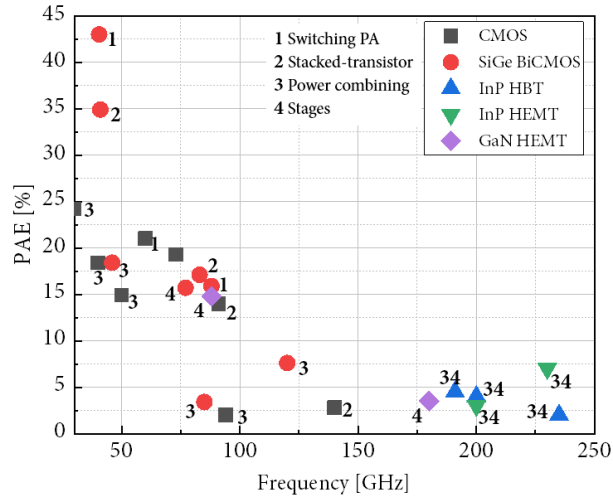


Fig. 2. 20 An overview of power added efficiency at mm-waves of different power amplifiers' topologies with respect to the fabrication technology. Data points based on [45][58][59][60].

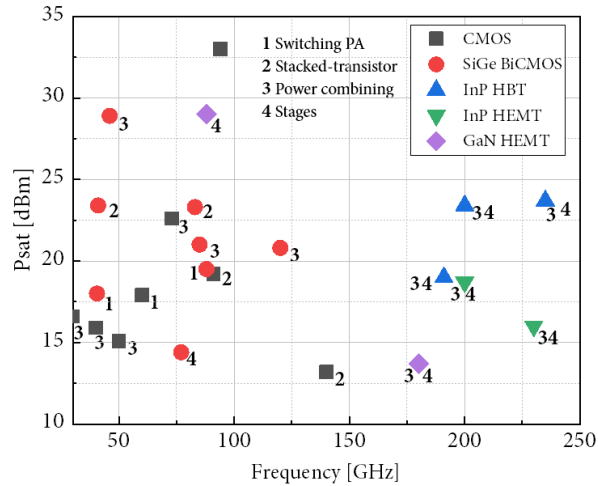


Fig. 2. 21 An overview of saturated output power at mm-waves of different power amplifiers' topologies with respect to the fabrication technology. Data points based on [45][58][59][60].

MILLIMETER WAVE PHOTONICS

Microwave photonics (MWP) can be defined as an interdisciplinary research area of optoelectronic devices operating at microwaves frequencies and their applications for signal processing in microwave systems [63]. The historical development of MWP is based upon fundamental breakthroughs in optical communications, for which, the invention of first lasers in 1960 [64][65] can be considered as a starting point [66]. Further improvement in cornerstone devices such as semiconductor lasers along with the development of electrooptic modulators and detectors, has enabled MWP to advance [67]. Moreover, with the availability of low-loss silica single mode fibers [68], a standard, coaxial cable-based transmission systems have been overtaken by photonic links, which offers superior properties in terms of losses. The key advantages of optical fiber communication systems include weight, size and cost reduction, in addition to lower attenuation, low dispersion, wide bandwidth, tuneability and high data rate transfers [69]. The development of optical-fiber amplifier has contributed to the demand of high-power photodiodes at longer wavelengths ($1.3 \mu\text{m} - 1.55 \mu\text{m}$) with improved saturation current and large-bandwidth efficiency [70]. Furthermore, as optical-to-electrical converters play a key-role in modern communication systems, advanced photodiode structures have been developed. Even if they have a lot of strong advantages over electrical techniques, RF optics have to carefully handle power consumption, noise figure and linearity to be applied in real systems.

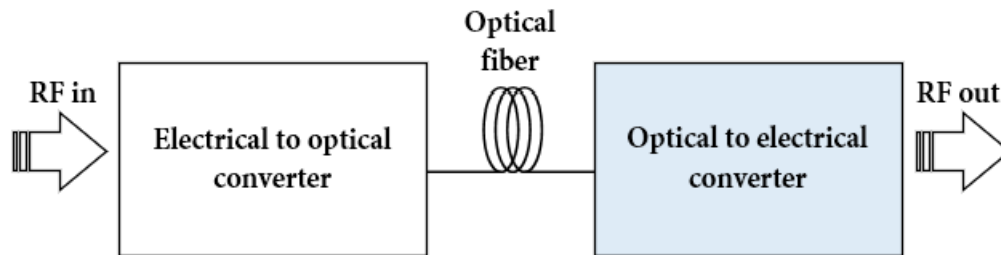


Fig. 2. 22 Schematic of microwave photonic link. The RF input signal is converted into optical domain and transmitted via optical fiber. The output RF signal is converted back into electrical domain.

The main areas of extensive research and applications of MWP include astronomy, spectroscopy, radars, antennas arrays, warfare systems, instrumentation and high-speed communication [66][67][69]. Furthermore, the dominant functions of MWP systems cover photonic generation, processing, distribution of microwave and mm-wave signals, photonic analog-to-digital conversion and radio-over-fibre systems [71].

As the MWP is an active and constantly growing area of research, the next generation termed Integrated Microwave Photonics (IMWP) is under intensive development and study [69]. The IMWP systems are less bulky, more power efficient and cost effective in comparison to standard MWP systems based on discrete optoelectronic devices [72][73]. The major advantage of IMWP is the usage and implementation of photonic integrated circuits (PICs), in which generation, processing, distribution and analysis of microwave and millimetre wave signals is performed.

Following subchapters describe fundamentals of photonic signal generation at mm-waves in various system architectures. Furthermore, brief discussion of most popular photodetectors and their crucial role in optical to electrical conversion is presented.

2.6 OPTICAL GENERATION OF MM-WAVES SIGNALS

Generation of mm-wave signals based on optics requires an optical source. The source can be based on two lasers, monolithically integrated or not, or on a mode-locked laser that will be “naturally” able, after photo-detection, to generate a high frequency electrical signal. It can also be obtained using a single mode laser source that is directly or externally amplitude or phase modulated. In the case of an electrically modulated sources, the phase noise of the generated signal will be a copy of the phase noise of the synthesizer. For other topologies there are phase noise reduction solutions that can be applied like injection locking, self-injection locking or Opto-Electronic Oscillator architectures.

2.6.1 Laser sources for optical generation of mm-wave signals

Optical sources are a critical part of modern communication systems. Along with the development of semiconductor technology, tuneable and very compact laser diodes have attracted strong interest in the research community [74]. High external efficiency and possibility of integration on the same chip, has made laser diode one of the most popular optical source employed in modern communication systems. Nowadays, due to constantly increasing demands in terms of performance and bandwidth, narrow-linewidth, low-threshold, high-speed and dynamic single-mode lasers are required [74]. Most utilized laser structures are DBRs (Distributed Bragg Reflector) and DFB lasers (Distributed-feedback). In this type of lasers diffraction gratings are integrated either inside gain region (DFB laser) or outside (DBR laser) by etching process of a periodic corrugation (see Fig. 2. 23).

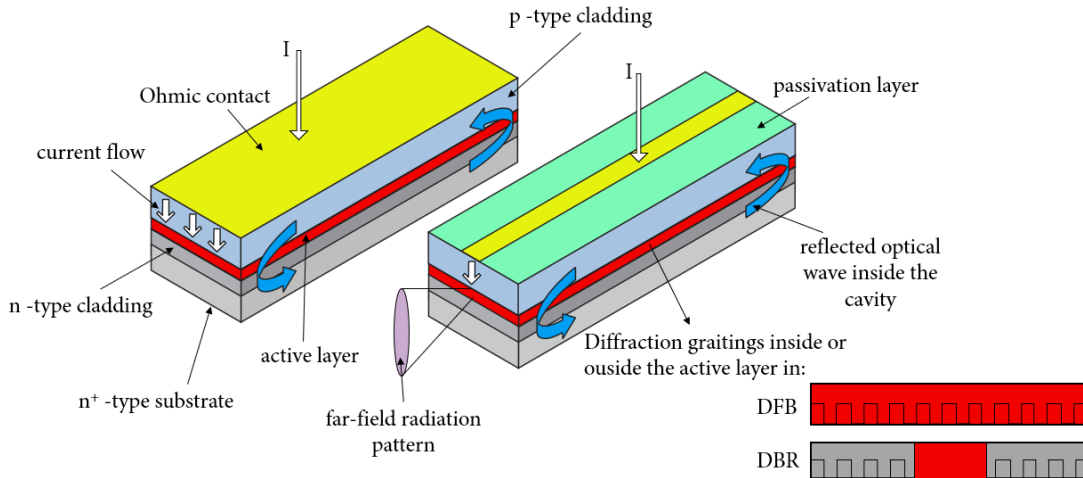


Fig. 2. 23 Schematics of the Fabry-Perot conventional cavity laser (left) and improved gain-guided stripe laser (right). Due to stripe-shape electrode, lasing is taking place only in the central region of the structure, effectively suppressing higher-order transversal modes.

2.6.2 Optical heterodyning

Optical heterodyning is the simplest continuous-wave (CW) technique to generate mm-wave signals in modern telecommunication systems [66][75][76]. In this technique, two laser sources are used (Fig. 2. 24) at different optical frequencies, that corresponds to required mmW or THz frequency. In most cases, the optical signals are combined with an optical coupler towards a photodetector (optical to electrical converter) via an optical fiber.

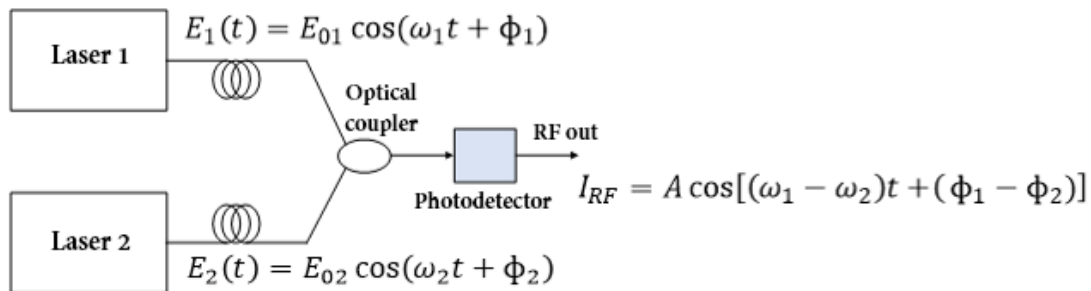


Fig. 2. 24 Simplified schematic of the optical heterodyning with two optical waves to generate mmW or THz signal. I_{RF} is a photodetector output current, A is a constant which is determined by E_{01} , E_{02} and the responsivity of the photodetector [77].

Assuming the same polarization and electric field amplitude of the two input optical beams (E_1, E_2), the superposition of the two signals results in signal electrical field (E_0), intensity (I_0) and photodetector current (i) [66][77][78]:

$$|E_0|^2 = |E_1 + E_2|^2 = |E_1|^2 + |E_2|^2 + 2|E_1||E_2|\cos[(\omega_1 - \omega_2)t + (\varphi_1 - \varphi_2)] \quad (2.8)$$

$$I_0 = I_1 + I_2 + 2\sqrt{I_1 I_2} \cos[(\omega_1 - \omega_2)t + (\varphi_1 - \varphi_2)] \quad (2.9)$$

$$i = \frac{\eta_0 q}{h\nu_1} P_1 + \frac{\eta_0 q}{h\nu_2} P_2 + \frac{\eta_{v_c} q}{h} \sqrt{\frac{P_1 P_2}{\nu_1 \nu_2}} \cos[(\omega_1 - \omega_2)t + (\varphi_1 - \varphi_2)] \quad (2.10)$$

If we assume that the power levels of lasers are equal ($P_{opt} \approx P_1 \approx P_2$), and the optical frequencies of the input waves are close in frequency with the difference frequency, ν_c , ($\nu_1 \approx \nu_2$; $\nu_c = |\nu_1 - \nu_2| \ll \nu_1, \nu_2$), then Eq. 2.10 can be simplified as:

$$i = 2s_0 P_{opt} + 2s_{v_c} P_{opt} \cos(2\pi\nu_c t + \Delta\varphi) \quad (2.11)$$

where $\Delta\varphi = \varphi_1 - \varphi_2$. The first term in Eq. 2.11 is the DC photocurrent, and the second AC term, is the desired oscillating signal at the difference frequency ν_c [66]. The AC current (i_{AC}) is usually fed into an antenna, and the radiated output RF power in the ideal case is [78]:

$$P_{RF} = \frac{1}{2} R_A (i_{AC})^2 \quad (2.12)$$

E_{01}, E_{02}	- amplitude terms
ω_1, ω_2	- angular frequency terms
φ_1, φ_2	- phase terms of the two optical waves
q	- electron charge
η_0	- photodetector's DC quantum efficiency
η_{v_c}	- photodetector's high frequency quantum efficiency
P_1, P_2	- laser power
ν_1, ν_2	- optical input waves frequencies
s_0, s_{v_c}	- photodetector's DC and high frequency responsivity
R_A	- radiation resistance of the antenna; typically, 50 Ω to 100 Ω

Heterodyning technique is a very efficient technique to generate signals up to THz frequencies. In order to reduce the system dimension and to reduce part of the noise sources the two lasers can be integrated in a single chip [79]. Signal generation with multi-wavelength sources like mode-locked lasers is another approach that has several advantages in comparison to the system with two free-running laser sources, as the generated signal has better phase correlation (due to the same laser cavity) and reference source is not needed [77] (Fig. 2. 25 - Fig. 2. 27). In this type of laser source, the laser modes are separated with a frequency f_0 that corresponds to the inverse of the round-trip time in the laser cavity. The phase noise of the generated signal

can be improved by direct electrical modulation of the mode-locked laser chip or feedback loop.

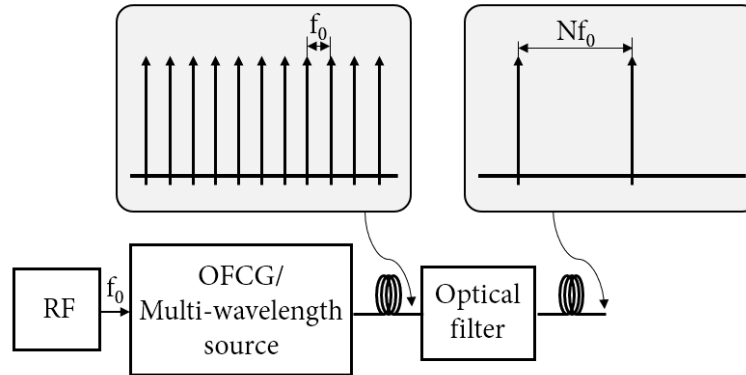


Fig. 2. 25 Simplified schematic of OFCG for mm-wave signal generation.

As this type of source generates a comb of optical frequencies, it will generate an electrical frequency comb after photo-detection with frequencies starting at f_0 and with all its harmonics, limited by the photodetector bandwidth. In this type of source all modes are phase-locked. Spectral power enhancement of 6 dB has been reported in comparison to conventional techniques at the same photocurrent levels [80]. A generalized factor for mm-wave spectral power enhancement can be derived for an optical pulse comprised of N comb lines with equal amplitudes of $\frac{1}{\sqrt{N}}$ as [80]:

$$\eta_N(f_{rep}) \equiv \frac{|\bar{P}_{N-line}(2\pi f_{rep})|^2}{|\bar{P}_{sin}(2\pi f_{rep})|^2} = \frac{\left(\frac{N-1}{N}\right)^2}{\frac{1}{4}} = 4 \left(1 - \frac{1}{N}\right)^2 \quad (2.13)$$

In addition to these techniques, using a special type of laser source is a worth to mention solution, using a single mode that can be directly modulated or externally modulated. In case of external modulation, it can be performed either with amplitude modulation or phase modulation. For these techniques, a Mach-Zehnder modulator (MZM) is used to generate high quality mm-wave signal [81]. With selected MZM bias point, at minimum or maximum transmission point, a frequency doubling or quadrupling is achieved, respectively. Notch filter is utilized in order to suppress optical sidebands and optical carrier when frequency-quadrupled signal is generated. Moreover, to generate signal with a higher multiplication factors, two cascaded MZMs with selected bias points can be employed [77]. Furthermore, as the systems with MZMs suffer from bias-drifting problem, an implementation of control circuit is necessary. In order to overcome this problem, MZM can be replaced with optical phase modulator, for which no dc bias is required. Nevertheless, such system requires

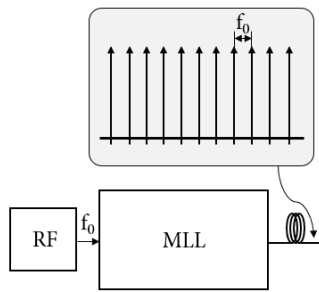


Fig. 2. 26 Simplified setup of MLL used to generate frequency combs.

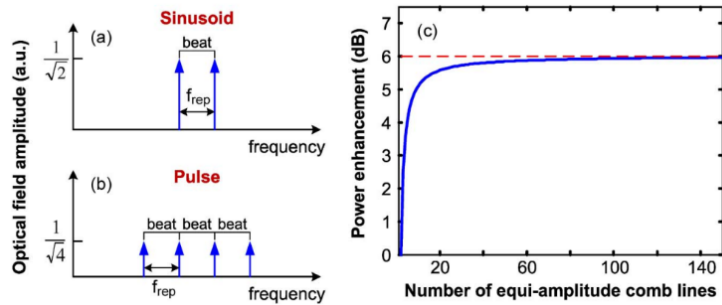


Fig. 2. 27 Schematic of the optical field amplitudes for (a) a time-domain sinusoid and (b) a time-domain pulse. (c) Result of theoretical MMW spectral power enhancements at f_{rep} with respect to the number of equi-amplitude comb lines [80].

an optical notch filter, i.e. Fiber Bragg grating (FBG), as the signal generated by phase modulator contains all the sidebands and the optical carrier.

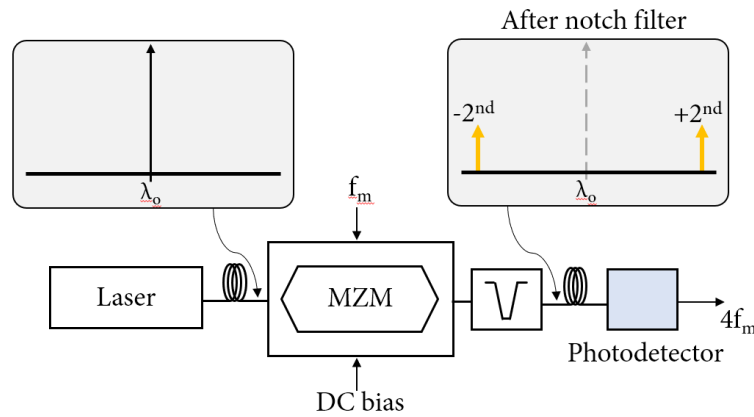


Fig. 2. 28 Setup with MZM biased at maximum transfer point for frequency quadrupling.

2.6.3 Phase noise reduction techniques

In order to achieve low-phase noise output signal, caused by phase difference of the free-running lasers, several techniques have been developed and implemented in the heterodyning systems. These include [66][71][75]:

1. Optical injection-locking (OIL): first experiments with semiconductor lasers were performed in 1980's [82][83]. Schematic of the optical injection locking arrangement is presented in Fig. 2. 29. It consists of a master laser, to which an RF signal is applied, and two slave lasers. Optical carrier and sidebands are generated at the output of the master laser due to frequency modulation. Signal is then

injected into two slave lasers, and injection locking is achieved when the two free-running wavelengths are close to the two sidebands (i.e. $\pm 2^{\text{nd}}$ order side bands). The phase of the optical output waves of the slave lasers is then in coherence. Slave lasers beating generates low phase noise mm-wave signal at the photodetector output, which phase noise is determined by the phase noise of the RF reference source. Moreover, the output signal frequency is equal to an integer multiple of the RF reference source frequency applied to the master laser.

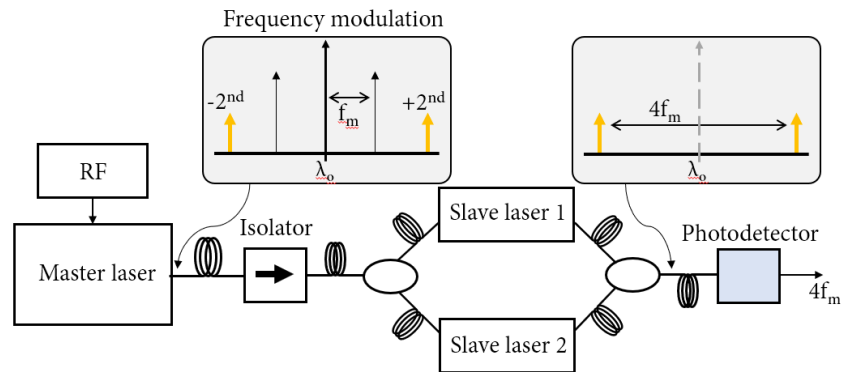


Fig. 2. 29 Setup for OIL of the slave lasers at $\pm 2^{\text{nd}}$ side bands.

- Optical phase lock loop (OPLL): another technique widely used to phase lock two free-running lasers for high quality mm-wave signal generation [84]. In Fig. 2. 30 a schematic to perform optical phase locking is presented. Optical signals from two laser sources are applied to a photodetector and mm-wave signal is generated due to heterodyning. The output signal is then injected to electrical phase detector compose of an electronic mixer and low-pass filter. The output voltage from the electrical phase detector is proportional to the phase difference between the generated mm-wave signal and the reference signal. The output voltage is sent to one of the input laser to adjust the injection current accordingly, and as a result, to change its phase. This loop mechanism leads to lock the phase terms of the two optical waves. Moreover, as the locking range is determined by the linewidth of the laser and the loop length, narrow linewidth lasers and short loops are mostly utilized in OPLLs. Furthermore, if a harmonic generator is used in the setup, an RF signal at relatively low frequency with different number of harmonics can be sent to the mixer to generate mm-wave signal. OPLL and OIL techniques are often employed in the same optical system for further improvement of the signal quality [85][86].

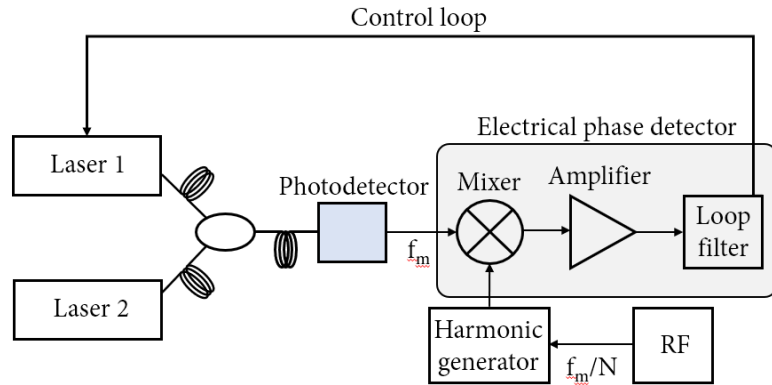


Fig. 2. 30 Setup for the OPLL with harmonic generator.

3. Optoelectronic oscillators, firstly proposed in 1994, can achieve highest spectral purity [87][88]. Basic configuration of an OEO is presented in Fig. 2. 31. It is based on the loop oscillator principle; the open loop gain has to balance out the losses and the oscillation frequency is inversely proportional to the fiber group delay [66]. OEO can generate the signal without the reference microwave source, and it can be extracted from electrical or optical part of the loop.

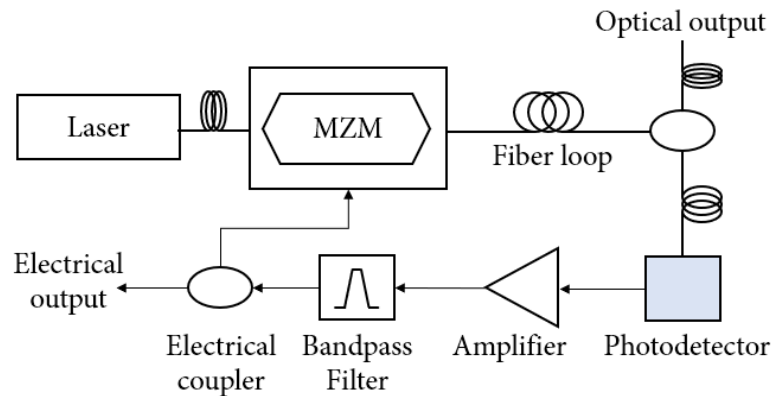


Fig. 2. 31 Schematic of a single loop OEO.

2.7 PHOTODETECTORS

Photodetectors are the fundamental building blocks in a photonic based communication system. These devices are responsible for the optical-to-electrical conversion of the signal. Working principle is based on optical generation of electron-hole pairs due to photon absorption in the semiconductor's intrinsic or depleted layer (as a result of the internal photoelectric effect [87]). For this process to occur, photon energy ($h\nu$) of the absorbed light must be equal or higher than the bandgap energy E_g of the absorber material (Fig. 2. 32a). The upper wavelength limit (λ_g) for photon absorption is given by [87]:

$$\lambda_g[\mu m] = \frac{1.24}{E_g[eV]} \quad (2.14)$$

$$h\nu \geq E_g = E_C - E_V, \quad (2.15)$$

where h is a Planck constant and ν is the photon frequency. If the photon energy is sufficiently high, an electron is excited from the valence band (E_V) to the conduction band (E_C). Moreover, application of bias voltage to the material, results in separation of electrons and holes. Photogenerated carriers travel through the material and consequently an electric current (photocurrent) can be detected in the electrical circuit [89]. Photodetectors used in the majority of modern telecommunication systems are based on:

1. pn-junction: pin photodiodes (pin-PDs) and uni-travelling carrier photodiodes (UTC PDs).
2. Bulk semiconductors: photoconductors (photoresistors).

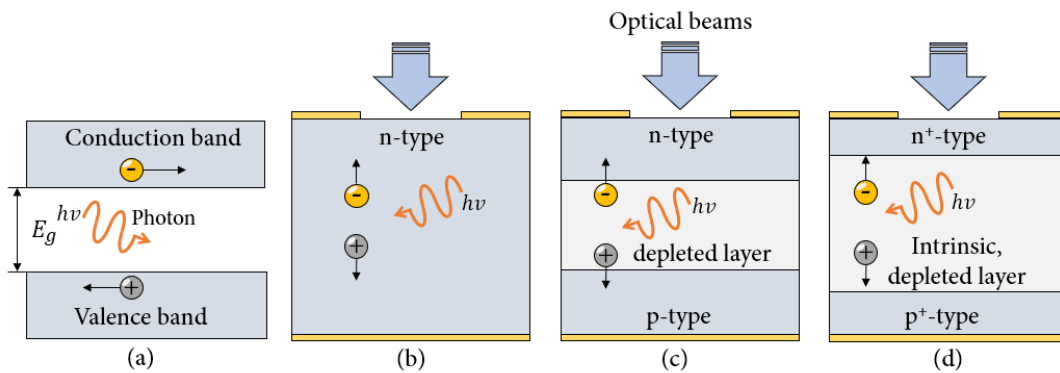


Fig. 2. 32 Simplified diagrams of photogeneration of electron-hole pair in a (a) semiconductor, (b) photoconductor, (c) pn photodiode and (d) pin photodiode.

Although indirect-bandgap (i.e. Si, Ge) and direct-bandgap (i.e. InP, GaAs) semiconductor materials can be exploited in photoconductors, the latter materials are more preferred due to higher absorption levels and speed [87][90]. Furthermore, as the majority of modern

communication system operates at 1.55 μm wavelengths, InP-based devices are a natural choice, with lattice matched compound semiconductors such as InGaAs and InGaAsP. Photoconductive switches, based upon low-temperature-grown GaAs or InGaAs (LT-GaAs/LT-InGaAs) or ErAs:InGaAs/InAlAs superlattices find applications as well.

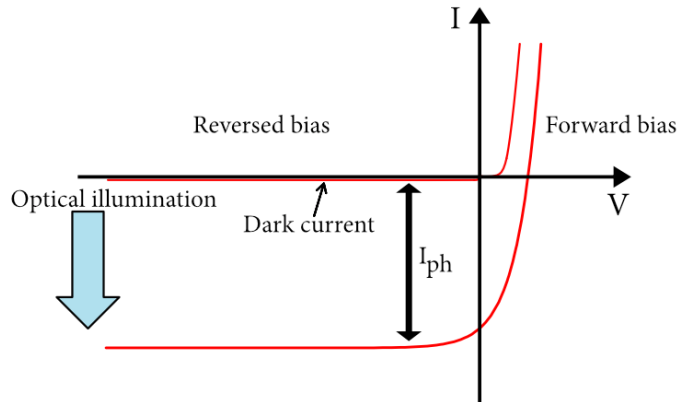


Fig. 2. 33 Typical photodiode I-V characteristic.

Photodiodes used in the telecommunication systems operates usually under reversed bias condition, that creates strong electric field in the junction and increases drift velocity of the carriers what reduces transit times [87]. There are several figures of merits common for the photodetectors. Summary of the most important ones are presented below in Table 1 [70][91].

Table 1 Photodetectors' parameters.

Parameter description	Definition
<p>External quantum efficiency (η_{ext}): measures the ability of a photodiode to convert light into electrical current. Ideal η_{ext} is equal to 1, meaning each photon generates a pair hole-electron.</p>	$\eta_{ext} = \frac{I_{Ph}}{q} \times \frac{hv}{P_{opt}} \quad (2.16)$ <p>I_{Ph} - photogenerated current P_{opt} - optical input power at frequency ν q - elementary charge ($-1.602 \times 10^{-19} \text{ C}$)</p>
<p>Responsivity (R_{PD}): a ratio of the photocurrent to optical input power. Maximum $R_{PD} = 1.25 \frac{\text{A}}{\text{W}}$, for $\eta_{ext} = 1$ and $\lambda = 1.55 \mu\text{m}$.</p>	$R_{PD} = \frac{I_{Ph}}{P_{opt}} = \frac{\eta_{ext} \lambda [\mu\text{m}]}{1.24} \left[\frac{\text{A}}{\text{W}} \right] \quad (2.17)$

<p>Polarization dependent loss (PDL): a ratio of the maximum and minimum responsivities for all polarization states of the input light.</p>	$\text{PDL} = 10 \log \left(\frac{R_{\max}}{R_{\min}} \right) [\text{dB}] \quad (2.18)$ <p>R_{\max} - maximum responsivity R_{\min} - minimum responsivity</p>
<p>3-dB bandwidth (f_{3dB}): frequency range from DC to cut-off frequency (frequency at which the electrical output power is 3 dB lower in comparison to the output power at a very low frequency). f_{3dB} is limited by the carrier transit times bandwidth (f_t) and RC-time constant bandwidth (f_{RC}).</p>	$f_{3dB} = \sqrt{\frac{1}{\frac{1}{f_t^2} + \frac{1}{f_{RC}^2}}} \quad (2.19)$ $f_t = \frac{3.5\bar{v}}{2\pi d_{abs}} \quad (\text{for } p\text{-}i\text{-}n \text{ PDs}) \quad (2.20)$ $f_{RC} = \frac{1}{2\pi R_{eff} C_{PD}} \quad (2.21)$ <p>\bar{v} - average carrier velocity d_{abs} - absorber layer thickness $R_{eff}(R_S + R_L)$ and C_{PD} - calculated from the equivalent circuit (Fig. 3. 4)</p>

2.7.1 p-i-n and UTC photodiodes

P-i-n-PDs, firstly introduced by J. Nishizawa and his research group in 1950 [92], are one of the most popular semiconductor photodetectors in photonics systems. Modern devices are based on a heterostructure with an intrinsic region between p- type and n-type semiconductor, as presented in Fig. 2. 32d. Light absorption occurs in the undoped region, where photogenerated carriers, with the influence of reverse external bias, move across the structure towards electrical contacts, and both carriers contribute to electrical response. As the holes' velocity is an order of magnitude lower than electrons' in the depletion region, the low velocity holes-transport dictates the total performance [93]. This leads to photo-generated holes accumulation in the depletion region, and as a consequence, in a space charge effect that decreases the electrical field (Fig. 2. 34). Moreover, along with the weaker electrical field, the carrier velocity is decreased as well, and as the final result the output current saturates. Uni-travelling-carrier photodiodes (UTC PDs) were introduced by Ishibashi in 1997 [94]. The UTC-PD band diagram is shown in Fig. 2. 35. Light absorption occurs in the p-type layer, where majority (holes) and minority carriers (electrons) are photogenerated. Electrons diffuse into the depleted collection layer and drift towards n-contact layer [93]. The diffusion block layer contributes to electrons motion toward the collection layer. Built-in field accelerates the electron diffusion process, and it is achieved as a result of doping-grading or bandgap-grading [95]. The built-in field reduces as well the electron travelling time. Moreover, the photogenerated majority holes respond very fast within the dielectric relaxation time by their collective motion, and therefore the absorption layer response is primarily determined by the electron transport [93][94][96]. What is more, as the electrons have higher mobility and drift

velocity in comparison to the holes, the device response and output saturation current are superior in comparison to p-i-n photodiodes determined by low-velocity hole-transport.

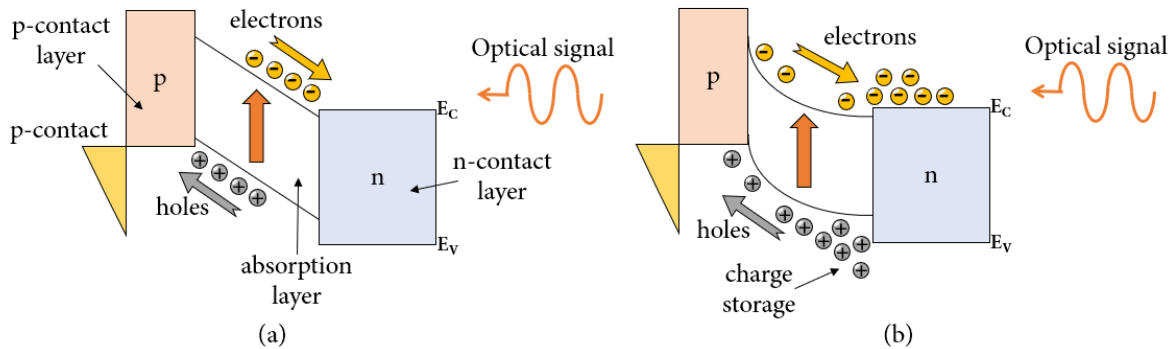


Fig. 2. 34 Band structure of conventional p-i-n photodiode (a) and modified band diagram (b) at high optical input [93].

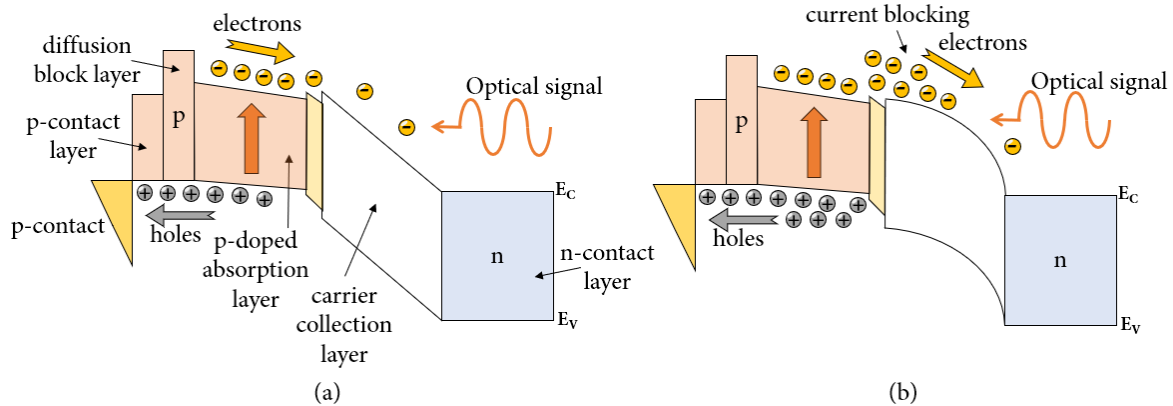


Fig. 2. 35 Band structure of conventional UTC photodiode (a) and modified band diagram (b) at high optical input [93].

Furthermore, by careful design of the absorption and depletion layer thickness, wide 3-dB bandwidth is obtainable. As presented in Fig. 2. 35, the conduction band discontinuity between absorption and carrier collection layer can result in current blocking which disturbs electron injection into the collection layer and causes current saturation [96]. Additional layers and proper grading/doping profiles are applied in order to smooth the conduction band. Another advantage of UTC-PDs over p-i-n PDs is the capability of low or zero bias voltage operation. With an optimized layer composition and doping design high electron velocity in the depletion layer can be sustained at a low electric field or with the built-in field of the pn-junction. Low-voltage operation reduces power consumption, heat sink design and improves reliability [93]. More detailed description about devices' limitations and solutions to increase output power are presented in Chapter 3.

2.7.2 Summary of p-i-n and UTC photodiodes

There are several reports and reviews that compare p-i-n and UTC photodiodes performances in mm-wave and THz ranges [99][100][101][102][103][104]. Recent state-of-the-art results are presented in Fig. 2. 36 and Fig. 2. 37. As can be seen, the highest output powers have been achieved for photodiodes array at 35 GHz and 48 GHz with 26 dBm and 21 dBm of output power, respectively [97]. The highest output power at 300 GHz have been achieved with power combining technique [98], with output power levels of 0.79 dBm. Moreover, the UTC photodiodes results clearly show higher output power performance in comparison to p-i-n photodiodes devices. Moreover, UTC with integrated amplifier can deliver 10 dBm at 109 GHz [100]. In Fig. 2. 37 results of UTC photodiodes integrated with antennas are presented [105][106][107][108][109]. Bow-tie and log-periodic antenna structures are utilized in the vast majority of the reported results, with the power levels greatly lower in comparison with single or photodiodes array approaches. Nevertheless, thanks to antenna integration, these types of structures could be more compact solutions for the transceiver design.

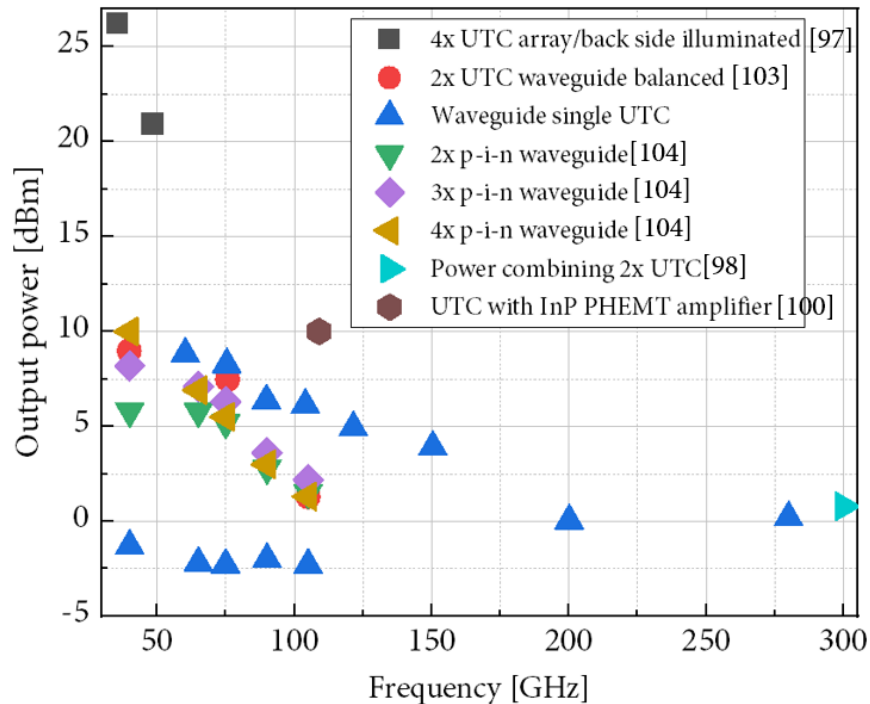


Fig. 2. 36 State-of-the-art of p-i-n and UTC photodiodes with highest output powers [97]-[104].

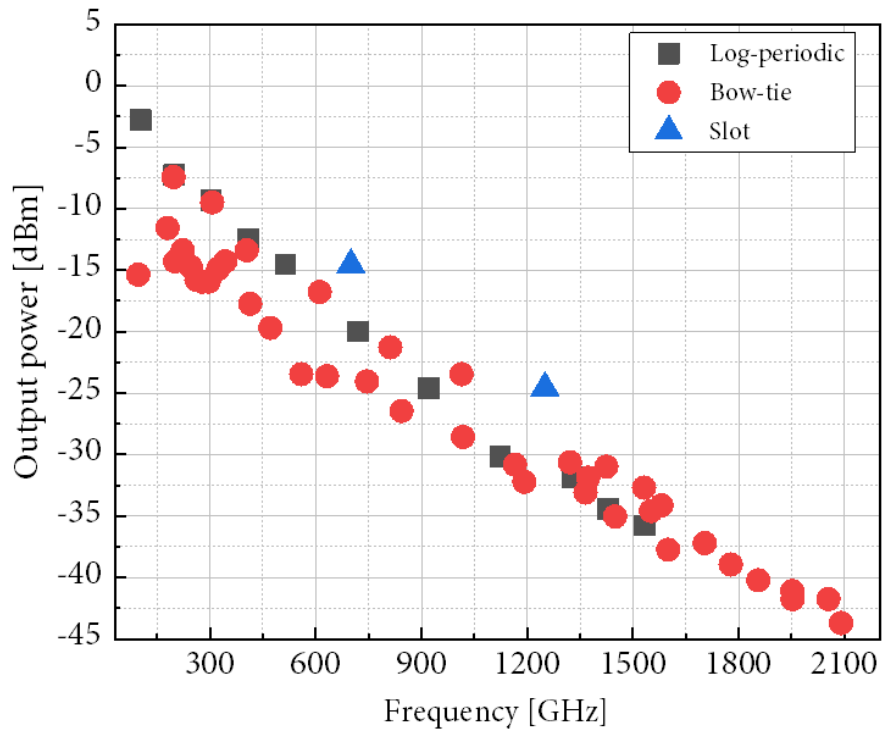


Fig. 2. 37 State-of-the-art of antenna-integrated photodiodes with highest output powers [105]-[109].

To conclude:

- **Uni-travelling PDs in comparison to p-i-n PDs achieve generally higher output power levels, especially at the frequencies above 100 GHz.**
- **Wider 3-dB bandwidth is another advantage over standard p-i-n PDs.**
- **Lower bias voltage and possibility of zero-biased operation allows much simpler design, reduction of the power consumption and cost.**

2.8 PHOTOCONDUCTIVE SWITCH

Generation of a tuneable signal at mm-waves and THz frequencies can be achieved with a photoconductive switch, firstly proposed by Auston in 1975 [110]. This type of photomixer consist of a highly resistive semiconductor material such as low-temperature-grown GaAs or InGaAs (LT-GaAs/ LT-InGaAs) and metal contact electrodes [78][112]. After illumination from a dual-mode or pulsed laser source, the light is absorbed in the photoconductive material between the contact electrodes. This leads to generation of electron-hole pairs. Under the influence of bias voltage applied to the electrodes, the free carriers are accelerated generating an ultrafast current pulse which can be radiated by an antenna. In the case of optical beating, signal frequency is equal to the frequency difference of the two optical laser beams. In Fig. 2. 38, a schematic of a typical photoconductive switch is presented.

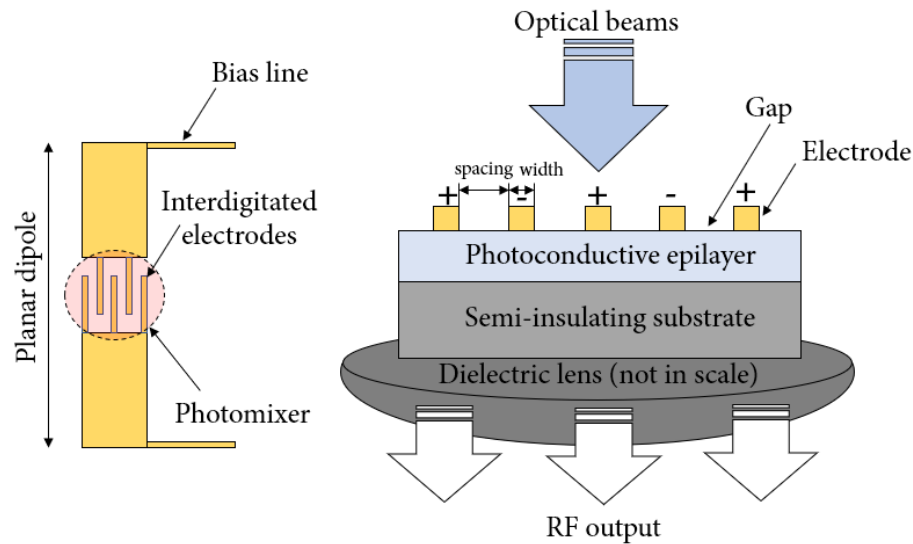


Fig. 2. 38 Top view and cross-sectional view of a photomixer with planar dipole antenna. Bottom side coupling of mm-wave/THz radiation via dielectric lens to free space. Adapted from [111].

Dimensions of the metallic fingers for CW operation (width and spacing), as well as the period are calculated to match the capacitance requirements. The active area diameter is of the same order as the laser beam diameter, typically $10\ \mu\text{m} \times 10\ \mu\text{m}$ [7]. Applied bias is determined based on material breakdown field and thermal properties. Thickness of photoconductive epilayer is typically ca. $1\ \mu\text{m}$. Deposition of a thin transparent dielectric layer on the structure can be used for passivation and as an antireflection coating. Majority of the photoconductive switches are based upon LT-GaAs material operating at $0.8\ \mu\text{m}$. Epitaxial growth at low temperatures allows to obtain required properties like very short carrier recombination lifetime, high dark

resistivity and relatively high carrier mobility [113]. In order to make photoconductive switches operational at 1.55 μm , InGaAs grown on InP substrate and Erbium Arsenide superlattice devices attracted attention of several research and development groups [78][114][115]. The obstacles in using LT-InGaAs material as a photo switch are in most cases due to difficulties to obtain consistent low dark current and short carrier lifetimes. This limitation could be overcome by introducing carrier trapping centers due to ion implantation or irradiation. Practical example of a photoconductive switch operating at mm-waves can be found in [114][115][116]. In this work photoconductive sampling and mixing of RF signals with nitrogen implanted InGaAs based structures were performed up to 67 GHz. Furthermore, a QPSK modulation up to 400 Mbit/s was carried out as a proof of concept of using photoconductive switch in data transmission systems. Reported results with mode-locked lasers has shown EVM of 22.9 % at 400 Mbit/s. Devices based on ErAs:In(Al)GaAs superlattice layer structure have been studied in [117]. Stated results for CW photomixing at 1.55 μm shows high dynamic range of 52 dB at 1 THz. These devices have been used in time-domain spectroscopy systems, reaching 6.5 THz of bandwidth [118]. Moreover, constant research on LT-GaAs based devices to improve photoresponse under 1.55 μm illumination by introducing Fabry-Pérot cavities has been carried on as well [113]. For LT-GaAs photoconductors operating at 0.8 μm wavelength, the output power reached 2.5 dBm at 252 GHz [119].

2.9 MILLIMETER WAVE ELECTRONICS AND PHOTONICS - SUMMARY

Based on the published results presented in previous sub-chapters, in Fig. 2. 39 and Fig. 2. 40 an overview of average output powers and phase noise levels are given, respectively. Diode-based and transistor-based solution can generally deliver higher output power levels in comparison to photonics solutions in the mm-wave frequencies. Nevertheless, these solutions suffer from higher phase noise levels. Moreover, tuning possibilities are much simpler to obtain in optical solutions, generating signal of high spectral quality. Furthermore, electrical solutions require mechanical tuning elements (i.e. Gunn diodes) or a change in bias voltage to tune the frequency up to a few GHz. The VCOs tuning range is wider compared to diode-based solutions, and can be estimated to be in the range of 9% up to 40% of the generated frequency.

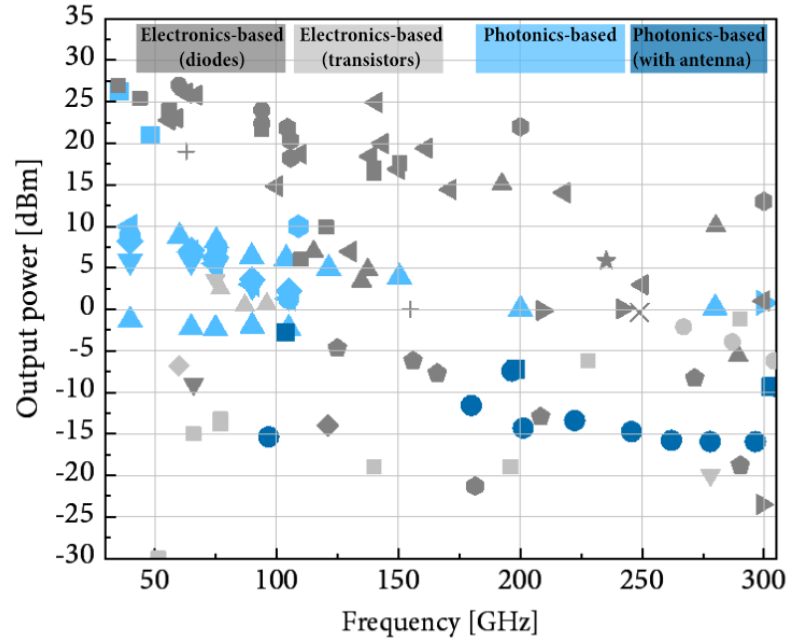


Fig. 2. 39 Output power levels of electronics-based and photonics-based solutions from 30 GHz to 300 GHz. Data points are based on reported results presented in previous sub-chapters.

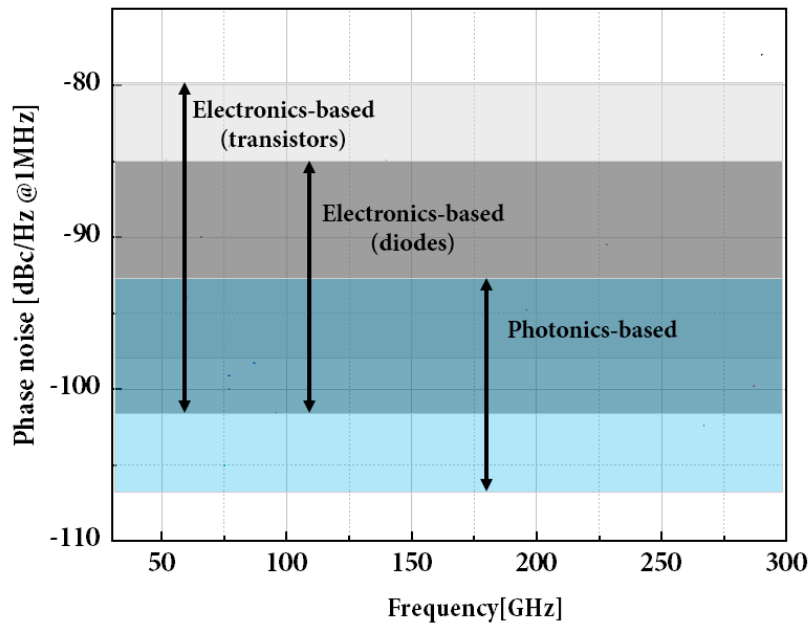


Fig. 2. 40 Average phase noise levels of electronics-based and photonics-based solutions from 30 GHz to 300 GHz. Data points are based on reported results presented in previous sub-chapters.

To conclude:

- **Photonics-based solutions can offer higher quality signals and much wider tunability in comparison to electronics-based solutions.**
- **Monolithic integration of several components such as lasers, modulators, couplers and UTC PDs on the same substrate gives possibility of cost reduction of the signal processing devices.**
- **In terms of output power levels photonics-based solutions require careful design in order to meet requirements of the modern telecommunication systems.**

REFERENCES

- [1] Wanlass, F. M. and Sah, C.T. “Nanowatt Logic Using Field-Effect Metal-Oxide Semiconductor Triodes,” International Solid State Circuits Conference Digest of Technical Papers (February 20, 1963) pp. 32-33.
- [2] S. Mao, S. Jones and G. D. Vendelin, “Millimeter-Wave Integrated Circuits,” in IEEE Journal of Solid-State Circuits, vol. 3, no. 2, pp. 117-123, June 1968.
- [3] A. A. Abidi, “CMOS microwave and millimeter-wave ICs: The historical background,” 2014 IEEE International Symposium on Radio-Frequency Integration Technology, Hefei, 2014, pp. 1-5.
- [4] I. A. Glover, S. R. Pennock, and P. R. Shepherd, Eds., Microwave Devices, Circuits and Subsystems for Communications Engineering. Chichester, UK: John Wiley & Sons, Ltd, 2005.
- [5] L. A. Samoska, “An Overview of Solid-State Integrated Circuit Amplifiers in the Submillimeter-Wave and THz Regime,” in IEEE Transactions on Terahertz Science and Technology, vol. 1, no. 1, pp. 9-24, Sept. 2011.
- [6] M. Urteaga, Z. Griffith, M. Seo, J. Hacker and M. J. W. Rodwell, “InP HBT Technologies for THz Integrated Circuits,” in Proceedings of the IEEE, vol. 105, no. 6, pp. 1051-1067, June 2017.
- [7] Carpintero, G., García Muñoz, L., Hartnagel, H., Preu, S., Räisänen, A. (2015). Semiconductor Terahertz Technology Devices and Systems at room temperature operation. John Wiley & Sons, Ltd.
- [8] B. Razavi, RF microelectronics, 2nd ed. Upper Saddle River, NJ: Prentice Hall, 2012.
- [9] A. Raffo and G. Crupi, Eds., Microwave wireless communications: from transistor to system level. Amsterdam: Elsevier, 2016.
- [10] S. Voinigescu, High-frequency integrated circuits. Cambridge; New York: Cambridge University Press, 2013.
- [11] R. Van Zyl, W. Perold, and R. Botha, ‘The Gunn-diode: fundamentals and fabrication’, in Proceedings of the 1998 South African Symposium on Communications and Signal Processing-COMSIG ’98 (Cat. No. 98EX214), Rondebosch, South Africa, 1998, pp. 407–412.
- [12] J. B. Gunn, ‘Microwave oscillations of current in III–V semiconductors’, Solid State Communications, vol. 1, no. 4, pp. 88–91, Sep. 1963.
- [13] H. Eisele, ‘Gunn or Transferred-Electron Devices and Circuits’, in Encyclopedia of RF and Microwave Engineering, K. Chang, Ed. Hoboken, NJ, USA: John Wiley & Sons, Inc., 2005.
- [14] W. Frank and M. Hayashibara, ‘Millimeter-Wave Silicon IMPATT Sources and Combiners for the 110–260-GHZ Range’, p. 7.

- [15] C. P. Wen, Y. S. Chiang, and E. J. Denlinger, 'Multi-layer epitaxially grown silicon impatt diodes at millimeter-wave frequencies', *Journal of Electronic Materials*, vol. 4, no. 1, pp. 119–129, Feb. 1975.
- [16] H. Eisele, '355 GHz oscillator with GaAs TUNNETT diode', *Electronics Letters*, vol. 41, no. 6, p. 329, 2005.
- [17] M. I. Maricar, A. Khalid, D. R. S. Cumming, and C. H. Oxley, 'Extraction of second harmonic from an InP based planar Gunn diode using diamond resonator for milli-metric wave frequencies', *Solid-State Electronics*, vol. 116, pp. 104–106, Feb. 2016.
- [18] J. D. Crowley, "InP Gunn diodes and millimeter-wave applications", *Proc. SPIE 10276, Millimeter and Microwave Engineering for Communications and Radar: A Critical Review*, 1027606 (14 December 1994).
- [19] A. Förster, J. Stock, S. Montanari, M. Lepsa, and H. Lüth, 'Fabrication and Characterisation of GaAs Gunn Diode Chips for Applications at 77 GHz in Automotive Industry', *Sensors*, vol. 6, no. 4, pp. 350–360, Apr. 2006.
- [20] L. Esaki and R. Tsu, 'Superlattice and Negative Differential Conductivity in Semiconductors', *IBM Journal of Research and Development*, vol. 14, no. 1, pp. 61–65, Jan. 1970.
- [21] H. Eisele, 'State of the art and future of electronic sources at terahertz frequencies', *Electronics Letters*, vol. 46, no. 26, p. S8, 2010.
- [22] C. A. King and K. K. Ng, 'Negative Resistance', in *Encyclopedia of RF and Microwave Engineering*, K. Chang, Ed. Hoboken, NJ, USA: John Wiley & Sons, Inc., 2005.
- [23] K. F. Brennan and A. S. Brown, *Theory of Modern Electronic Semiconductor Devices*. Hoboken, NJ, USA: John Wiley & Sons, Inc., 2002.
- [24] J. Yun, 'Compact Solid-State Electronic Terahertz Devices and Circuits', in *Terahertz Biomedical Science and Technology*, J.-H. Son, Ed. CRC Press, 2014, pp. 67–92.
- [25] H. Eisele, '480 GHz oscillator with an InP Gunn device', *Electronics Letters*, vol. 46, no. 6, p. 422, 2010.
- [26] H. Eisele, I. Farrer, E. H. Linfield, and D. A. Ritchie, 'High-performance millimeter-wave superlattice electronic devices', *Applied Physics Letters*, vol. 93, no. 18, p. 182105, Nov. 2008.
- [27] H. Eisele, A. Rydberg, and G. I. Haddad, 'Recent advances in the performance of InP Gunn devices and GaAs TUNNETT diodes for the 100-300-GHz frequency range and above', *IEEE Transactions on Microwave Theory and Techniques*, vol. 48, no. 4, pp. 626–631, Apr. 2000.
- [28] H. Eisele, L. Li, and E. H. Linfield, 'High-performance GaAs/AlAs superlattice electronic devices in oscillators at frequencies 100–320 GHz', *Applied Physics Letters*, vol. 112, no. 17, p. 172103, Apr. 2018.

- [29] A. Khalid et al., 'A Planar Gunn Diode Operating Above 100 GHz', *IEEE Electron Device Letters*, vol. 28, no. 10, pp. 849–851, Oct. 2007.
- [30] A. Khalid et al., 'Planar Gunn-type triode oscillator at 83 GHz', *Electronics Letters*, vol. 43, no. 15, p. 837, 2007.
- [31] J. Wang et al., 'High Performance Resonant Tunneling Diode Oscillators for THz Applications', in *2015 IEEE Compound Semiconductor Integrated Circuit Symposium (CSICS)*, New Orleans, LA, USA, 2015, pp. 1–4.
- [32] T. Maekawa, H. Kanaya, S. Suzuki, and M. Asada, 'Oscillation up to 1.92 THz in resonant tunneling diode by reduced conduction loss', *Applied Physics Express*, vol. 9, no. 2, p. 024101, Feb. 2016.
- [33] M. Feiginov, H. Kanaya, S. Suzuki, and M. Asada, '1.46 THz RTD oscillators with strong back injection from collector', 2014, pp. 1–2.
- [34] M. Feiginov, C. Sydlo, O. Cojocari, and P. Meissner, 'Resonant-tunnelling-diode oscillators operating at frequencies above 1.1 THz', *Applied Physics Letters*, vol. 99, no. 23, p. 233506, Dec. 2011.
- [35] E. Lindberg, 'The Barkhausen Criterion (Observation ?)', p. 60, 2010.
- [36] A. S. Sedra and K. C. Smith, *Microelectronic circuits*, International seventh edition. New York: Oxford University Press, 2016.
- [37] N. Somjit, I. Robertson, and M. Chongcheawchamnan, *Microwave and Millimetre-Wave Design for Wireless Communications*. Chichester, UK: John Wiley & Sons, Ltd, 2016.
- [38] T. S. Rappaport, J. N. Murdock, and F. Gutierrez, 'State of the Art in 60-GHz Integrated Circuits and Systems for Wireless Communications', *Proceedings of the IEEE*, vol. 99, no. 8, pp. 1390–1436, Aug. 2011.
- [39] D. A. Neamen, *Microelectronics: circuit analysis and design*, 4th ed. New York: McGraw-Hill, 2010.
- [40] B. Razavi, *Design of analog CMOS integrated circuits*, Second edition. New York, NY: McGraw-Hill Education, 2017.
- [41] R. Wanner, R. Lachner, and G. R. Olbrich, 'A SiGe monolithically integrated 75 GHz push-push VCO', in *Digest of Papers. 2005 Topical Meeting on Silicon Monolithic Integrated Circuits in RF Systems, 2005.*, San Diego, CA, USA, 2005, pp. 375–378.
- [42] K. W. Tang, S. Leung, N. Tieu, P. Schvan, and S. P. Voinigescu, 'Frequency Scaling and Topology Comparison of Millimeter-wave CMOS VCOs', in *2006 IEEE Compound Semiconductor Integrated Circuit Symposium*, San Antonio, TX, 2006, pp. 55–58.
- [43] R. Wanner, R. Lachner, and G. R. Olbrich, 'A SiGe monolithically integrated 75 GHz push-push VCO', in *Digest of Papers. 2005 Topical Meeting on Silicon Monolithic Integrated Circuits in RF Systems, 2005.*, San Diego, CA, USA, 2005, pp. 375–378.

- [44] R. Wanner, R. Lachner, G. R. Olbrich, and P. Russer, 'A SiGe Monolithically Integrated 278 GHz Push-Push Oscillator', in 2007 IEEE/MTT-S International Microwave Symposium, Honolulu, HI, USA, 2007, pp. 333–336.
- [45] A. Cathelin et al., 'Design for millimeter-wave applications in silicon technologies', in ESSCIRC 2007 - 33rd European Solid-State Circuits Conference, Muenchen, Germany, 2007, pp. 464–471.
- [46] M. Seo et al., 'InP HBT IC Technology for Terahertz Frequencies: Fundamental Oscillators Up to 0.57 THz', IEEE Journal of Solid-State Circuits, vol. 46, no. 10, pp. 2203–2214, Oct. 2011.
- [47] S. P. Voinigescu, S. Shopov, J. Bateman, H. Farooq, J. Hoffman, and K. Vasilakopoulos, 'Silicon Millimeter-Wave, Terahertz, and High-Speed Fiber-Optic Device and Benchmark Circuit Scaling Through the 2030 ITRS Horizon', Proceedings of the IEEE, vol. 105, no. 6, pp. 1087–1104, Jun. 2017.
- [48] H. Koo, C.-Y. Kim, and S. Hong, 'A G-Band Standing-Wave Push–Push VCO Using a Transmission-Line Resonator', IEEE Transactions on Microwave Theory and Techniques, vol. 63, no. 3, pp. 1036–1045, Mar. 2015.
- [49] S. T. Nicolson et al., 'Design and Scaling of W-Band SiGe BiCMOS VCOs', IEEE Journal of Solid-State Circuits, vol. 42, no. 9, pp. 1821–1833, Sep. 2007.
- [50] A. Malko, T. Bryllert, J. Vukusic, and J. Stake, 'Silicon Integrated InGaAs/InAlAs/AlAs HBV Frequency Tripler', IEEE Electron Device Letters, vol. 34, no. 7, pp. 843–845, Jul. 2013.
- [51] D. Moro-Melgar, O. Cojocari, I. Oprea, M. Rickes, and H. Hoefle, 'Single-Chip 135-160 GHz Doubler with more than 150 mW Output Power based on Discrete Schottky Diodes', p. 3, 2018.
- [52] B. Alderman et al., 'High Power Frequency Multipliers to 330 GHz', p. 2.
- [53] Z. Zong, M. Babaie, and R. B. Staszewski, 'A 60 GHz Frequency Generator Based on a 20 GHz Oscillator and an Implicit Multiplier', IEEE Journal of Solid-State Circuits, vol. 51, no. 5, pp. 1261–1273, May 2016.
- [54] Z. Zong, P. Chen, and R. B. Staszewski, 'A Low-Noise Fractional-N Digital Frequency Synthesizer With Implicit Frequency Tripling for mm-Wave Applications', IEEE Journal of Solid-State Circuits, pp. 1–13, 2018.
- [55] M. Božanić and S. Sinha, Millimeter-Wave Low Noise Amplifiers. Cham: Springer International Publishing, 2018.
- [56] K. Iniewski, Wireless technologies: circuits, systems, and devices. Boca Raton: CRC Press/Taylor & Francis, 2008.

- [57] J. du Preez and S. Sinha, *Millimeter-Wave Power Amplifiers*. Cham: Springer International Publishing, 2017.
- [58] H. Hashemi, ‘Millimeter-wave power amplifiers & transmitters’, in 2017 IEEE Custom Integrated Circuits Conference (CICC), Austin, TX, 2017, pp. 1–8.
- [59] M. Vigilante and P. Reynaert, ‘A Wideband Class-AB Power Amplifier With 29–57-GHz AM–PM Compensation in 0.9-V 28-nm Bulk CMOS’, *IEEE Journal of Solid-State Circuits*, vol. 53, no. 5, pp. 1288–1301, May 2018.
- [60] K. Datta and H. Hashemi, ‘Performance Limits, Design and Implementation of mm-Wave SiGe HBT Class-E and Stacked Class-E Power Amplifiers’, *IEEE Journal of Solid-State Circuits*, vol. 49, no. 10, pp. 2150–2171, Oct. 2014.
- [61] M. Urteaga, Z. Griffith, M. Seo, J. Hacker, and M. J. W. Rodwell, ‘InP HBT Technologies for THz Integrated Circuits’, *Proceedings of the IEEE*, vol. 105, no. 6, pp. 1051–1067, Jun. 2017.
- [62] A. Margomenos et al., ‘GaN Technology for E, W and G-Band Applications’, in 2014 IEEE Compound Semiconductor Integrated Circuit Symposium (CSICS), La Jolla, CA, USA, 2014, pp. 1–4.
- [63] A. J. Seeds, ‘Microwave photonics’, *IEEE Transactions on Microwave Theory and Techniques*, vol. 50, no. 3, pp. 877–887, Mar. 2002.
- [64] T. H. Maiman, “Stimulated optical radiation in ruby masers,” *Nature*, vol. 187, pp. 493–494, 1960.
- [65] A. Javan, W. R. Bennett, Jr., and D. R. Herriott, “Population inversion and continuous optical maser oscillation in a gas discharge containing a He–Ne mixture,” *Phys. Rev. Lett.*, vol. 6, pp. 106–110, 1961.
- [66] S. Iezekiel, Ed., *Microwave photonics: devices and applications*. Chichester, U.K.; Hoboken, NJ: Wiley, 2009.
- [67] J. Capmany and D. Novak, ‘Microwave photonics combines two worlds’, *Nature Photonics*, vol. 1, no. 6, pp. 319–330, Jun. 2007.
- [68] K. C. Kao and G. A. Hockham, ‘Dielectric-fibre surface waveguides for optical frequencies’, vol. 133, no. 3, p. 8, 1986.
- [69] D. Marpaung, C. Roeloffzen, R. Heideman, A. Leinse, S. Sales, and J. Capmany, ‘Integrated microwave photonics: Integrated microwave photonics’, *Laser & Photonics Reviews*, vol. 7, no. 4, pp. 506–538, Jul. 2013.
- [70] K. Kato, S. Hata, K. Kawano, and A. Kozen, “Design of ultrawide-band, high-sensitivity p-i-n photodetectors”, *IEICE Trans. Electron.*, vol. E76-C, pp. 214–221, 1993.
- [71] J. Yao, ‘A Tutorial on Microwave Photonics’, p. 9, 2012.

- [72] J. E. Bowers, T. Komljenovic, J. Hulme, M. Davenport, and C. Zhang, 'Integrated photonics for MWP', in 2016 IEEE Photonics Conference (IPC), Waikoloa, HI, USA, 2016, pp. 1–2.
- [73] F. van Dijk et al., 'Integrated InP Heterodyne Millimeter Wave Transmitter', IEEE Photonics Technology Letters, vol. 26, no. 10, pp. 965–968, May 2014.
- [74] G. Morthier and P. Vankwikelberge, Handbook of distributed feedback laser diodes, Second edition. Boston: Artech House, 2013.
- [75] T. Nagatsuma, H. Ito, and T. Ishibashi, 'High-power RF photodiodes and their applications', Laser & Photonics Review, vol. 3, no. 1–2, pp. 123–137, Feb. 2009.
- [76] I. Aldaya, G. Campuzano, C. Del-Valle-Soto, A. Aragón-Zavala, and G. Castañón, 'Impact of the mobile terminal scheme on millimeter-wave radio over fiber systems based on photonic heterodyning techniques', Optical and Quantum Electronics, vol. 49, no. 6, Jun. 2017.
- [77] J. Yao, 'Microwave Photonics', Journal of Lightwave Technology, vol. 27, no. 3, pp. 314–335, Feb. 2009.
- [78] S. Preu, G. H. Döhler, S. Malzer, L. J. Wang, and A. C. Gossard, 'Tunable, continuous-wave Terahertz photomixer sources and applications', Journal of Applied Physics, vol. 109, no. 6, p. 061301, Mar. 2011.
- [79] F. van Dijk, A. Accard, A. Enard, O. Drisse, D. Make, and F. Lelarge, 'Monolithic dual wavelength DFB lasers for narrow linewidth heterodyne beat-note generation', in 2011 International Topical Meeting on Microwave Photonics jointly held with the 2011 Asia-Pacific Microwave Photonics Conference, Singapore, Singapore, 2011, pp. 73–76.
- [80] F.-M. Kuo et al., 'Spectral Power Enhancement in a 100 GHz Photonic Millimeter-Wave Generator Enabled by Spectral Line-by-Line Pulse Shaping', IEEE Photonics Journal, vol. 2, no. 5, pp. 719–727, Oct. 2010.
- [81] Guohua Qi, Jianping Yao, J. Seregelyi, S. Paquet, and C. Belisle, 'Generation and distribution of a wide-band continuously tunable millimeter-wave signal with an optical external modulation technique', IEEE Transactions on Microwave Theory and Techniques, vol. 53, no. 10, pp. 3090–3097, Oct. 2005.
- [82] S. Kobayashi and T. Kimuw, 'Injection Locking in AlGaAs Semiconductor Laser', IEEE Journal of Quantum Electronics, vol. QE-16, Sept. 1980, p. 915-917.
- [83] F. Mogensen, H. Olesen, and G. Jacobsen, 'Locking conditions and stability properties for a semiconductor laser with external light injection', IEEE Journal of Quantum Electronics, vol. 21, no. 7, pp. 784–793, Jul. 1985.
- [84] U. Gliese et al., 'A wideband heterodyne optical phase-locked loop for generation of 3-18 GHz microwave carriers', IEEE Photonics Technology Letters, vol. 4, no. 8, pp. 936–938, Aug. 1992.

- [85] L. A. Johansson and A. J. Seeds, 'Fibre-integrated heterodyne optical injection phase-lock loop for optical generation of millimetre-wave carriers', in 2000 IEEE MTT-S International Microwave Symposium Digest (Cat. No.00CH37017), Boston, MA, USA, 2000, vol. 3, pp. 1737–1740
- [86] K. Balakier et al., 'Optical injection locking of monolithically integrated photonic source for generation of high purity signals above 100 GHz', *Optics Express*, vol. 22, no. 24, p. 29404, Dec. 2014.
- [87] B. E. A. Saleh and I. John Wiley & Sons, *Fundamentals of Photonics* (Second Edition). Wiley-Interscience, 1991.
- [88] X. Yao and L. Maleki, "Optoelectronic microwave oscillator," *J. Opt. Soc. Am. B* 13, 1725-1735 (1996).
- [89] S. Ramo, 'Currents Induced by Electron Motion', *Proceedings of the IRE*, vol. 27, no. 9, pp. 584–585, Sep. 1939.
- [90] G. Ghione, 'Semiconductor Devices for High-Speed Optoelectronics', p. 481.
- [91] H. Venghaus and N. Grote, Eds., *Fibre Optic Communication*, vol. 161. Cham: Springer International Publishing, 2017.
- [92] G. W. A. Dummer, *Electronic inventions and discoveries: electronics from its earliest beginnings to the present day*, 3rd rev. and expanded ed. Oxford [Oxfordshire]; New York: Pergamon Press, 1983.
- [93] T. Nagatsuma and H. Ito, 'High-Power RF Uni-Traveling-Carrier Photodiodes (UTC-PDs) and Their Applications', in *Advances in Photodiodes*, G.-F. Dalla Betta, Ed. InTech, 2011.
- [94] T. Ishibashi, N. Shimizu, S. Kodama, H. Ito, T. Nagatsuma, and T. Furuta, 'Uni-Traveling-Carrier Photodiodes', in *Ultrafast Electronics and Optoelectronics* (1997), paper UC3, 1997, p. UC3.
- [95] A. Beling and J. C. Campbell, 'InP-Based High-Speed Photodetectors', *Journal of Lightwave Technology*, vol. 27, no. 3, pp. 343–355, Feb. 2009.
- [96] T. Ishibashi, T. Furuta, H. Fushimi, and H. Ito, 'Photoresponse characteristics of uni-traveling-carrier photodiodes', presented at the Symposium on Integrated Optics, San Jose, CA, 2001, p. 469.
- [97] A. S. Cross, Q. Zhou, A. Beling, Y. Fu, and J. C. Campbell, 'High-power flip-chip mounted photodiode array', *Optics Express*, vol. 21, no. 8, p. 9967, Apr. 2013.
- [98] H.-J. Song, K. Ajito, Y. Muramoto, A. Wakatsuki, T. Nagatsuma, and N. Kukutsu, 'Uni-Travelling-Carrier Photodiode Module Generating 300 GHz Power Greater Than 1 mW', *IEEE Microwave and Wireless Components Letters*, vol. 22, no. 7, pp. 363–365, Jul. 2012.

- [99] Q. Li et al., 'High-Power Evanescently Coupled Waveguide MUTC Photodiode With >105-GHz Bandwidth', *Journal of Lightwave Technology*, vol. 35, no. 21, pp. 4752–4757, Nov. 2017.
- [100] T. Umezawa, K. Akahane, A. Kanno, N. Yamamoto, K. Kashima and T. Kawanishi, "High conversion gain, low power consumption W-band photoreceiver integrated with UTC-PD and InP-PHEMT amplifier," 2015 International Topical Meeting on Microwave Photonics (MWP), Paphos, 2015, pp. 1-4.
- [101] J.-W. Shi et al., 'Extremely High Saturation Current-Bandwidth Product Performance of a Near-Ballistic Uni-Traveling-Carrier Photodiode With a Flip-Chip Bonding Structure', *IEEE Journal of Quantum Electronics*, vol. 46, no. 1, pp. 80–86, Jan. 2010.
- [102] J.-M. Wun et al., 'Photonic High-Power Continuous Wave THz-Wave Generation by Using Flip-Chip Packaged Uni-Traveling Carrier Photodiodes and a Femtosecond Optical Pulse Generator', *Journal of Lightwave Technology*, vol. 34, no. 4, pp. 1387–1397, Feb. 2016.
- [103] G. Zhou et al., 'High-Power InP-Based Waveguide Integrated Modified Uni-Traveling-Carrier Photodiodes', *Journal of Lightwave Technology*, vol. 35, no. 4, pp. 717–721, Feb. 2017.
- [104] G. Zhou, P. Runge, S. Lankes, A. Seeger, and M. Schell, 'Waveguide integrated pin-photodiode array with high power and high linearity', in 2015 International Topical Meeting on Microwave Photonics (MWP), Paphos, Cyprus, 2015, pp. 1–4.
- [105] I. D. Henning et al., 'Broadband Antenna-Integrated, Edge-Coupled Photomixers for Tuneable Terahertz Sources', *IEEE Journal of Quantum Electronics*, vol. 46, no. 10, pp. 1498–1505, Oct. 2010.
- [106] T. Ishibashi, Y. Muramoto, T. Yoshimatsu, and H. Ito, 'Unitraveling-Carrier Photodiodes for Terahertz Applications', *IEEE Journal of Selected Topics in Quantum Electronics*, vol. 20, no. 6, pp. 79–88, Nov. 2014.
- [107] H. Ito and T. Ishibashi, 'Photonic Terahertz-Wave Generation Using Slot-Antenna-Integrated Uni-Traveling-Carrier Photodiodes', *IEEE Journal of Selected Topics in Quantum Electronics*, vol. 23, no. 4, pp. 1–7, Jul. 2017.
- [108] C. C. Renaud, M. Natrella, C. Graham, J. Seddon, F. Van Dijk, and A. J. Seeds, 'Antenna Integrated THz Uni-Traveling Carrier Photodiodes', *IEEE Journal of Selected Topics in Quantum Electronics*, vol. 24, no. 2, pp. 1–11, Mar. 2018.
- [109] E. Rouvalis, C. C. Renaud, D. G. Moodie, M. J. Robertson, and A. J. Seeds, 'Continuous Wave Terahertz Generation From Ultra-Fast InP-Based Photodiodes', *IEEE Transactions on Microwave Theory and Techniques*, vol. 60, no. 3, pp. 509–517, Mar. 2012.

- [110] D. H. Auston, 'Picosecond optoelectronic switching and gating in silicon', *Applied Physics Letters*, vol. 26, no. 3, pp. 101–103, Feb. 1975.
- [111] E. R. Brown, 'THz Generation by Photomixing in Ultrafast Photoconductors', *Int. J. Hi. Spe. Ele. Syst.*, vol. 13, no. 02, pp. 497–545, Jun. 2003.
- [112] D. Saeedkia and S. Safavi-Naeini, 'Terahertz Photonics: Optoelectronic Techniques for Generation and Detection of Terahertz Waves', *Journal of Lightwave Technology*, vol. 26, no. 15, pp. 2409–2423, Aug. 2008.
- [113] M. Billet, P. Latzel, F. Pavanello, G. Ducournau, J.-F. Lampin, and E. Peytavit, 'Resonant cavities for efficient LT-GaAs photoconductors operating at $\lambda = 1550$ nm', *APL Photonics*, vol. 1, no. 7, p. 076102, Oct. 2016.
- [114] C. Graham, R. Gwilliam, and A. Seeds, 'Nitrogen ion implanted InP based photo-switch', *Optics Express*, vol. 20, no. 24, p. 26696, Nov. 2012.
- [115] R. Horváth, J.-F. Roux, J. Poëtte, and B. Cabon, 'Optoelectronic mixing with photoconductive switch and semiconductor mode-locked laser', p. 3.
- [116] R. Horvath, J.-F. Roux, J.-L. Coutaz, J. Poette, B. Cabon, and C. Graham, 'Ultrafast InGaAs photoswitch for RF signal processing', in *2017 International Conference on Optical Network Design and Modeling (ONDM)*, Budapest, 2017, pp. 1–5.
- [117] A. D. J. F. Olvera, H. Lu, A. C. Gossard, and S. Preu, 'Continuous-wave 1550 nm operated terahertz system using ErAs:In(Al)GaAs photo-conductors with 52 dB dynamic range at 1 THz', *Optics Express*, vol. 25, no. 23, p. 29492, Nov. 2017.
- [118] U. Nandi, J. C. Norman, A. C. Gossard, H. Lu, and S. Preu, '1550-nm Driven ErAs:In(Al)GaAs Photoconductor-Based Terahertz Time Domain System with 6.5 THz Bandwidth', *Journal of Infrared, Millimeter, and Terahertz Waves*, vol. 39, no. 4, pp. 340–348, Apr. 2018.
- [119] E. Peytavit, P. Latzel, F. Pavanello, G. Ducournau, and J.-F. Lampin, 'CW Source Based on Photomixing With Output Power Reaching 1.8 mW at 250 GHz', *IEEE Electron Device Letters*, vol. 34, no. 10, pp. 1277–1279, Oct. 2013.

CHAPTER 3

DESIGN AND RF SOLUTIONS TO INCREASE OUTPUT POWER

Millimeter-wave photonic-based technology is able to deliver high quality signals with superior tunability in comparison to electronics-based solutions. Unfortunately, UTC and p-i-n photodiodes are limited due to physical mechanism such as space charge screening or thermal effects [1]. In Fig. 3. 1 an output power vs. optical input power is presented in comparison to the ideal response. With input power increase, the output power level reaches saturation, and photodiode operates outside linear region. Joule heating of the absorption region increases at high photocurrent densities and can result in catastrophic failure of the device. Fortunately, due to constant progress in device modelling, epitaxial technology and lithography processing, the impact of some of the limiting factors can be reduced. In this chapter some of the most utilized approaches in design and RF solutions to increase the output power are presented.

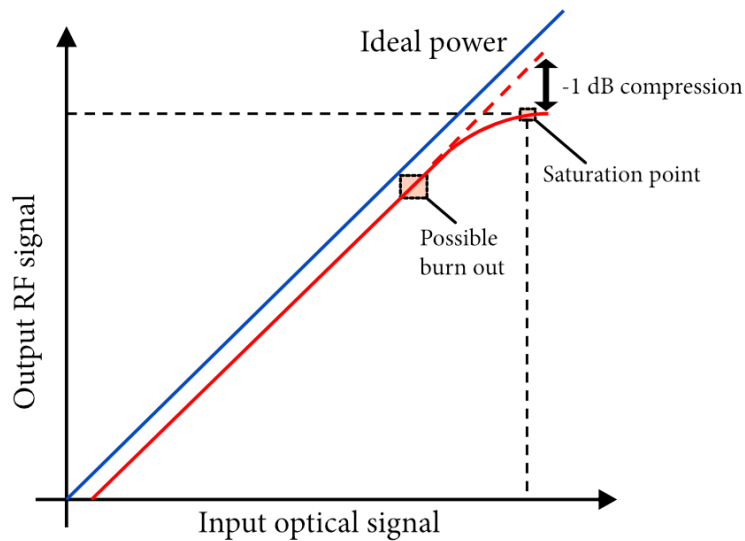


Fig. 3. 1 Typical curve of -1 dB compression point of photodiode.

3.1 UTC PHOTODIODE - LIMITATIONS

Investigation of the physical limitations of the UTC photodiode structure and the photoresponse characteristics are studied in [2][3][5]. The Boltzmann transport equations, the drift-diffusion model or charge-control model and the Poisson equation are used to examine the small-signal frequency response of the absorption and the collection layer of the UTC PD. Detailed descriptions of the parameters, approximations, boundary conditions and derivation procedures necessary to obtain fundamental equations are given in [2]-[7].

As mentioned in previous chapter (2.7.1), light absorption (Fig. 3. 2) occurs in a thin p-type layer where holes generation, as they are the majority carriers, do not limit the high-frequency response (photogenerated holes respond fast within the dielectric relaxation time τ_R). Moreover, only the photogenerated minority electrons diffuse/drift into the transport *i* (intrinsic) region [2][5]. By introduction of compositional and/or doping grading it is possible to effectively reduce the electron travelling time in the absorption layer (built-in field). Furthermore, the absorption and carrier transport layers can be designed and optimized independently, which is also another advantage over traditional p-i-n PD. Moreover, in the UTC PD design, the band profile should ease the path of the electrons between absorption and transport layer to minimize the transit time. This can be obtained with a thin layer of InGaAsP placed between the absorber and the transport/collection layers. In addition, the UTC PD design has many similarities with the design of base-collector junction of bipolar transistor or HBT [15], and therefore several band profile engineering approaches can be utilized to model absorption and collection layer i.e. by band-gap grading. Furthermore, the electron velocity overshoot phenomenon, taking place in the depletion layer, is also used to improve operational speed and output current of UTC PD structure [8].

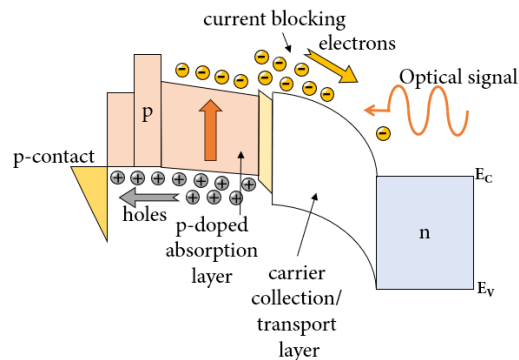


Fig. 3. 2 Band structure of conventional UTC photodiode at high optical input.

Based on the reported studies in [2]-[7][15], the operational speed of the UTC PD is mainly determined by the electron diffusion time in the absorption layer, therefore the absorption layer thickness (W_A) is examined to obtain optimal layer composition. What is more, due to p-InGaAs material properties (large mobility of minority electrons), the electron diffusion velocity can be very large in the absorption layer, if the thickness of this layer is optimized. The 3-dB bandwidth for UTC photodiode can be expressed as [15]:

$$f_{3dB} \cong 1/2\pi \left(\frac{W_a^2}{3D_e} + \frac{W_a}{V_{th}} \right), \quad (3.1)$$

where the diffusion coefficient of minority electrons $D_e = \mu_n kT/q$, and k is the Boltzmann constant, V_{th} is thermionic emission velocity of electrons ($2.5 \times 10^7 \frac{cm}{s}$ in InGaAs), μ_n is the minority electron mobility, T is the temperature, and q is the electron charge. Eq. 3.1 demonstrates that f_{3dB} is inversely proportional to W_a^2 except when the absorption layer is very thin. In Fig. 3, a relationship between the 3-dB bandwidth and the absorption layer thickness is presented. Dotted line shows the calculated tendency of the carrier transit times contributions in the absorption and collection layers for UTC PDs. These results correspond well with experimental data at low optical inputs, but not in the case when the absorption layer is extremely thin, what might be associated with increasing influence of parasitic elements in the device or signal broadening in the electrical waveguide [2].

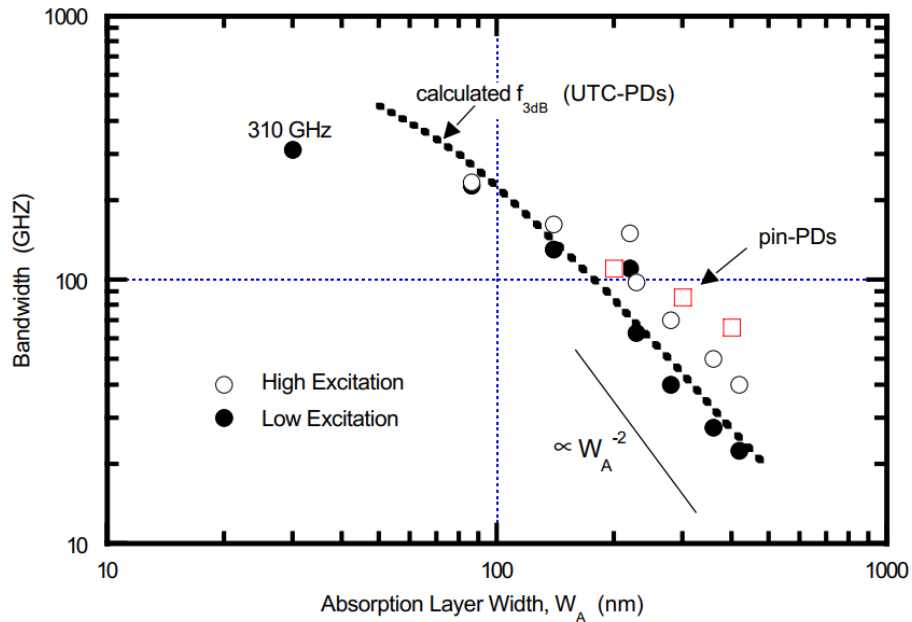


Fig. 3. 3 Relationship between 3-dB bandwidth for InP/InGaAs UTC-PDs and p-i-n PDs [2].

The relative frequency response of a photodiode ($B(f)$) can be expressed as [15]:

$$B(f) = \frac{1}{\left(1 + \left(\frac{f}{BW_{CR}}\right)^2\right) \times \left(1 + \left(\frac{f}{BW_{TR}}\right)^2\right)} \quad (3.2)$$

where f is the frequency, BW_{RC} is the RC time constant limited bandwidth equal to $\frac{1}{2\pi RC}$, and BW_{TR} is the carrier transit time limited bandwidth. The carrier transit times and RC-time constant are the two main bandwidth limiting factors. The photodiode can be described as an ideal current source $I(f)$, in parallel with junction capacitance (C_{PD}), resistance (R_P), and a series resistance (R_S), C_P and L_P are the parasitic inductance and capacitance from electrical interconnections. External load resistor (R_L) is usually equal to 50Ω or to antenna impedance. Moreover, an optional resistor can be implemented close to the photodiode, reducing the effective load but a half of the output current will be lost. More advanced equivalent circuit models of a UTC photodetector integrated with an antenna and fabricated in III-V Lab has been investigated in [13][14], with good agreement between simulation and measurement results up to 110 GHz.

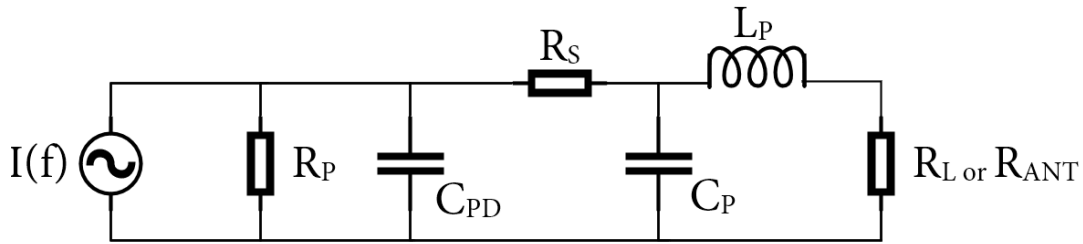


Fig. 3. 4 Equivalent circuit of lumped element photodetector.

When $R_P \gg R_S + R_L$, the f_{RC} can be calculated as [16]:

$$f_{RC} = \frac{1}{2\pi R_{eff} C_{PD}}, \quad (3.3)$$

where $R_{eff} = R_S + R_L$, and $C_{PD} = \epsilon_0 \epsilon_r \frac{S}{d_{intrinsic}}$, S is a photodiode cross section, $d_{intrinsic}$ is a thickness of intrinsic layer, ϵ_r and ϵ_0 are the dielectric constant of a semiconductor and vacuum permeability, respectively. Furthermore, in order to reduce some of the limitations caused by the space-charge and thermal effects, photodiodes with dual-depletion region (DDR), partially-depleted absorber (PDA) and modified UTC (MUTC) have been developed [9][10][11]. The DDR PD can be characterized by a transparent drift layer between the intrinsic absorber and the n-type contact layer [9][16].

With careful design of the layer thickness DDR PDs exhibit smaller junction capacitance in comparison to standard p-i-n photodiodes. The PDA PD structure provides higher

responsivities than a standard UTC PDs. It is achieved due to additional p-doped and n-doped absorber layers on each side of the i region, which balance the hole and electron densities within the depletion region [10]. Modified UTC photodiodes are composed of undoped i -InGaAs layer between p-type InGaAs absorber and i -InP drift layer [11]. With optimized layer structure MUTC are able to reach very high saturation currents. Moreover, flip-chip bonding onto high-thermal conductivity sub-mounts such as AlN or diamond substrates greatly improves maximum output power levels [19].

To conclude:

- **By careful design of the UTC PDs very wide bandwidth operation is achievable (above 100 GHz).**
- **Due to unique properties of p-InGaAs material as well as the carrier transport mechanism, the output power levels are higher in comparison to standard p-i-n PD.**
- **The output power is reduced mainly due to space-charge effect and thermal limitation of the device, but thanks to the layer stack modification some of the limitations of the classic UTC PD structure can be overcome.**

3.2 PHOTODIODES - TOPOLOGIES

Most of the p-i-n and UTC photodetectors used in the telecommunication systems are vertically illuminated structures with top or back illumination (Fig. 3. 5). In this type of devices, there is a known trade-off in performance in terms of bandwidth and quantum efficiency. The responsivity can be calculated as:

$$\mathcal{R}_{PD} = \mathcal{R}_{ideal} (1 - R_0)(1 - e^{-\alpha d_{abs}}) \quad (3.4)$$

where, α is the absorption coefficient, d_{abs} is the absorber thickness and R_0 is the reflectance at the air-semiconductor interface [16]. With thicker absorber, quantum efficiency is higher,

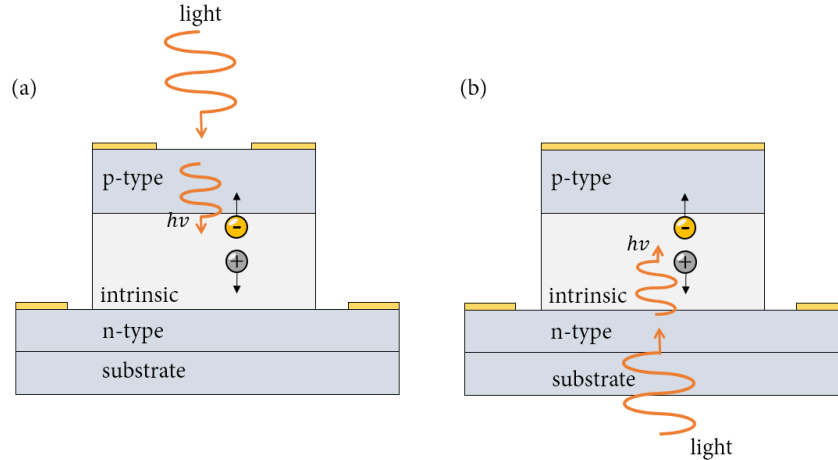


Fig. 3. 5 Top (a) and back (b) illuminated p-i-n photodiodes.

but it results in a longer carrier transit time that reduces the bandwidth. Despite the simplest vertical structure photodiode, an edge/side illuminated waveguide (WG-PDs) and evanescently-coupled WG-PDs are utilized (Fig. 3. 6). The side-illuminated photodiode due to the design can overcome some of the vertical structure bandwidth limitations [17]. As the input optical waveguide with embedded or adjacent absorbing layers is employed, the photogenerated carriers have to transit only the thin absorption/depletion region. Therefore, the thickness of the absorber layer determines the carrier transit times, and the responsivity is controlled by the length of the detector. In the evanescently coupled WG-PD, the photodiode is positioned on the top of the passive waveguide (Fig. 3. 6b). This design improves absorption uniformity along the device length and high-power capabilities [17]. Responsivity of a single mode WG-PD is given by [20]:

$$\mathcal{R}_{\text{WGPd}} = \mathcal{R}_{\text{ideal}} (1 - R_0) \eta_c (1 - \exp(-\Gamma_{xy} \alpha l_{PD})) \quad (3.5)$$

η_c - input coupling efficiency

Γ_{xy} - confinement factor in the xy-plane within absorbing layer

l_{PD} - PD length

WG-PDs suffer from sensitive alignment of the input optical fiber. Fiber to chip coupling is very often performed with tapered optical fiber or more complex solutions with additional optics are utilized to efficiently illuminate the device. Integration of a taper can improve coupling efficiency and increase alignment tolerances. Furthermore, the waveguide and evanescently-coupled PDs have been further modified towards distributed structures to enhance the bandwidth such as travelling-wave PDs and velocity-matched/periodically loaded travelling-wave PDs (Fig. 3. 7) [17][18]. Based on the reported results (Ch. 2.7.2) back-illuminated photodiodes achieved higher output power levels, but evanescently coupled WG-

PDs are more suited for the monolithic integration in PICs and constant progress in technology reduces the gap between two design approaches.

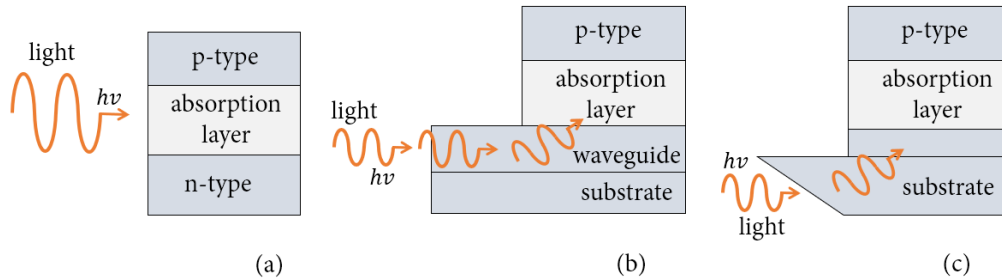


Fig. 3. 6 Waveguide (a), evanescently-coupled (b) and with refractive facet (c) p-i-n PD.

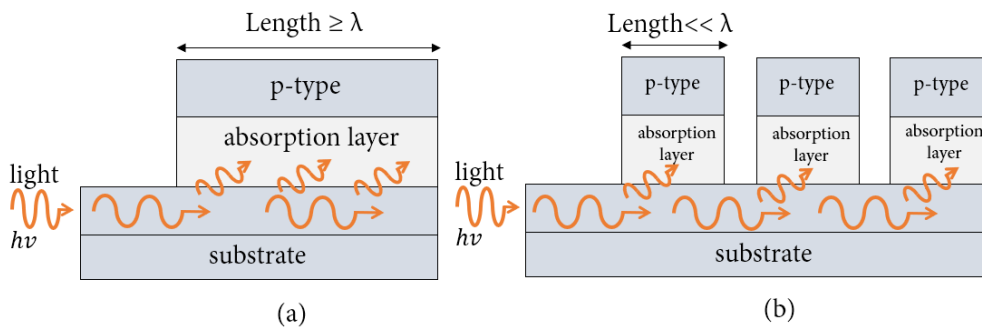


Fig. 3. 7 Simplified distributed structures of a travelling-wave PD (a) and (b) a velocity-matched PDs.

3.2.1 Distributed photodetectors

Travelling-wave (TWPD) and velocity-matched photodetectors (VMPD) have been developed to overcome RC bandwidth limitation of the lumped-element WG-PD [17][21]. In the TWPD, the absorption region covers the entire length of the microwave transmission line that is placed on the top of the structure. This type of solution leads to velocity mismatch between microwave phase velocity and the optical group velocity, what limits the bandwidth of this design [21][22]. Moreover, the characteristic line impedance is usually below 50Ω because of capacitive loading from the absorption layer. To overcome these limitations, the VMPD (although very often referred as TWPD) structure has been introduced. It is composed of periodically distributed discrete photodiodes along the transmission line. Due to separation between the photodiodes, the capacitive loading is mitigated. With careful design of the distance and of the transmission line geometry, the characteristic impedance can be matched with the external load, leading to a phase match between the propagating optical and electrical signals. Nevertheless, impedance matching is very often achieved for practical reasons with an integrated matching resistor and consequently with a half of output current loss. The device presented in Fig. 3. 8 achieved -2.5 dBm at 150 GHz and f_{3dB} of 80 GHz [23]. Moreover,

measurements up to 400 GHz have been performed with output power of -34 dBm. Recent results of TWPD with MUTC PDs flip-chip bonded onto transmission lines on AlN substrate has been reported in [24]. High RF output power of 21 dBm up to 48 GHz for four back-illuminated MUTC have been recorded (Fig. 3. 9).

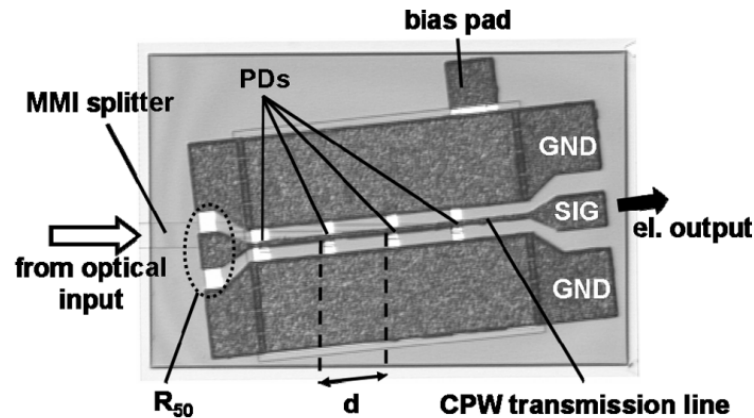


Fig. 3. 8 Micrograph of the TWPD (p-i-n PDs) chip with $d = 90 \mu\text{m}$. The input signal is fed from the left via mode converter and rib waveguide into MMI splitter [23].

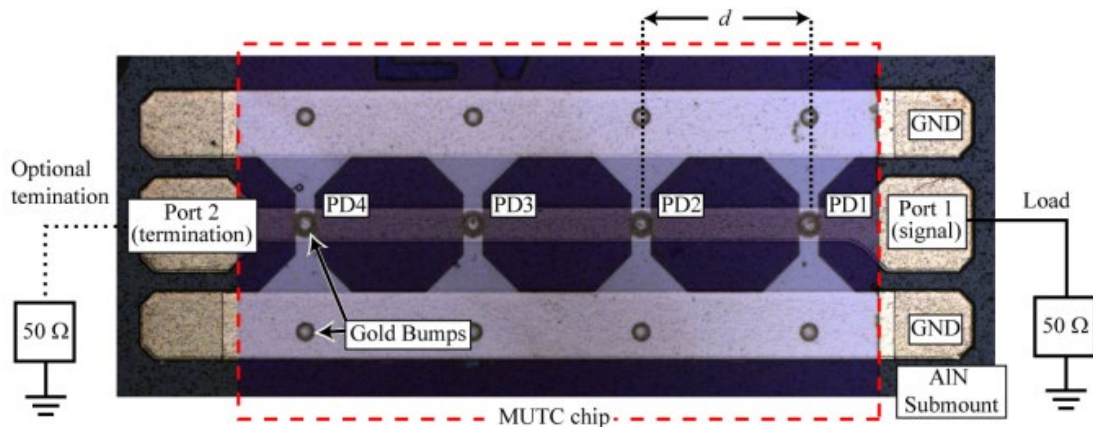


Fig. 3. 9 MUTC chip with four diodes and AlN submount with transmission line [24].

To conclude:

- **Top and back-illuminated UTC PDs deliver high output power levels and responsivity but narrower bandwidths in comparison to waveguide PDs.**

- **Waveguide UTC PDs have great advantage over top and back-illuminated PDs as they can be monolithically integrated with other optical components.**
- **Thanks to the distributed design approach some of the RC bandwidth limitations can be overcome and higher output power levels can be achieved.**

3.3 ANTENNA ARRAYS AND POWER COMBINED PHOTODETECTORS

Photodiode array and power combining techniques are one of the most efficient way to increase the output power [25]. The highest output power level reported so far is achieved with four photodiodes in a distributed photodetector configuration, with phase matched combined outputs (Fig. 3. 9 [24]). Array of evanescently-coupled waveguide p-i-n photodiodes have been presented in [26]. The structure consists of spot size converter, MMI (1xN) and PD array integrated on single chip (Fig. 3. 10). Photodiodes are in a parallel connection and the photocurrent is the sum of all employed photodetectors. Moreover, the output power level and linearity increases, but the f_{3dB} is decreasing with higher number of PDs. It is caused due to rising capacitance with the number of the parallel connected photodiodes. Furthermore, at higher frequencies, obtained results indicates better performance for the array of two and three PDs with output power of 1.5 dBm and 2.2 dBm, respectively. Back-illuminated UTC

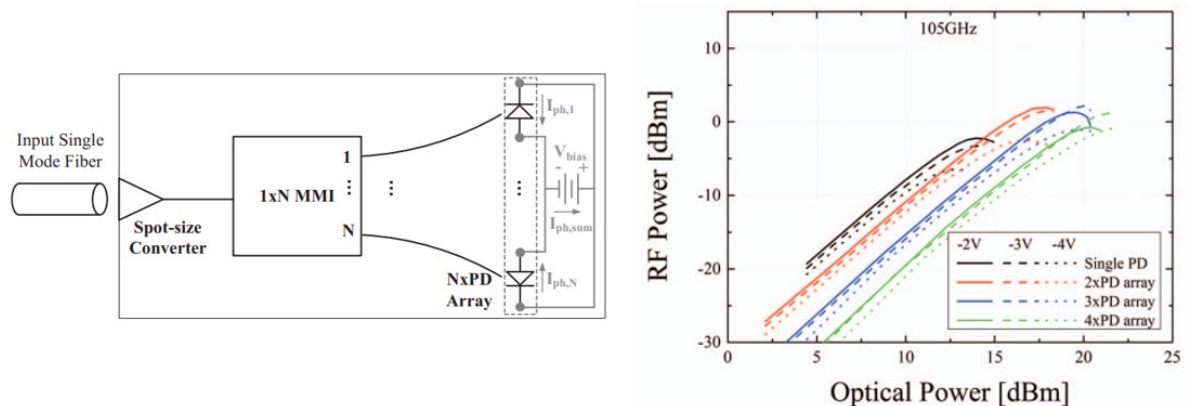


Fig. 3. 10 Diagram of the evanescently-coupled p-i-n photodiode arrays (left) and RF power at 105 GHz vs. optical input power (right) at different bias voltage [26].

photodiodes with microstrip antenna array arranged in a square grid with 500 μm spacing operating at 300 GHz have been reported in [27]. Antennas have been fed by UTC photodiode under the dielectric layer through a via. Schematic illustration of the module is presented in Fig. 3. 11. Measured radiation power of -9.2 dBm with a Goly cell, for a single antenna element, and estimation for the 3x3 array of 0 dBm is reported. Moreover, this has been the first demonstration of an antenna array that coherently combines the power of radiation at 300 GHz emitted by each antenna element.

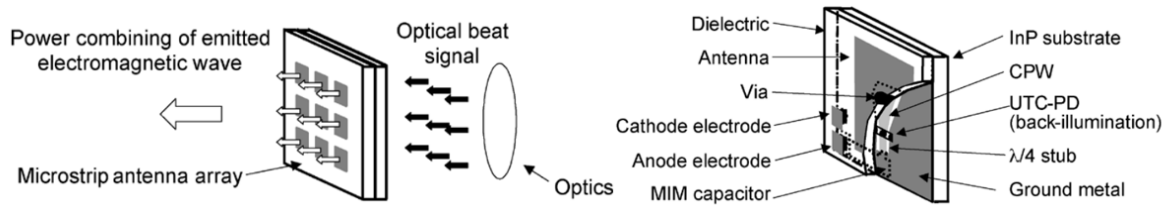


Fig. 3. 11 Schematic illustration of the microstrip antenna array (left) and antenna element (right) [27].

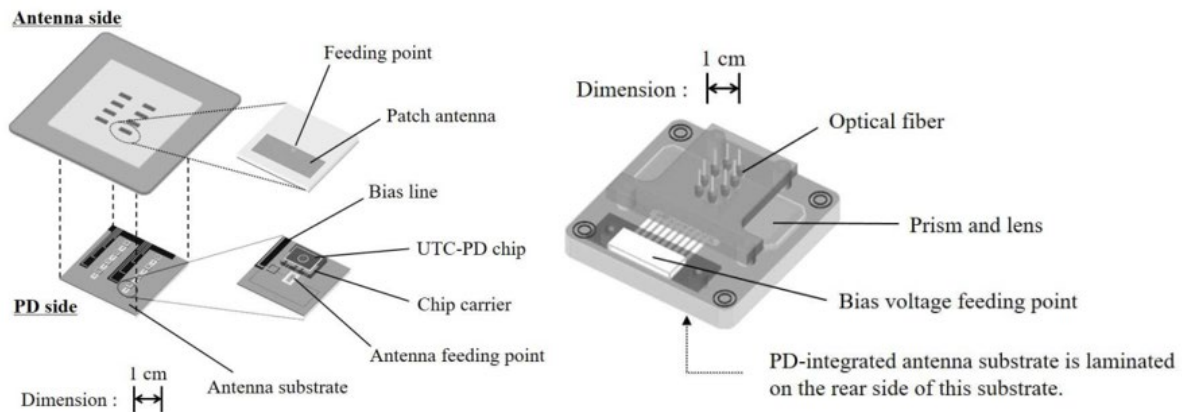


Fig. 3. 12 Overall structure of an antenna module for 60 GHz applications [29].

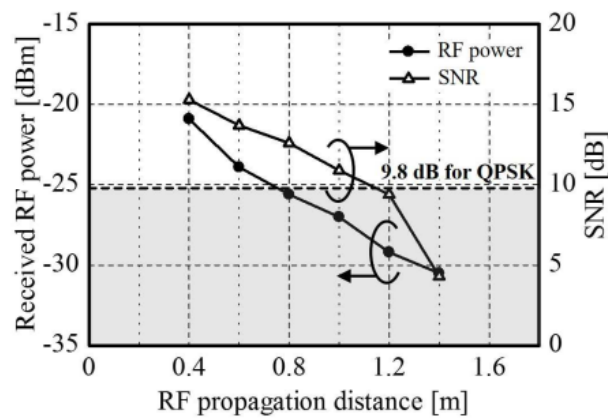


Fig. 3. 13 Received RF powers and SNR values for the QPSK signal as a function of the RF propagation distance [29].

More recent design with a similar approach of an 4x2 patch antenna array module for 60 GHz applications is presented in Fig. 3. 12 [28][29]. Antenna substrate consist of patch antennas with via holes for wire bonding to chip carriers as well wire bonded to coplanar lines. On the coplanar lines a UTC PDs are mounted by flip-chip bonding. Moreover, optical signal feeding substrate consist of optical fibers, prisms and lenses used for focusing the optical signal for each PD. Measurement result proved beam steering capabilities of the proposed complex system by tuning the wavelength of the optical signal. Furthermore, transmission of a 3.5-Gbit/s QPSK

signal with beam forming operation has been performed with received RF power of -20 dBm at 40 cm distance (Fig. 3. 13)[29]. Another example of UTC array integrated with bow-tie antennas and also with a planar lightwave circuit is investigated in [30]. The overview of the

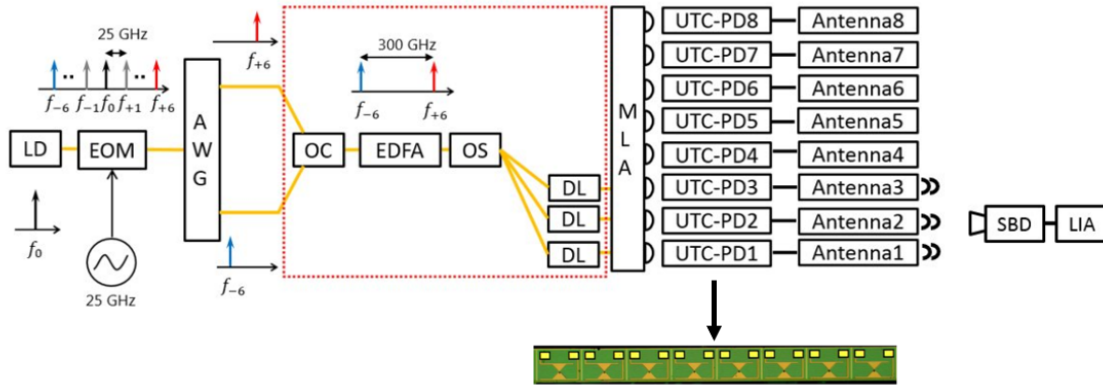


Fig. 3. 14 Overview of the setup with array of bow-tie antenna integrated UTC PDs, optical delay lines (DL) and Schottky barrier diode as a power detector (SBD)[30].

experimental setup is presented in Fig. 3. 14. Distance between bow-tie antenna and SBD was about 5 cm. Light is coupled into UTC with micro-lens array (MLA). Reported results of synchronously combined antennas reveal that power is not only a sum of radiation of each element. An enhancement of peak power or directional gain has been recorded. Application of planar lightwave circuit for electrical phase control has been tested and reported results are similar to that with DLs-based system.

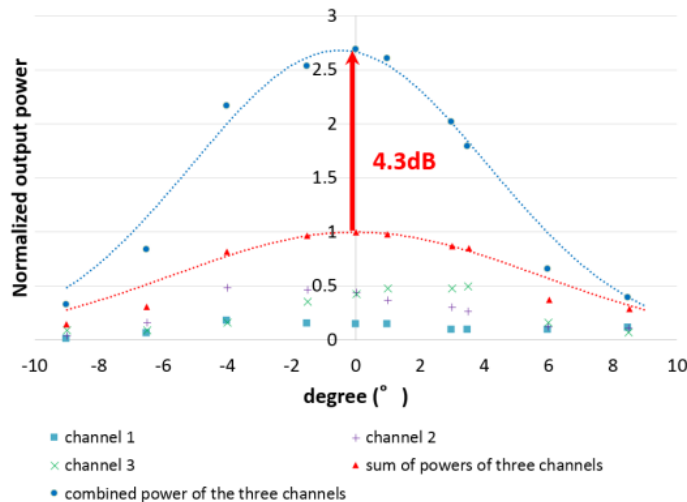


Fig. 3. 15 Output power of the system with delay lines [30].

Module with power combined UTC photodiodes at 300 GHz with output power of 0.8 dBm measured with power meter have been reported in [31]. In this design T-junction for power combiner of two parallel connected back-illuminated UTC PDs is utilized. Fabricated chip and schematic diagram of WR-3 waveguide module package is presented in Fig. 3. 16. Although, the bandwidth of the device is reduced due to T-junction power combiner, module provides enough bandwidth for telecommunication applications. Wilkinson power combiners

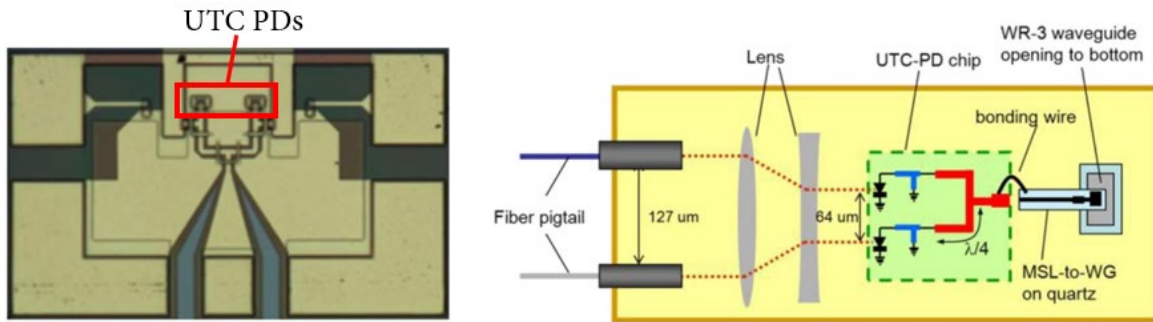


Fig. 3. 16 Top view (left) of fabricated UTC PDs with T-junction power combiner and schematic of the package module (right) [31].

with back-illuminated p-i-n photodiodes firstly proposed in [32][33] achieved output power of 30 dBm at lower frequencies up to 5 GHz. Similar approach at 20 GHz is reported in [34][35]. Two and four back-illuminated PDA photodiodes have been integrated with Wilkinson power combiner with and without tuning stubs. Both type of designs improves output power levels and linearity in comparison to discrete PDs. The OIP3 of 47 dBm at 20 GHz for four-way combiner is reported.

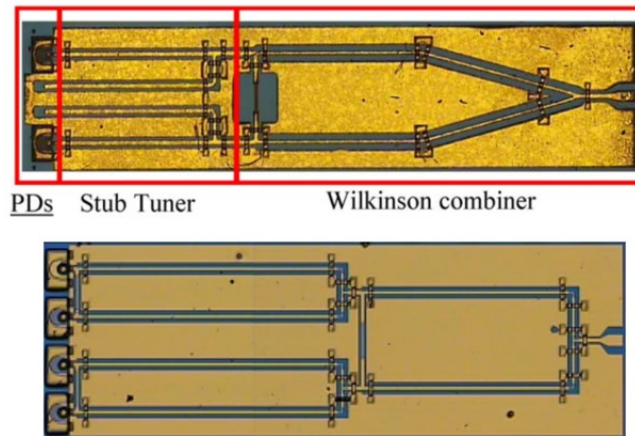


Fig. 3. 17 Two-way (top) and four-way (bottom) Wilkinson power combiner with back-illuminated photodiodes [34][35].

3.4 DESIGN AND RF SOLUTIONS TO INCREASE OUTPUT POWER – CONCLUSIONS

To briefly conclude previously presented results, the most promising approaches reported in the literature that can greatly increase output power levels are based on:

- Array of photodiodes.
- Power combining techniques.
- Antenna arrays.

Single-photodiode structures, although notably improved due to constant research and development, are less performant in comparison to multiple device designs. As reported, by simple increase of number of photodiodes implemented in the design, output power levels can be improved but with the cost of bandwidth reduction. Further improvements are required such as implementation of power combining techniques in the circuit architecture. Nevertheless, with increasing frequency, circuit design becomes very challenging and additional issues arise i.e. impedance mismatch between photodiodes and circuit components. Furthermore, an antenna-array is as well promising approach that can improve output power levels, but it also requires careful design to obtain wideband operation, impedance matching and compactness.

In this PhD thesis, after presenting and describing the most promising solutions to increase output power levels, power combining technique and antenna-array approaches are chosen for the final PIC design.

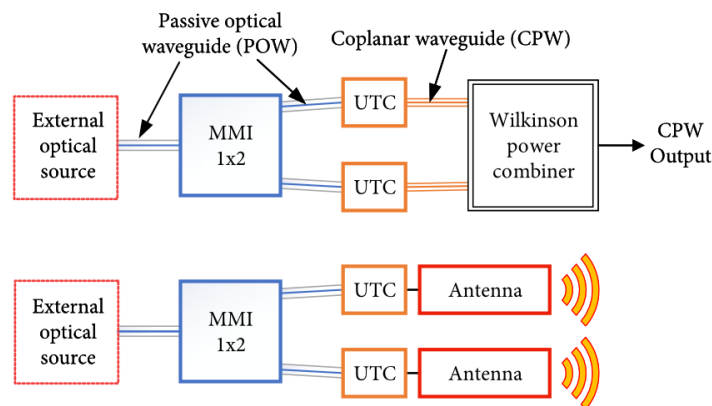


Fig. 3. 18 Schematic example of proposed PICs with 2-way Wilkinson power combiner (top) and 2x antenna-integrated photodiodes array (bottom).

In the design with power combiner, two and four UTC PDs are implemented. For the antenna-arrays, several configurations are chosen with two and three UTC PDs. Next chapter is dedicated to present the PIC design and simulation results of proposed solutions.

REFERENCES

- [1] K. J. Williams, ‘Comparisons between dual-depletion-region and uni-travelling-carrier p-i-n photodetectors’, *IEE Proceedings - Optoelectronics*, vol. 149, no. 4, pp. 131–137, Aug. 2002.
- [2] T. Ishibashi, T. Furuta, H. Fushimi, and H. Ito, ‘Photoresponse characteristics of uni-traveling-carrier photodiodes’, presented at the Symposium on Integrated Optics, San Jose, CA, 2001, p. 469.
- [3] T. Ishibashi, S. Kodama, N. Shimizu, and T. Furuta, ‘High-Speed Response of Uni-Traveling-Carrier Photodiodes’, *Japanese Journal of Applied Physics*, vol. 36, no. Part 1, No. 10, pp. 6263–6268, Oct. 1997.
- [4] A. Jünger, *Transport equations for semiconductors*. Berlin: Springer, 2009.
- [5] M. N. Feiginov, ‘Analysis of limitations of terahertz p-i-n uni-traveling-carrier photodiodes’, *Journal of Applied Physics*, vol. 102, no. 8, p. 084510, Oct. 2007.
- [6] K. Kato, S. Hata, K. Kawano, and A. Kozen, “Design of ultrawide-band, high-sensitivity p-i-n photodetectors”, *IEICE Trans. Electron.*, vol. E76-C, pp. 214–221, 1993.
- [7] J. Harari, G. Jin, J. P. Vilcot, and D. Decoster, ‘Theoretical study of p-i-n photodetectors’ power limitations from 2.5 to 60 GHz’, *IEEE Transactions on Microwave Theory and Techniques*, vol. 45, no. 8, pp. 1332–1336, Aug. 1997.
- [8] T. Ishibashi, Y. Muramoto, T. Yoshimatsu, and H. Ito, ‘Unitraveling-Carrier Photodiodes for Terahertz Applications’, *IEEE J. Select. Topics Quantum Electron.*, vol. 20, no. 6, pp. 79–88, Nov. 2014.
- [9] F. J. Effenberger, ‘Ultrafast, Dual-Depletion Region, InGaAdInP p-i-n Detector’, *JLT*, vol. 14, no. 8, p. 6, 1996.
- [10] Xiaowei Li et al., ‘High-saturation-current InP-InGaAs photodiode with partially depleted absorber’, *IEEE Photonics Technology Letters*, vol. 15, no. 9, pp. 1276–1278, Sep. 2003.
- [11] D.-H. Jun, J.-H. Jang, I. Adesida, and J.-I. Song, ‘Improved Efficiency-Bandwidth Product of Modified Uni-Traveling Carrier Photodiode Structures Using an Undoped Photo-Absorption Layer’, *Japanese Journal of Applied Physics*, vol. 45, no. 4B, pp. 3475–3478, Apr. 2006.
- [12] G. H. Döhler et al., ‘THz-photomixer based on quasi-ballistic transport’, *Semiconductor Science and Technology*, vol. 20, no. 7, pp. S178–S190, Jul. 2005.
- [13] M. Natrella et al., ‘Accurate equivalent circuit model for millimetre-wave UTC photodiodes’, *Optics Express*, vol. 24, no. 5, p. 4698, Mar. 2016.
- [14] M. Natrella et al., ‘Modelling and measurement of the absolute level of power radiated by antenna integrated THz UTC photodiodes’, *Optics Express*, vol. 24, no. 11, p. 11793, May 2016.

- [15] H. Ishikawa, Ed., *Ultrafast all-optical signal processing devices*. Chichester, West Sussex, England; Hoboken, NJ, USA: Wiley, 2008.
- [16] H. Venghaus and N. Grote, Eds., *Fibre Optic Communication*, vol. 161. Cham: Springer International Publishing, 2017.
- [17] A. Beling and J. C. Campbell, 'InP-Based High-Speed Photodetectors', *Journal of Lightwave Technology*, vol. 27, no. 3, pp. 343–355, Feb. 2009.
- [18] T. Nagatsuma, H. Ito, and T. Ishibashi, 'High-power RF photodiodes and their applications', *Laser & Photonics Review*, vol. 3, no. 1–2, pp. 123–137, Feb. 2009.
- [19] Q. Zhou, A. S. Cross, A. Beling, Y. Fu, Z. Lu, and J. C. Campbell, 'High-Power V-Band InGaAs/InP Photodiodes', *IEEE Photonics Technology Letters*, vol. 25, no. 10, pp. 907–909, May 2013.
- [20] K. Kato, S. Hata, K. Kawano, and A. Kozen, "Design of ultrawide-band, high-sensitivity p-i-n photodetectors", *IEICE Trans. Electron.*, vol. E76-C, pp. 214–221, 1993.
- [21] S. Iezekiel, Ed., *Microwave photonics: devices and applications*. Chichester, U.K.; Hoboken, NJ: Wiley, 2009.
- [22] K. S. Giboney, J. W. Rodwell, and J. E. Bowers, 'Traveling-wave photodetector theory', *IEEE Transactions on Microwave Theory and Techniques*, vol. 45, no. 8, pp. 1310–1319, Aug. 1997.
- [23] A. Beling, J. C. Campbell, H.-G. Bach, G. G. Mekonnen, and D. Schmidt, 'Parallel-Fed Traveling Wave Photodetector for >100-GHz Applications', *Journal of Lightwave Technology*, vol. 26, no. 1, pp. 16–20, Jan. 2008.
- [24] A. S. Cross, Q. Zhou, A. Beling, Y. Fu, and J. C. Campbell, 'High-power flip-chip mounted photodiode array', *Optics Express*, vol. 21, no. 8, p. 9967, Apr. 2013.
- [25] T. Nagatsuma, H. Ito, and T. Ishibashi, 'High-power RF photodiodes and their applications', *Laser & Photonics Review*, vol. 3, no. 1–2, pp. 123–137, Feb. 2009.
- [26] G. Zhou, P. Runge, S. Lankes, A. Seeger, and M. Schell, 'Waveguide integrated pin-photodiode array with high power and high linearity', in *2015 International Topical Meeting on Microwave Photonics (MWP)*, Paphos, Cyprus, 2015, pp. 1–4.
- [27] N. Shimizu and T. Nagatsuma, 'Photodiode-integrated microstrip antenna array for subterahertz radiation', *IEEE Photonics Technology Letters*, vol. 18, no. 6, pp. 743–745, Mar. 2006.
- [28] T. Hirasawa, K. Furuya, M. Oishi, S. Akiba, J. Hirokawa, and M. Ando, 'Integrated photonic array-antennas in RoF system for MMW-RF antenna beam steering', in *2015 International Topical Meeting on Microwave Photonics (MWP)*, Paphos, Cyprus, 2015, pp. 1–4.
- [29] M. Oishi, T. Hirasawa, K. Furuya, S. Akiba, J. Hirokawa, and M. Ando, '3.5-Gbit/s QPSK Signal Radio-Over-Fiber Transmission With 60-GHz Integrated Photonic Array-Antenna Beam Forming', *Journal of Lightwave Technology*, vol. 34, no. 20, pp. 4758–4764, Oct. 2016.

- [30] K. Sakuma, J. Haruki, G. Sakano, K. Kato, S. Hisatake, and T. Nagatsuma, 'Coherent THz wave combiner composed of arrayed uni-traveling carrier photodiodes and planar lightwave circuit', presented at the SPIE OPTO, San Francisco, California, United States, 2016, p. 97471O.
- [31] H.-J. Song, K. Ajito, Y. Muramoto, A. Wakatsuki, T. Nagatsuma, and N. Kukutsu, 'Uni-Travelling-Carrier Photodiode Module Generating 300 GHz Power Greater Than 1 mW', IEEE Microwave and Wireless Components Letters, vol. 22, no. 7, pp. 363–365, Jul. 2012.
- [32] Tsutomu Nagatsuka, Shigetaka Itakura, Kiyohide Sakai, and Yoshihito Hirano, 'High-power microwave photodiode array for radio over fiber applications', in OECC/ACOFT 2008 - Joint Conference of the Opto-Electronics and Communications Conference and the Australian Conference on Optical Fibre Technology, Sydney, Australia, 2008, pp. 1–2.
- [33] S. Itakura et al., 'High-Current Backside-Illuminated Photodiode Array Module for Optical Analog Links', Journal of Lightwave Technology, vol. 28, no. 6, pp. 965–971, Mar. 2010.
- [34] Y. Fu, H. Pan, and J. C. Campbell, 'Photodiodes With Monolithically Integrated Wilkinson Power Combiner', IEEE Journal of Quantum Electronics, vol. 46, no. 4, pp. 541–545, Apr. 2010.
- [35] Y. Fu, H. Pan, Z. Li, and J. Campbell, 'High linearity photodiode array with monolithically integrated Wilkinson power combiner', in 2010 IEEE International Topical Meeting on Microwave Photonics, Montreal, QC, Canada, 2010, pp. 111–113.

CHAPTER 4

RF AND OPTICAL DESIGN AND SIMULATIONS

General design topology of photonic integrated circuits for high power millimeter wave generation developed during this PhD thesis is presented in Fig. 4. 1. The RF and the optical design and simulations are obtained with Ansys HFSS [1], FIMMWAVE Photon Design [2], and RSoft Photonics BeamProp [3] software.

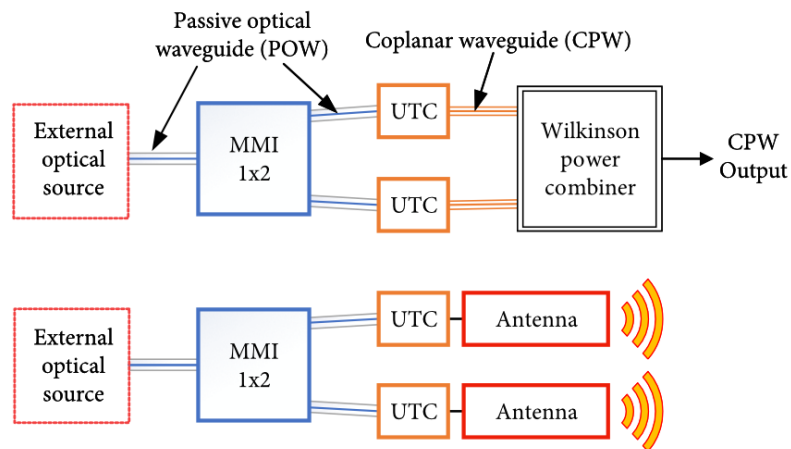


Fig. 4. 1 Schematic example of proposed PICs with 2-way Wilkinson power combiner (top) and 2x antenna-integrated photodiodes array (bottom).

Designed PICs consist of single-mode passive optical waveguides, MMI couplers, edge-coupled waveguide UTC photodiodes integrated with single antenna structures or with antenna arrays. Solutions with antenna-arrays target W-band frequency range with the possibility of application at higher frequencies. Single UTC PDs presented in Chapter 4.2 with different dimensions of width and length have been also designed, investigated and included in the final processing. PICs with the Wilkinson power combiner employing two and four UTC photodiodes are presented in Chapter 4.3. The Wilkinson power combiner is chosen among other power combiners as it can provide isolation between the input signals and it can be theoretically lossless. Solutions with integrated power combiners target E-band frequencies. For the circuits design with antenna-integrated structures, a folded-dipole and bow-tie antenna types are chosen in order to test more narrow-band (folded-dipole) and more wide-band (bow-tie) approach as well as to provide compact circuit architecture. Chapter 4.4 is dedicated to present the theory and the design of the antenna structures, as well as the simulation results. The optical waveguides, S-bends and MMI couplers employed in the PICs topology are described in Chapter 4.5. Fabrication process is presented in Chapter 5.

4.1 TRANSMISSION LINE AND WAVEGUIDES

In order to transmit an RF signal between a source (i.e. UTC photodiode) and the load (i.e. CPW output) a transmission line or a waveguide is required. The equivalent circuit of a transmission line can be represented by distributed elements of L (inductance), R (resistance), C (capacitance) and G (conductance) per unit length (Fig. 4. 2).

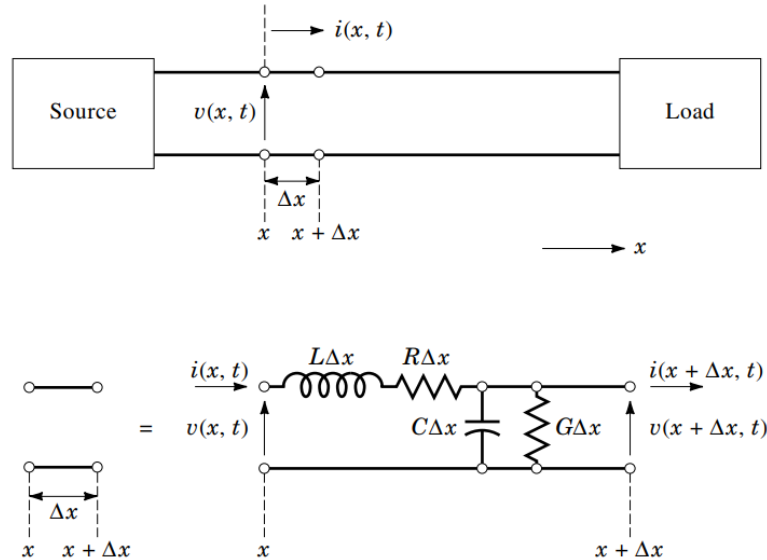


Fig. 4. 2 Transmission line equivalent circuit [5].

With the help of the Kirchoff's voltage and current law we can obtain [5]:

$$v(x, t) = \text{Re}[V(x)e^{i\omega t}] \quad (4.1)$$

$$i(x, t) = \text{Re}[I(x)e^{i\omega t}] \quad (4.2)$$

Final wave equation is given by:

$$\frac{d^2V(x)}{dx^2} - \gamma^2V(x) = 0, \quad (4.3)$$

where, γ is the wave propagation constant expressed as:

$$\gamma = [(R + i\omega L)(G + i\omega C)]^{\frac{1}{2}} = \alpha + i\beta \quad (4.4)$$

Where, α is attenuation constant in nepers per unit length and β is a phase constant in radians per unit length. General solution to Eq. (4.3) for voltage is expressed as a summation of forward and reflected wave propagating in the $+x$ and $-x$ directions, respectively:

$$V(x) = V_+e^{-\gamma x} + V_-e^{\gamma x} \quad (4.5)$$

The current in the frequency domain can be expressed by:

$$I(x) = \frac{\gamma}{R+i\omega L} (V_+ e^{-\gamma x} + V_- e^{\gamma x}) \quad (4.6)$$

Finally, the characteristic impedance is defined as:

$$Z_0 = \frac{R+i\omega L}{\gamma} = \sqrt{\frac{R+i\omega L}{G+i\omega C}} \quad (4.7)$$

For a lossless transmission line ($R = G = 0$; $\alpha = 0$; $\beta = \omega\sqrt{LC}$), characteristic impedance is equal to:

$$Z_0 = \sqrt{\frac{L}{C}}, \quad (4.8)$$

with corresponding guided wavelength, $\lambda_{guided} = \frac{2\pi}{\beta} = \frac{2\pi}{\omega\sqrt{LC}}$ and phase velocity, $v_{phase} = \frac{\omega}{\beta} = \frac{1}{\sqrt{LC}}$.

Reflection coefficient along the line can be defined as:

$$\Gamma(x) = \frac{\text{reflected } V(x)}{\text{incident } V(x)} = \frac{V_- e^{\gamma x}}{V_+ e^{-\gamma x}} = \frac{V_-}{V_+} e^{2\gamma x} \quad (4.9)$$

Reflection coefficient at load is given by:

$$\Gamma_L = \frac{V_-}{V_+} = \Gamma(0) \quad (4.10)$$

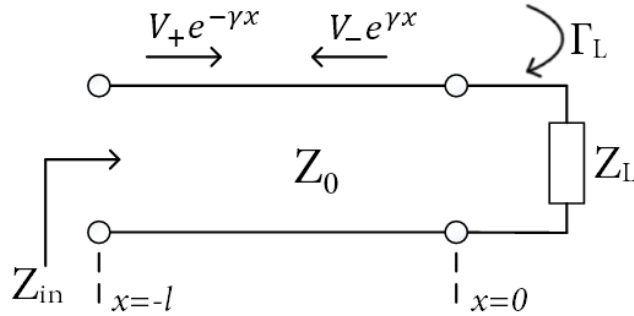


Fig. 4. 3 Terminated transmission line with characteristic impedance Z_0 connected to a load Z_L .

If transmission line is connected to a load Z_L and $Z_0 \neq Z_L$, then:

$$Z_L = Z_0 \frac{1+\Gamma_L}{1-\Gamma_L} \quad (4.11)$$

$$Z_{in} = Z_0 \frac{Z_L + Z_0 \tanh \gamma l}{Z_0 + Z_L \tanh \gamma l} \quad (4.12)$$

There are several types of possible transmission lines and waveguides configurations that can be applied in the microwave circuit design and described with respective formulas [4][5]. The most utilized in the microwave photonics circuit designs are microstrip lines and coplanar waveguides (Fig. 4. 4). The latter ones, firstly introduced by Cheng P. Wen [6], are

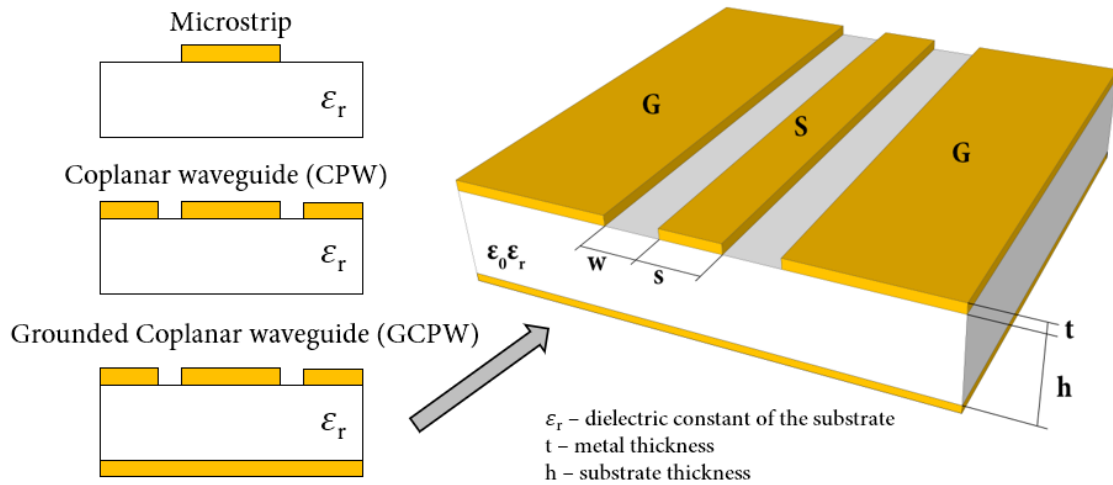


Fig. 4. 4 Cross-sections of microstrip, coplanar/grounded coplanar waveguide and schematic of GCPW with metal electrodes (GSG). The GCPW can be also referred as CBCPW (Conductor-Backed Coplanar Waveguide).

preferred due to larger range of possible characteristic impedances ($30 \Omega - 150 \Omega$), possibility of more compact and more broadband design [7]. Furthermore, coplanar waveguides simplify on-wafer measurements with CPW probes, and there is no need for vias as the ground planes are on the chip surface. Moreover, the back metallization has to be taken into account during the design process. If the chip is going to be mounted onto a metal carrier or a submount, the ground planes in GCPW behaves like parallel plate resonator capacitively coupled to CPW, which can result in unexpected patch antenna mode resonances [8]. Electric field distribution of quasi-TEM mode (coplanar mode/even mode) which is used in the circuit design is

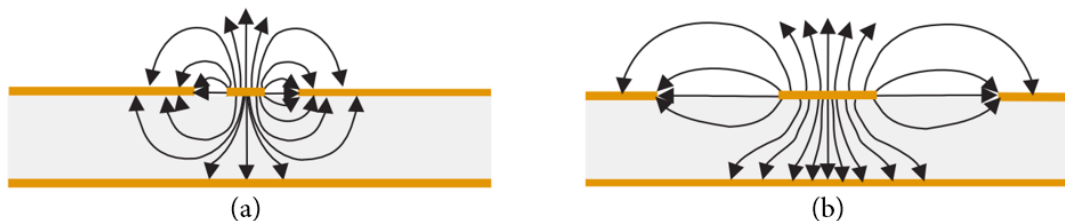


Fig. 4. 5 Electric field distribution of a GCPW with (a) dominant coplanar mode and (b) the microstrip mode.

presented in Fig. 4. 5. The odd mode (microstrip mode) is normally suppressed by air-bridge

connections and proper geometrical design [9]. Characteristic impedance of the GCPW from Fig. 4. 4 can be estimated by conformal mapping technique and experimental validation as [7][10]:

$$Z_0 = \frac{60 \pi}{\sqrt{\epsilon_{eff}}} \frac{1}{\frac{K(k')}{K(k)} + \frac{K(k_3)}{K(k'_3)}} \quad (4.13)$$

Where effective dielectric constant (ϵ_{eff}) is equal to:

$$\epsilon_{eff} = \frac{1 + \epsilon_r \frac{K(k') K(k_3)}{K(k) K(k'_3)}}{1 + \frac{K(k') K(k_3)}{K(k) K(k'_3)}} \quad (4.14)$$

Function $K(k)$ is the complete elliptic integral of the first kind,

$$k = \frac{s}{s+2w} \quad (4.15)$$

$$k' = \sqrt{1 - k^2} \quad (4.16)$$

$$k_3 = \frac{\tanh\left(\frac{\pi s}{4h}\right)}{\tanh\left(\frac{\pi(s+2w)}{4h}\right)} \quad (4.17)$$

$$k'_3 = \sqrt{1 - k_3^2} \quad (4.18)$$

4.1.1 S-parameters

Scattering parameters are widely used in order to model and characterize mm-wave frequency systems [1]. S-parameters are complex variables relating voltages of the reflected waves to the incident waves and can be measured with vector network analysers, as well as, calculated with dedicated simulation software (i.e. Ansys HFSS). These parameters can be related with ABCD, Z- and Y-parameters used for circuit analysis. Schematic example of a two-port network is presented in Fig. 4. 6, where the S-parameters are given by [5]:

$$b_1 = s_{11}a_1 + s_{12}a_2 \quad (4.19)$$

$$b_2 = s_{21}a_1 + s_{22}a_2 \quad (4.20)$$

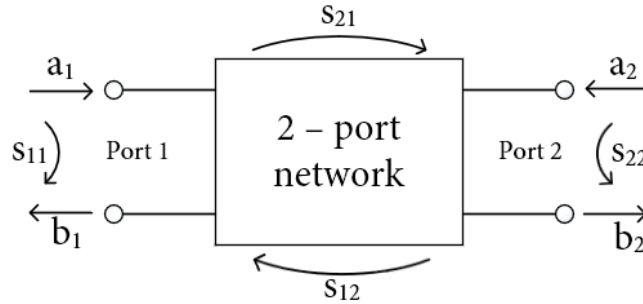


Fig. 4. 6 S-parameters of the two-port network.

The S-parameters can be defined as:

$$s_{11} = \frac{b_1}{a_1} \Big|_{a_2=0} = \Gamma_1 = \text{reflection coefficient at port 1 with } a_2 = 0$$

$$s_{21} = \frac{b_2}{a_1} \Big|_{a_2=0} = T_{21} = \text{transmission coefficient from port 1 to 2 with } a_2 = 0$$

$$s_{22} = \frac{b_2}{a_2} \Big|_{a_1=0} = \Gamma_2 = \text{reflection coefficient at port 2 with } a_1 = 0$$

$$s_{12} = \frac{b_1}{a_2} \Big|_{a_1=0} = T_{12} = \text{transmission coefficient from port 2 to 1 with } a_1 = 0$$

The return loss can be found by:

$$RL = 20 \log \left| \frac{a_1}{b_1} \right| = 20 \log \left| \frac{1}{s_{11}} \right| \text{ in dB} \quad (4.21)$$

The attenuation or insertion loss is given by:

$$IL = \alpha = 20 \log \left| \frac{a_1}{b_2} \right| = 20 \log \left| \frac{1}{s_{21}} \right| \text{ in dB} \quad (4.22)$$

The phase shift of the network is the phase of s_{21} .

4.1.2 Impedance matching

Impedance matching and tuning techniques are very often applied in the RF system design in order to transfer maximum power from the source to the load and to avoid unwanted reflections that may lead to standing waves (Fig. 4. 2)[11]. The maximum power is delivered (assuming the source is matched to the line) if the load is matched to the line and the power loss in the feed line is minimized [4]. There are several types of matching networks which can be distinguished in terms of complexity, bandwidth, implementation and adjustability. The most utilized are [4][9]:

- Lumped element matching networks (L-networks): uses two reactive elements to match Z_L to a transmission line. At higher frequencies, the R, L and C can be realized

with dedicated techniques for microwave integrated circuits due to undesirable effects of lumped elements.

- Stub-tuning: in this technique a single/double open-circuited or short-circuited length of transmission line is employed. Parallel or in series connection to the feed line are possible and lumped element can be avoided in the RF design. Practical example of stub-tuning is presented in Fig. 3. 17.
- Transformers (Fig. 4. 7): there are several types, but one of the simplest is a quarter-wave transformer ($\lambda_0/4$). It is used to match real load impedance to a transmission line. Application of several sections can broaden the bandwidth in this type of transformer. The characteristic impedance of the matching section is given as [4]:

$$Z_1 = \sqrt{Z_0 Z_L} \quad (4.21)$$

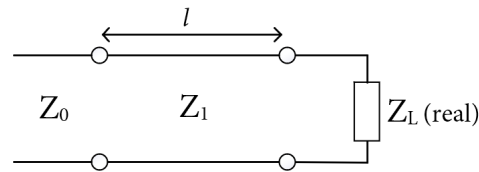


Fig. 4. 7 Single section quarter-wave transformer with $l = \frac{\lambda_0}{4}$ and electrical length $\frac{\pi}{2}$ at the design frequency f_0 .

- Tapered lines: these types of structures used in RF design can be considered as a continuously tapered transformer. Different types of tapers such as exponential, triangular or Klopfenstein are able to deliver different pass band characteristics [4].

Although conjugate matching condition results in maximum power transfer to the load for a fixed generator impedance, this does not guarantee a system with best efficiency [4]. Moreover, based on Bode-Fano criterion the bandwidth of the matching network is limited to the theoretical optimum and the ideal matching is only possible to a finite number of discrete frequencies [11].

4.2 UTC PDS WITH CPW OUTPUT - DESIGN

The objective of this chapter is to present the evanescently coupled UTC PDs structures that are included in the design and fabrication. This type of structure can be easily integrated with other photonic circuit elements as presented in Fig. 4. 1. Several dimensions of the PDs have been investigated and are presented in Fig. 4. 8. The overview of a photodiode structure with CPW output is presented in Fig. 4. 9.

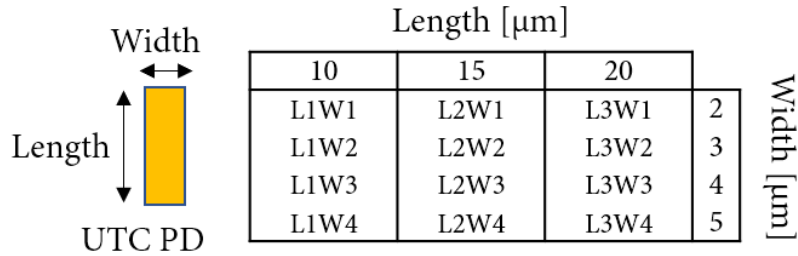


Fig. 4. 8 UTC PDs dimensions and abbreviations.

In order to simulate the S-parameters of the UTC PD with CPW output and calculate the reflections of the input (s_{11}), the output (s_{22}) and the transmission losses (s_{12} or s_{21}) in Ansys HFSS, all structures are placed inside the air box with ground plane. It serves as a ground for a coplanar waveguide. Specific dimensions for coplanar waveguide have been calculated with a dedicated calculator included in the Ansys software in order to meet required parameters such as low input and output reflections as well as low transmission losses. The GSG pads dimensions are presented in Fig. 4. 9. Structure is inside the air “box”, which size is adjusted to 60 GHz. In order to simulate the presence of the metal under the chip, a ground layer is added. The UTC PD structure employed in the simulation is defined as a lumped element, with defined values of resistance and capacitance. The value of inductance is not simulated. Moreover, lumped ports are utilized for the signal excitation in a driven modal solution type. Parameters used in the simulations are as follows:

- InP substrate thickness: 125 μm with dielectric constant of 12.5, tangent loss ca. 0.001.
- Excitation port type: Lumped port with 50 Ω impedance.
- UTC PD: lumped element with $R= 50 \Omega$ and C depending on the UTC dimensions,

Based on the theoretical calculations (for the UTC collector layer thickness of 300 nm), the UTC PDs capacitance varies from 7.4 fF (UTC L1W1) to 37 fF (L3W4). These values are presented in Fig. 4. 10 and used in HFSS simulations. Values of series resistance have been investigated and reported in [12][13] where III-V Lab UTC photodiodes have been studied. Based on reported results, series resistance should not exceed 50 Ω and this value is used in the HFSS simulations. Moreover, the close up view of the modelled and simulated UTC PD structure with GCPW and lumped port used for excitation is presented in Fig. 4. 11. Simulation results for various UTC PD with CPW output are presented in subchapter 4.2.1.

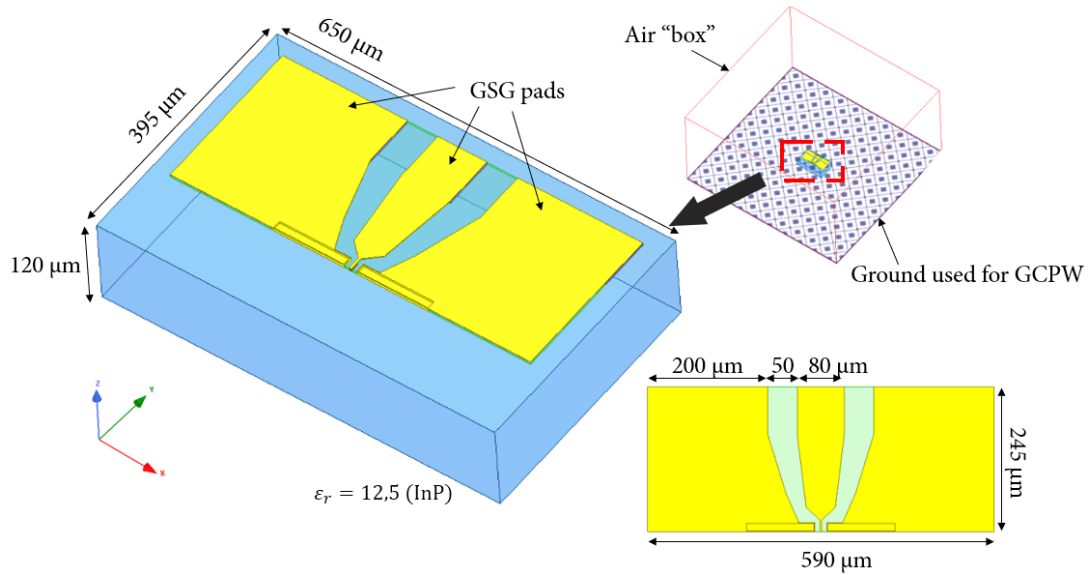


Fig. 4. 9 UTC PD structure with CPW output dimensions optimized during simulations to obtain low loss properties.

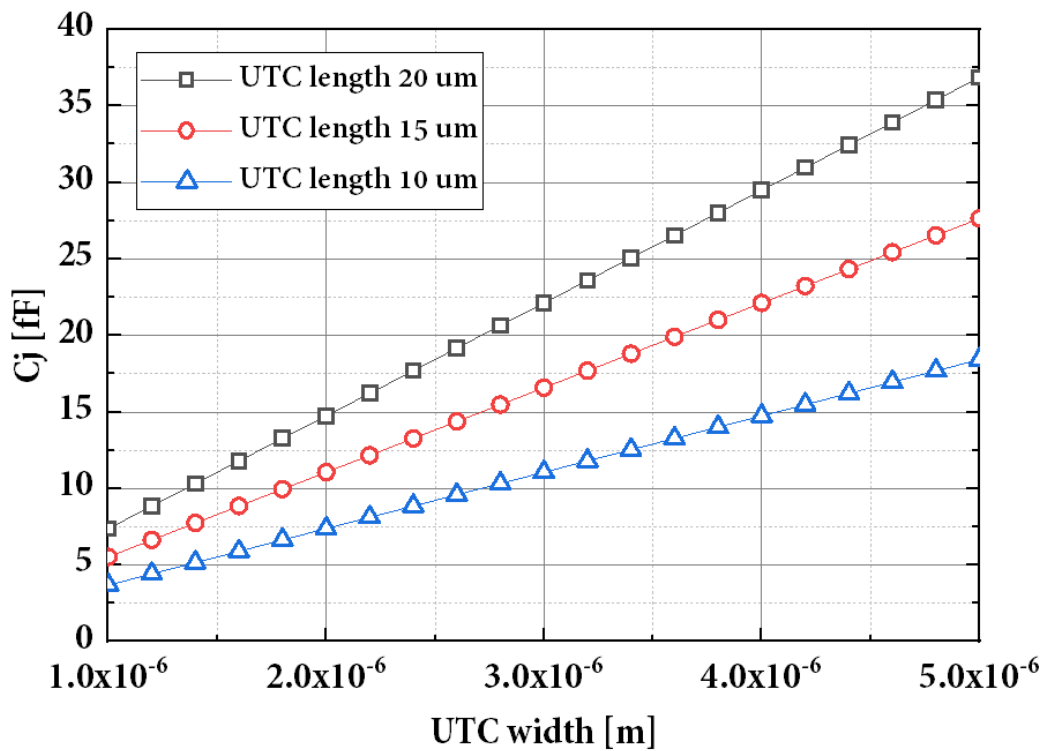


Fig. 4. 10 Theoretical UTC PD capacitance vs. UTC PD dimension.

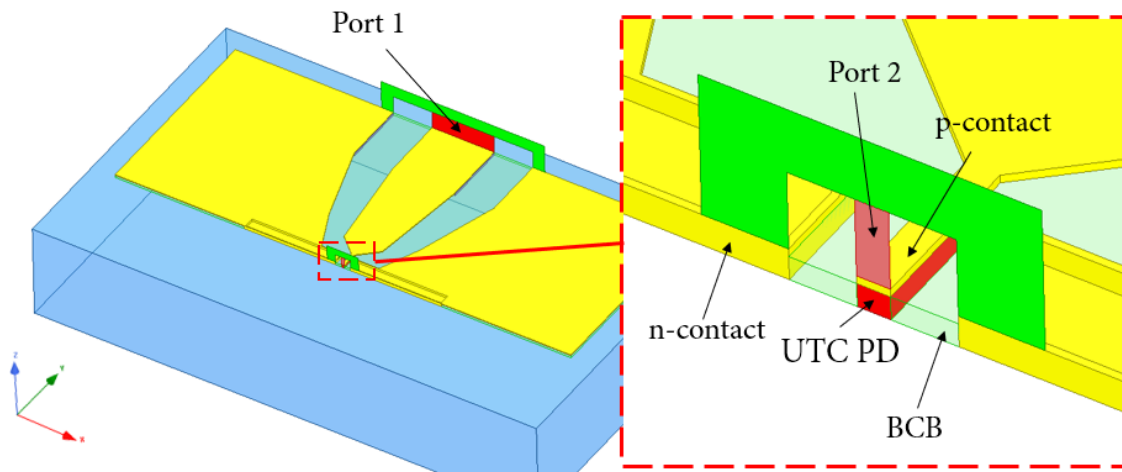


Fig. 4. 11 Close up view of a UTC PD structure simulated as a Lump element with adapted values of R and C.

Additional structure has been designed within the cooperation with Fiwin5G project partners from UC3M in Spain. UTC PD with GCPW with adapted CPW output dimensions design to be matched with the circuit from UC3M is presented in Fig. 4. 12. The dimensions of UTC PD are the same as for L2W3.

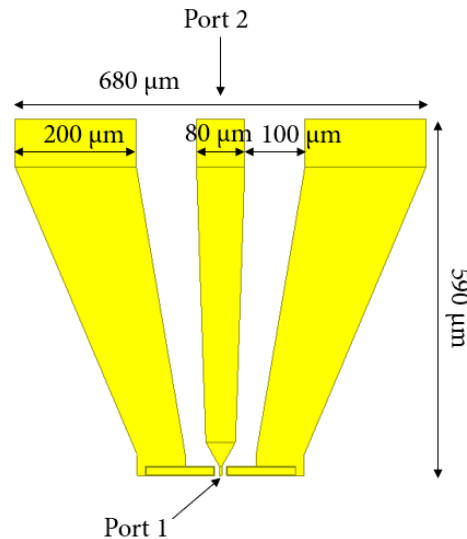


Fig. 4. 12 UTC PD (L2W3) with adapted CPW output dimensions.

4.2.1 UTC PD with CPW – simulation results and summary

The S-parameters of the designed UTC PDs with GCPW, are simulated with frequency sweep from 1 GHz to 110 GHz. Simulations include some of the material parameters such as dielectric loss tangent (InP: 0.001 [14]), but they do not include i.e. doping levels. Presented s-parameters, as mentioned in sub-chapter 4.1.1, are used for the circuit characterization in terms of input (s_{11}), output (s_{22}) and transmission (s_{12} or s_{21}) losses. It is in correspondence to port assignment from Fig. 4. 11. Simulation results for the designed structures with the same width are presented from Fig. 4. 13 to Fig. 4. 16. Based on the results, values of transmission loss differ slightly from 0.08 dB to 0.13 dB (at 60 GHz) over the entire frequency range, up to 110 GHz. Moreover, S_{22} and S_{11} values are under -20 dB over the entire frequency range, which also prove that GCPW dimensions chosen for the designs are in good match condition with 50 Ω CPW output. As can be noticed, the s_{11} and s_{22} change most dynamically for the structures with the width of 3 μm (Fig. 4. 14) in comparison with other investigated architectures. The least influenced structures over the length range are structures with 4 μm of UTC PD width. The UTC PD L2W3 dimensions are chosen for the design of PICs with Wilkinson power combiners and antenna-integrated devices. These dimensions are considered to be optimal from the simulated group (see Fig. 4. 8). It is also reported in [12] that UTC PDs of 4 μm width and 15 μm of length are in good agreement between the simulations and the measurements results. The comparison for all simulated dimensions is presented in Fig. 4. 17.

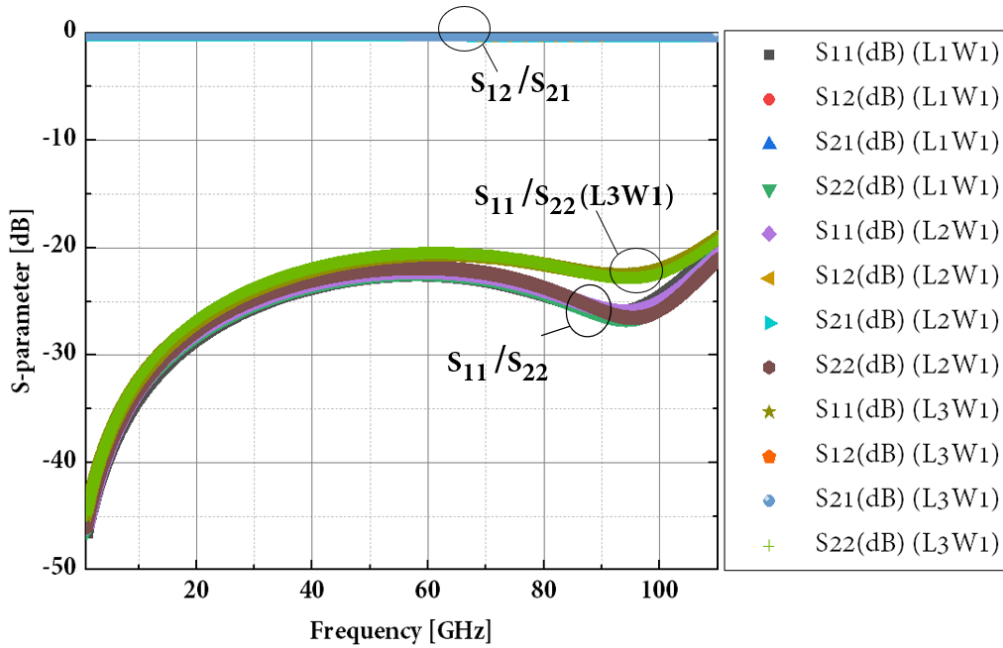


Fig. 4. 13 S-parameters for L1W1, L2W1 and L3W1 at frequency sweep from 1 GHz up to 110 GHz. Source (port) impedance: 50 Ω .

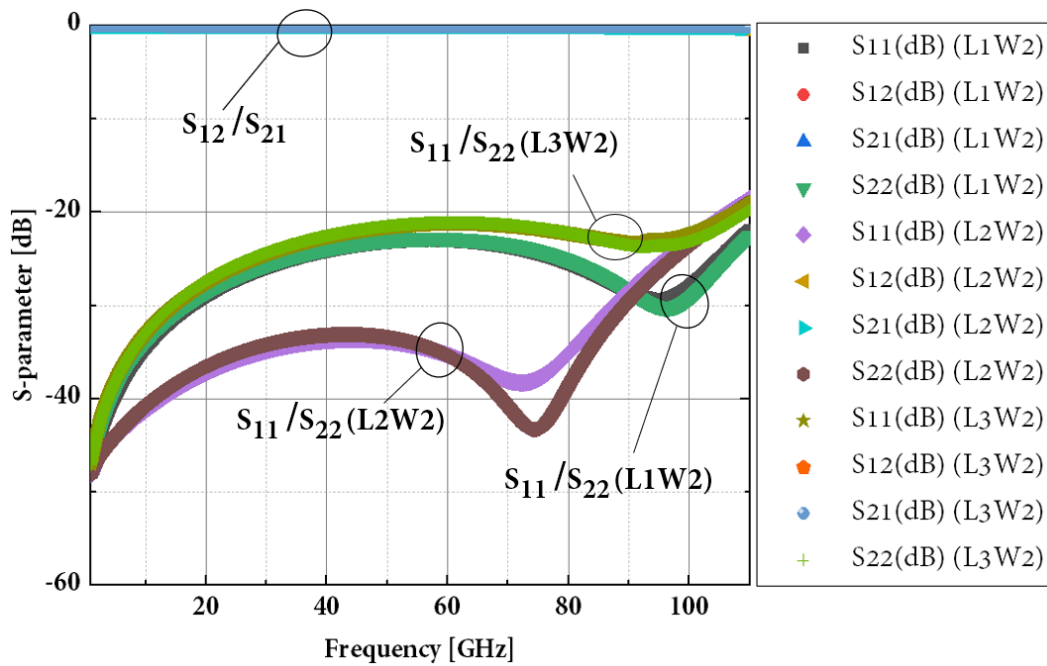


Fig. 4. 14 S-parameters for L1W2, L2W2 and L3W2 at frequency sweep from 1 GHz up to 110 GHz. Source (port) impedance: 50 Ω .

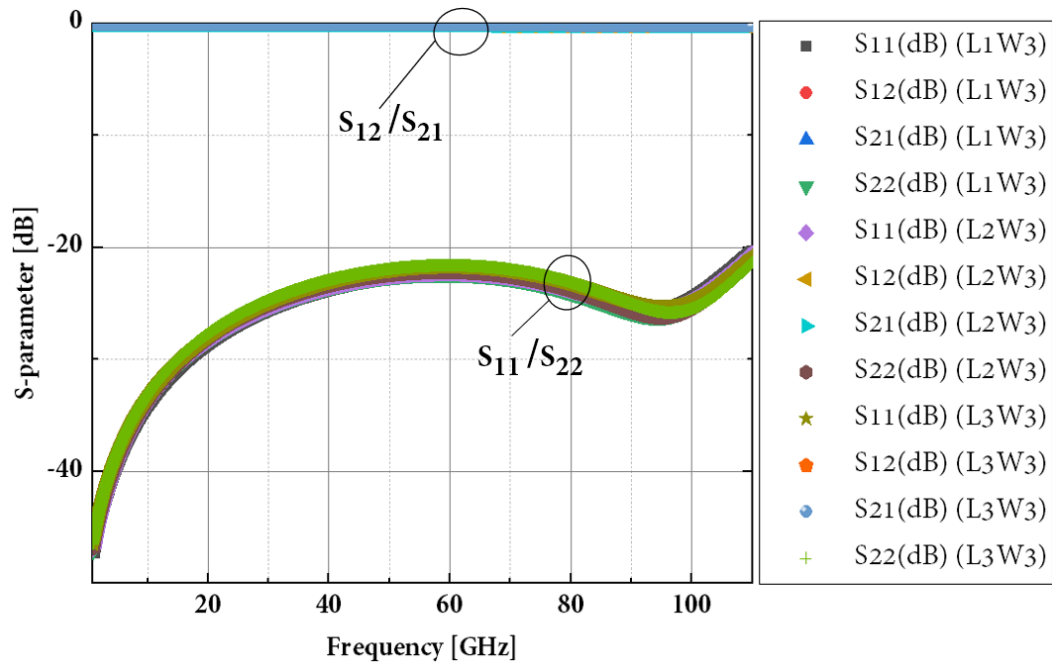


Fig. 4. 15 S-parameters for L1W3, L2W3 and L3W3 at frequency sweep from 1 GHz up to 110 GHz. Source (port) impedance: 50 Ω .

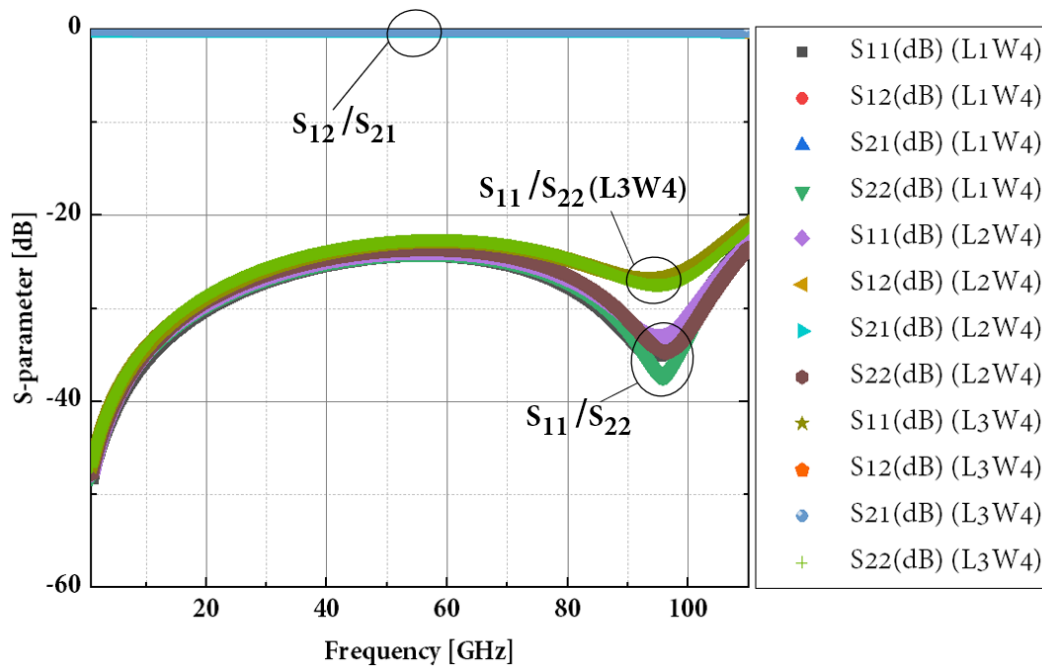


Fig. 4. 16 S-parameters for L1W4, L2W4 and L3W4 at frequency sweep from 1 GHz up to 110 GHz. Source (port) impedance: 50 Ω .

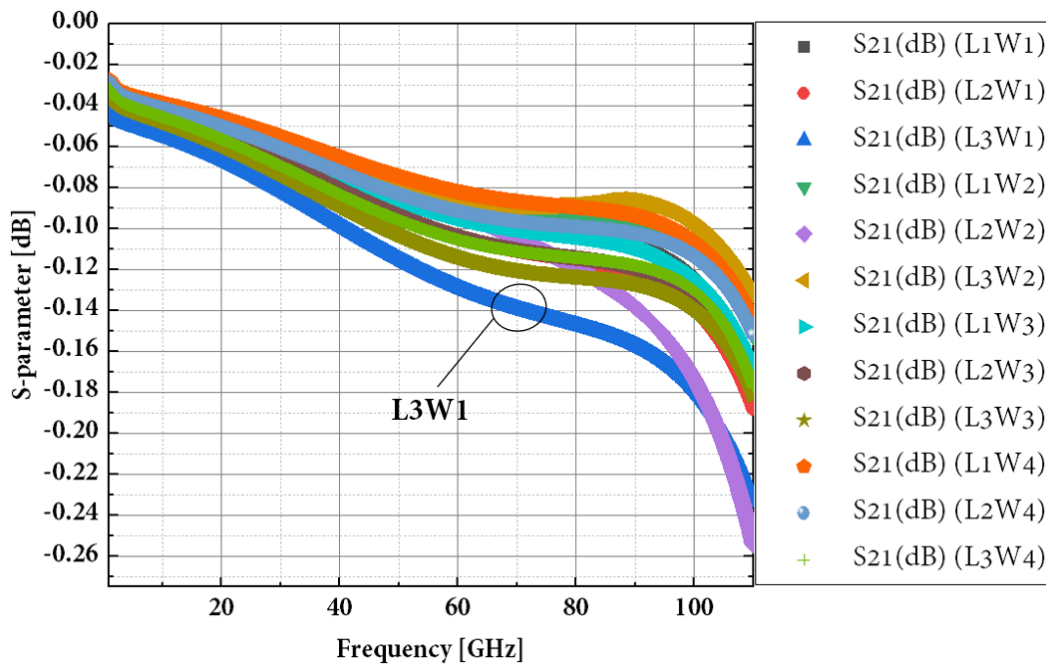


Fig. 4. 17 Family of S_{21} characteristics for all UTC PD dimensions from 1 GHz to 110GHz.

Furthermore, the investigation of the UTC with CPW output up to 300 GHz has been performed. Obtained simulation results shows the frequency range after which the CPW

structure loses its properties as a transmission line. The frequency bandwidth presented in Fig. 4. 18 is about 110 GHz, from 1 GHz to 110 GHz, with additional 10 GHz between 190 GHz - 200 GHz, with well-matched input (s_{11}) and output (s_{22}) ports. The bandwidth between 230 GHz - 280 GHz, although it can be potentially used does not provide very well-matched s_{11} . An example of the E-field distribution of L2W3 UTC PD structure is presented in Fig. 4. 19. It can be observed that the E-field is confined within the CPW dimensions, partially inside the structure as well as above the top metallization layer.

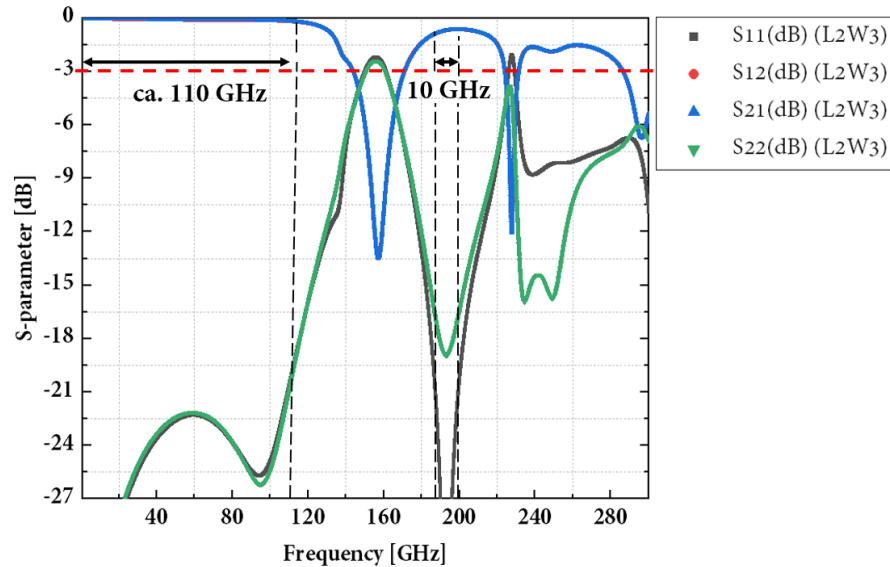


Fig. 4. 18 Bandwidth of the UTC PD L2W3 from 1 GHz to 300 GHz.

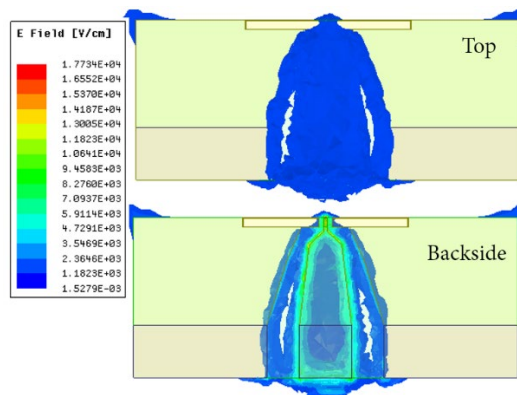


Fig. 4. 19 E-field distribution in UTC PD L2W3 at 60 GHz.

Simulation results for the structure specially designed for the cooperation between III-V Lab and UC3M (Fig. 4. 12) are presented in Fig. 4. 20. The output dimensions have an impact on the transmission parameters. The s_{11} and s_{22} are below -10 dB for almost entire frequency range. Transmission s_{21} varies from -0.3 dB up to -0.7 dB. A resonant behaviour can be also

observed at 70 GHz, where the input s_{11} is perfectly match, but other parameters slightly deteriorates.

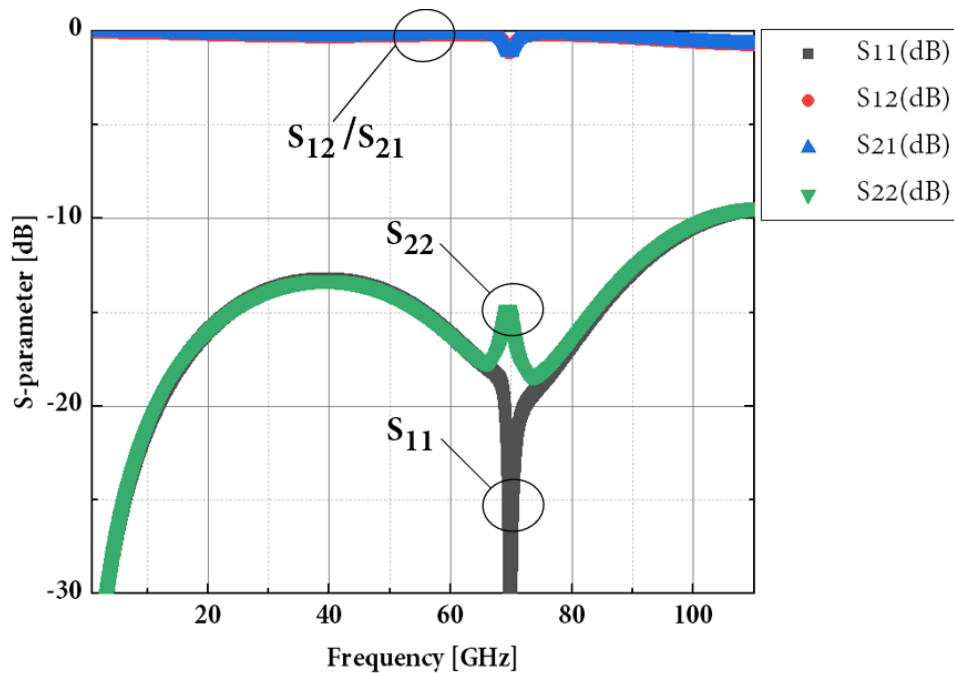


Fig. 4. 20 S-parameters for UTC PD with adapted CPW output dimensions from Fig. 4. 12 at frequency sweep from 1 GHz up to 110 GHz. Source (port) impedance: 50 Ω .

To conclude:

- Designed UTC PDs with CPW outputs are in good match to 50 Ω .
- Transmission losses are low, up to 0.13 dB (but some of the InP material losses might be higher in real-life structures).
- Input and output reflection losses are low and below -20 dB.
- Design with adapted CPW output dimensions is more lossy in terms of input reflections, but below -10 dB.
- Based on the simulated results for UTC PD L2W3 (4 μm x 15 μm) - these dimensions are chosen for the design with Wilkinson power combiners and antenna-integrated structures.

4.3 WILKINSON POWER COMBINER

The objective of this chapter is to present the Wilkinson power combiner employed in the novel PIC design investigated in this PhD thesis. As presented in Chapter 3.3, power combining techniques has found several applications in high frequency circuits in order to increase the output power. Among different power combiner designs, Wilkinson power combiner (also works as a divider), invented by E. J. Wilkinson in 1960 [15], can combine signals from the input ports and provide isolation between them. In the simplest form, it consists of quarter-wave transformers, transmission lines and an isolation resistor. The two-way Wilkinson power combiner is presented in Fig. 4. 21 with a symmetry plane in the midplane. The isolation resistor between the two input ports is used to uncouple the lines in such a manner that a signal possibly reflected from an unmatched load at one of the ports will not affect the other [16]. Moreover, if the output ports are matched, the Wilkinson power combiner is theoretically a lossless network. In order to compute a scattering matrix of the combiner, an even-odd mode analysis is required [1][10][16]. Based on this analysis, the inspected circuit can be simplified into a two-port network for a symmetric (even) and non-symmetric (odd) port excitation.

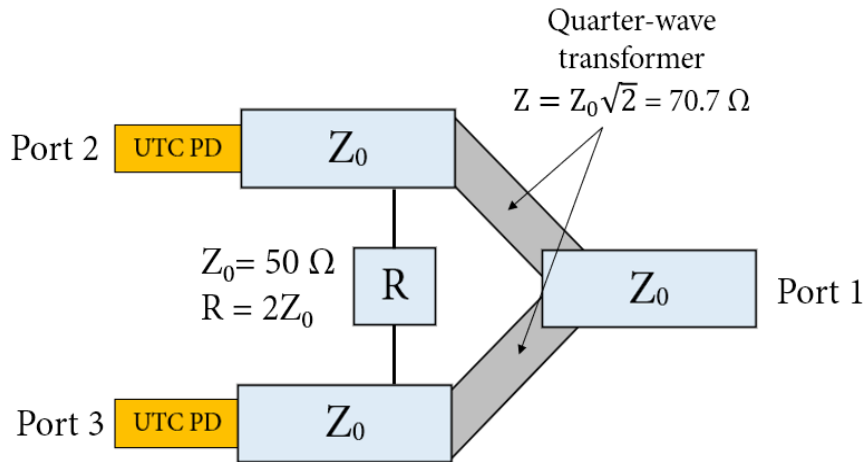


Fig. 4. 21 Schematic of Wilkinson power combiner.

The following scattering matrix at the matching condition at the center frequency (due quarter-wave transformer) can be established for the Wilkinson combiner [16]:

$$[S] = \frac{-i}{\sqrt{2}} \begin{bmatrix} 0 & 1 & 1 \\ 1 & 0 & 0 \\ 1 & 0 & 0 \end{bmatrix} \quad (4.22)$$

Device is matched at all ports ($s_{11} = s_{22} = s_{33}$), and ports 2 and 3 are uncoupled ($s_{23} = 0$). Moreover, an N-way Wilkinson power combiner can be constructed by a cascaded design of the 2-way combiners.

4.3.1 2-way Wilkinson power combiner - design

The overview of the designed 2-way Wilkinson power combiner is presented in the Fig. 4. 22. As already mentioned in chapter 4.2, the UTC PD L2W3 ($15 \mu\text{m} \times 4 \mu\text{m}$) is chosen to be implemented in the final design. In Fig. 4. 23 the principle design dimensions of the GCPW are given. The length of the quarter-wave transformer at 60 GHz, based on the calculation, is around $480 \mu\text{m}$ with $15 \mu\text{m}$ width for a $125 \mu\text{m}$ of InP thickness and $1 \mu\text{m}$ of metallisation thickness. Material properties included in the simulation are the same as mentioned in sub-chapter 4.2.1. The position and width of the under-bridge connections that are necessary to connect the inner and the outer ground planes (see Fig. 4. 24) is established via HFSS simulations and it has a strong impact on the device behaviour. Moreover, the isolation resistor, as it is necessary to be placed before quarter-wave transformer, requires electrical connection to the signal path. This connection introduces high losses and as well it has been optimized during the HFSS simulations. In order to reduce the impact, the isolation resistor is placed under the signal path and it is split into two smaller resistors with 50Ω resistance (100Ω is required in total resistance) as presented Fig. 4. 24. The output contact pads are placed on InP substrate, and not directly on the BCB. It is done to increase the robustness of the contact pads used for the CPW probe measurements. Furthermore, the 2-way Wilkinson power combiner without isolation resistor has been designed and investigated as well. The overview of the structure is presented in Fig. 4. 25. All the dimensions are the same as for structure with the isolation resistors.

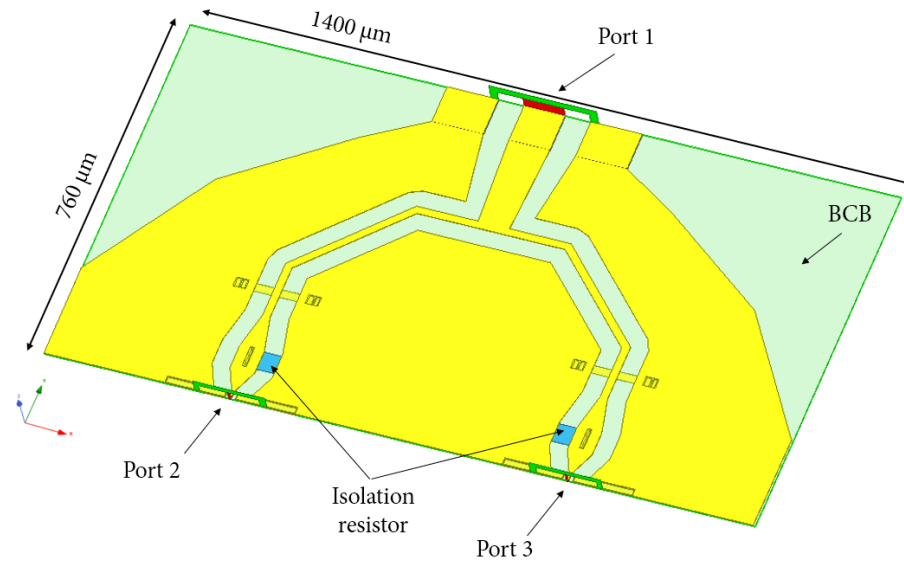


Fig. 4. 22 The overview of the 2-way Wilkinson power combiner with isolation resistors.

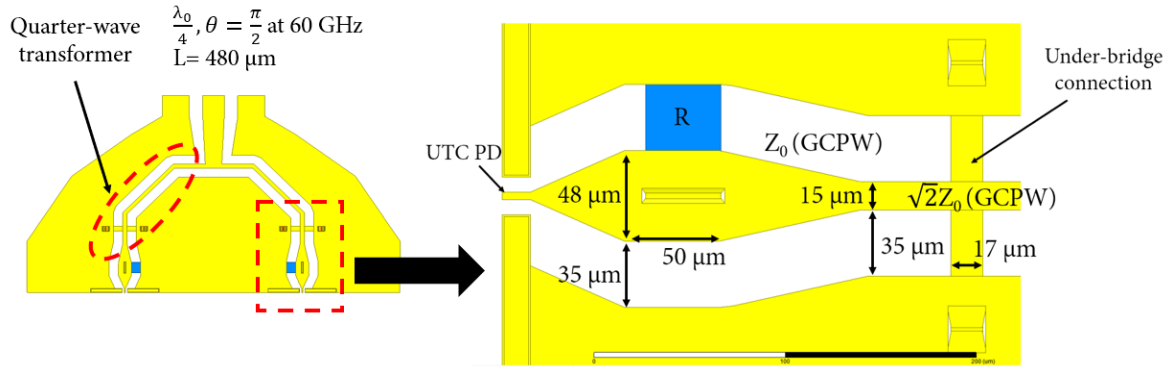


Fig. 4. 23 Design details of input Z_0 CPW (top view).

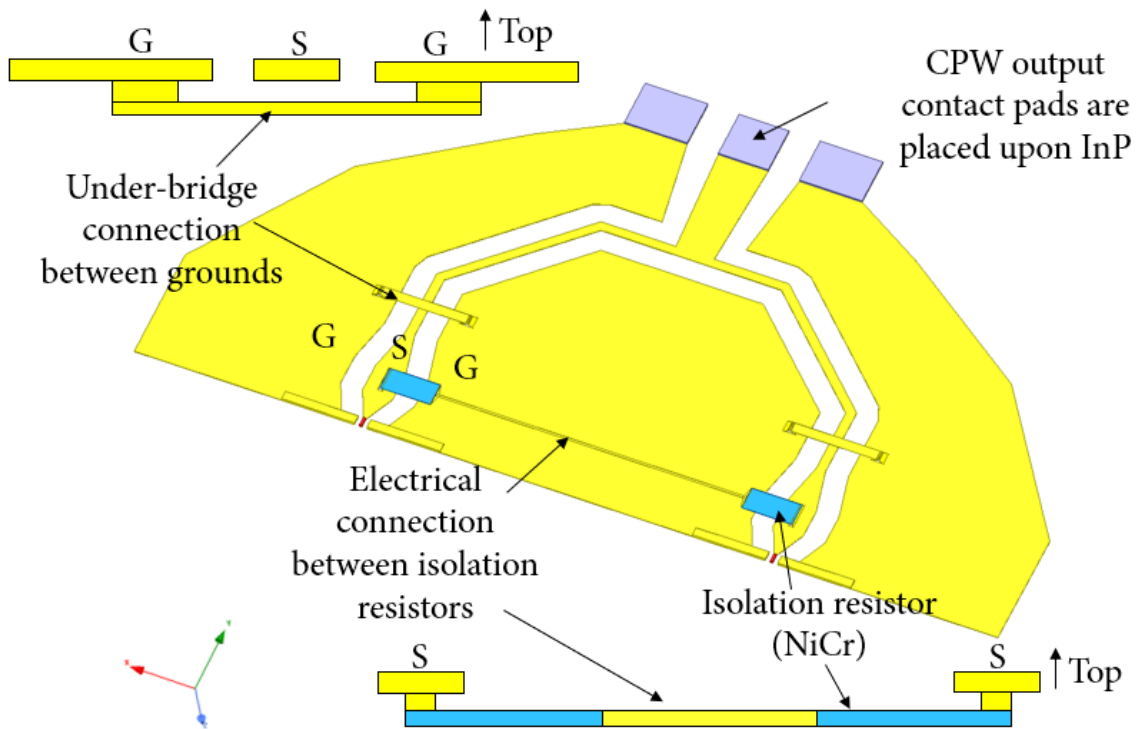


Fig. 4. 24 The backside overview of the 2-way Wilkinson with isolation resistors with simplified cross-sections of under-bridge connections and connections to the resistors.

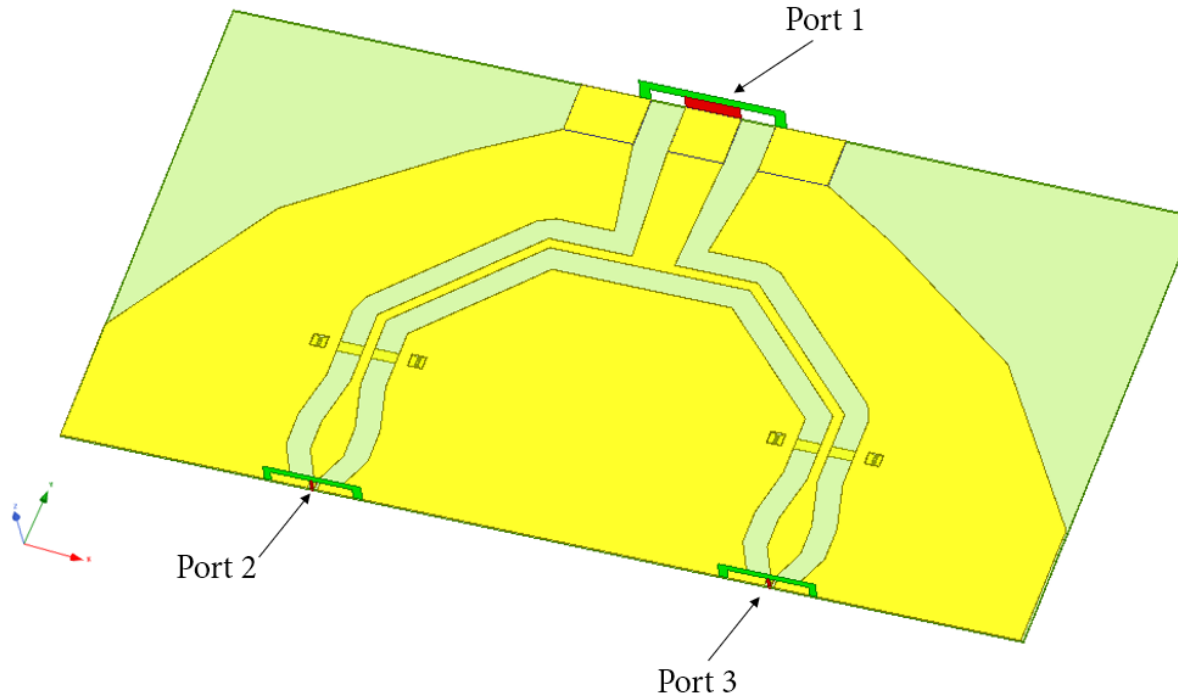


Fig. 4. 25 The overview of the 2-way Wilkinson power combiner without isolation resistors.

4.3.2 2-way Wilkinson power combiner - simulation results

The S-parameters of the 2-way Wilkinson device are simulated with the frequency sweep from 1 GHz to 110 GHz, although the structure is optimized for E-band and W-band (60 – 110 GHz). Similar to the UTC PD simulations, the s-parameters are used to characterize designed circuit in terms of inputs (s_{22} ; s_{33}), output (s_{11}), transmission (s_{31} or s_{21}) losses and isolation (s_{23} and s_{32}) between port 2 and port 3 as presented in Fig. 4. 25. Based on the theory presented in sub-chapter 4.3, the ideal 2-way Wilkinson power combiner transmission loss is equal to -3 dB. It corresponds to perfect combined (or split) signals from port 2 and port 3 towards port 1. Simulated s-parameters for the 2-way Wilkinson power combiner with isolation resistor are presented in Fig. 4. 26 and Fig. 4. 27. It can be observed, that device has a flat, low-loss response of the transmitted signals (s_{31}/s_{21}) over a wide frequency range. Unfortunately, due to resonant circuit behaviour, the optimal frequency bands (marked in a light blue colour) are reduced. Moreover, it can be noticed that at 34 GHz combiner achieved acceptable level of isolation between the input signals (s_{32}/s_{23}) and transmission loss of -2.1 dB but the s_{11} parameter is of high value at that frequency. For the frequencies above 60 GHz the s_{11} matching is better, and values are below -19 dB. The transmission loss is of -1.5 dB. The input signals isolation at its peak value is of -13 dB.

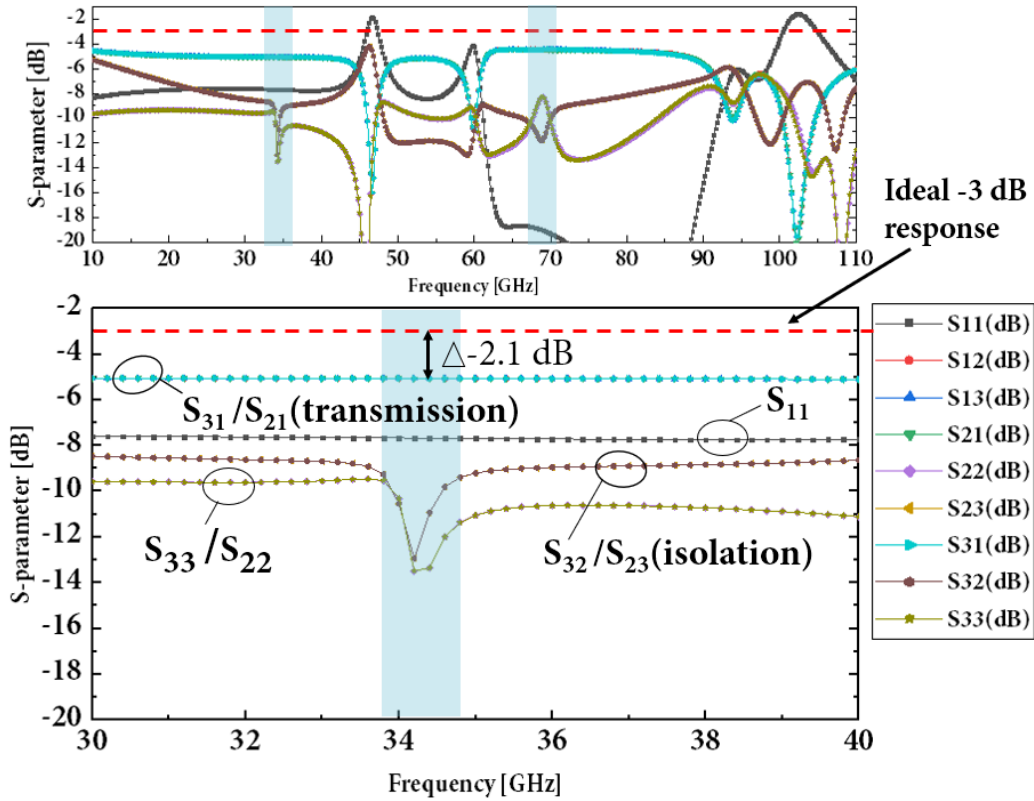


Fig. 4. 26 S-parameters of the 2-way Wilkinson power combiner from 1 GHz to 110 GHz (top) and from 30 GHz to 40 GHz (bottom). Port impedance: 50 Ω .

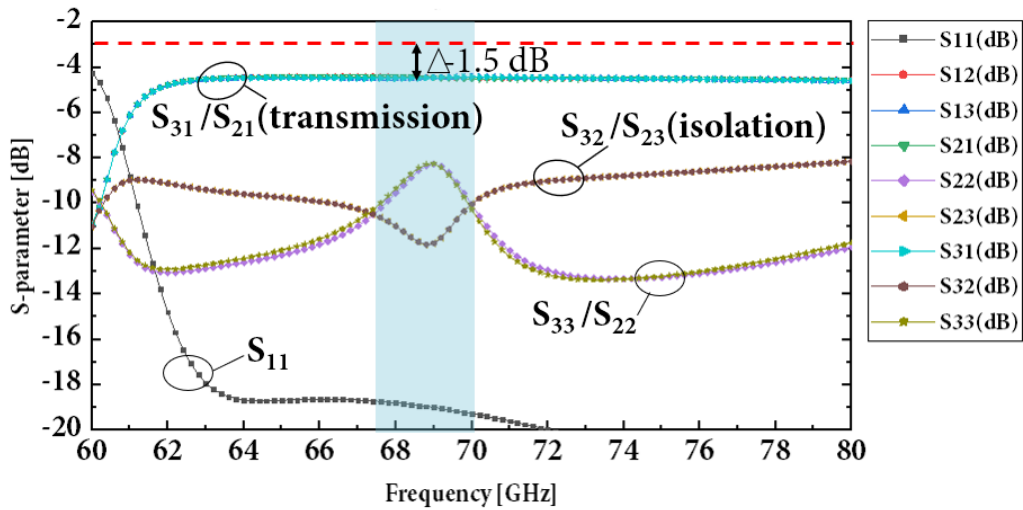


Fig. 4. 27 S-parameters for 2-way Wilkinson power combiner with isolation resistors from 60 GHz to 80 GHz. Source (port) impedance: 50 Ω .

In order to compare the loss caused by the isolation resistors present in the circuit design structure without these resistors is investigated. In Fig. 4. 28 and Fig. 4. 29 the s-

parameters of the 2-way Wilkinson power combiner without isolation resistors are presented. As can be observed, circuit achieves better matching condition in all frequency ranges in comparison to the design with isolation resistors. Moreover, at 34 GHz the s_{11} achieves comparable values of ca. -9 dB, but the loss of the transmitted signal is much lower, and is equal to ca. -0.7 dB. Furthermore, from 60 GHz to 80 GHz, the influence of the isolation resistor is observed in the s_{22} and s_{33} values. In addition, in this frequency range the transmission loss of the transmitted signal is improved and is of -0.3 dB.

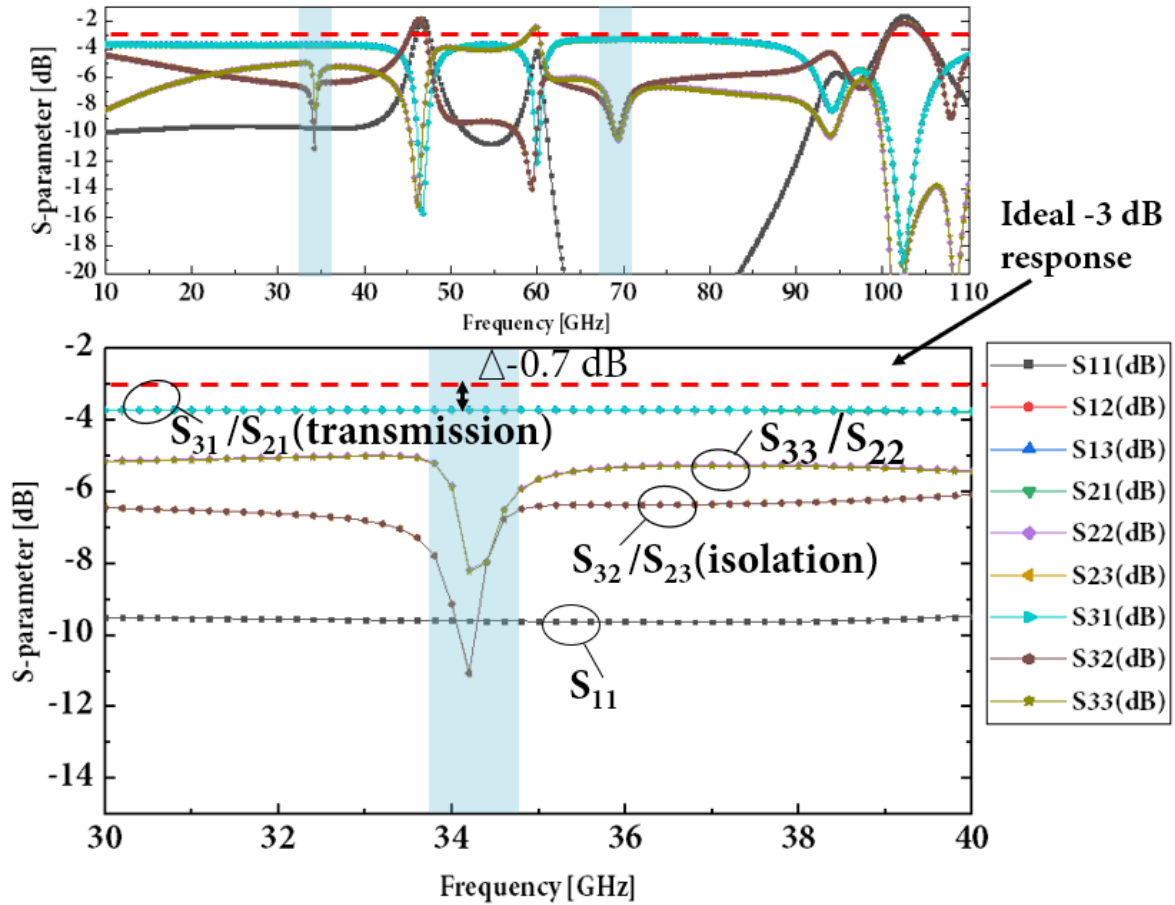


Fig. 4. 28 S-parameters of the 2-way Wilkinson power combiner without isolation resistors from 1 GHz to 110 GHz (top) and from 30 GHz to 40 GHz (bottom). Source (port) impedance: 50 Ω .

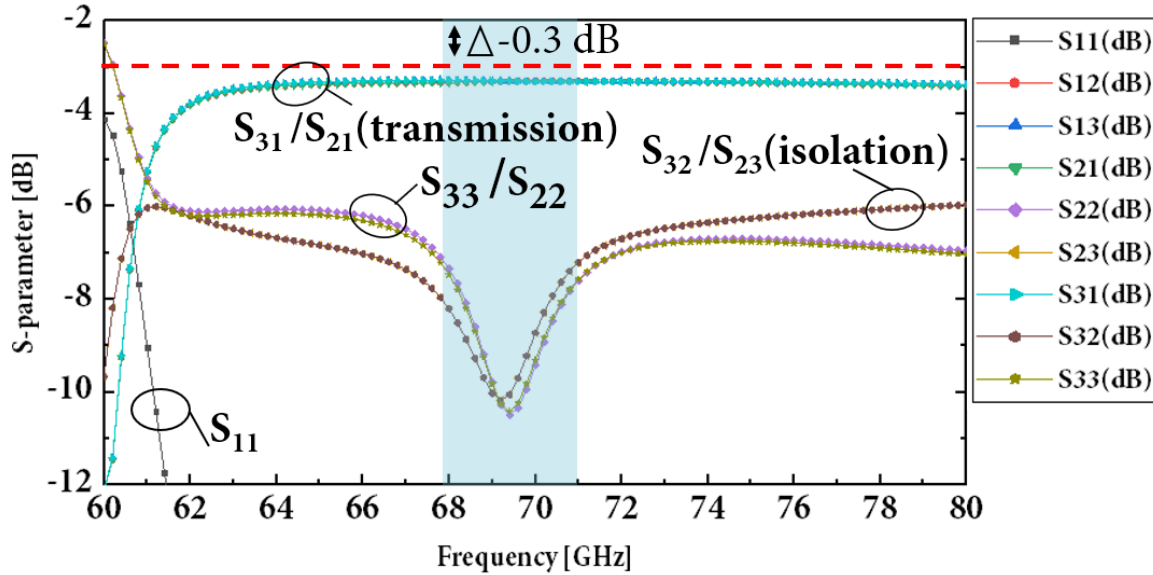


Fig. 4. 29 S-parameters for 2-way Wilkinson power combiner without isolation resistors from 60 GHz to 80 GHz. Source (port) impedance: 50 Ω .

Another important aspect of the power combiner design is the phase difference between the combined signals. Symmetry of the structure plays very important role and as mentioned in the introduction, it is also required in the Wilkinson power combiner design. Based on the simulation data for the design with and without isolation resistors, results are very comparable and phases of s_{21} and s_{31} are almost perfectly similar. The difference is below 1 degree in the frequency ranges of interest as presented in Fig. 4. 30 and Fig. 4. 31. An example of the E-field distribution for the 2-way Wilkinson power combiner with isolation resistor at 68 GHz is presented in Fig. 4. 32. Short summary of the 2-way Wilkinson power combiners parameters are presented in sub-chapter 4.3.5.

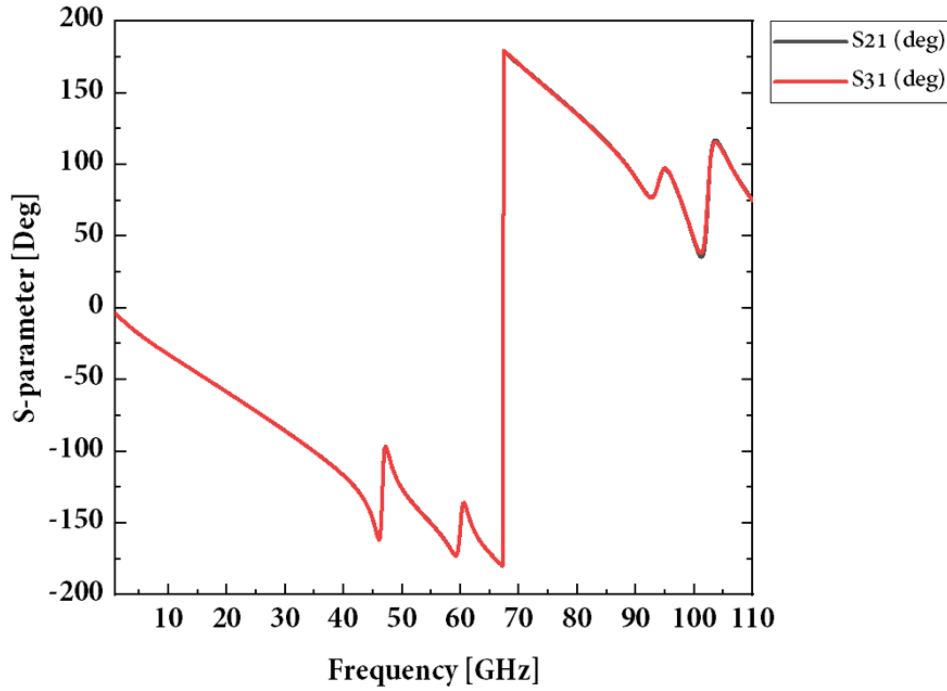


Fig. 4. 30 The phase of the combined signals s_{21} and s_{31} for the 2-way Wilkinson power combiner with isolation resistors.

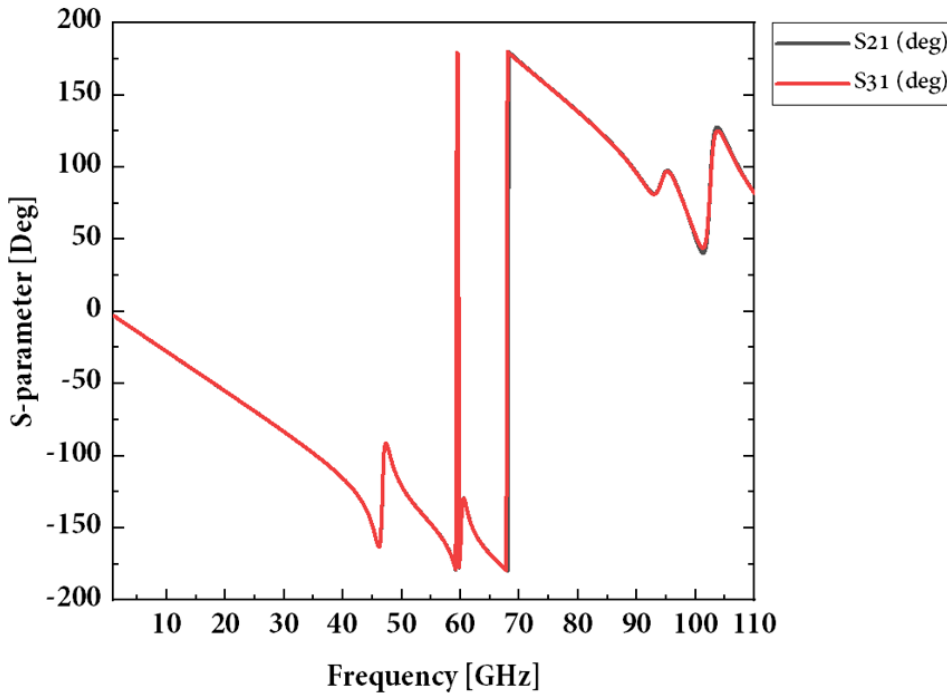


Fig. 4. 31 The phase of the combined signals s_{21} and s_{31} for the 2-way Wilkinson power combiner without isolation resistors.

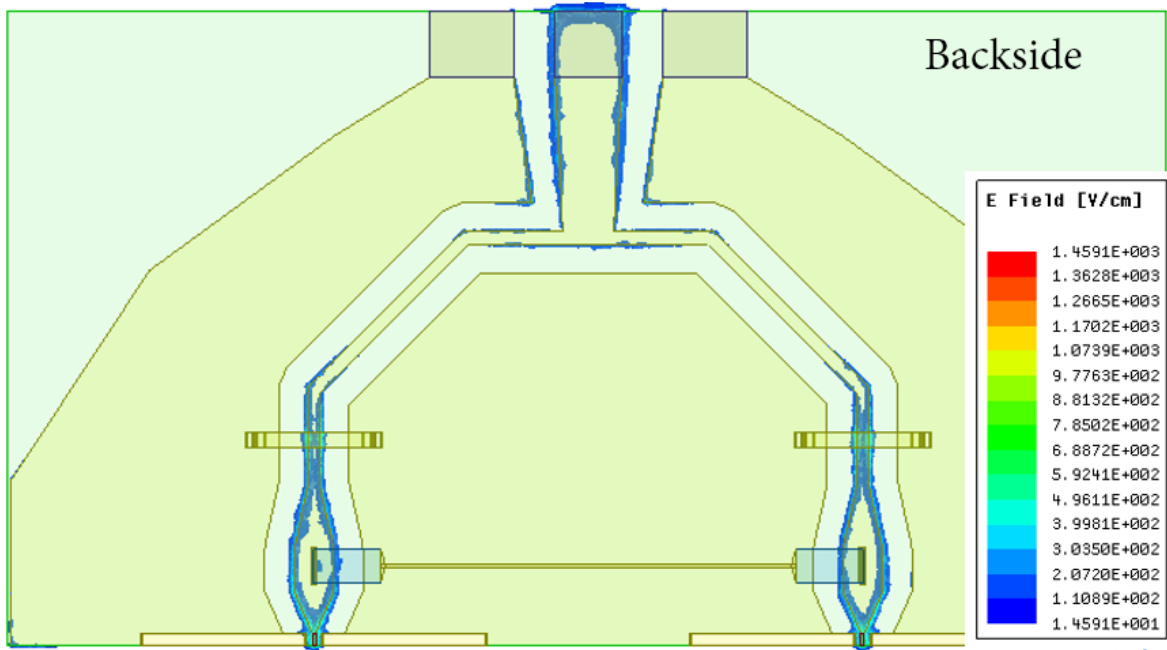


Fig. 4. 32 Example of the E-field distribution for the 2-way Wilkinson power combiner with isolation resistor at 68 GHz.

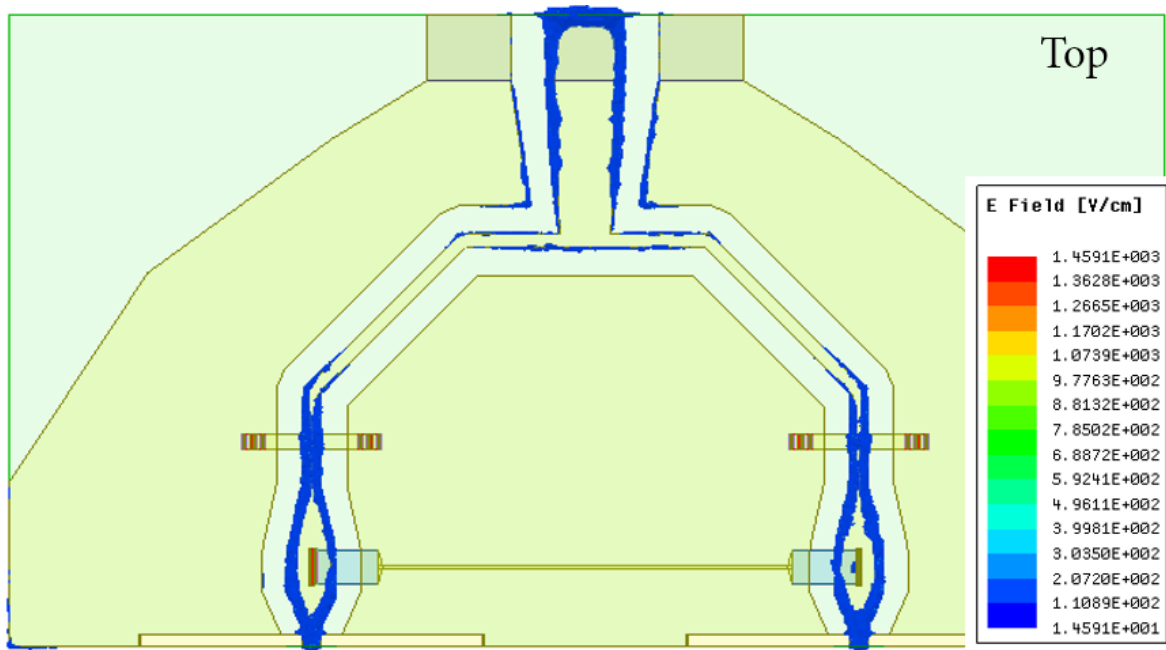


Fig. 4. 33 Example of the E-field distribution for the 2-way Wilkinson power combiner with isolation resistor at 68 GHz.

4.3.3 4-way Wilkinson power combiner - design

The overview and ports assignment used in the simulation are presented in Fig. 4. 34. Construction of the 4-way power combiner is based on the cascade of the 2-way combiners. The UTC dimensions are the same as for the UTC PD L2W3 ($15 \mu\text{m} \times 4 \mu\text{m}$). Majority of the element's dimensions such as the quarter-wave transformer, CPWs or isolation resistors are the same. Nevertheless, some elements of the design have to be adapted due to bigger area of the device. Furthermore, position and width of the under-bridge connections are modified and have been optimized via HFSS simulations after test of different designs in an iterative way. As expected, they have strong impact on the device behaviour. Moreover, in order to compare the influence of the isolation resistors in the signal losses, the 4-way Wilkinson power combiner without isolation resistors is also investigated. All the dimensions are the same as for structure with the isolation resistors.

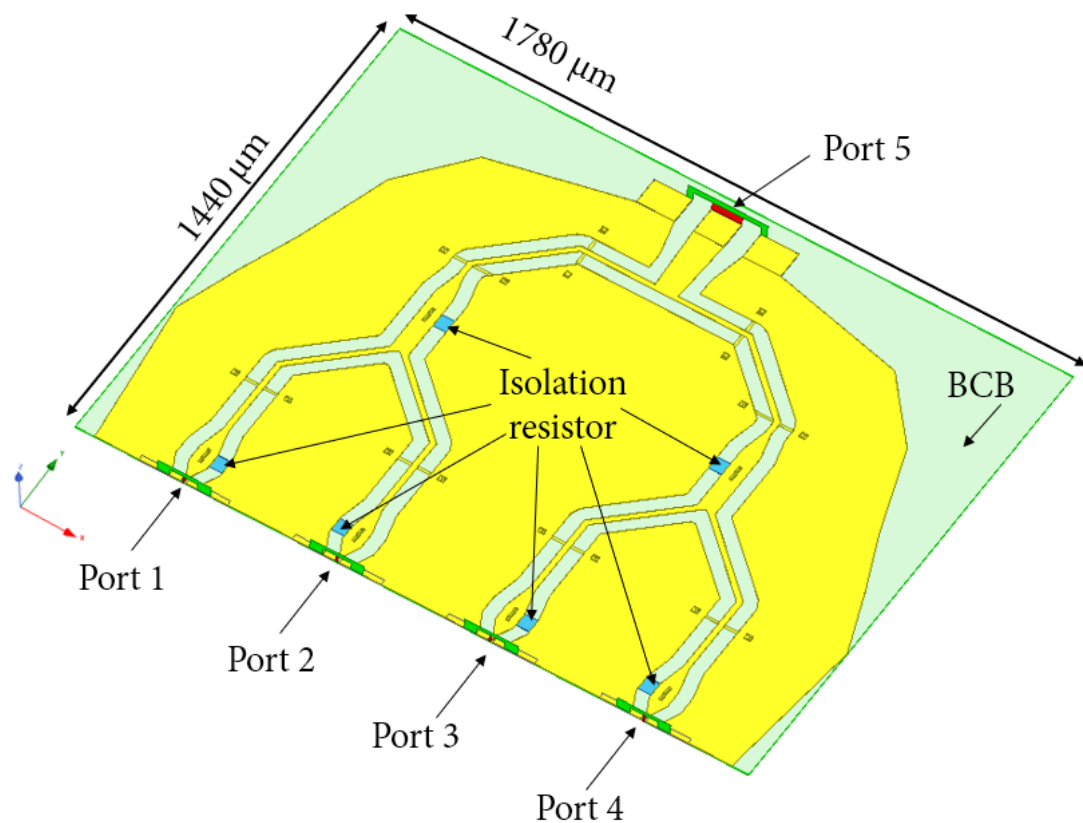


Fig. 4. 34 The overview of the 4-way Wilkinson power combiner with isolation resistors and port assignments.

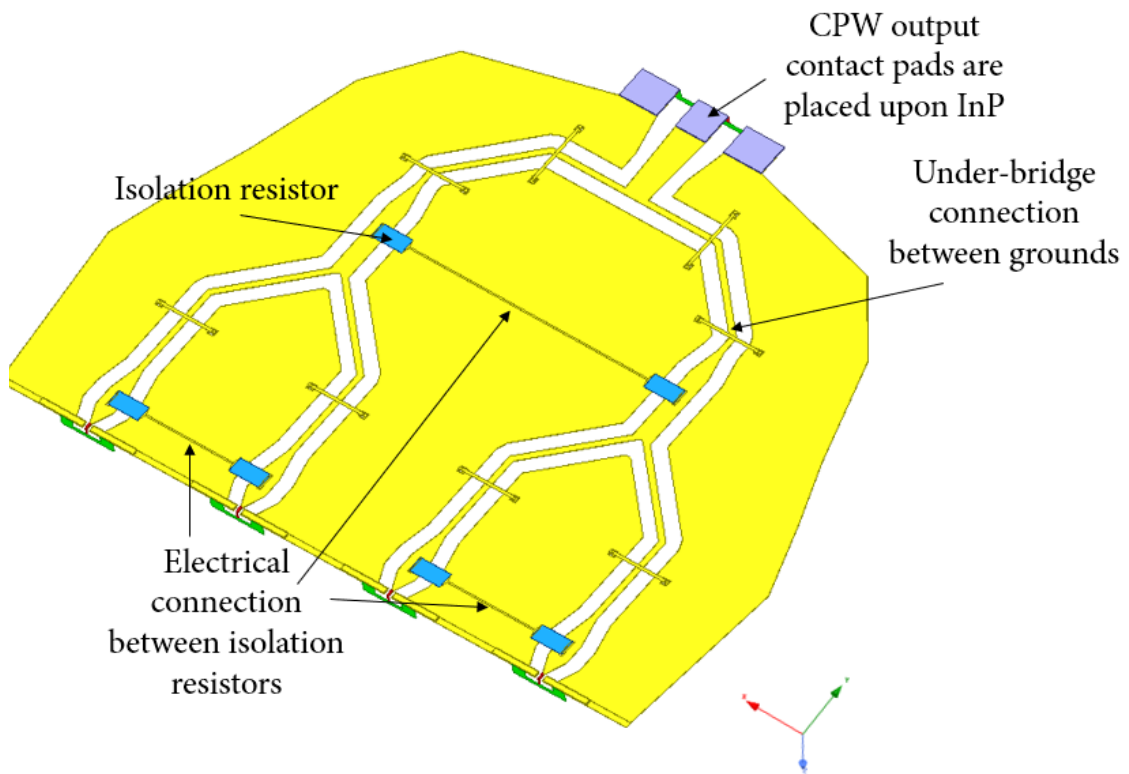


Fig. 4. 35 The backside overview of the 4-way Wilkinson with isolation resistors.

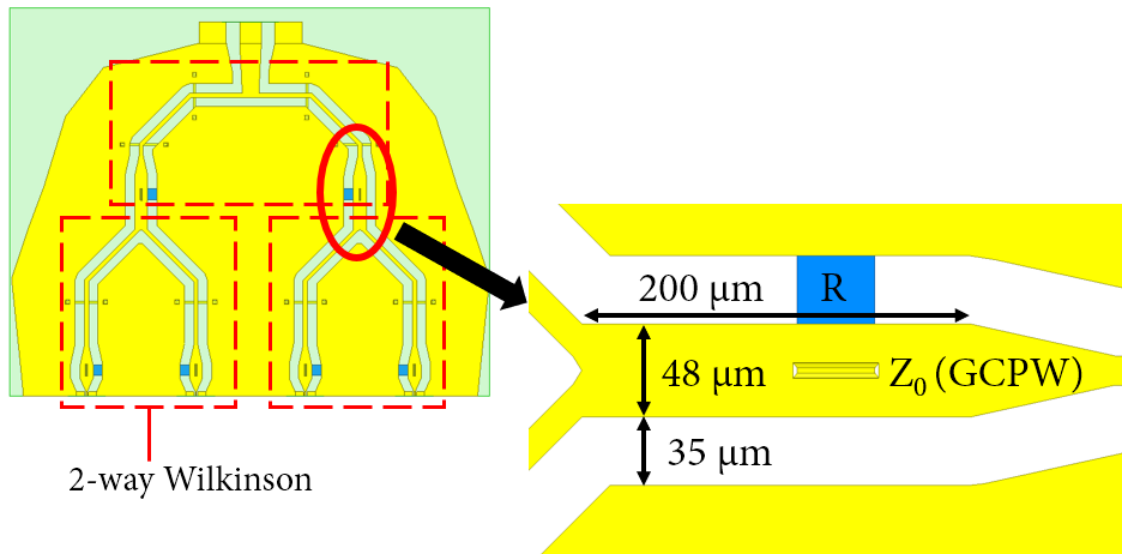


Fig. 4. 36 Top view of 4-way Wilkinson power combiner and cascade design principle.

4.3.4 4-way Wilkinson power combiner - simulation results

The S-parameters of the 4-way Wilkinson device are simulated with the frequency sweep from 10 GHz to 110 GHz, although the structure is optimized for E-band and W-band (60 – 110 GHz). Similar to the 2-way Wilkinson power combiner simulations, the s-parameters are used to characterize designed circuit in terms of inputs (S_{11} , S_{22} , S_{33} , S_{44}), output (S_{55}), transmission (S_{51} , S_{52} , S_{53} , S_{54}) losses and isolation between the input ports, as presented in Fig. 4. 34. Based on the theory presented in sub-chapter 4.3, the ideal 4-way Wilkinson power combiner transmission loss is equal to -6 dB. It corresponds to perfectly combine (or split) signals from input ports towards port 5. Simulations of the 4-way Wilkinson with isolation resistors are presented from Fig. 4. 37 to Fig. 4. 39. As can be observed, the device experience much stronger resonant behaviour in comparison to 2-way Wilkinson power combiner. Moreover, it is also a very challenging task to design perfectly symmetric and compact circuit, as with more complex high frequency circuit structure the position of the elements such as under-bridge connections is critical. Based on the simulation results, the frequency ranges at which circuit achieves optimal behaviour are narrowed to about 1.5 GHz. First optimum is around 47 GHz. At that frequency, the inputs reflections (Fig. 4. 37) are about -14 dB, transmission loss is of -3.5 dB (Fig. 4. 38) and isolation of - 8 dB (Fig. 4. 39).

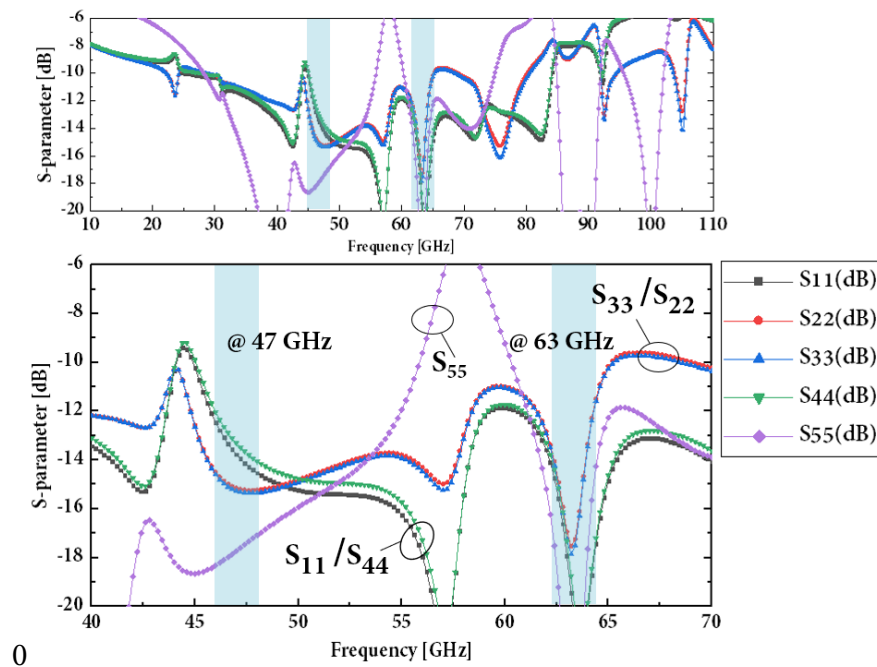


Fig. 4. 37 S-parameters of the 4-way Wilkinson power combiner from 10 GHz to 110 GHz (top) and from 40 GHz to 70 GHz (bottom). Source (port) impedance: 50 Ω .

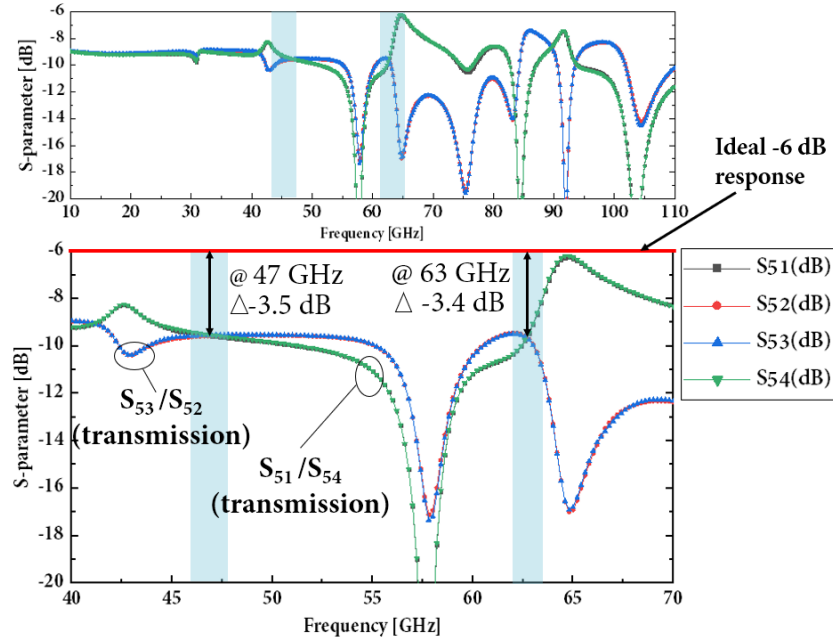


Fig. 4.38 S-parameters (transmission) of the 4-way Wilkinson power combiner from 10 GHz to 110 GHz (top) and from 40 GHz to 70 GHz (bottom). Source (port) impedance: 50 Ω .

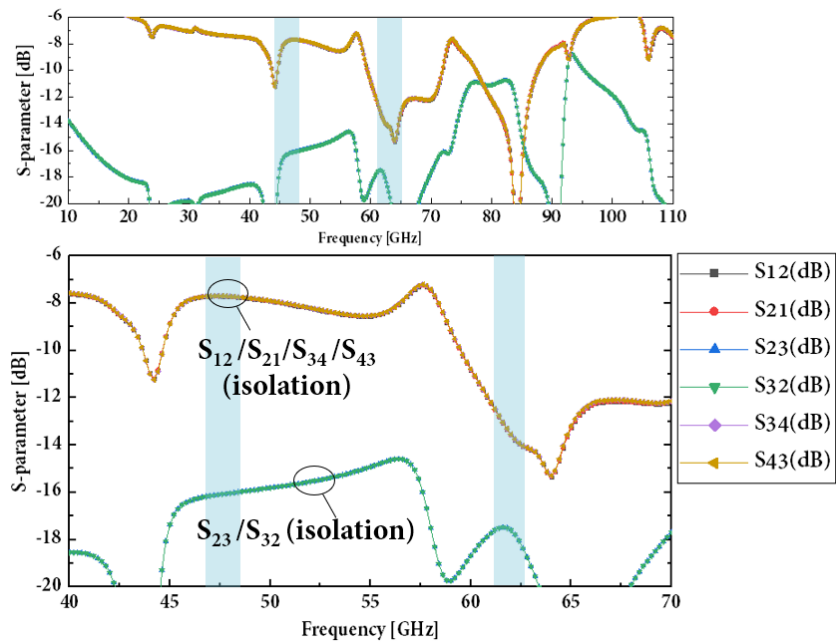


Fig. 4.39 S-parameters (isolation) of the 4-way Wilkinson power combiner from 10 GHz to 110 GHz (top) and from 40 GHz to 70 GHz (bottom). Source (port) impedance: 50 Ω .

Transmission loss is high due to the presence of isolation resistors on the signal path, as it is also observed in the 2-way combiner. Another frequency at which circuit has an optimum is at 63 GHz. At that frequency, the input reflections are below -17 dB, transmission loss is of -3.4 dB with -14 dB of isolation level. Better results are obtained for the 4-way Wilkinson power combiner without isolation resistors. The s-parameters are presented from Fig. 4. 40 to Fig. 4. 42. Optimum frequencies are at 43 GHz and 63 GHz, where input reflections are about -10 dB. Moreover, transmission loss is lower, and is of -0.5 dB at 43 GHz, and -0.9 dB at 63 GHz. Isolation of -8 dB and -10 dB, at 43 GHz and 63 GHz is achieved, respectively. Furthermore, based on the simulation results, the phase of the transmitted signals is not perfectly matched, as presented in Fig. 4. 43 and Fig. 4. 44. At lower frequencies, for both designs, at which optimum is found, the phase difference is below 1° and 5° , but at the second optimum, the phase difference is high, reaching 61° . Moreover, it is also observed that signals at port 1 and port 4, as well as at port 2 and port 3 are matched not only in phase, but also undergoes the same influence of input reflections and transmission losses. This also shows, that device suffer from imperfect symmetry. One of the consequences will also be additional losses due to the phase mismatch when the signals are combined.

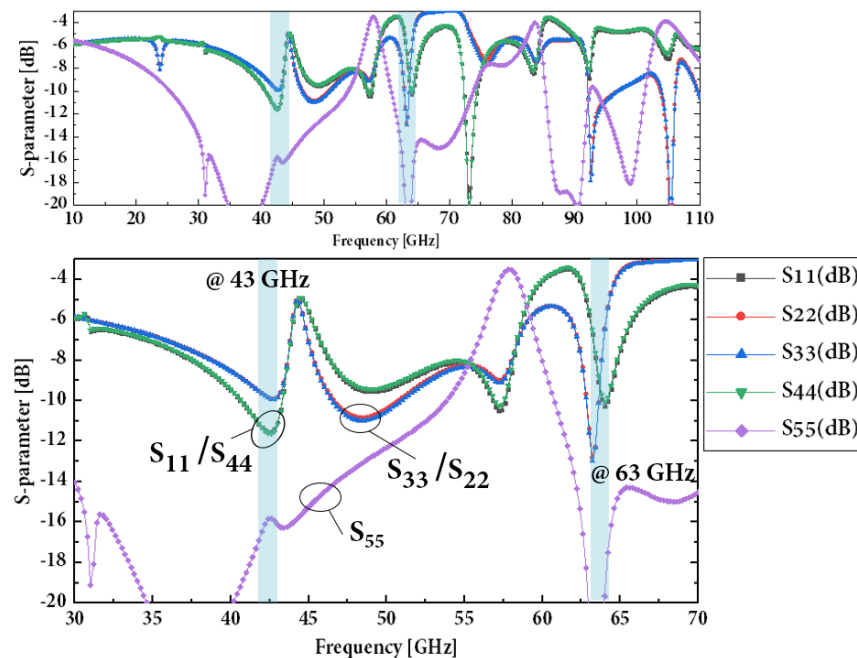


Fig. 4. 40 S-parameters of the 4-way Wilkinson power combiner without isolation resistor from 10 GHz to 110 GHz (top) and from 40 GHz to 70 GHz (bottom). Source (port) impedance: 50 Ω .

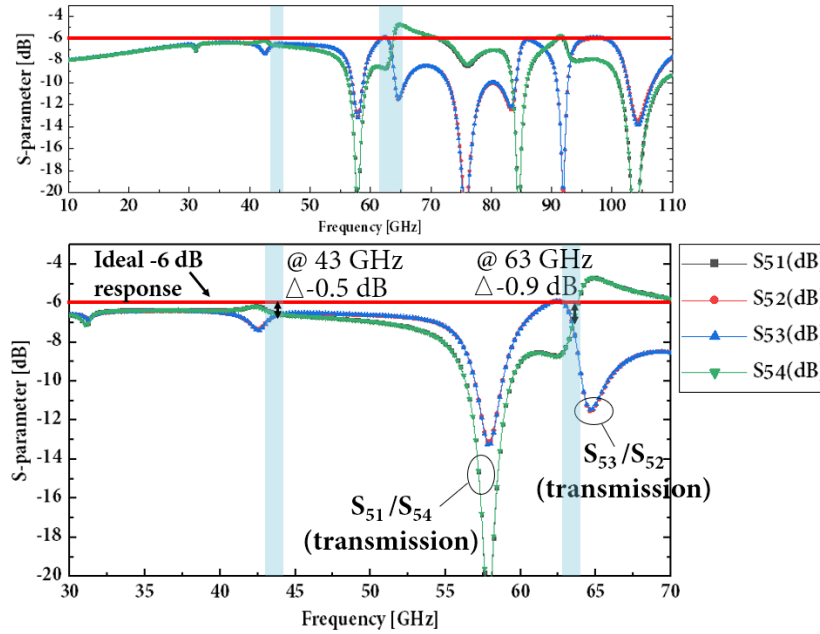


Fig. 4.41 S-parameters (transmission) of the 4-way Wilkinson power combiner without isolation resistor from 10 GHz to 110 GHz (top) and from 40 GHz to 70 GHz (bottom). Source (port) impedance: 50 Ω .

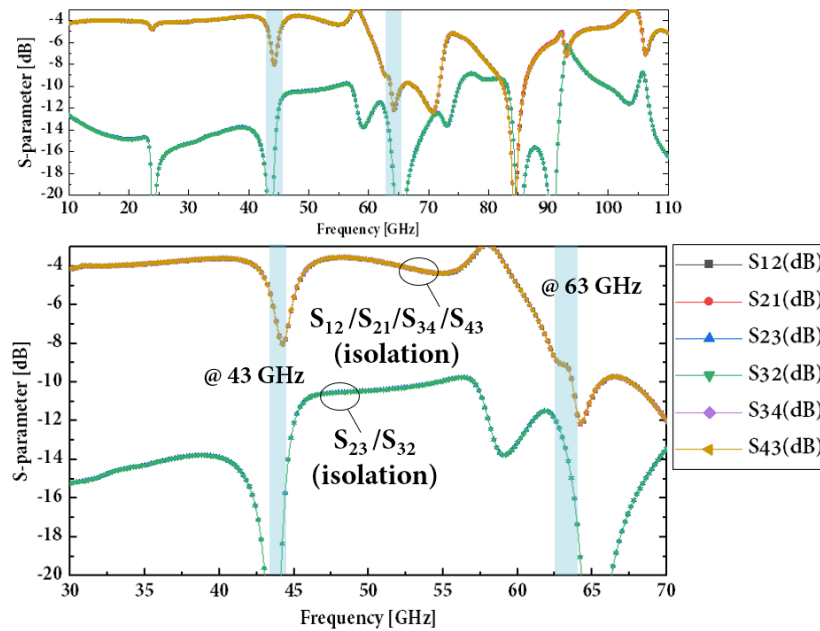


Fig. 4.42 S-parameters (isolation) of the 4-way Wilkinson power combiner without isolation resistor from 10 GHz to 110 GHz (top) and from 40 GHz to 70 GHz (bottom). Source (port) impedance: 50 Ω .

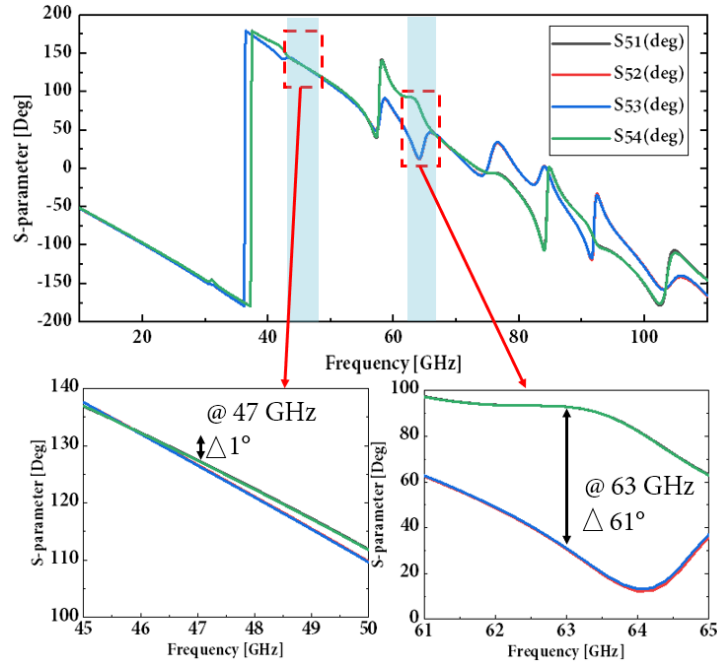


Fig. 4. 43 S-parameters (phase) of the 4-way Wilkinson power combiner from 10 GHz to 110 GHz (top) and around optimum value of 47 GHz and 63 GHz (bottom). Source (port) impedance: 50 Ω .

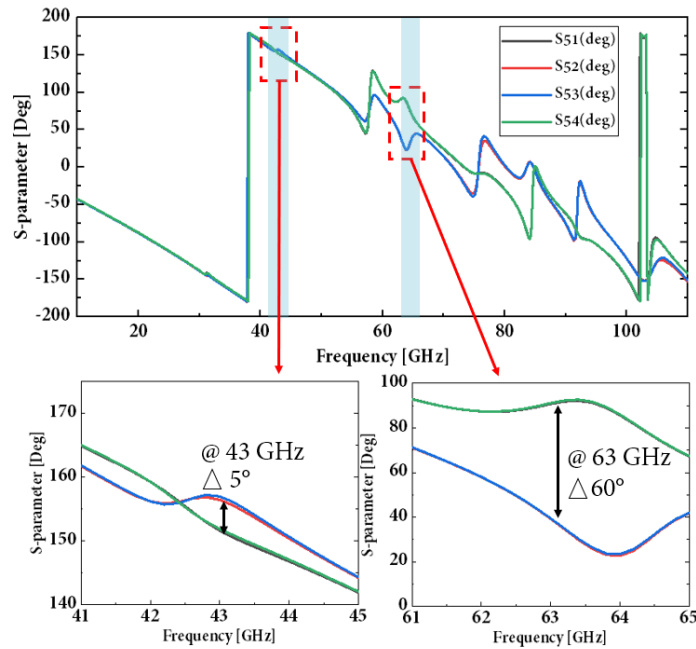


Fig. 4. 44 S-parameters (phase) of the 4-way Wilkinson power combiner without isolation resistor from 10 GHz to 110 GHz (top) and around optimum value of 47 GHz and 63 GHz (bottom). Source (port) impedance: 50 Ω .

Examples of the E-field distribution are presented from Fig. 4. 45 to Fig. 4. 48 for both type of structures, from the top and backside view. Such as in the case of 2-way combiner, the influence of the connection to isolation resistor is clearly seen in the field distribution. In Fig. 4. 49 a close-up view of the E-field distribution at the inputs are also presented, where the difference between the structures can be observed. Presence of the metallic connection to isolation resistor consequently leads to higher transmission loss. Summary of the 4-way Wilkinson power combiners is presented in sub-chapter 4.3.5.

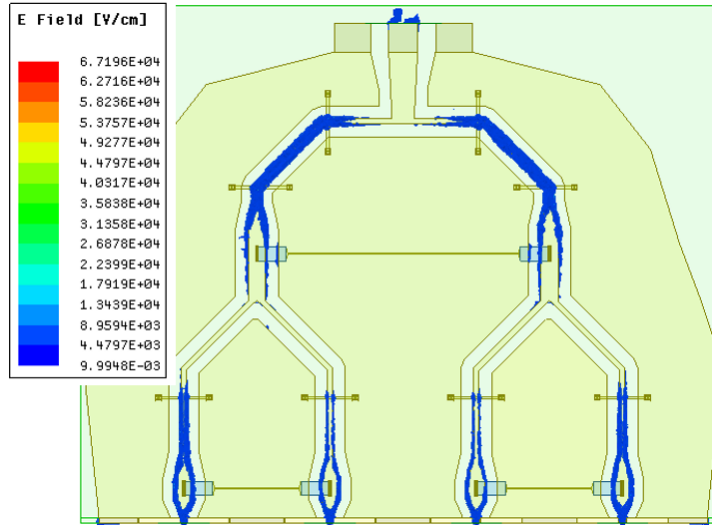


Fig. 4. 45 Top view of E-field distribution for the 4-way Wilkinson power combiner with isolation resistors at 63 GHz.

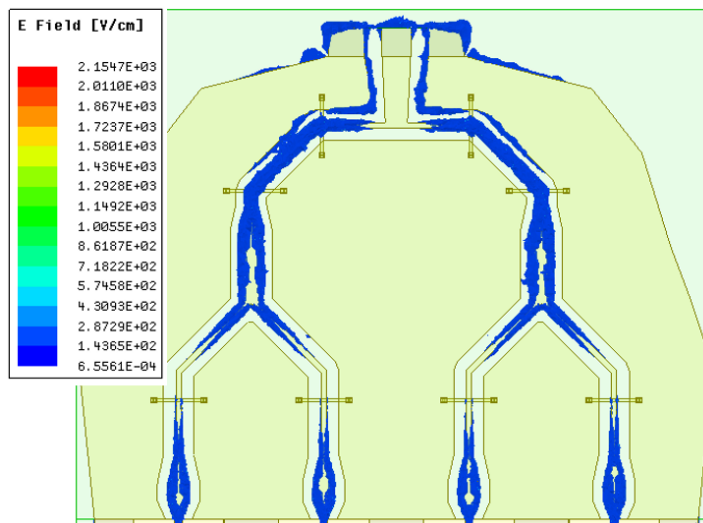


Fig. 4. 46 Top view of E-field distribution for the 4-way Wilkinson power combiner without isolation resistors at 63 GHz.

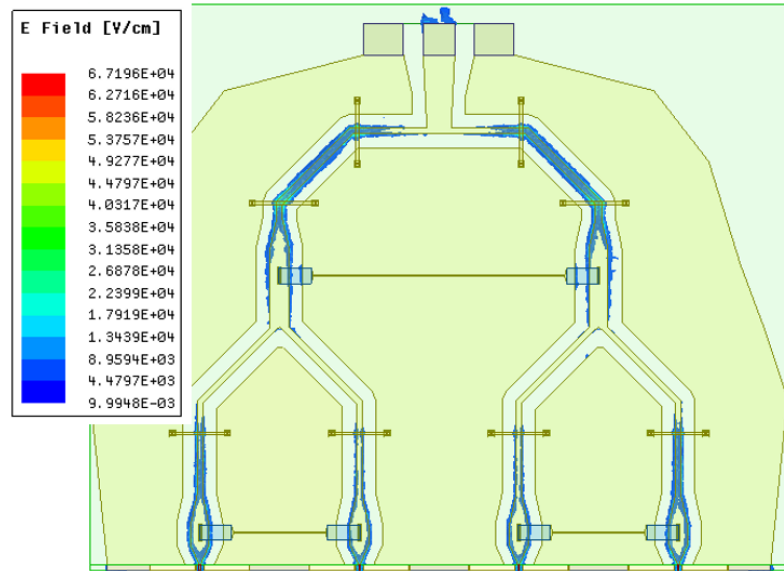


Fig. 4. 47 Backside view of E-field distribution for the 4-way Wilkinson power combiner with isolation resistors at 63 GHz.

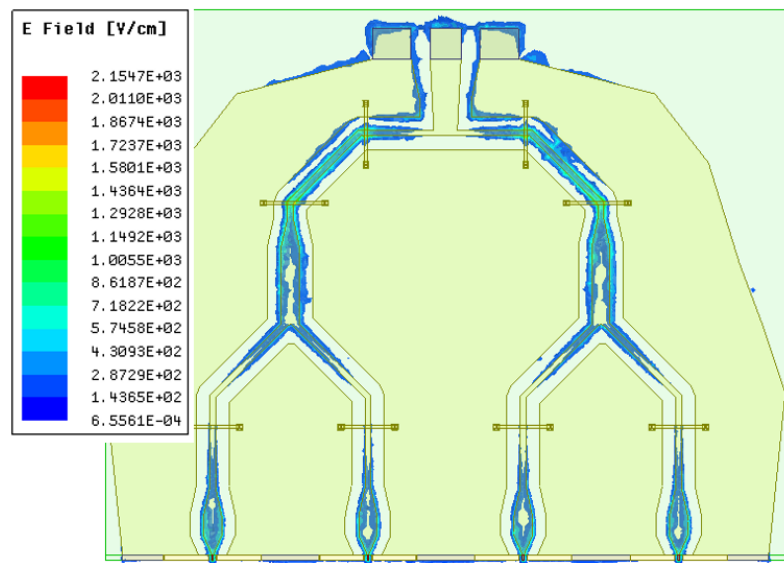


Fig. 4. 48 Backside view of E-field distribution for the 4-way Wilkinson power combiner without isolation resistors at 63 GHz.

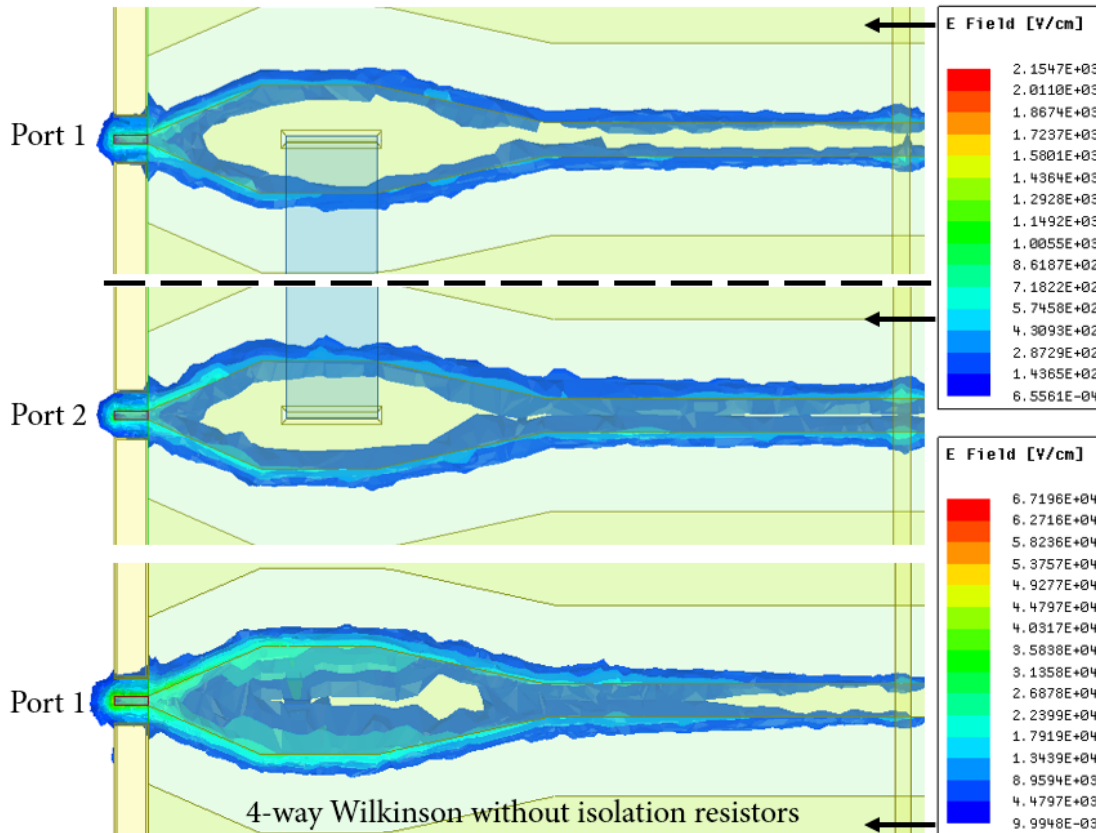


Fig. 4. 49 Top view of E-field distribution for the 4-way Wilkinson power combiner with isolation resistors at 63 GHz at port 1 and port 2, and for the device without isolation resistors (bottom figure).

4.3.5 Wilkinson power combiners - summary

Fig. 4. 50 and Fig. 4. 51 present the summary of the s-parameters for both type of Wilkinson power combiners. As already discussed, circuit without isolation resistor is less lossy in terms of transmission and output match for the 2-way Wilkinson. Phase difference for both of the design is comparable and is below/or about 1° in the entire frequency range. Moreover, bandwidths of the 2-way power combiner circuits are also comparable, but the design with the isolation resistor presents possibility of being wider. Structures of 4-way Wilkinson are much more resonant and more challenging in terms of symmetry in comparison to 2-way design. Moreover, presence of the isolation resistors has much bigger impact on the device behaviour as well. Although the isolation and the inputs match are comparable in both types of 4-way Wilkinson, the transmission loss is much higher in the device with isolation resistor.

	2-way Wilkinson	2-way Wilkinson without isolation resistors
Bandwidth	ca. 6 GHz (66 GHz - 71 GHz)	ca. 5 GHz (67 GHz - 71 GHz) (34 GHz - 35 GHz)
Transmission (s_{21}/s_{31})	- 0.7 dB	- 0.3 dB
Isolation (s_{23}/s_{32})	- 12 dB	- 10 dB
Output match (s_{11})	- 19 dB	<< -20 dB
Input match (s_{22}/s_{33})	- 9 dB	- 10 dB
Phase difference (s_{21}/s_{31})	ca. 1°	ca. 1°

Fig. 4. 50 Summary of the s-parameters for the 2-way Wilkinson power combiner with and without isolation resistors.

	4-way Wilkinson	4-way Wilkinson without isolation resistors
Bandwidth	ca. 3 GHz (ca. 1.5 GHz @ 47 GHz) (ca. 1.5 GHz @ 63 GHz)	ca. 3 GHz (ca. 1.5 GHz @ 43 GHz) (ca. 1.5 GHz @ 63 GHz)
Transmission ($s_{51}/s_{52}/s_{53}/s_{54}$)	- 3.5 dB @ 47 GHz - 3.4 dB @ 63 GHz	- 0.5 dB @ 47 GHz - 0.9 dB @ 63 GHz
Isolation ($s_{12}/s_{21}/s_{34}/s_{43}$)	- 8 dB @ 47 GHz - 14 dB @ 63 GHz	- 8 dB @ 47 GHz - 10 dB @ 63 GHz
Isolation (s_{23}/s_{32})	-16 dB @ 47 GHz -18 dB @ 63 GHz	<< - 20 dB @ 47 GHz - 14 dB @ 63 GHz
Output match (s_{55})	-18 dB @ 47GHz << - 20 dB @ 63 GHz	-16 dB @ 43GHz << - 20 dB @ 63 GHz
Input match ($s_{11}/s_{22}/s_{33}/s_{44}$)	-13 dB @ 47 GHz << - 18 @ 63 GHz	-10 dB @ 43 GHz -10 dB @ 63 GHz
Phase difference ($s_{51}/s_{52}/s_{53}/s_{54}$)	ca. 1° @ 47 GHz ca. 61° @ 63 GHz	ca. 5° @ 43 GHz ca. 60° @ 63 GHz

Fig. 4. 51 Summary of the s-parameters for the 4-way Wilkinson power combiner with and without isolation resistors.

To conclude:

- **The 2-way Wilkinson power combiner, based on the simulation results, is much less lossy structure in comparison to 4-way design. Moreover, the 2-way Wilkinson design with isolation resistor shows higher transmission losses due to the presence of the resistor on the transmission path with the corresponding electrical connections (see Fig. 4. 24).**
- **The phase difference, in the 2-way Wilkinson design with and without isolation resistor, between the signals is very low, ca. 1° in the entire frequency range (see Fig. 4. 30 and Fig. 4. 31).**
- **The 2-way Wilkinson design without isolation resistor shows the possibility of having wider bandwidth.**
- **The 4-way Wilkinson design is very challenging due to imperfect symmetry of the structure, and as a consequence has more lossy behaviour in comparison to 2-way design.**
- **Operational bandwidths for the 2-way and 4-way power combiner designs are narrow and in total are about 3 GHz.**
- **Moreover, in the 4-way Wilkinson power combiner the phase difference between the inputs is considerably high (see Fig. 4. 43 and Fig. 4. 44) due to imperfect symmetry.**

4.4 ANTENNA INTEGRATED UTC PDS

The objective of these subchapters is to present the design and simulation results for the antenna-integrated devices for W-band applications. It is preceded by brief theoretical introduction to antenna design principles. As discussed in Chapter 2 and presented in Fig. 2. 36 and Fig. 2. 37, antenna-integrated photodiodes deliver lower output power levels in comparison to single or power combined devices. Nevertheless, despite certain limitations, antenna integration approach can simplify transmitter and receiver design and greatly improve compactness. Moreover, closely spaced antenna array structure is able to combine power from each of the single antennas, what can considerably improve the total output power levels. There are several parameters used for antenna performance description, with detailed explanation provided in [17][18][19]. Some of the most fundamental are:

1. Radiation pattern, $F(\theta, \phi)$: represents antenna radiated field in different directions of space at a fixed distance, usually in spherical coordinates.

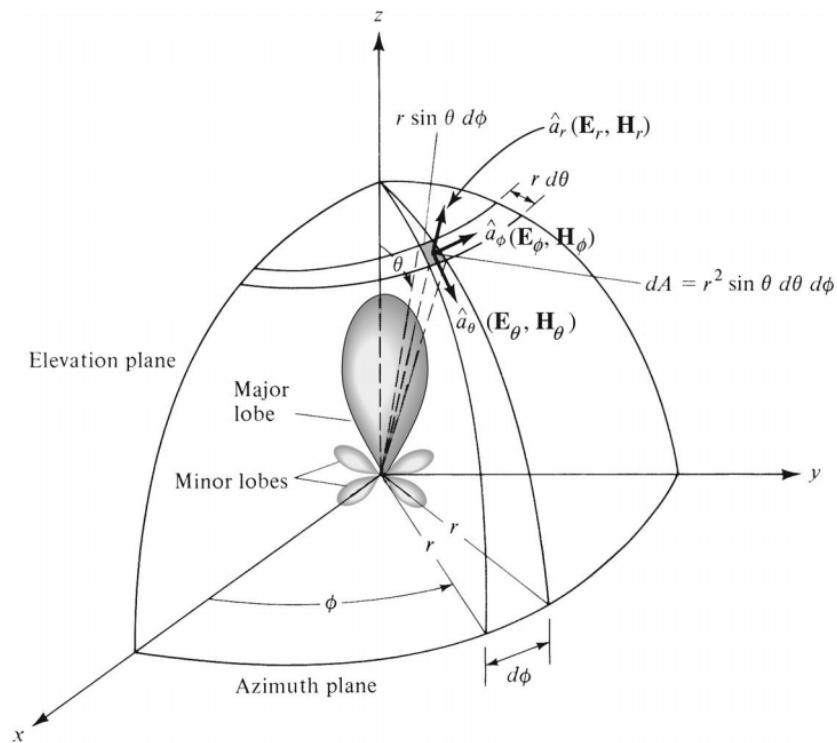


Fig. 4. 52 Coordinate system for antenna analysis and radiation pattern with major and minor lobes [17].

2. Directivity, D : defined as ratio of power density in the direction of the pattern peak to the average power density at the same distance from the antenna.

3. Gain, G (or radiation efficiency e_{rad} , where $G=e_{rad}D$): directivity reduced by the losses on the antenna.
4. Impedance, Z_{ant} : defined as input impedance at the antenna terminals. It is a complex number, depending on frequency and can be defined as sum of resistance and reactance:

$$Z_{ant}(\omega) = R_{ant}(\omega) + iX_{ant}(\omega) \quad (4.23)$$

The resistive part of 4.23 consist of two components, the radiation resistance (R_r) and loss resistance (R_{loss}):

$$R_{ant} = R_r + R_{loss} \quad (4.24)$$

The R_r can be defined as a value of resistance needed to dissipate the same power as the one radiated through the free-space by an antenna, and the R_{loss} represents the loss of the antenna power that is not radiated. Power delivered to the antenna can be described as:

$$P_{delivered} = P_{rad} + P_{loss} = \frac{1}{2}R_r|I_{ant}|^2 + \frac{1}{2}R_{loss}|I_{ant}|^2 \quad (4.25)$$

Where, I_{ant} is the current at the input terminals (factor $\frac{1}{2}$ is present because it is a peak value in the time waveform).

5. Bandwidth: frequency range where performance parameters meet acceptable values.

Moreover, among several antenna topologies, the most utilized for integration with UTC photodiodes can be divided into two groups [17][18][19]:

1. Self-complementary planar antennas: if the shape of the metallic and non-metallic parts of the antenna is the same and it can be brought into coincidence by rotation, the antenna is self-complementary. These types of antenna are often design to be broadband, for which the impedance over frequency change is constant or periodic in a logarithmic fashion, and $Z_{ant} = \frac{Z_{free-space/intrinsic\ medium}}{2}$. The most widely used topologies are:
 - a. Log-periodic toothed: as presented in Fig. 4. 53, firstly introduced by DuHamel and Isbell in 1966 [20]. This type of antenna structure has a log-periodic, circular-toothed topology with bow angles $\beta_1 + \beta_2 = 90^\circ$ for a self-complementary condition. The expansion and tooth-width parameter are equal to $k_1 = \frac{R_{n+1}}{R_n}$ and $k_2 = \frac{r_n}{R_n}$, respectively [18].

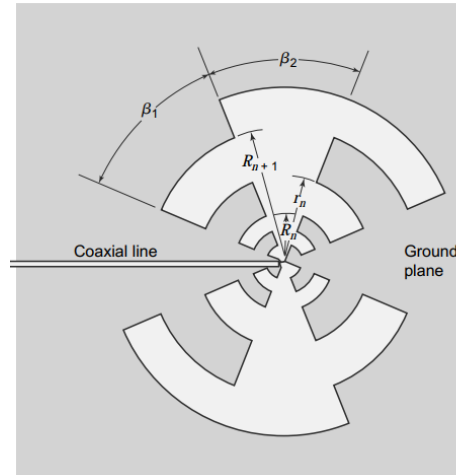


Fig. 4. 53 Example of log-periodic toothed planar antenna [18].

- b. Bow-tie: introduced by Brown and Woodward in 1952 [21], as presented in Fig. 4. 54 is a flat-plane version of biconical antenna. For a self-complementary condition $\alpha = 90^\circ$.

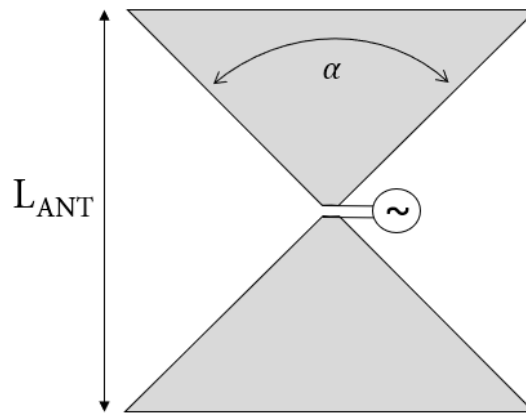


Fig. 4. 54 Example of bow-tie antenna.

- Resonant planar antennas: these types of antennas operate at single or narrow frequency bands. The design can be better adapted, in comparison to broadband topologies, to provide good matching condition with integrated photodiodes. Among resonant topologies the most popular are dipole antennas. As presented in Fig. 4. 55 in its simplest form, it consists of a two conducting arms with a feeding point in the middle and $L_{ANT} = \frac{\lambda}{2}$, with adjusted value of w and w_{gap} . Modification of these two arms leads to other topologies i.e. folded-dipole or meander-dipole antennas, with more information in [22].

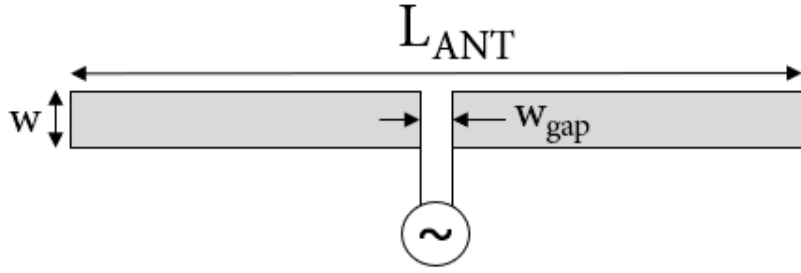


Fig. 4. 55 Example of dipole antenna.

In addition, if antenna is placed upon i.e. InP substrate, the guided wavelength (λ_g) can be calculated as [30]:

$$\lambda_g = \frac{\lambda_0}{\sqrt{\epsilon_{effective}}} \quad (4.26)$$

where $\epsilon_{effective} = \frac{1+\epsilon_r}{2}$. The above equation is used in the calculation of the antenna dimensions presented in the next sub-chapter. Furthermore, the DC bias of the photodiode integrated with an antenna is another important aspect of the circuit design, although in common approach, use of an external (not integrated on the chip) commercially available components is popular. An example of a lumped element bias T network, which is crucial in the electronic-based system designs, is presented in Fig. 4. 56. More details can be found in [23][24][25][26]. The DC bias network work principle is to decouple the RF and DC part of the signal through the circuit blocks in a way that the RF signal is not transmitted through the DC terminals. Moreover, at high frequency, distributed elements are preferred in the topology that serves as an inductor and capacitor i.e. microstrip line and radial stub, respectively [27][28]. If an antenna-integrated device is biased via i.e. needle directly on the antenna or on the bias pads, without any bias T elements, some part of the signal is going to be lost. In addition, silicon hemispherical lenses are very often employed in the measurement setups for an antenna-integrated UTC PDs characterization [29][30].

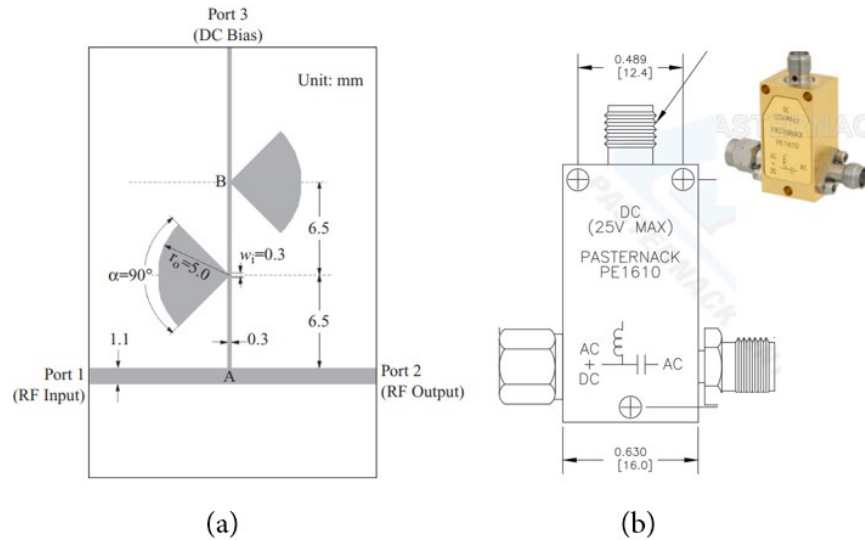


Fig. 4.56 Example of a microstrip bias T network with a bandstop filter for RF choke [25] (a) and (b) an example of a commercially available bias T from 0.1 MHz to 50 GHz [26].

Antenna-arrays are very often utilized in the RF system design to increase the directivity and enlarge the antenna dimensions without increasing the dimensions of each of the single antenna element [17][18]. Moreover, in the majority of the array design approaches, each individual antenna has the same dimensions and the total field of the antenna array is determined by the vector addition of the fields that are radiated by each element. Nevertheless, it is very challenging to design very directive antenna pattern as it depends on [17]:

- The geometrical configuration of the array (linear, circular, rectangular etc.)
- The relative distance between the elements.
- The excitation amplitude and phase of the individual antennas.
- The relative pattern of the individual elements.

What is more, in the array design, an array factor (AF) can be established as a function of the geometry and the excitation phase. With the variation of the distance and/or phase between the elements, the characteristics of the array factor and of the total field ($E(\text{total})$) of the array can be controlled and described as [17]:

$$E(\text{total}) = [E(\text{single element at reference point})] \times [\text{array factor}] \quad (4.27)$$

The equation 4.27 is also referred as pattern multiplication for an array of identical elements. Furthermore, each antenna array has its own array factor which depends on the conditions mentioned above. Among linear array designs with uniform distribution the most common are:

- Broadside.

- Ordinary end-fire.
- Scanning (phased).
- Planar.

Each of the linear array types has specific direction of the maximum radiation for the corresponding distance between the elements and are presented in Fig. 4. 57. Direction of the θ_0 corresponds with the z axis direction i.e. $\theta_0 = 180^\circ$ is towards -z axis as presented in Fig. 4. 58 where the example of the broadside and broadside/end-fire amplitude patterns are depicted. More theoretical details about antenna arrays and design principles are provided in [17]-[19].

Array	Distribution	Type	Direction of Maximum	Element Spacing
Linear	Uniform	Broadside	$\theta_0 = 90^\circ$ only $\theta_0 = 0^\circ, 90^\circ, 180^\circ$ simultaneously	$d_{\max} < \lambda$ $d = \lambda$
Linear	Uniform	Ordinary end-fire	$\theta_0 = 0^\circ$ only $\theta_0 = 180^\circ$ only $\theta_0 = 0^\circ, 90^\circ, 180^\circ$ simultaneously	$d_{\max} < \lambda/2$ $d_{\max} < \lambda/2$ $d = \lambda$
Linear	Uniform	Hansen-Woodyard end-fire	$\theta_0 = 0^\circ$ only $\theta_0 = 180^\circ$ only	$d \simeq \lambda/4$ $d \simeq \lambda/4$
Linear	Uniform	Scanning	$\theta_0 = \theta_{\max}$ $0 < \theta_0 < 180^\circ$	$d_{\max} < \lambda$

Fig. 4. 57 Maximum element spacing (d) to maintain one or two amplitude maxima of a linear array [17].

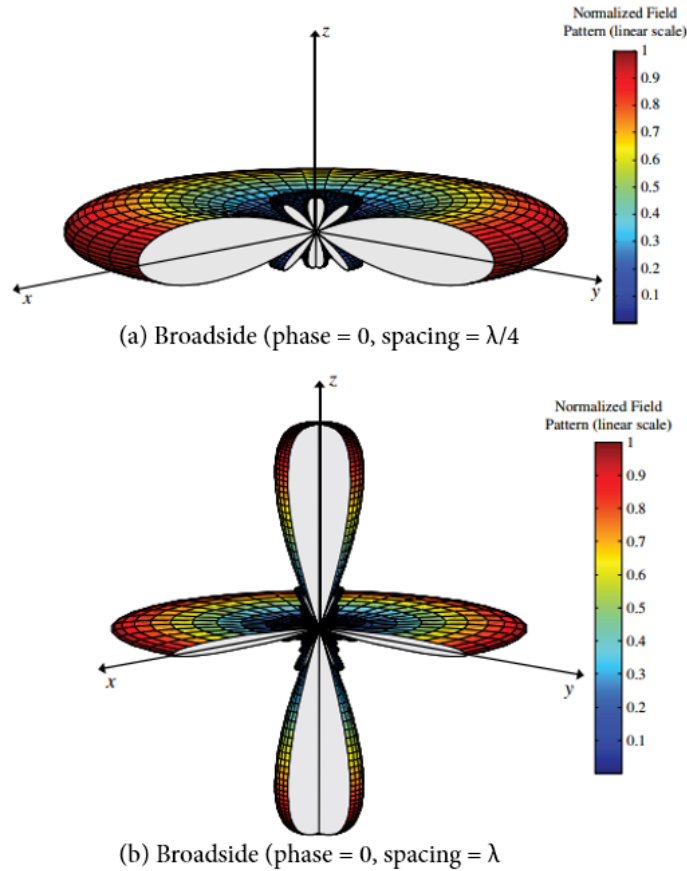


Fig. 4. 58 Example of the amplitude patterns for broadside (maxima $\theta_0 = 90^\circ$) and broadside/end-fire for 10-element array (maxima $\theta_0 = 0^\circ, 90^\circ$ and 180°). [17].

4.4.1 3x folded-dipole antenna-integrated UTC PD - design

An overview of the designed 3x folded-dipole antenna-integrated UTC PD structure is presented in Fig. 4. 59. As mentioned in the introduction, W-band is the target frequency range for the antenna-based solutions with the possibility of application at higher frequencies. Antenna dimensions, presented in Fig. 4. 60, correspond to $\lambda_g = 90$ GHz ($L: 1240 \mu\text{m}$) based on Eq. 4.26. Moreover, as reported in [22], by adjusting antenna dimensions such as B, antenna impedance can be adapted. Furthermore, it can be also observed that, the DC bias elements require a lot of space on the chip. Radial stubs, that serves as capacitors in the LC-circuit are adjusted by iterative means during HFSS simulations. Passive optical waveguides and MMI are presented in sub-chapter dedicated to optical design. UTC PD dimensions chosen for the design are L2W3 ($15 \mu\text{m} \times 4 \mu\text{m}$). All dimensions are optimized with HFSS software in order to cover wide spectrum of frequencies, although folded-dipole antennas do not provide wideband properties. Furthermore, study of the antenna array impedance is also investigated. In the HFSS simulations all assigned source power (UTC PD) are of 0 dBm (1 mW). As

mentioned in the introduction, the relative distance between the antennas and the excitation amplitude and phase of the individual antennas are some of the main parameters that influence the direction of the propagation of the linear antenna arrays. In the 3x folded-dipole antenna-integrated design the distance d is kept to ca. $\lambda/2$. Based on the theory given in [17] the amplitude maxima of the radiation should be found towards 0° and/or 180° as presented in Fig. 4. 58, where 0° is towards z and 180° toward $-z$ axis, but it does not include the side-lobes that can appear due to the specific array design. Moreover, due to the constant optical delay between the UTC PDs (see Fig. 4. 65) and corresponding antenna structures, a constant phase shift is generated. Obtained phase shift is linear with respect to the frequency and it is utilized in the True Time Delay systems (TTD). The TTD systems have several advantages over the standard and complex antenna-array systems based on the phase-shifters that generate a constant phase shift with respect to the frequency [17][31]. Furthermore, the TTD systems overcome the main limiting factor of the standard array systems offering a squint-free operation. The squint-free operation means that the angle of the radiated beam is not shifted in the undesired direction during the frequency change. In addition, within the TTD systems two main categories can be distinguished that are based on the variable length delay lines or variable propagation velocity lines. Both categories offer different performance characteristics in terms of loss, bandwidth and complexity [32]. Moreover, along with the development of photonic-based technology, optically-fed antenna structures can possibly offer more compact and lower loss solutions to the systems based on the digital and the RF electronics. More details about optically-fed antenna-arrays in several configurations can be found in [33]-[36]. In the HFSS software it is not possible to directly implement the optical delay time, the corresponding phase of the RF signal with respect to the optical distance is introduced instead in the definition of the antenna excitation signal. The radiation patterns of the designed array with and without the optical delay compensation are simulated and the results are presented in the following chapter.

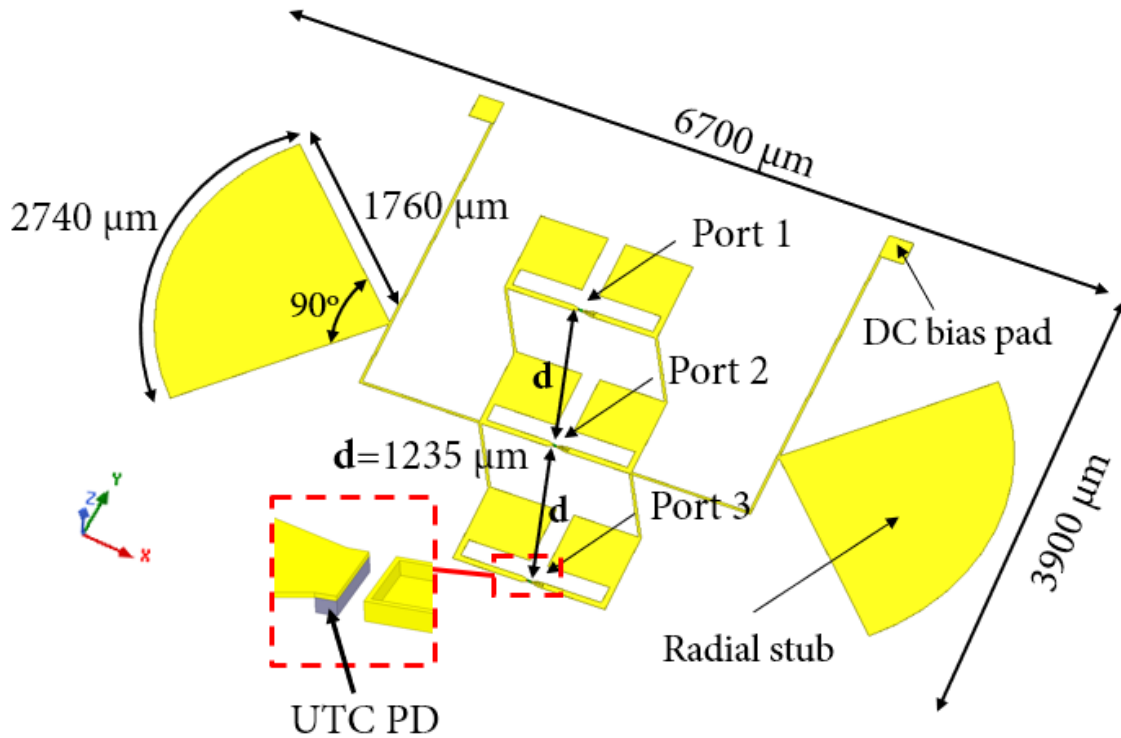


Fig. 4. 59 Overview of the 3x folded-dipole antenna-integrated UTC PDs with bias T circuit and ports assignment.

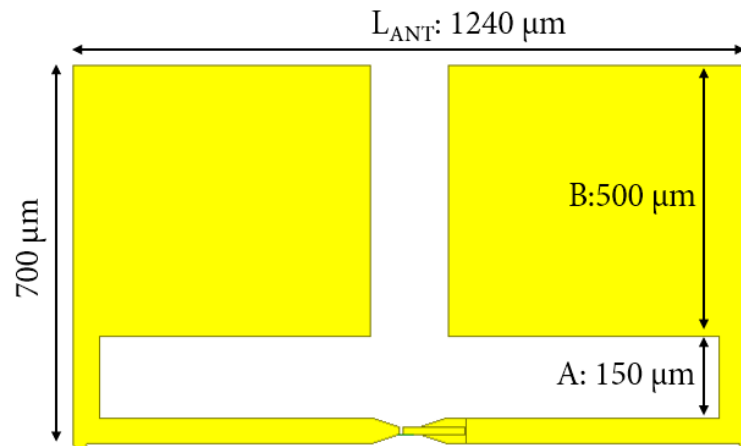


Fig. 4. 60 Dimensions of a single folded-dipole antenna-integrated UTC PD.

4.4.2 3x folded-dipole antenna-integrated UTC PD – simulation results

The s-parameters of the 3x folded-dipole antenna-integrated UTC PD device is simulated with the frequency sweep from 30 GHz to 300 GHz. Similar to the previously described simulations, the s-parameters are used to characterize designed circuit in terms of

input reflections (s_{11} , s_{22} , s_{33}) according to port assignments presented in Fig. 4. 59. Based on the simulation results depicted in Fig. 4. 61 and Fig. 4. 62, there are a couple of frequency bands at which values of input reflections are below -10 dB (marked in light blue).

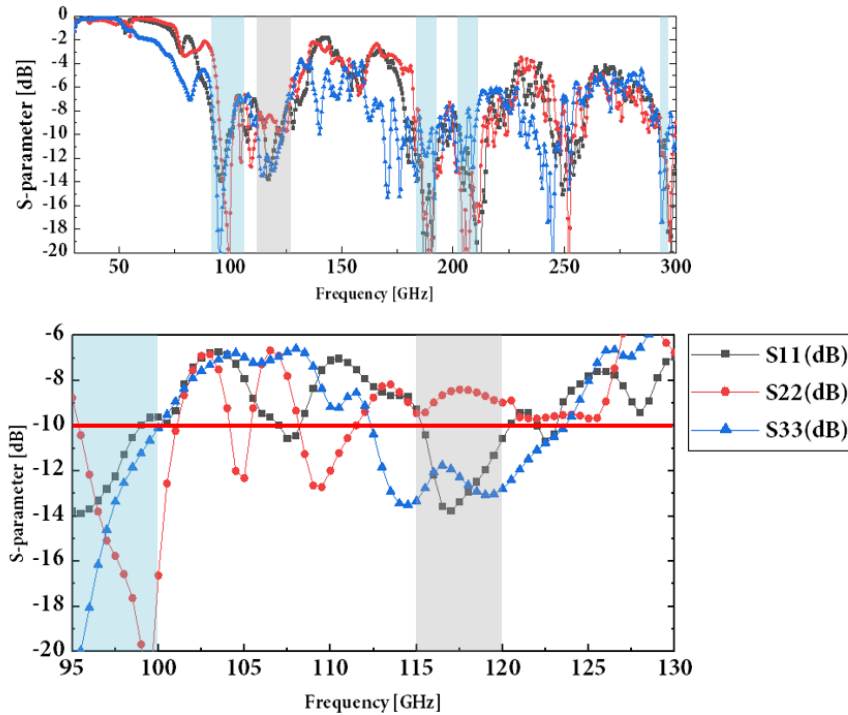


Fig. 4. 61 S-parameters of input reflections for the 3x folded-dipole antenna-integrated UTC PD from 30 GHz to 300 GHz and 95 GHz to 130 GHz. Source (port) impedance: 50Ω .

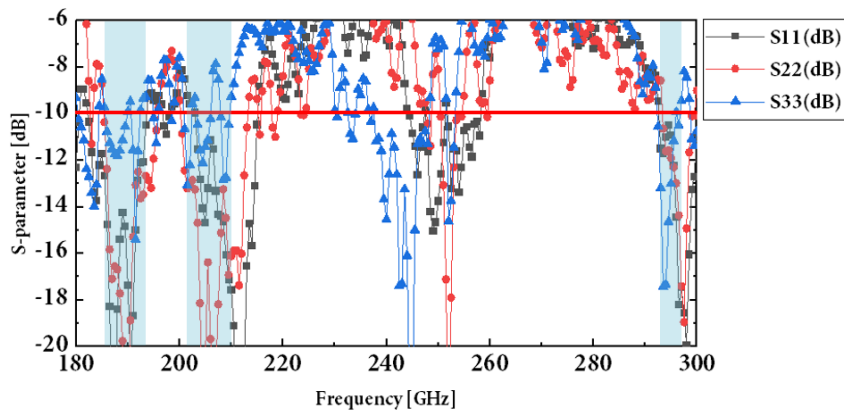


Fig. 4. 62 S-parameters of input reflections for the 3x folded-dipole antenna-integrated UTC PD from 180 GHz to 300 GHz. Source (port) impedance: 50Ω . First frequency range is from 95 GHz – 100 GHz, with additional 5 GHz between 115 GHz and 120 GHz, but with input reflections of -8 dB for one of the antennas. Additional frequency bands are from 185 GHz – 192 GHz, 203 GHz – 210 GHz and at 293 GHz - 296 GHz. Total frequency bandwidth is 22 GHz. Results of the antenna impedances are presented in Fig. 4. 63

and Fig. 4. 64. According to the simulation, it is as well a challenging task to match the antenna array impedance with 50Ω impedance of the UTC PD.

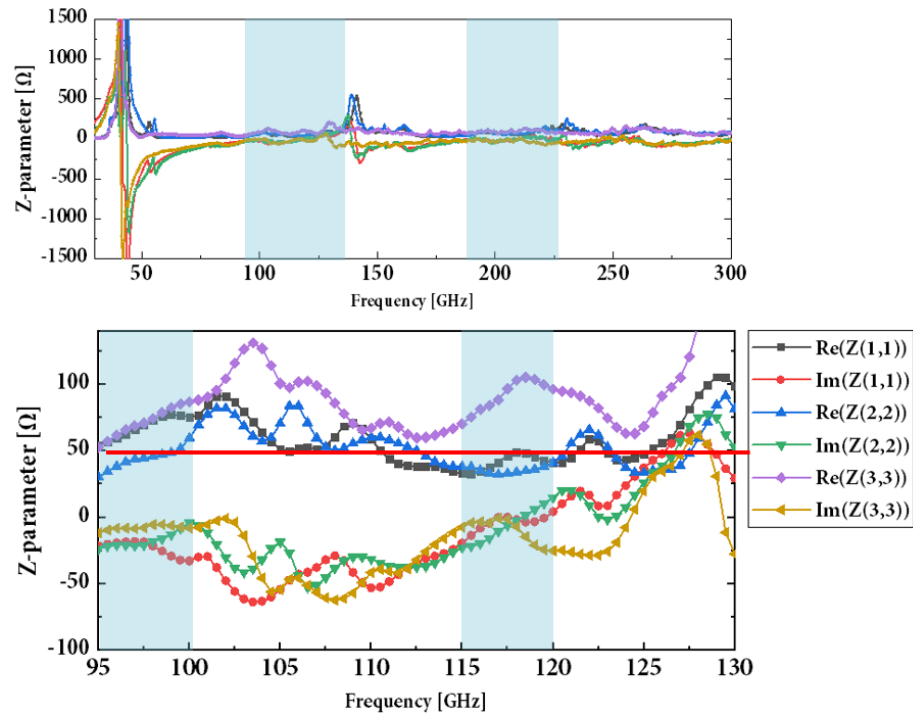


Fig. 4. 63 Z-parameters of input reflections for the 3x folded-dipole antenna-integrated UTC PD from 30 GHz to 300 GHz and 95 GHz to 130 GHz. Source (port) impedance: 50Ω .

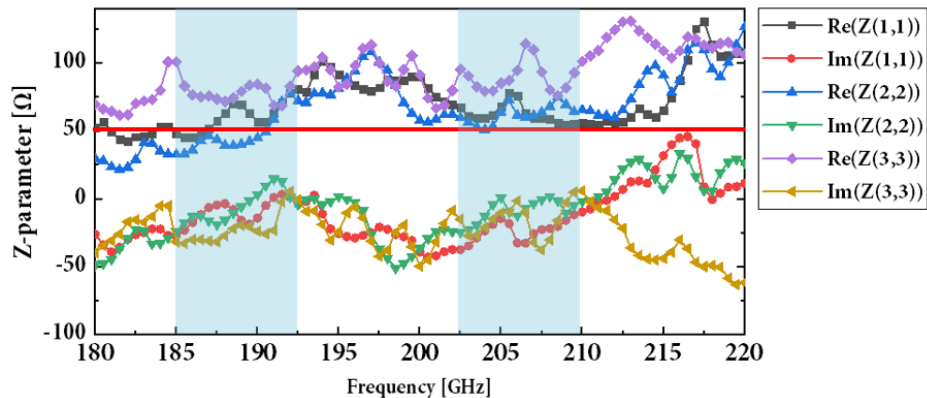


Fig. 4. 64 Z-parameters of input reflections for the 3x folded-dipole antenna-integrated UTC PD from 180 GHz to 220 GHz. Source (port) impedance: 50Ω .

In Fig. 4. 65 the 3x folded-dipole antenna structure with optical waveguides and the beam pointing direction are presented (more details about the optical design are given in chapter 4.5). The angle θ_s presented in Fig. 4. 65 can be as well found as frequency independent in the TTD system and it influences the radiation pattern [33][34]. The calculated angle is ca. 47° .

The angle of maximum radiation θ_{max} at 95 GHz is also calculated, and is ca. 2° , which corresponds to the simulations and the theory as the maximum radiation should be found towards 0° and 180° . It is important to note that the simulations are performed without SI lens. The three-dimensional radiation pattern is presented in Fig. 4. 66 at 100 GHz. As can be observed, the majority of the radiation is directed towards the bottom of the substrate. Another example of the radiation patterns at 95 GHz, 100 GHz and 190 GHz are presented in Fig. 4. 67. Moreover, as mentioned in the introduction and presented in Fig. 4. 65, the optical delay time cannot be directly introduced in the HFSS simulation software. To compensate this delay, an introduction of the phase shift of the electrical RF signal that correspond to the optical delay is applied in the simulations (example of the calculation at 95 GHz is presented in Fig. 4. 65) and obtained radiation patterns are presented in Fig. 4. 68. Based on the simulation result without the delay compensation in the HFSS simulation, the maximum gain has been achieved at 95 GHz with 4.7 dB and with radiation efficiency of 96 %. For this antenna design, the highest front-to-back ratio (FTBR) of 11 dB has been achieved at 95 GHz and it is the highest in comparison to all other antenna designs. Obtained values are improved when the optical compensation is introduced in the HFSS simulation. The highest gain is achieved at 190 GHz with 6 dB and the FTBR is of 15 dB. Nevertheless, the time compensation requires further analysis as it cannot be directly defined in the HFSS simulation. More detailed antenna parameters comparison is given in subchapter 4.4.4.

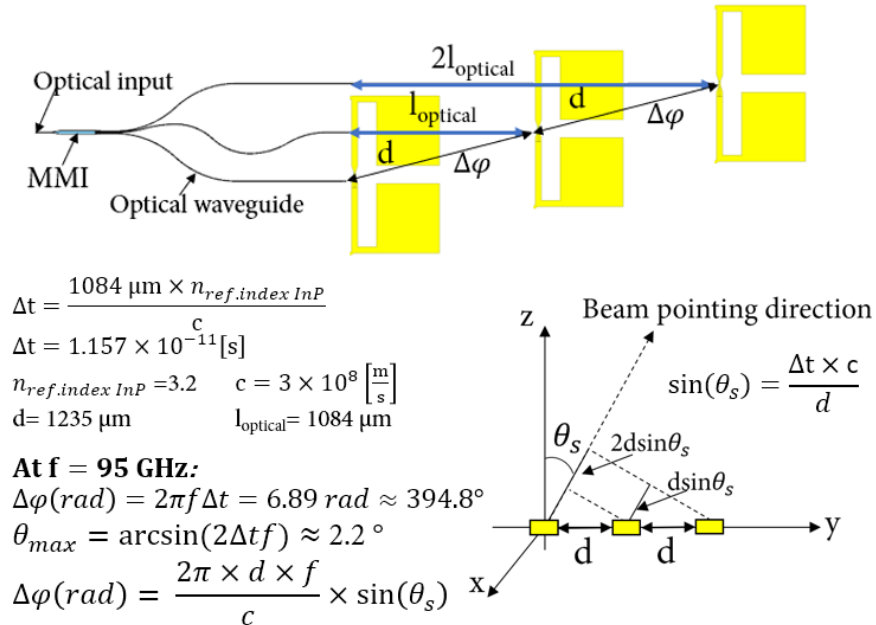


Fig. 4. 65 The 3x folded-dipole antenna integrated UTC PD with optical waveguides, the beam pointing direction with the steering angle and calculation of the time delay. Equations based on [17][34].

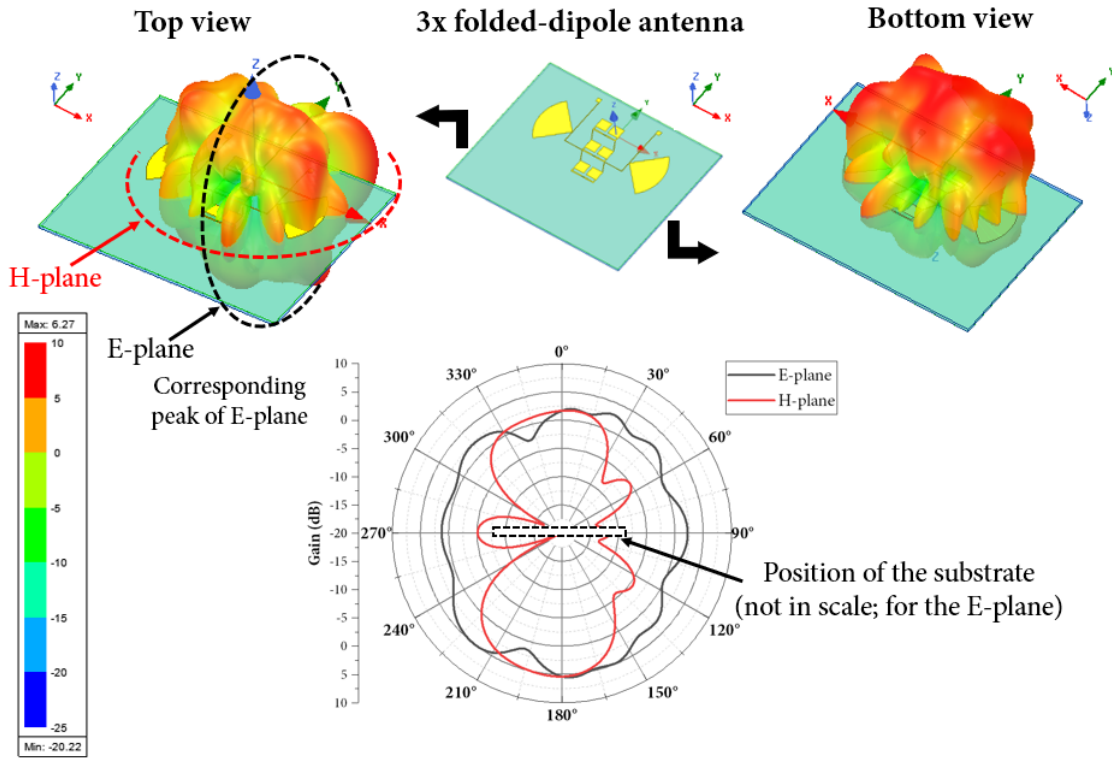


Fig. 4.66 Three-dimensional radiation pattern (scale: 0.5) of the 3x folded-dipole antenna-integrated UTC PD at 100 GHz and the E-plane and H-plane gain patterns.

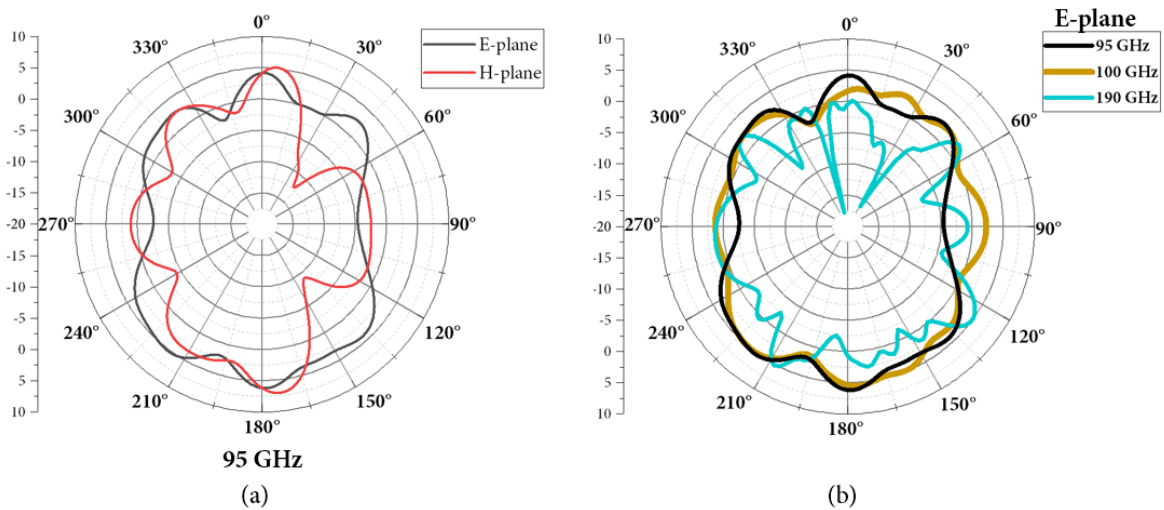


Fig. 4.67 E-plane and H-plane gain pattern at 95 GHz (a) and (b) evolution of E-plane gain pattern from 95 GHz up to 190 GHz of the 3x folded-dipole antenna-integrated UTC PD.

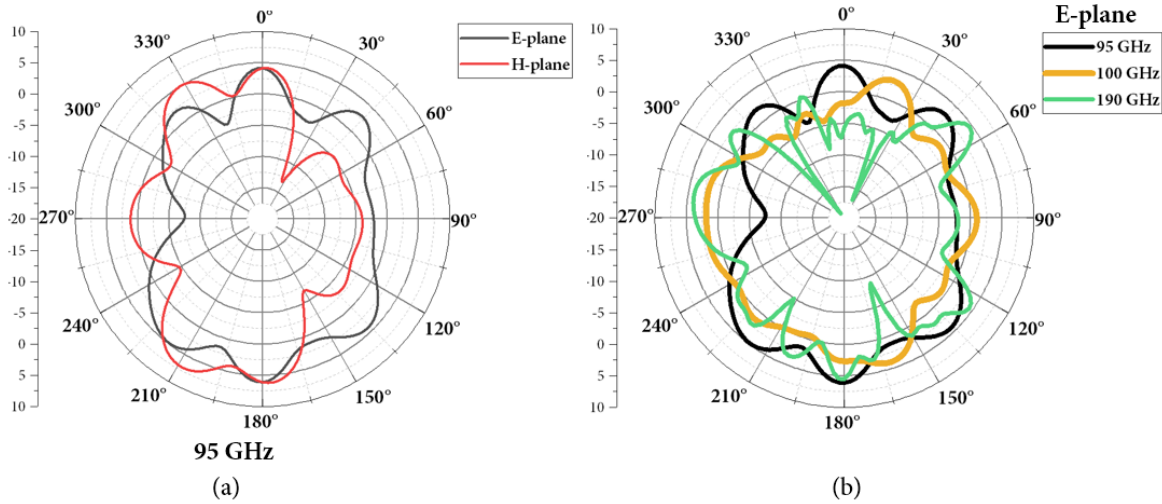


Fig. 4. 68 E-plane and H-plane gain pattern at 95 GHz (a) and (b) evolution of E-plane gain pattern from 95 GHz up to 190 GHz of the 3x folded-dipole antenna-integrated UTC PD with a time delay compensation.

4.4.3 Bow-tie antenna-integrated UTC PDs – design

The overview of the 3x bow-tie antenna-integrated UTC PD structure is presented in Fig. 4. 69. Single antenna dimensions are presented in Fig. 4. 70, correspond to $\lambda_g = 130$ GHz ($L: 900 \mu\text{m}$) based on Eq. 4.26. Other antenna dimensions are optimized with HFSS software in order to cover wide spectrum of frequencies. Radial stubs, that serves as capacitors in the LC-circuit are adjusted by iterative means during HFSS simulations as well. Passive optical waveguides and MMI are presented in sub-chapter dedicated to optical design. UTC PD dimensions chosen for the design are L2W3 ($15 \mu\text{m} \times 4 \mu\text{m}$). As can be observed, 3x bow-tie antenna array has the biggest dimensions, as radial stubs need to be bigger to block RF signal from reaching DC pads. Furthermore, study of the antenna array impedance is also investigated for all of the configurations. Moreover, bow-tie antennas are also studied in additional design configurations presented from Fig. 4. 71 to Fig. 4. 73. All these configurations have the same single antenna dimensions, but radial stubs dimensions are adjusted accordingly. Configurations with 2x bow-tie antenna structure, as well as, 2x bow-tie and 1x bow-tie have two independent optical inputs designed for the cooperation between III-V Lab and UC3M.

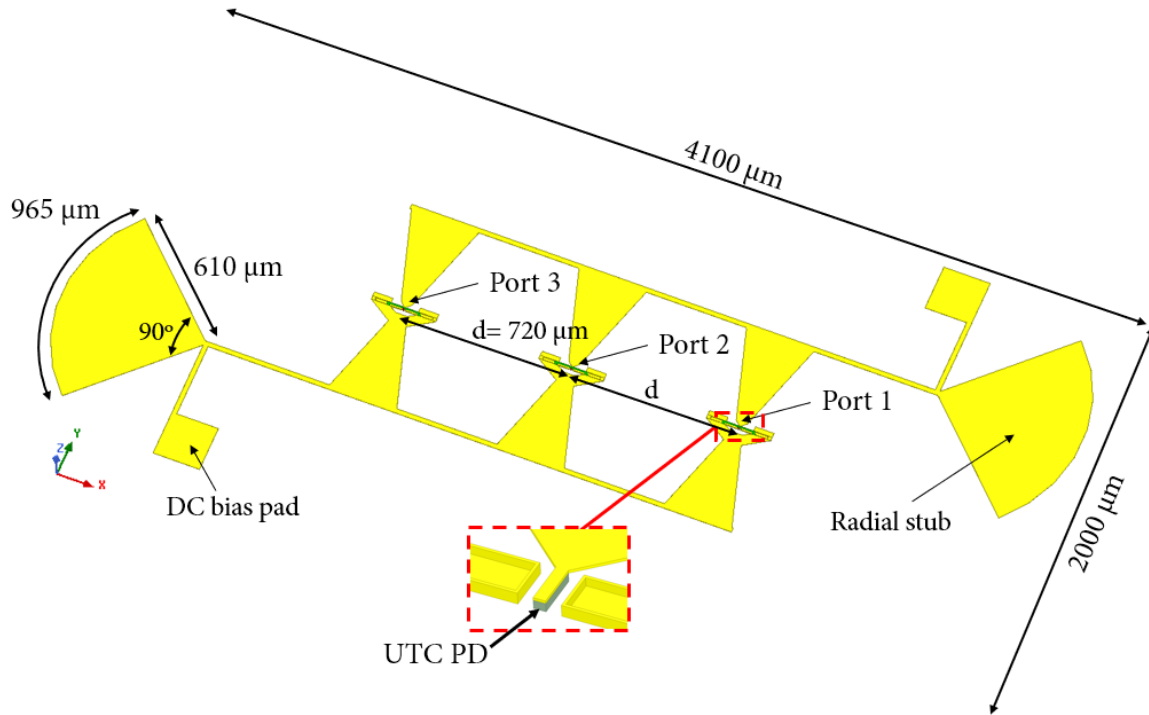


Fig. 4. 69 Overview of the 3x bow-tie antenna-integrated UTC PDs with bias circuit and ports assignment.

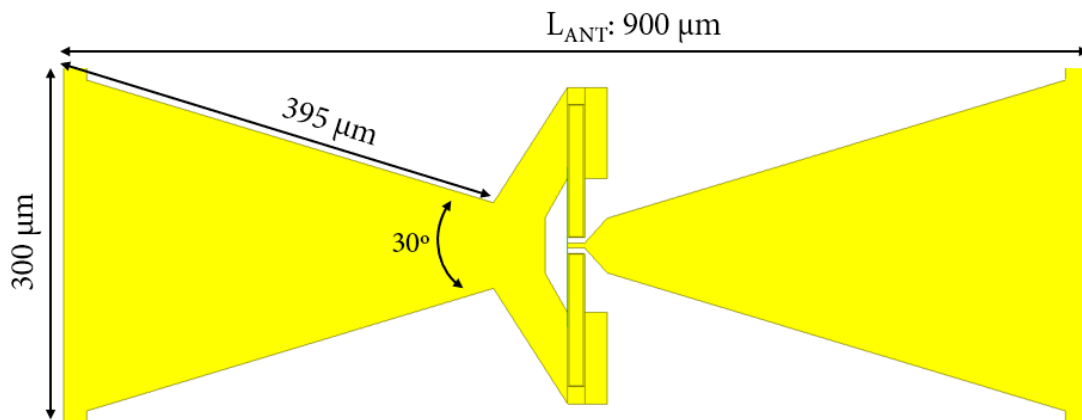


Fig. 4. 70 Dimensions of a single bow-tie antenna-integrated UTC PD.

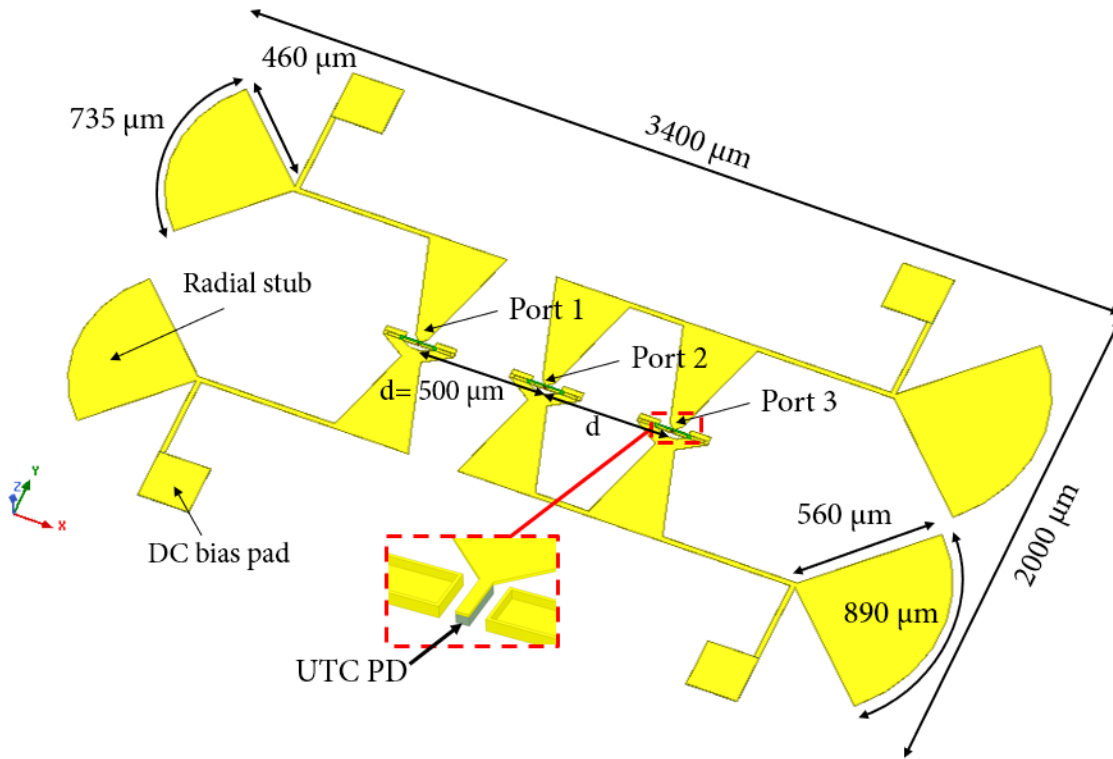


Fig. 4. 71 Overview of the 2x bow-tie and separated 1x bow-tie antenna-integrated UTC PDs with bias circuit and ports assignment.

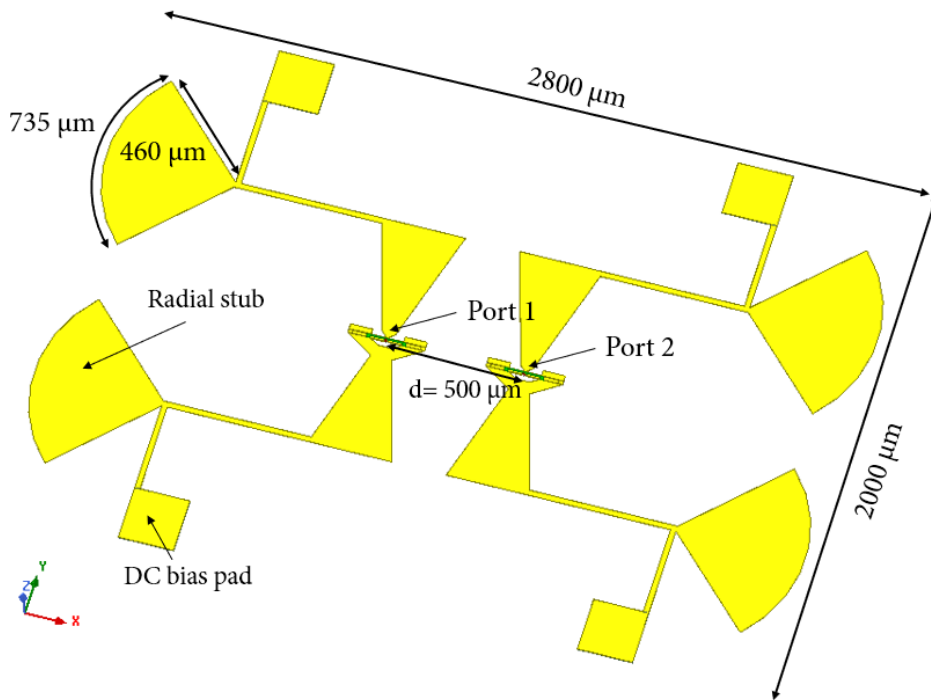


Fig. 4. 72 Overview of the separated 2x bow-tie antenna-integrated UTC PDs with bias circuit and ports assignment.

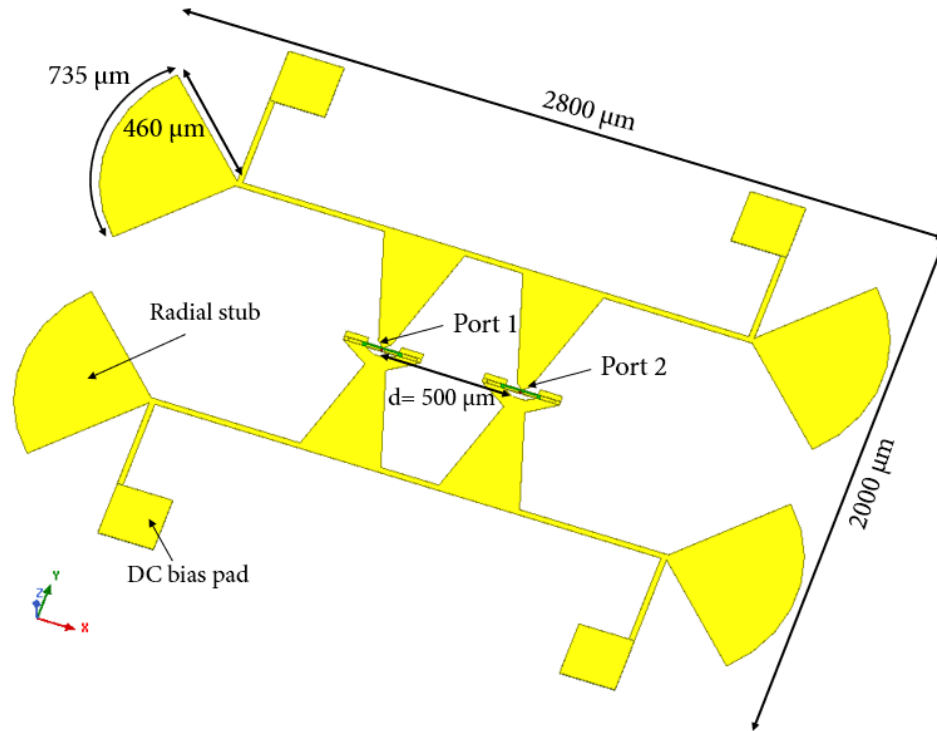


Fig. 4.73 Overview of the connected 2x bow-tie antenna-integrated UTC PDs with bias circuit and ports assignment.

4.4.3.1 3x bow-tie antenna-integrated UTC PDs – simulation results

The s-parameters of the 3x bow-tie antenna-integrated UTC PD device is simulated with the frequency sweep from 30 GHz to 300 GHz. Similar to the previously described simulations, the s-parameters are used to characterize designed circuit in terms of input reflections (S_{11} , S_{22} , S_{33}) according to port assignments presented in Fig. 4.69. Based on the simulation results, several frequency ranges at which input reflection parameters are below -10 dB can be found, as presented in Fig. 4.74 and Fig. 4.75. From 85 GHz up to 156 GHz five smaller frequency ranges can be distinguished. Above 184 GHz and 245 GHz wider frequency bands are found. In total 46 GHz bandwidth is achieved. Based on the simulation results, matching 50 Ω UTC PD impedance with 3x bow-tie antennas is as well a challenging task. Nevertheless, over the entire frequency range, value of the impedance difference is usually lower in comparison to folded-dipole design. It is possible to find several frequencies at which impedance difference is below 10 Ω .

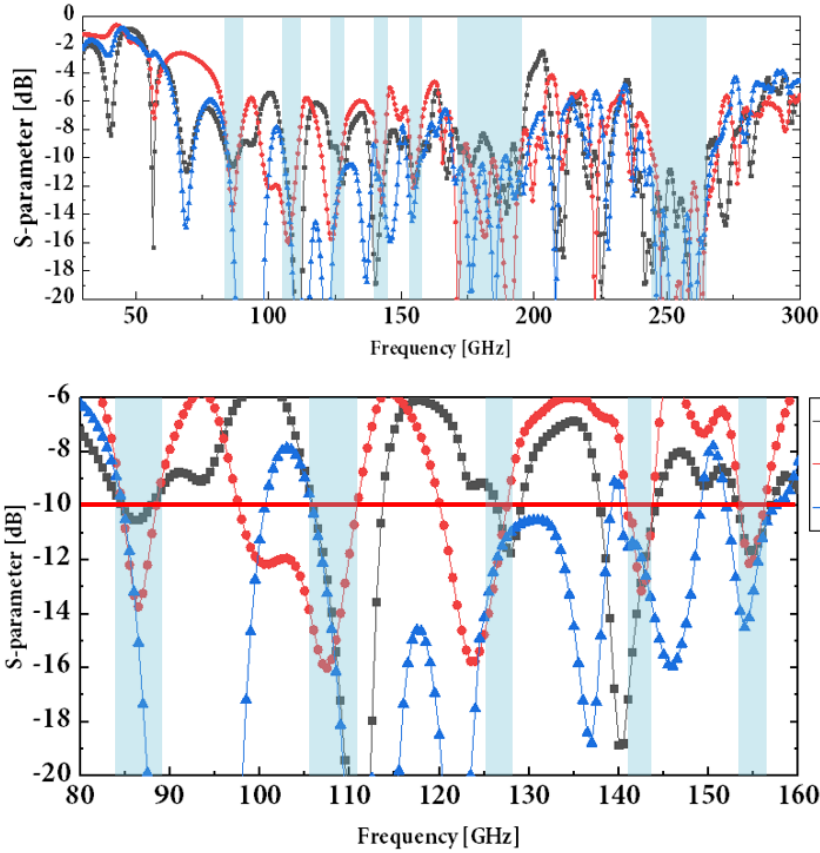


Fig. 4. 74 S-parameters of input reflections for the 3x bow-tie antenna-integrated UTC PD from 30 GHz to 300 GHz and 80 GHz to 160 GHz. Source (port) impedance: 50 Ω .

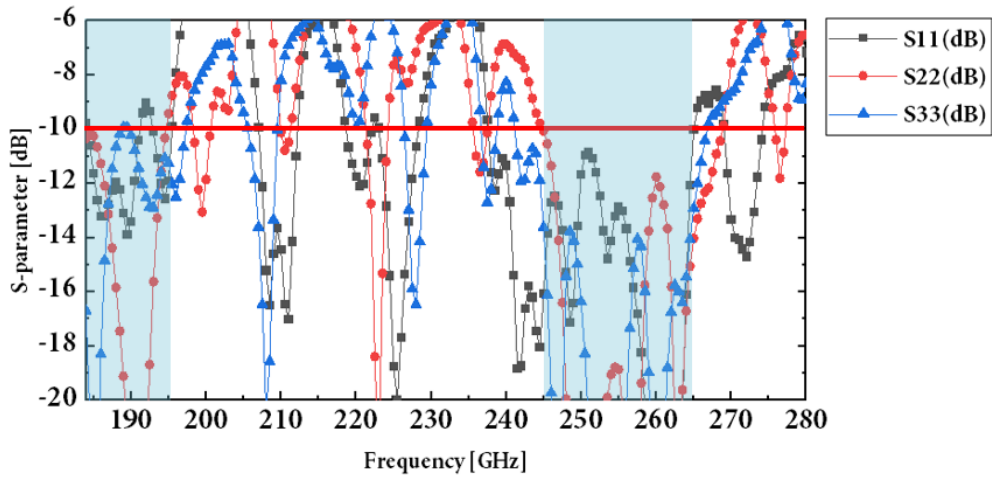


Fig. 4. 75 S-parameters of input reflections for the 3x bow-tie antenna-integrated UTC PD from 180 GHz to 280 GHz. Source (port) impedance: 50 Ω .

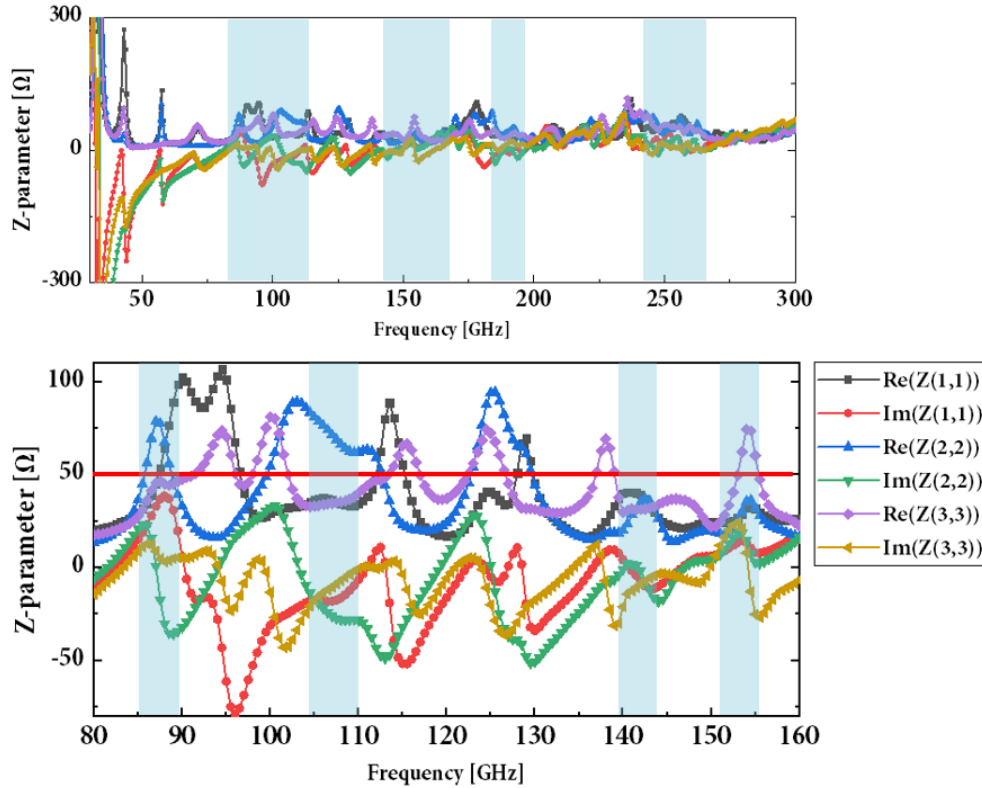


Fig. 4.76 Z-parameters of input reflections for the 3x bow-tie antenna-integrated UTC PD from 30 GHz to 300 GHz and 80 GHz to 160 GHz. Source (port) impedance: 50 Ω .

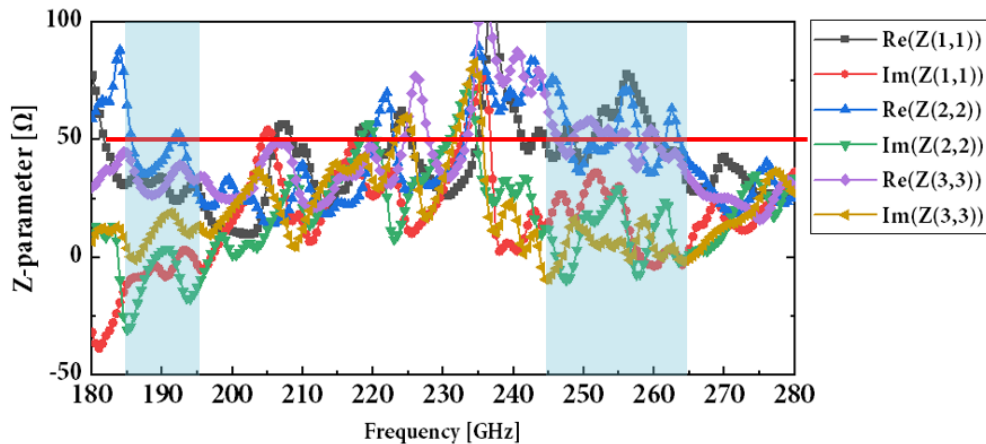


Fig. 4.77 Z-parameters of input reflections for the 3x bow-tie antenna-integrated UTC PD from 180 GHz to 280 GHz. Source (port) impedance: 50 Ω .

Furthermore, examples of radiation pattern are presented from Fig. 4.78 to Fig. 4.80 at 130 GHz, 150 GHz and 250 GHz. Simulation are performed without SI lens. Radiation efficiency is higher in comparison to folded-dipole design. Maximum gain has been achieved at 250 GHz, reaching 5.3 dB. Highest value of FTBR of 4.4 dB is achieved at 110 GHz. Summary of the antenna parameters is given in subchapter 4.4.4.

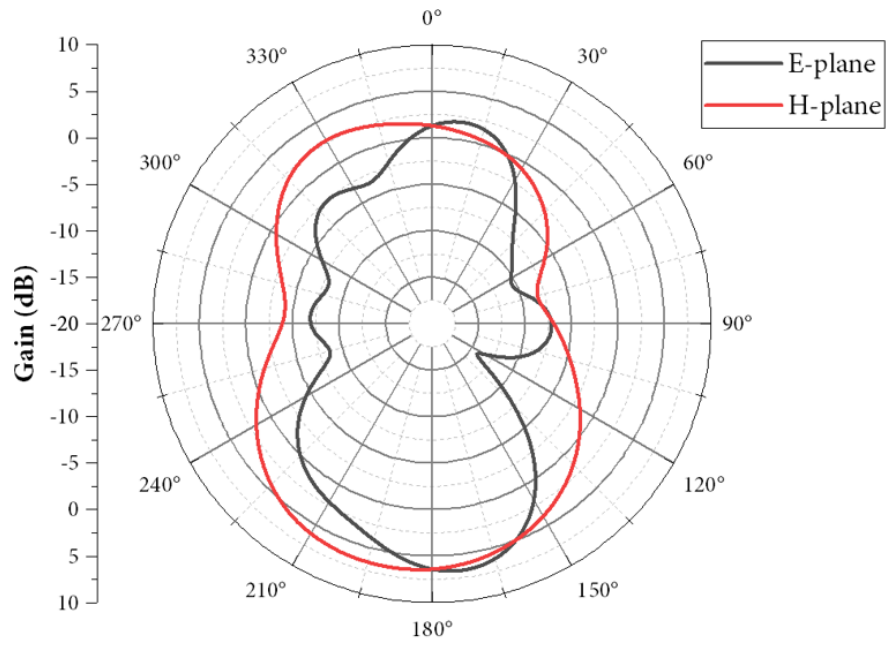


Fig. 4. 78 E-plane and H-plane gain pattern of the 3x bow-tie antenna-integrated UTC PD at 110 GHz.

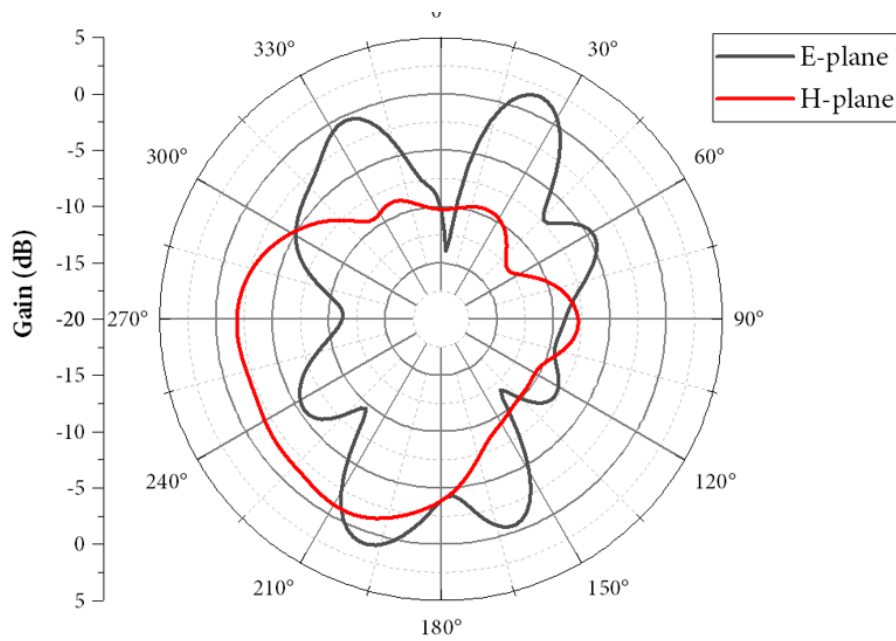


Fig. 4. 79 E-plane and H-plane gain pattern of the 3x bow-tie antenna-integrated UTC PD at 150 GHz.

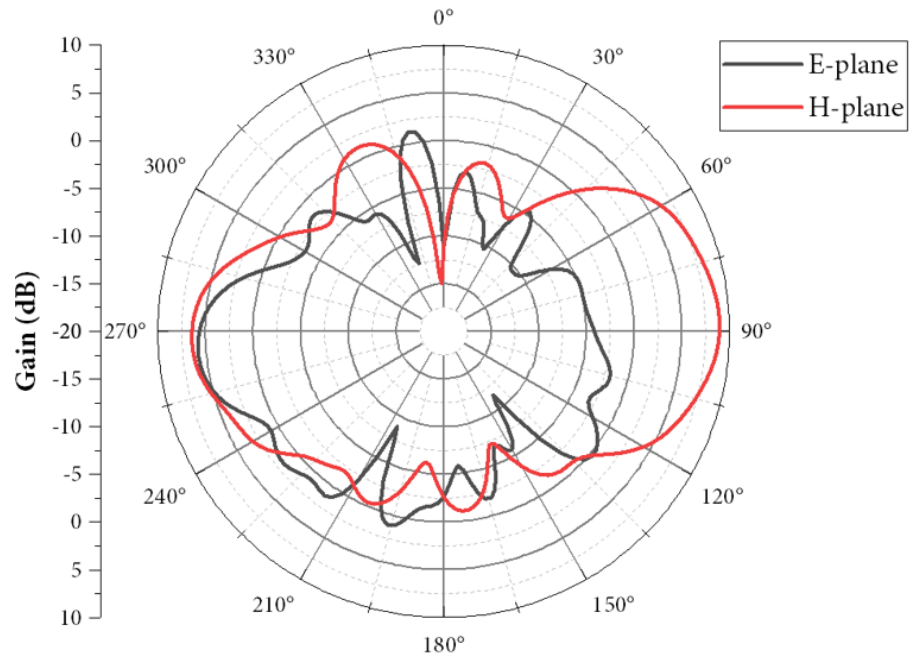


Fig. 4. 80 E-plane and H-plane gain pattern of the 3x bow-tie antenna-integrated UTC PD at 250 GHz.

4.4.3.2 2x bow-tie and separated 1x bow-tie antenna-integrated UTC PD – simulation results

Simulation results for the 2x bow-tie and separated 1x bow-tie antenna-integrated UTC PDs are presented in Fig. 4. 81. As it can be seen, frequency ranges are more localized between 122 GHz up to 174 GHz with two additional bands of 3 GHz at 83 GHz and 250 GHz. Total bandwidth at which input reflections are below -10 dB is about 38 GHz.

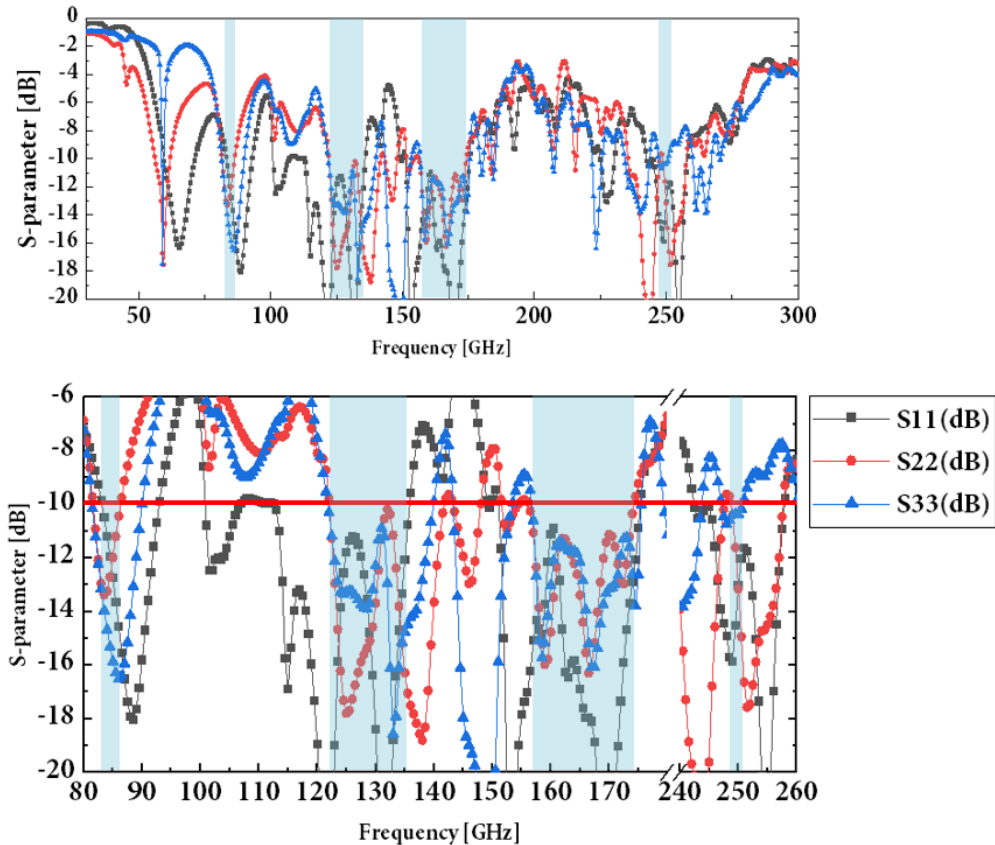


Fig. 4. 81 S-parameters of input reflections for the 2x bow-tie and separated 1x bow-tie antenna-integrated UTC PD from 30 GHz to 300 GHz and 80 GHz to 260 GHz. Source (port) impedance: 50 Ω .

Moreover, impedance matching for this antenna configuration is also more challenging in comparison to 3x bow-tie antenna structure. Nonetheless, for the frequency band between 156 GHz – 174 GHz impedance difference can be found below 10 Ω . Examples of radiation pattern are presented from Fig. 4. 83 to Fig. 4. 85. Radiation efficiency is about 96 %. Highest value of gain of 4.1 dB has been achieved at 130 GHz. Values of FTBR are very comparable over the entire mm-wave frequency range. Summary of the antenna parameters is given in subchapter 4.4.4.

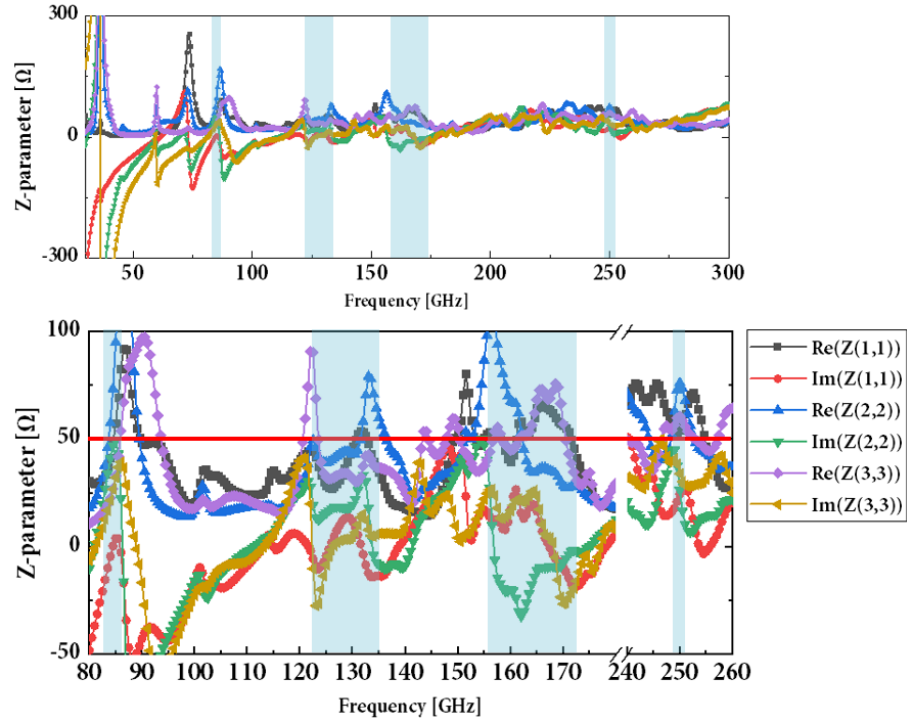


Fig. 4. 82 Z-parameters of input reflections for the 2x bow-tie and separated 1x bow-tie antenna-integrated UTC PD from 30 GHz to 300 GHz and 80 GHz to 260 GHz. Source (port) impedance: 50 Ω.

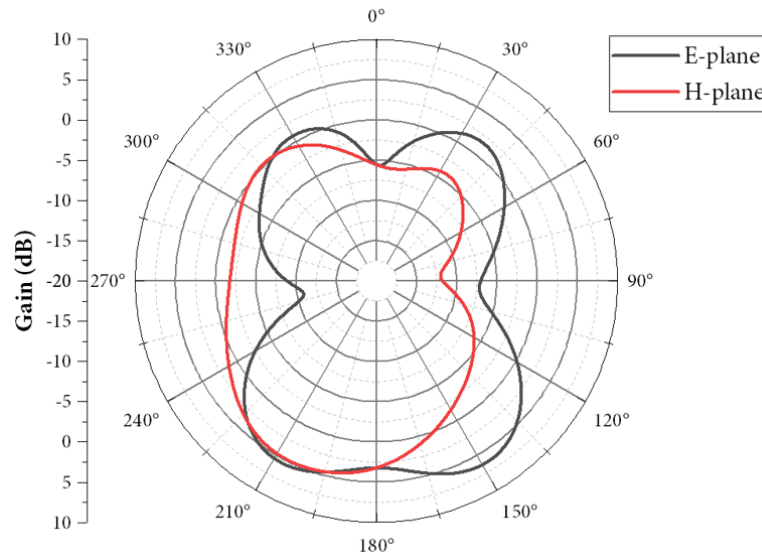


Fig. 4. 83 E-plane and H-plane gain pattern of the 2x bow-tie and 1x separated bow-tie antenna-integrated UTC PD at 110 GHz.

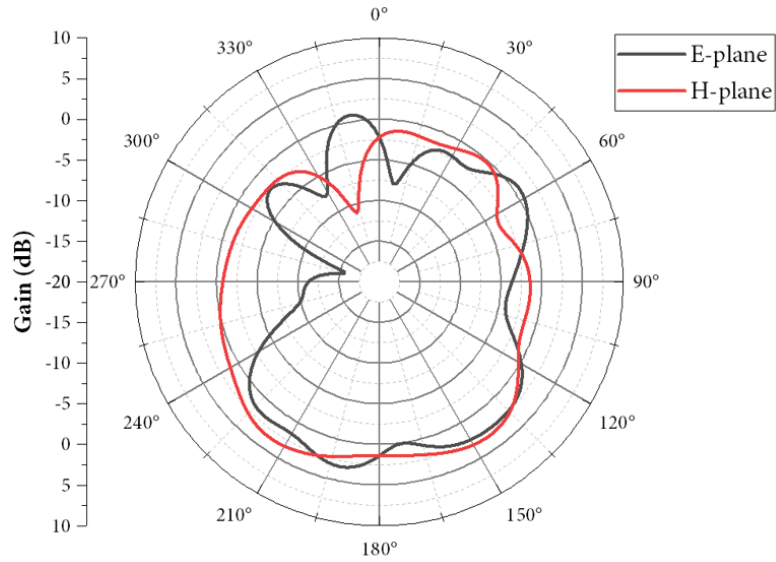


Fig. 4. 84 E-plane and H-plane gain pattern of the 2x bow-tie and 1x separated bow-tie antenna-integrated UTC PD at 150 GHz.

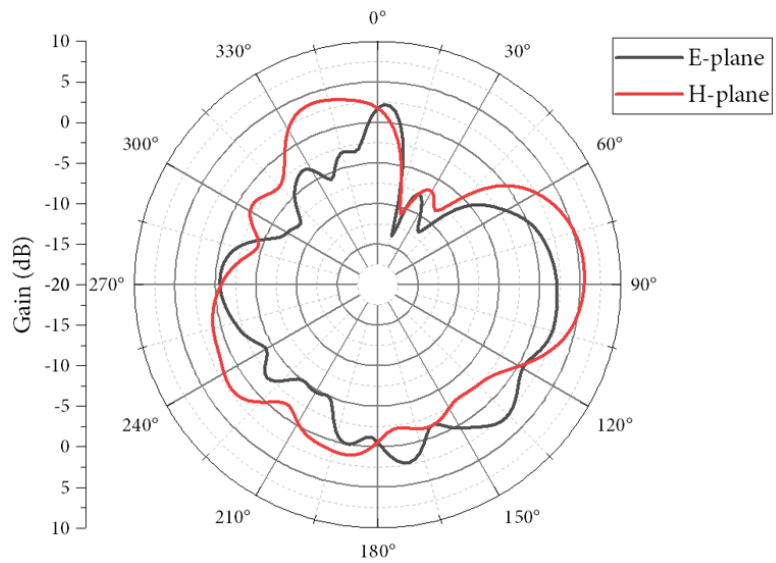


Fig. 4. 85 E-plane and H-plane gain pattern of the 2x bow-tie and 1x separated bow-tie antenna-integrated UTC PD at 250 GHz.

4.4.3.3 Separated and connected 2x bow-tie antenna-integrated UTC PD – simulation results

Simulation results for the structures with 2x bow-tie antennas, separated and connected are presented below. Both configurations are very wide band, resulting in 126 GHz and 119 GHz of bandwidth, for separated and connected configuration, respectively. In both cases, the widest frequency band at which input reflections are below -10 dB are situated between 110 GHz – 180 GHz. Moreover, simulation results of the impedance values are similar for both of the structure. The impedance values are in better match condition to 50 Ω in comparison to other antenna configurations.

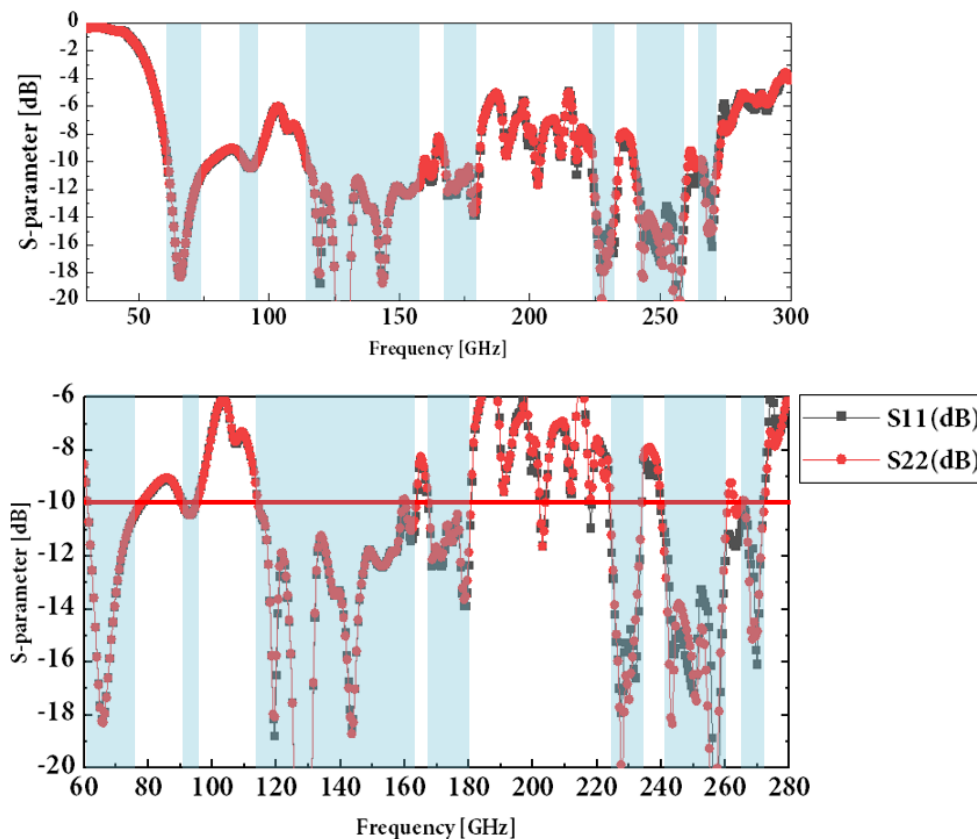


Fig. 4. 86 S-parameters of input reflections for the separated 2x bow-tie antenna-integrated UTC PD from 30 GHz to 300 GHz and from 60 GHz to 280 GHz. Source (port) impedance: 50 Ω .

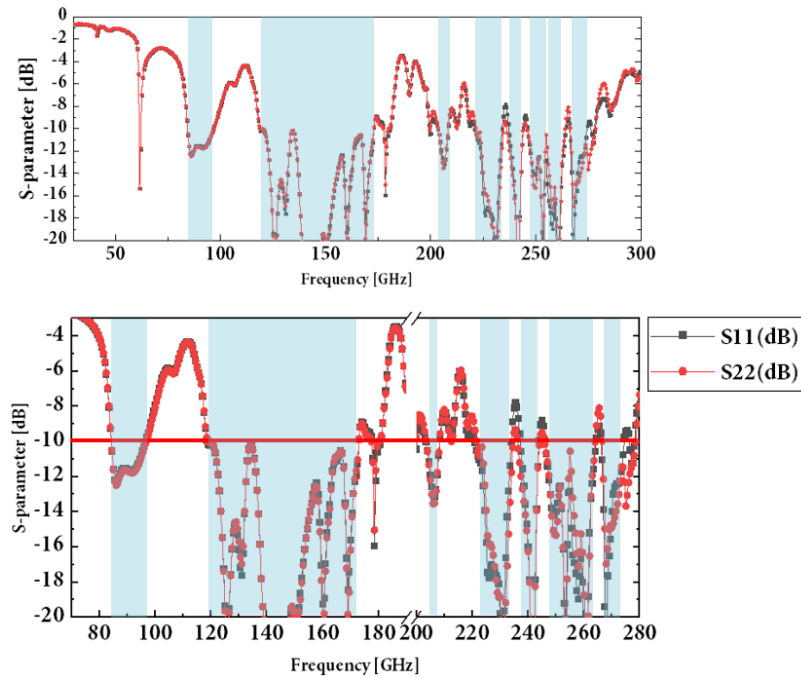


Fig. 4. 87 S-parameters of input reflections for the connected 2x bow-tie antenna-integrated UTC PD from 30 GHz to 300 GHz and from 70 GHz to 280 GHz. Source (port) impedance: 50Ω .

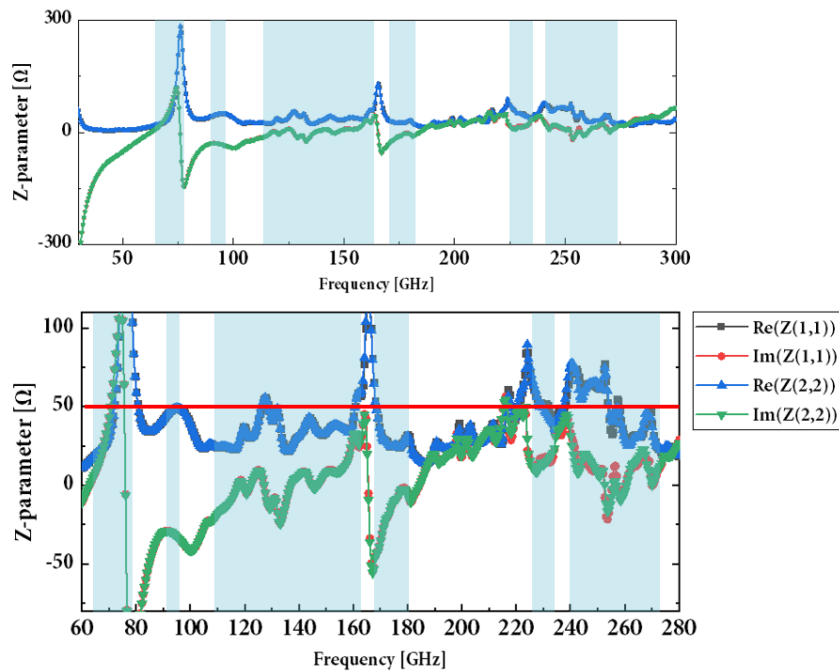


Fig. 4. 88 Z-parameters of input reflections for the separated 2x bow-tie antenna-integrated UTC PD from 30 GHz to 300 GHz and 60 GHz to 280 GHz. Source (port) impedance: 50Ω .

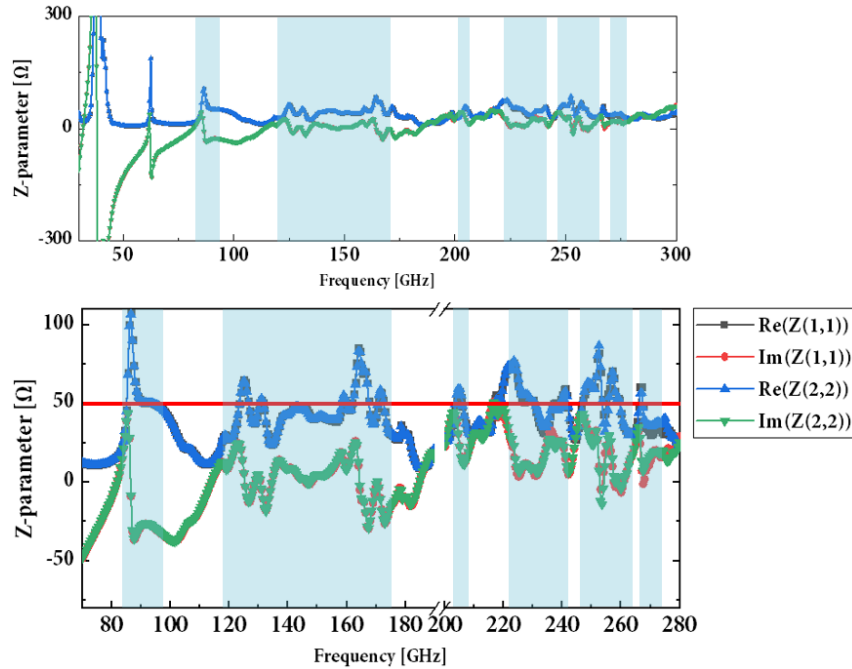


Fig. 4. 89 Z-parameters of input reflections for the connected 2x bow-tie antenna-integrated UTC PD from 30 GHz to 300 GHz and 70 GHz to 280 GHz. Source (port) impedance: 50 Ω .

Examples of radiation pattern are presented in Fig. 4. 90 - Fig. 4. 95 for both type of antenna configuration. As can be observed, radiation patterns at 130 GHz are very similar, but with increasing frequency the differences become bigger. For both designs the radiation efficiency is at the same level of ca. 94 %. Moreover, values of gain are comparable, although the highest value is obtained at 250 GHz for the separated antenna design. Values of the impedance are usually below 50 Ω . Summary of the antenna parameters is given in subchapter 4.4.4.

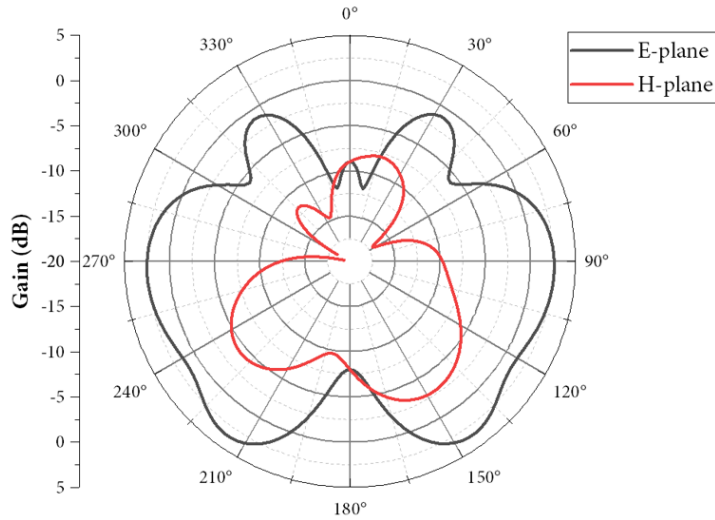


Fig. 4. 90 E-plane and H-plane gain pattern of the separated 2x bow-tie antenna-integrated UTC PD at 130 GHz.

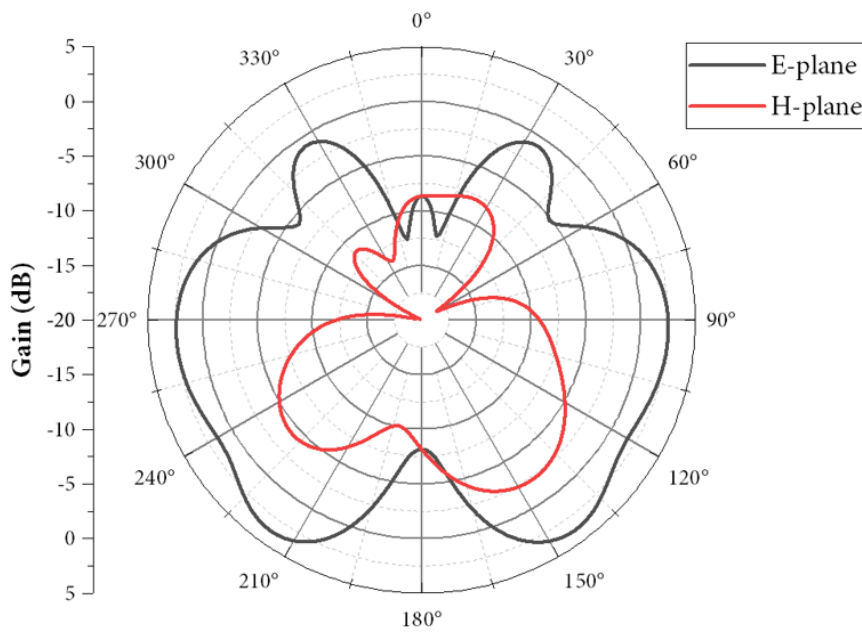


Fig. 4. 91 E-plane and H-plane gain pattern of the connected 2x bow-tie antenna-integrated UTC PD at 130 GHz.

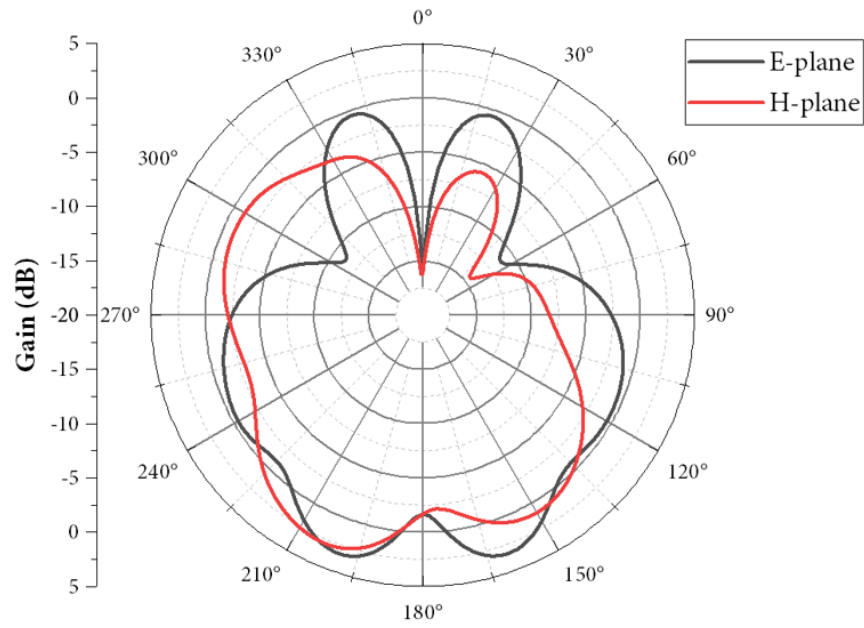


Fig. 4. 92 E-plane and H-plane gain pattern of the separated 2x bow-tie antenna-integrated UTC PD at 150 GHz.

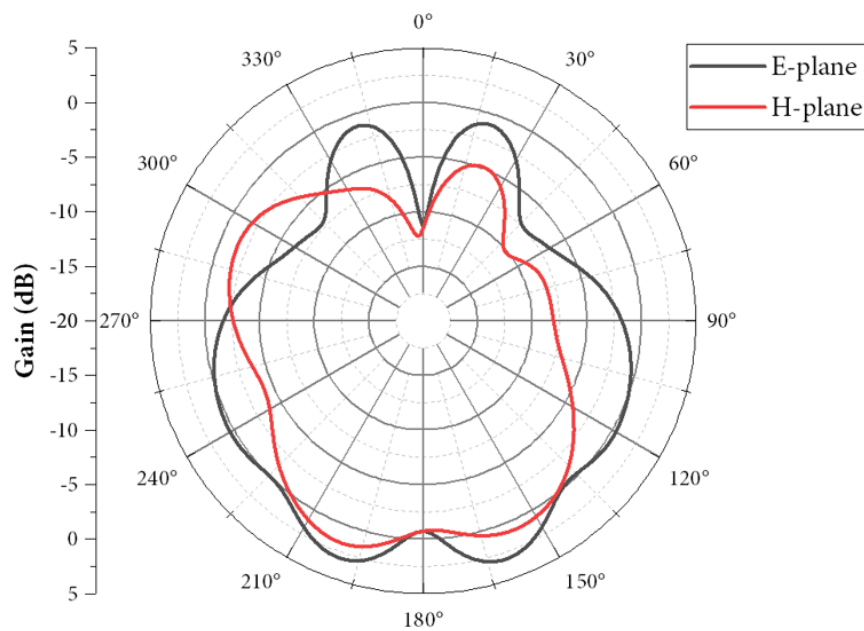


Fig. 4. 93 E-plane and H-plane gain pattern of the connected 2x bow-tie antenna-integrated UTC PD at 150 GHz.

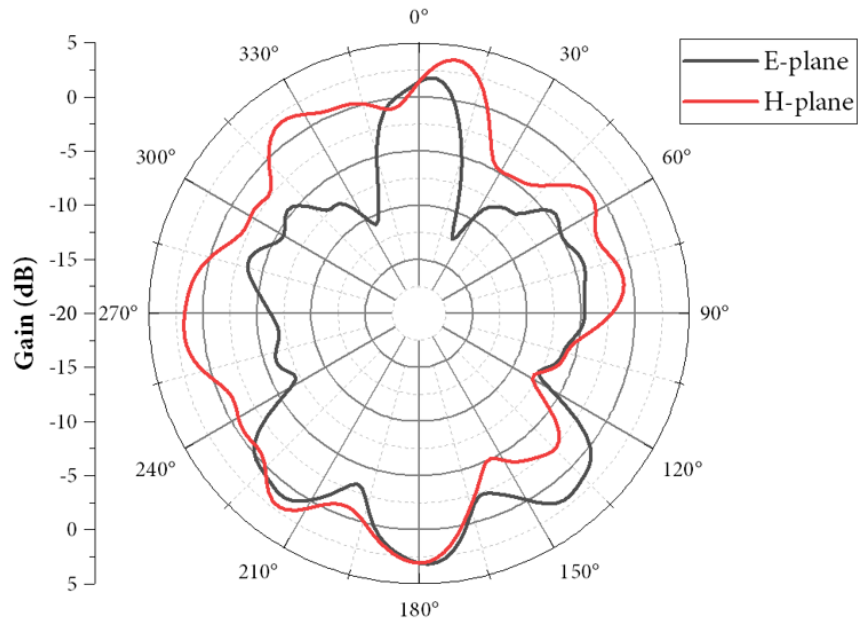


Fig. 4. 94 E-plane and H-plane gain pattern of the separated 2x bow-tie antenna-integrated UTC PD at 250 GHz.

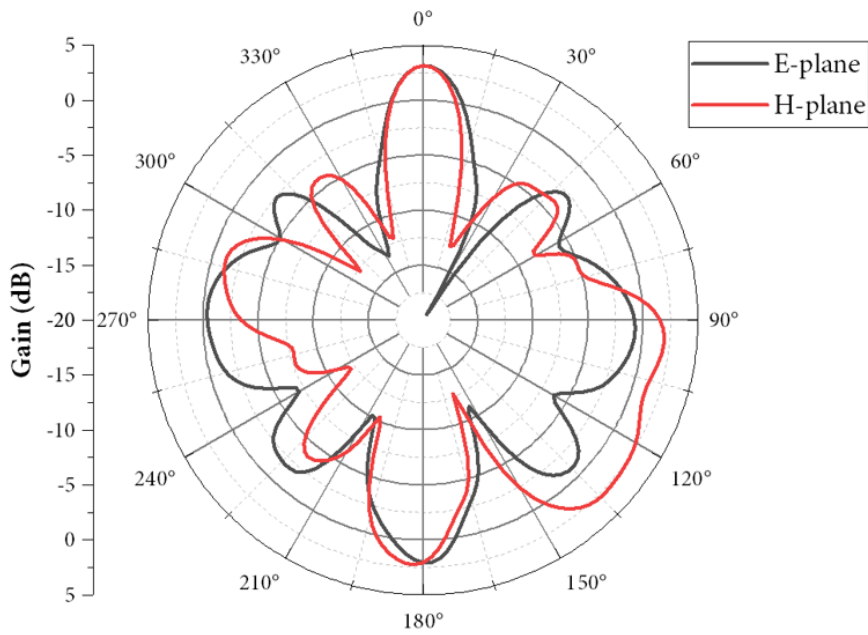


Fig. 4. 95 E-plane and H-plane gain pattern of the connected 2x bow-tie antenna-integrated UTC PD at 250 GHz.

4.4.4 Antenna-integrated UTC PDs – summary

Detailed comparison of the antenna parameters for all previously described configurations are presented in Fig. 4. 96 and Fig. 4. 97. As already mentioned, the biggest bandwidths are achieved for the separated and connected 2x bow-tie antennas of 126 GHz and 119 GHz, respectively. The folded-dipole antenna design is the most narrow-band in comparison to other design, with estimated bandwidth of 22 GHz. The 3x bow-tie antenna-integrated UTC PDs has much bigger bandwidth of 46 GHz. Moreover, values of radiation efficiency for folded-dipoles are the lowest, but FTBR of 15 dB is the highest obtained value compared to all the designs. Radiation efficiency for all of the proposed design is very high, and generally above 90 %. Furthermore, based on the simulation results, impedance match to 50 Ω is very challenging. The best impedance match to 50 Ω is achieved for the 2x bow-tie antennas. The highest value of gain for 3x folded-dipole antenna of 5.9 dB is achieved at 95 GHz. For the 3x bow-tie antenna design, the gain of 5.3 dB is obtained at 250 GHz. The gain of 2x bow-tie is generally below 2 dB, and is the lowest in comparison to other structures.

	Antenna structure		
	3 x folded-dipole	3 x bow-tie	2 x bow-tie separated 1 x bow-tie
Bandwidth [GHz]	ca. 22	ca. 46	ca. 38
Reflection coefficients ($s_{11}/s_{22}/s_{33}$) <-10 dB	95 GHz – 100 GHz 185 GHz – 192 GHz 203 GHz – 210 GHz 293 GHz – 296 GHz	85 GHz – 88 GHz 105 GHz – 110 GHz 140 GHz – 144 GHz 153 GHz – 156 GHz 184 GHz – 195 GHz 245 GHz – 265 GHz	83 GHz – 86 GHz 122 GHz – 136 GHz 156 GHz – 174 GHz 247 GHz – 250 GHz
Radiation efficiency [%]	@95 GHz: 96 @190 GHz: 93 @95 GHz: 96* @190 GHz: 93*	@110 GHz: 96 @150 GHz: 96 @250 GHz: 95	@110 GHz: 96 @150 GHz: 96 @250 GHz: 96
Gain [dB]	@95 GHz: 4.7 @190 GHz: 3.7 @95 GHz: 4.9* @190 GHz: 6*	@110 GHz: 3.8 @150 GHz: 1.1 @250 GHz: 5.3	@130 GHz: 4.1 @150 GHz: 1.9 @250 GHz: 3.1
Radiated power/ Accepted power [mW] System power: 3 mW	@95 GHz: 2.6/2.7 @190 GHz: 2/1.9 @95 GHz: 2.7*/2.6* @190 GHz: 2.8*/2.6*	@110 GHz: 2.3/2.4 @150 GHz: 2.2/2.3 @250 GHz: 1.9/2	@130 GHz: 2.8/2.9 @150 GHz: 2.5/2.6 @250 GHz: 2.5/2.6
Front to Back Ratio [dB]	@95 GHz: 4 @190 GHz: 11 @95 GHz: 14* @190 GHz: 15*	@110 GHz: 4.4 @150 GHz: 1.3 @250 GHz: 1.8	@130 GHz: 3.6 @150 GHz: 2.6 @250 GHz: 3.6
Impedance [Ω]	@95 GHz: $Z_{11}=55 - 35i$ $Z_{22}=37 - 36i$ $Z_{33}=61 - 33i$ @190 GHz: $Z_{11}=56 - 13i$ $Z_{22}=45 + 3i$ $Z_{33}=84 - 23i$	@110 GHz: $Z_{11}=34 - 6i$ $Z_{22}=62 - 28i$ $Z_{33}=40 - 0.4i$ @150 GHz: $Z_{11}=25 + 6i$ $Z_{22}=20 + 4i$ $Z_{33}=21 + 0.8i$ @250 GHz: $Z_{11}=41 + 27i$ $Z_{22}=41 + 16i$ $Z_{33}=56 + 11i$	@110 GHz: $Z_{11}=47 + 11i$ $Z_{22}=43 + 19i$ $Z_{33}=31 + 4.6i$ @150 GHz: $Z_{11}=52 + 40i$ $Z_{22}=38 + 35i$ $Z_{33}=55 + 4.2i$ @250 GHz: $Z_{11}=54 + 24i$ $Z_{22}=76 + 26i$ $Z_{33}=60 + 34i$

*results with time delay compensation

Fig. 4. 96 Comparison between the simulated parameters of 3x folded-dipole, 3x bow-tie and 2x bow-tie separated 1x bow-tie antenna-integrated UTC PDs structures.

	Antenna structure	
	2 x bow-tie separated	2 x bow-tie connected
Bandwidth [GHz]	ca. 126	ca. 119
Reflection coefficients (s_{11}/s_{22}) <-10 dB	61 GHz – 78 GHz 90 GHz – 95 GHz 114 GHz – 163 GHz 167 GHz – 180 GHz 224 GHz – 234 GHz 240 GHz – 272 GHz	84 GHz – 97 GHz 119 GHz – 173 GHz 203 GHz – 208 GHz 221 GHz – 234 GHz 237 GHz – 243 GHz 246 GHz – 264 GHz 266 GHz – 274 GHz
Radiation efficiency [%]	@130 GHz: 93 @150 GHz: 94 @250 GHz: 95	@130 GHz: 93 @150 GHz: 95 @250 GHz: 94
Gain [dB]	@130 GHz: 1.6 @150 GHz: 1.9 @250 GHz: 2.3	@130 GHz: 1.7 @150 GHz: 1.9 @250 GHz: 1.8
Radiated power/ Accepted power [mW] System power: 2 mW	@130 GHz: 1.3/1.4 @150 GHz: 1.7/1.8 @250 GHz: 1.8/1.9	@130 GHz: 1.3/1.4 @150 GHz: 1.8/1.9 @250 GHz: 1.6/1.7
Front to Back Ratio [dB]	@130 GHz: 3 @150 GHz: 2.4 @250 GHz: 1.5	@130 GHz: 3 @150 GHz: 2.7 @250 GHz: 1.3
Impedance [Ω]	@130 GHz: $Z_{11}=Z_{22}=41 - 12i$ @150 GHz: $Z_{11}=34 + 9i$ $Z_{22}=34 + 8i$ @250 GHz: $Z_{11}=64 + 8i$ $Z_{22}=64 + 6i$	@130 GHz: $Z_{11}=46 + 4i$ $Z_{22}=46 + 5i$ @150 GHz: $Z_{11}=41 + 4i$ $Z_{22}=47 + 5i$ @250 GHz: $Z_{11}=62 + 27i$ $Z_{22}=62 + 24i$

Fig. 4. 97 Comparison between the simulated parameters of separated and connected 2x bow-tie antenna-integrated UTC PDs structures.

To conclude:

- **Folded-dipole antennas, as expected and based on the simulation results, are more narrowband in comparison to bow-tie antenna designs. The total bandwidth is about 22 GHz.**
- **Impedance matching to 50 ohms is a challenging task for the array design, but the simulated values are in a good matching condition in the dedicated frequency bands.**
- **Moreover, the folded-dipole design has the highest value of FTBR among the design antennas, which confirms directional behaviour (see Fig. 4. 67).**
- **Gain levels as presented in the summary in Fig. 4. 96 are higher in comparison to bow-tie antenna design.**
- **The 3x bow-tie antenna design has ca. 46 GHz of bandwidth, which is almost double in comparison to 3x folded-dipole design. The impedance matching to 50 ohms, based on the simulated values, is in a good matching condition in the dedicated frequency bands.**
- **Based on the radiation patterns, as presented in Fig. 4. 78 - Fig. 4. 80, the 3x bow-tie design is less directional than the 3x folded-dipole design.**
- **The 2x bow-tie and 1x bow-tie with two separate optical inputs achieved 38 GHz of bandwidth. The impedance matching to 50 ohms, based on the simulated values, is in a good match condition for the dedicated frequency bands.**
- **The 2x bow-tie separated and connected design achieved 119 and 126 GHz of bandwidth, respectively, which is the widest bandwidth among all of the designs. Impedance matching to 50 ohms, based on the simulated values is in a good match condition for the dedicated frequency bands.**
- **The radiation patterns of the bow-tie designs are generally less directional in comparison to 3x folded-dipole design.**

4.5 OPTICAL DESIGN AND SIMULATIONS

The objective of this subchapter is to present passive optical waveguides, S-bends and MMIs that are employed in the power combiners and antenna-based topologies presented in the previous subchapters. Optical design was performed with FIMMWAVE Photon Design and RSoft Photonics BeamProp software. Prior the simulation results, a very brief theoretical introduction is given, as detailed explanation of the applied Maxwell's equations in the optical waveguide design can be found in the dedicated literature [37][38][39].

4.5.1 Passive optical waveguides – introduction

Total internal reflection is one the most fundamental concept utilized in the optical communication systems [37]. For a planar waveguide presented in Fig. 4. 98, the refractive index of the film layer (n_f) is higher than the refractive index of the substrate (n_s) and the cover (n_c) and usually n_s is higher than n_c .

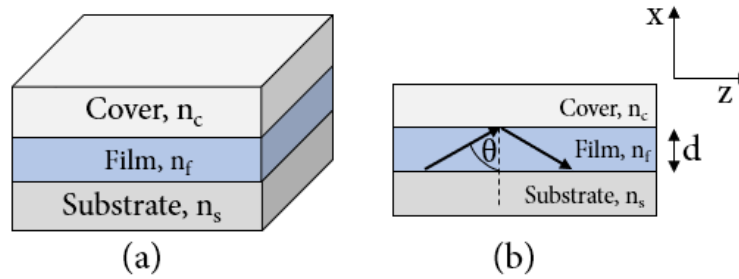


Fig. 4. 98 Asymmetric planar waveguide (a) and (b) zig-zag trajectory of a ray inside the film layer.

The critical angles which define total internal reflection for cover-film interface (θ_{1c}) and film-substrate (θ_{2c}) can be described by [37]:

$$\theta_{1c} = \arcsin \left(\frac{n_c}{n_f} \right) \quad (4.26)$$

$$\theta_{2c} = \arcsin \left(\frac{n_s}{n_f} \right) \quad (4.27)$$

For $n_f > n_s > n_c$, the critical angles follow the relation $\theta_{2c} > \theta_{1c}$ and depending on the angle θ , we can distinguish three situations:

1. $\theta < \theta_{1c}$, in that state, the ray penetrates the cover and the substrate, as the radiation is not confined to the film layer and this condition is referred as radiation modes.

2. $\theta_{1c} < \theta < \theta_{2c}$, in this situation light is totally reflected at the cover-film interface, but it can enter the substrate. This is referred as substrate radiation modes or substrate modes.
3. $\theta_{2c} < \theta < \frac{\pi}{2}$, this state is the most relevant case in the integrated optics as it corresponds to guided mode. The light is confined in the film layer and it does not enter the cover nor the substrate.

Furthermore, as the ray pass round trip inside the film (Fig. 4. 98b), the transversal phase shift appears that correspond to the layer thickness d , and additional phase shifts is caused by total internal reflection at the two boundaries (cover and substrate) [37]. The condition for the guided modes is established on constructive interference for which only a discreet number of angles fulfils it and the total transversal phase shift in a round trip is an integral number of 2π . The self-consistency condition (or transversal resonance condition) for constructive interference in asymmetric planar waveguides can be expressed by:

$$2k_0n_f d \cos\theta - \phi_c - \phi_s = 2\pi m, \quad (4.28)$$

where m is the mode order, k_0 is the wavevector, ϕ_c and ϕ_s are the phase shifts at the upper and lower boundaries, and $\phi = 2k_x d = 2k_0n_f d \cos\theta$. The propagation constant of the mode β_m is the component of the wavevector along the propagation direction and the relation with the propagation angle can be described as:

$$\beta_m = k_0n_f d \sin\theta_m \quad (4.29)$$

Ray optics approach is used for the qualitative description of light behaviour, such as type of modes, number of modes and propagation constant, but it does not provide the information about optical fields or intensity distribution [38]. Dielectric waveguides that find application in the most of integrated photonics designs can be classified into five types of structures presented in Fig. 4. 99. Structure (a) from figure Fig. 4. 99 can be referred as a two-dimensional waveguide (2D), for which properties of fields distribution and index profiles can be calculated in a closed form and the waveguide width (y-direction) is treated as infinitely large [38]. As a consequence, guided fields in 2D can be classified as transverse electric (TE) or transverse magnetic (TM) modes. For the three-dimensional (3D) structures with rectangular boundaries (Fig. 4. 99a-4.96e) guided fields are confined in the y-direction as well, and as a result the guided modes are not pure TE or TM but can be generally described as hybrid modes [38][39]. Based on method published by Goell [40], hybrid modes can be labelled by the strong transverse electric field component. If the dominant electric field component is in the x direction (or y) and if the electric field distribution has $p-1$ nulls in the x direction and $q-1$ nulls in the y direction, the hybrid mode can be identified as E_{pq}^x or E_{pq}^y , where the superscript

denotes dominant transverse electric field component. Analysis of the 3D waveguides fields is very complicated and special techniques have been developed in order to approximate the results. Some of the most utilized methods are the Marcanti's and the effective index method [38][41]. In the first method the 3D waveguide is replaced by two 2D waveguides.

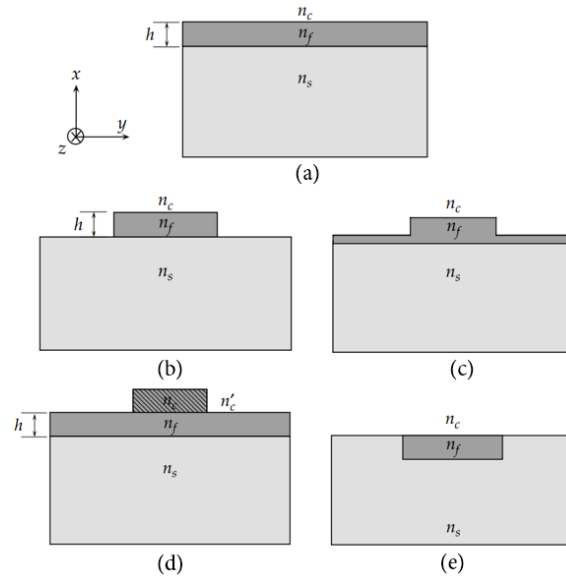


Fig. 4. 99 Types of the most common dielectric waveguides: (a) thin film waveguide, (b) raised strip or channel waveguide, (c) ridge or rib waveguide, (d) strip-loaded waveguide, (e) buried or embedded strip waveguide [38].

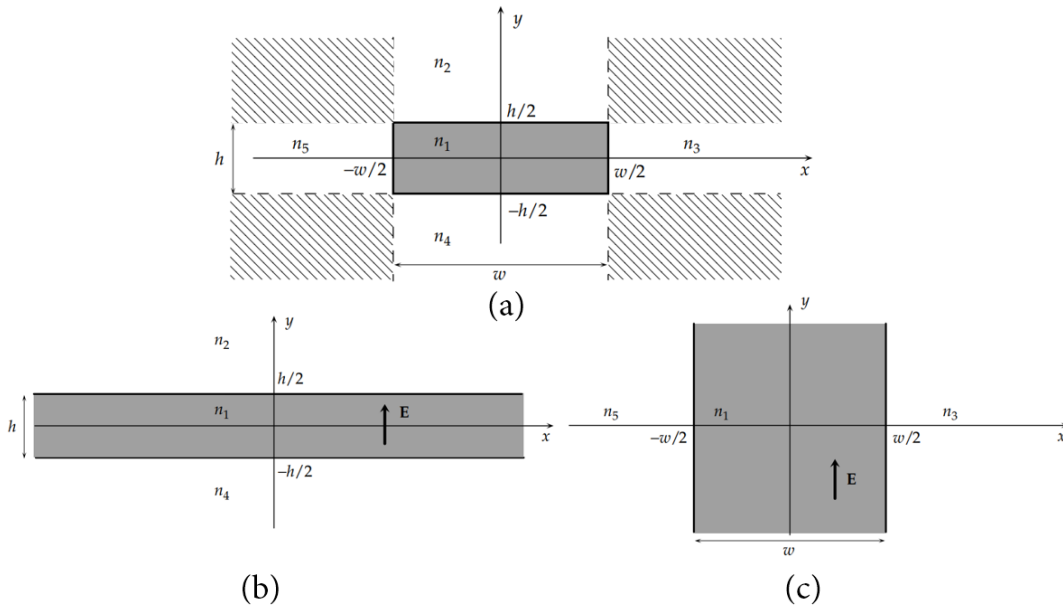


Fig. 4. 100 Example model used for analysis of (a) a rectangular waveguide, (b) waveguide h , and (c) waveguide w [38].

As presented in Fig. 4. 100, fields in the corners are ignored and the two 2D waveguides are solved independently. In the effective index method approach the 2D waveguides are related. Waveguide h, as depicted in Fig. 4. 100b, is solved firstly to obtain effective index n_{eff} which is then used to define second waveguide w (Fig. 4. 100c). The propagation constant of waveguide w is an approximation for the original 3D waveguide [37][38]. Another commonly used method to calculate photonic integrated devices is Beam Propagation Method based on finite differences. More details can be found in [38] and [43].

4.5.2 Ridge optical waveguides and S-bends – design and simulation results

Simplified structure of optical waveguide investigated in the circuits design for single UTC PDs, power combiners and antenna-integrated devices is presented in Fig. 4. 101. Ridge and deep ridge structure type of optical waveguides have been initially investigated and simulated. The optical waveguide core is composed of 300 nm of InGaAsP. Moreover, as the cover (cladding) thickness is reduced to 1.2 μm of InP due to reduced availability of other substrates at the time of fabrication, it has been a challenging task to design compact S-bends necessary for the circuit's design. Too sharp angle of S-bend could result in a big loss or even complete lack of light propagation. Another obstacle faced during the design of S-bends were the substantial dimensions of the structures needed for the final fabrication process. Top view of UTC PD with straight optical waveguide is presented in Fig. 4. 102. Dimension of the optical waveguide have been optimized to obtain single mode behaviour. In both programs, similar values of the effective refractive index of 3.191 and 3.188 are calculated for ridge and deep ridge structure, respectively. Moreover, in both types of optical waveguides, mode propagation is well confined. Example of the structure definition used for calculation of mode propagation in deep ridge structure can be seen in Fig. 4. 103 and Fig. 4. 104. Very comparable simulation results are obtained for both type of structure with a straight waveguide of 2000 μm length (Fig. 4. 105).

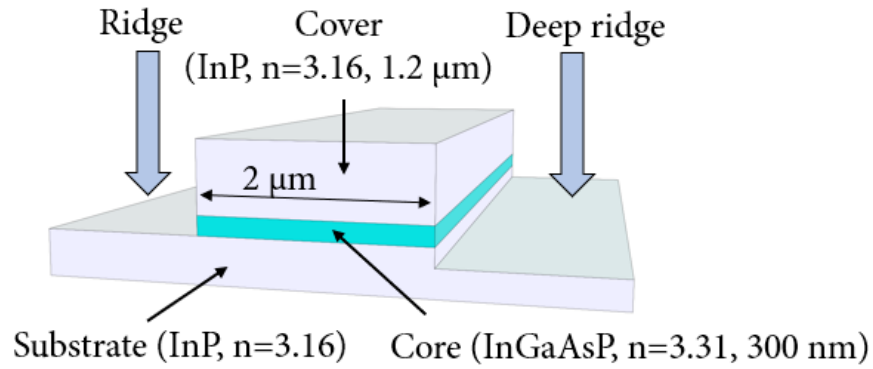


Fig. 4. 101 Simplified ridge and deep ridge passive optical waveguide structure with material and thickness parameters used for the simulations.

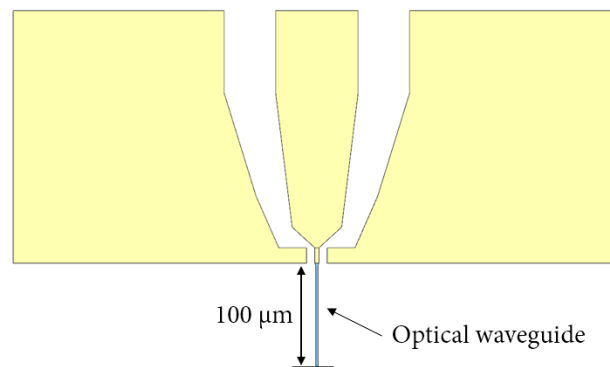


Fig. 4. 102 Top view of the UTC PD with a straight optical waveguide structure.

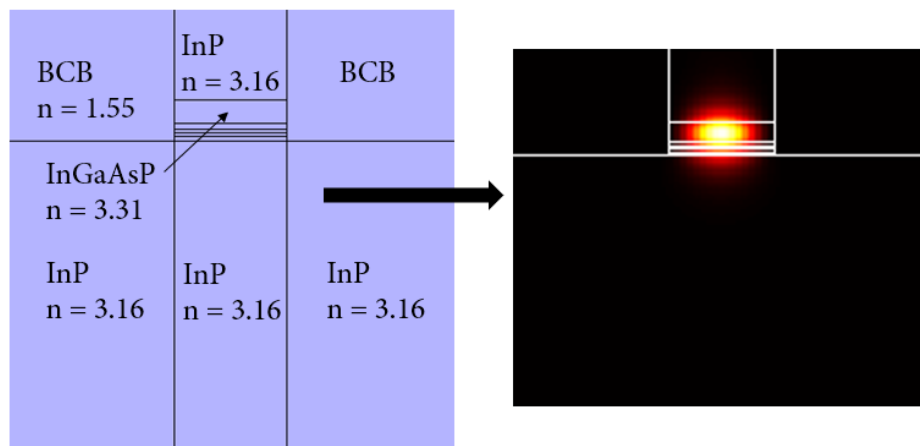


Fig. 4. 103 Example of the deep ridge optical waveguide definition used in FIMMWAVE and overview of propagated mode inside the structure.

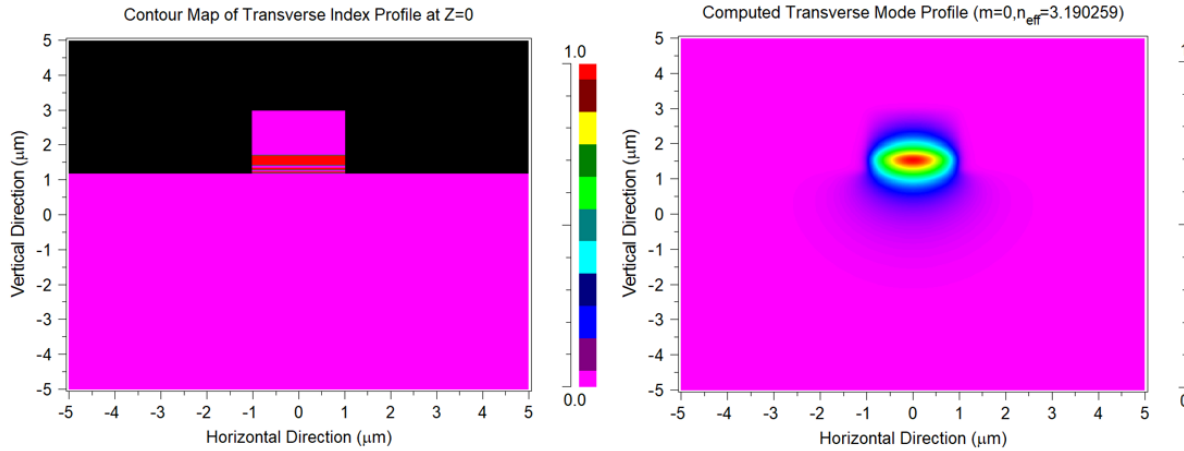


Fig. 4.104 Example of deep ridge optical waveguide definition used in BeamPROP and overview of propagated mode inside the structure.

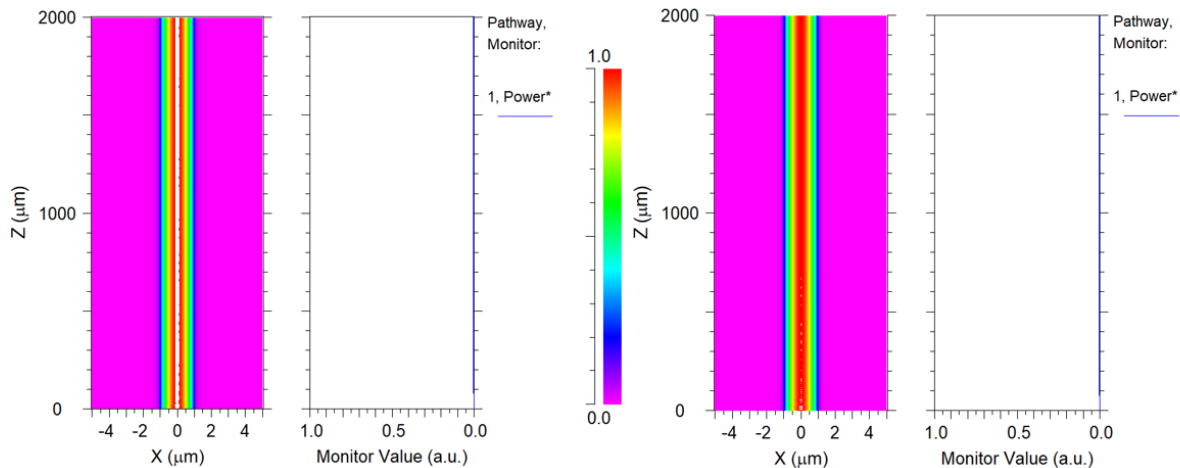


Fig. 4.105 Comparison between simulation results for the ridge (left) and the deep ridge (right) optical waveguides with 2000 μm .

Furthermore, simulation of the coupling from optical waveguide towards UTC PD structure have been as well investigated for all of the UTC widths. In Fig. 4.106 simulation of light coupled from ridge optical waveguide to UTC PD absorber layer (InGaAs) is presented. It can be seen that part of the light is successfully absorbed inside the InGaAs layer of the UTC PD structure. Contour plots of a cross-section for optical waveguide and UTC PD are shown as well. Additional contour plots at the edge and inside the UTC PD L2W3 are presented in Fig. 4.107 where light absorption inside InGaAs layer is clearly observed. Moreover, a confinement factor (Γ) has been calculated, based on the simulations, in the absorber region at fixed UTC length (15 μm) with the width variable from 2 μm to 5 μm for the modes propagating inside this region. This parameter gives the information about the ratio of power confined in the absorber to the total power. Obtained values are presented in Fig. 4.108. For

the UTC PD with 5 μm in width, value of Γ is 0.62, which is also the highest value obtained in comparison to other widths. For the UTC L2W3 (15 μm x 4 μm) confinement factor is equal to 0.5.

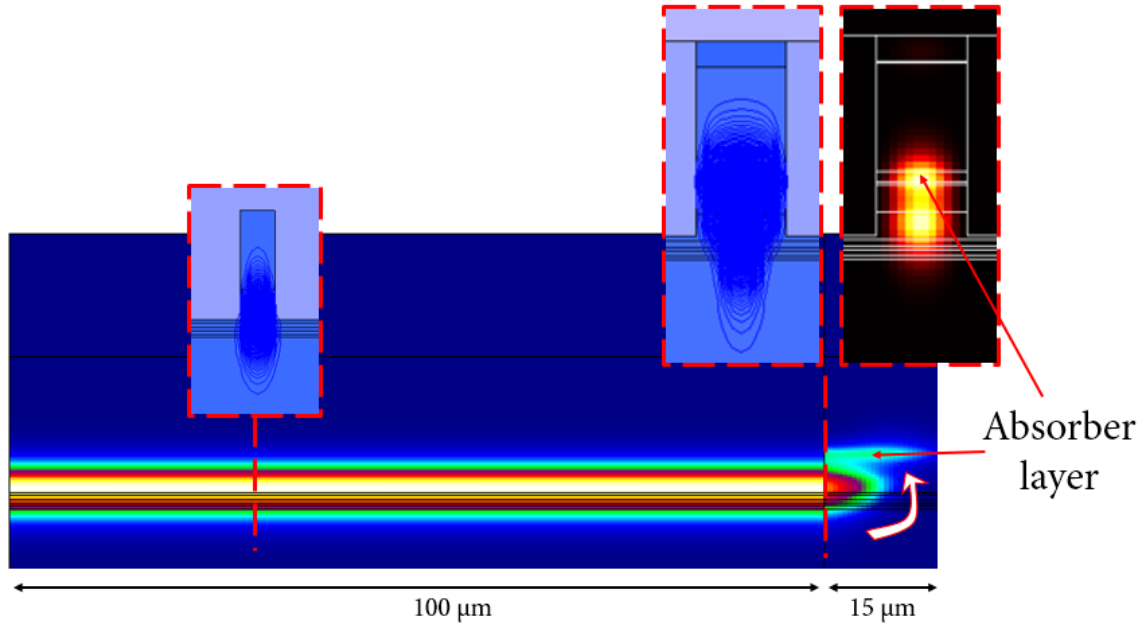


Fig. 4. 106 Example of light propagation inside ridge optical waveguide of 100 μm length to UTC PD (L2W3) absorber layer.

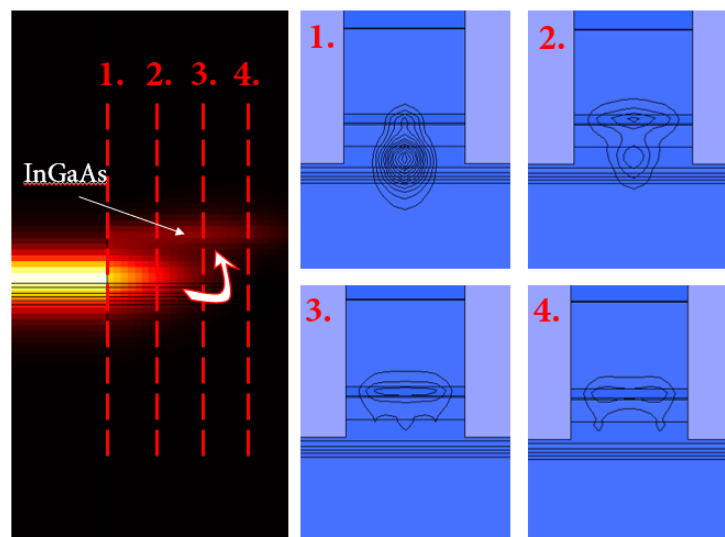


Fig. 4. 107 Cross sections contour plots of mode propagation at the edge and inside of UTC PD L2W3 structure.

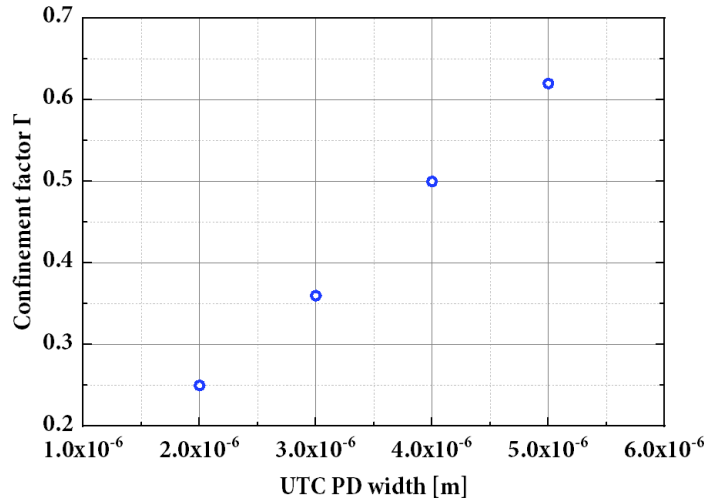


Fig. 4. 108 Confinement factor for UTC PD InGaAs absorber layer.

S-bend structures are another important component in the integrated optical circuits design [44]. Several S-bend structures have been investigated for the final circuit. Parameter definition and data for the simulated S-bends are presented in Fig. 4. 109 and Fig. 4. 110. Comparison between different S-bend with fixed length of 1000 μm and with variable S-bend angles is presented in Fig. 4. 111. Values of calculated loss (represented by power monitor value) rise with the angle and this parameter has a crucial impact on the loss. Moreover, for a very long S-bend structure (i.e. 2000 μm of length) a considerable amount of loss has to be taken under consideration. Results for a deep ridge optical waveguides structures are very comparable, but with usually slightly higher loss.

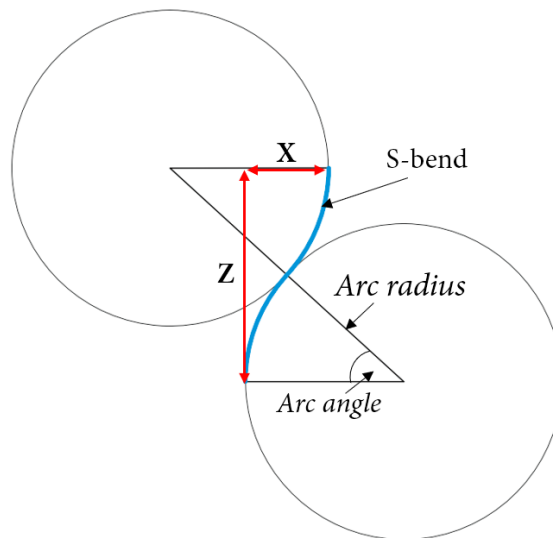


Fig. 4. 109 S-bend parameter definition.

S-bends						
	X: 150 μm	X: 200 μm	X: 250 μm	X: 300 μm	X: 350 μm	X: 750 μm *Length: 2000 μm
Loss [%]	ca. 13	ca. 14	ca. 15	ca. 18	ca. 25	ca. 43
Arc radius [μm]	1704	1300	1062	908	802	1521
Arc angle [$^\circ$]	17	22.6	28	33.4	38.6	41

Fig. 4. 110 Data of simulated S-bend ridge waveguides structures.

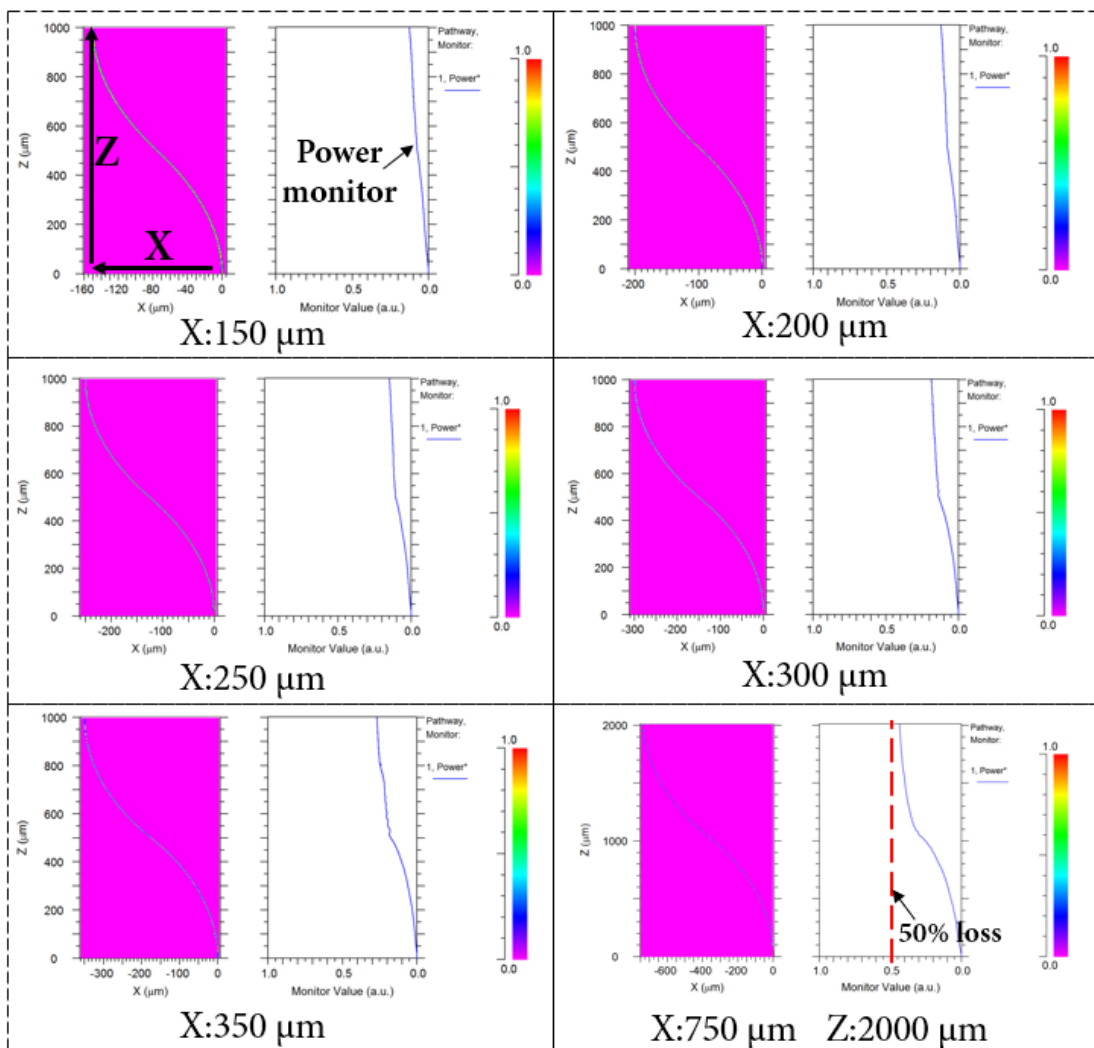


Fig. 4. 111 Example comparison of different ridge optical waveguide S-bends.

In Fig. 4. 112 an overview of the optical part of the circuit for 3x folded-dipole antenna integrated UTC PD structure is presented.

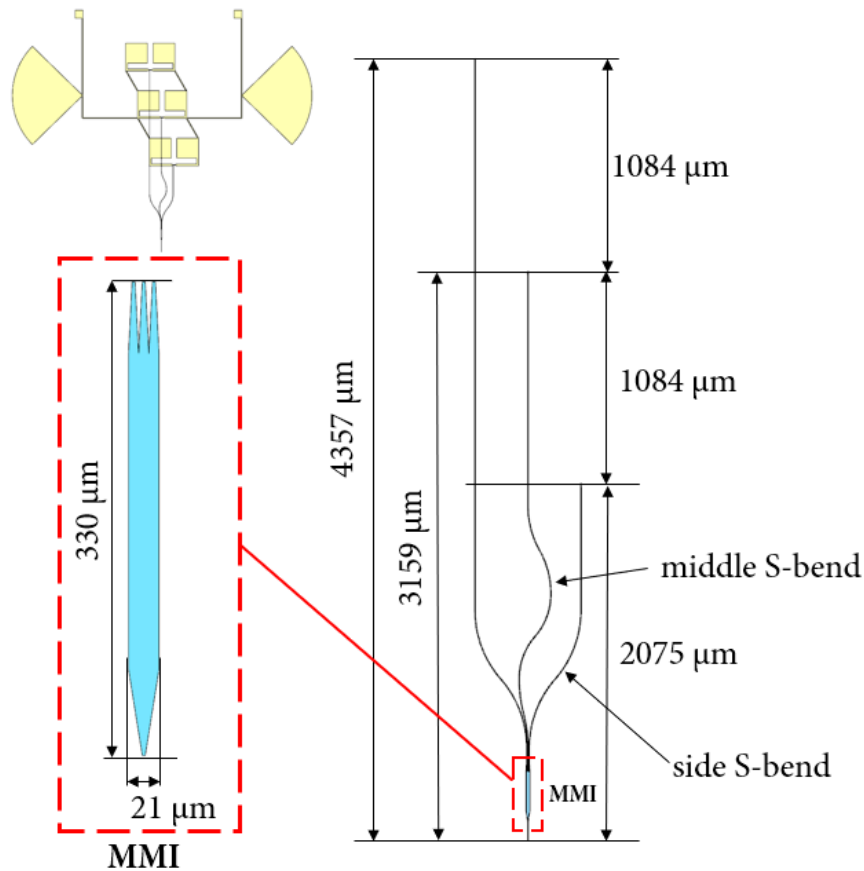


Fig. 4. 112 Overview of optical waveguides and MMI for a 3x folded-dipole antenna integrated UTC PD structure.

As can be seen, it is composed of 1x3 MMI, S-bends and straight optical waveguides. Optical length has been designed in order to have the same optical delay for each of the UTC PD, and is equal to 1084 μm . Simulations of the S-bends used in this structure for a ridge and deep ridge optical waveguide are presented in Fig. 4. 113. Calculated loss of middle S-bend is around 45 % and 60 %, for the ridge and deep ridge, respectively. Side S-bend loss, according to simulation results should not exceed 50 %.

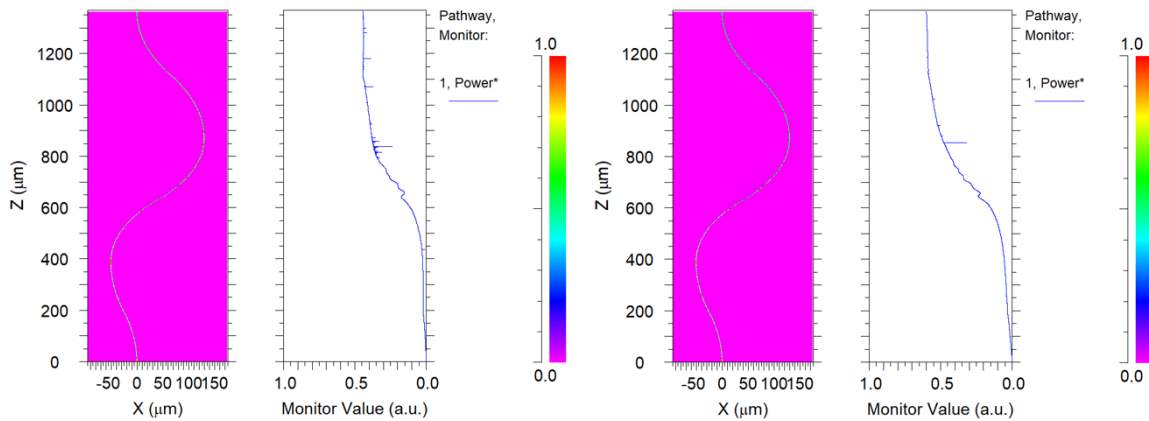


Fig. 4. 113 Comparison between simulation results for a ridge and deep ridge S-bend structure (middle S-bend) applied in 3x folded-dipole antenna-integrated UTC PD.

In Fig. 4. 114 an overview of 3x bow-tie antenna-integrated UTC PD is presented. Simulation of the middle S-bends is presented in Fig. 4. 115. In this structure losses for the middle S-bend for ridge and deep ridge structure are similar and based on the simulation result should not exceed 60%.

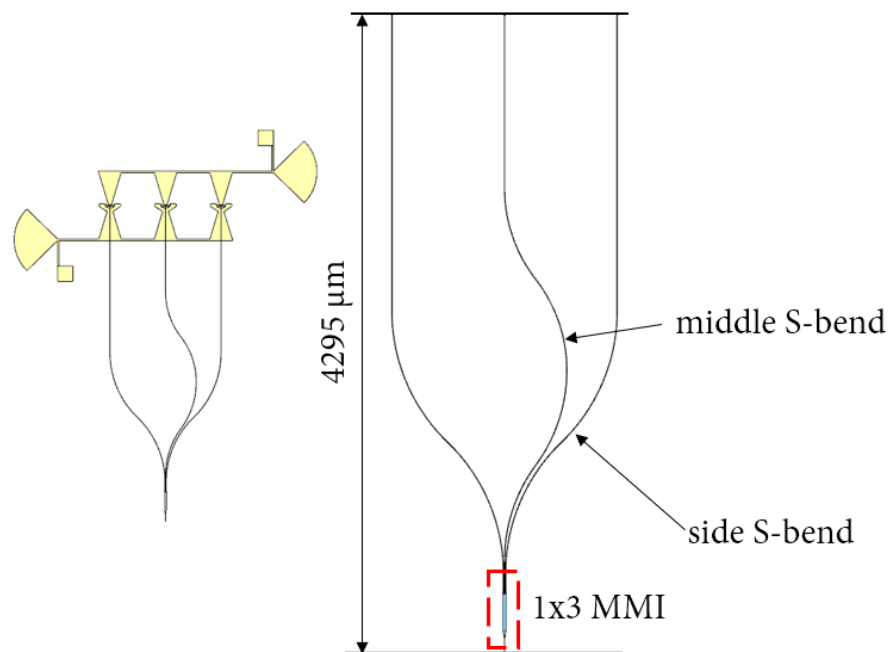


Fig. 4. 114 Overview of optical waveguides and MMI for a 3x bow-tie antenna-integrated UTC PD structure.

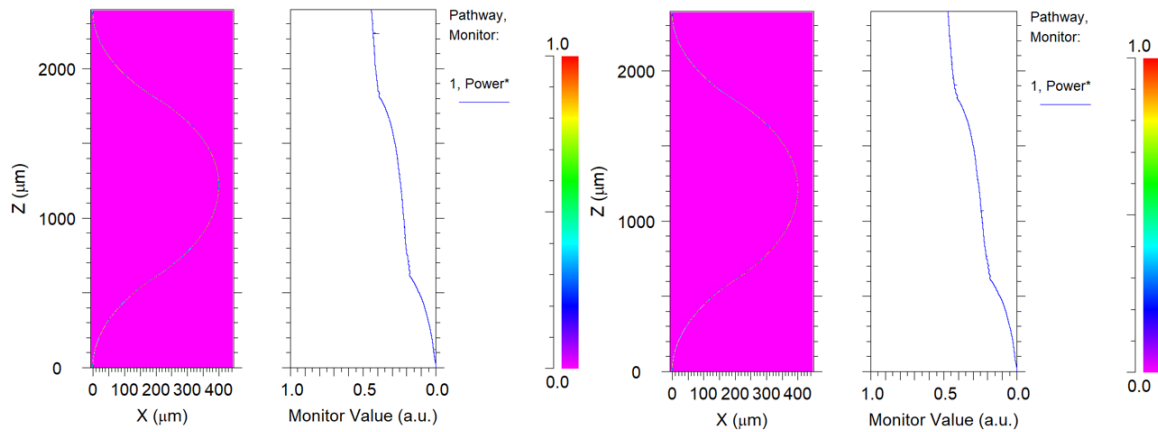


Fig. 4.115 Comparison between simulation results for a ridge and deep ridge S-bend structure (middle S-bend) applied in 3x bow-tie antenna-integrated UTC PD.

The same value of loss is also considered for the side S-bend. Overview of an optical part of the circuit of Wilkinson power combiner integrated with UTC PDs is presented in Fig. 4.116. As can be noticed, 1x2 MMIs are applied in both designs to reassure equal light division towards UTC PDs. Simulation results for utilized S-bends in the 4-way Wilkinson power combiner are presented in Fig. 4.117. Ridge and deep ridge loss results are very comparable.

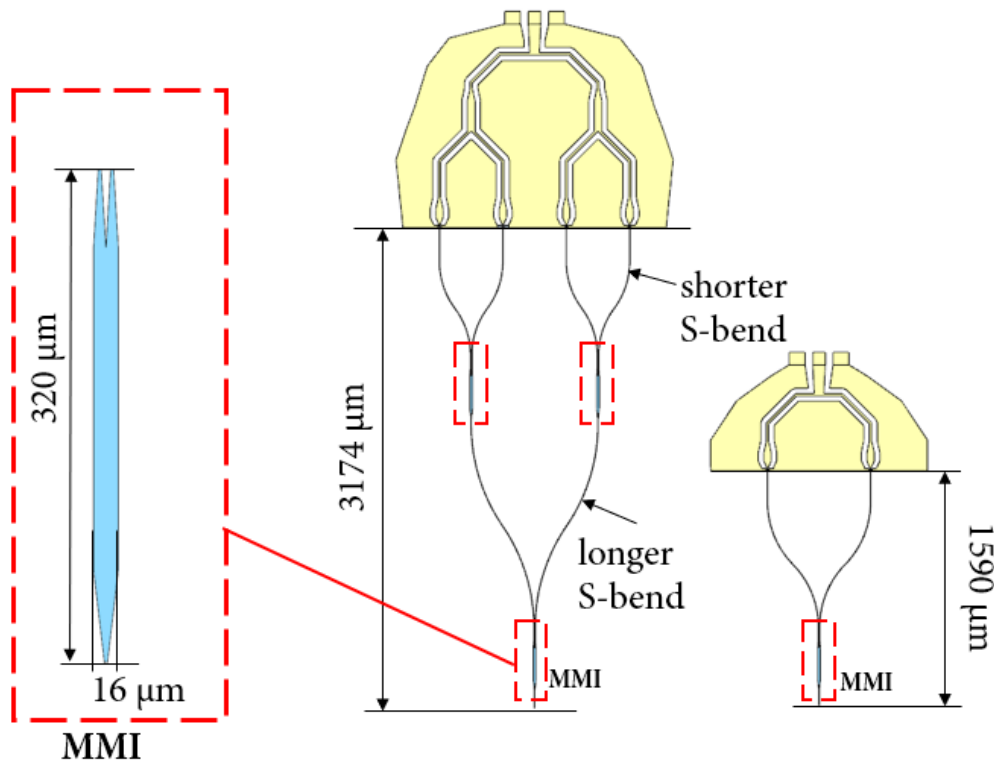


Fig. 4.116 4-way and 2-way Wilkinson power combiner with optical waveguides and 1x2 MMIs.

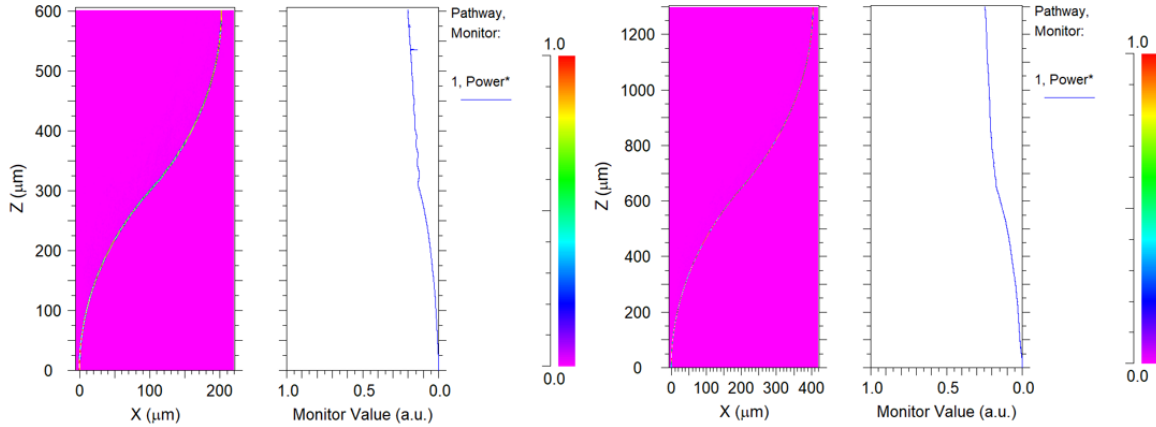


Fig. 4. 117 Simulation results of shorter (left) and longer (right) ridge S-bend of 4-way Wilkinson power combiner.

Simulation results of the S-bend used in 2-way Wilkinson power combiner is presented in Fig. 4. 118. Unfortunately, S-bend loss are quite high, and based on the simulations could reach up to 70 %.

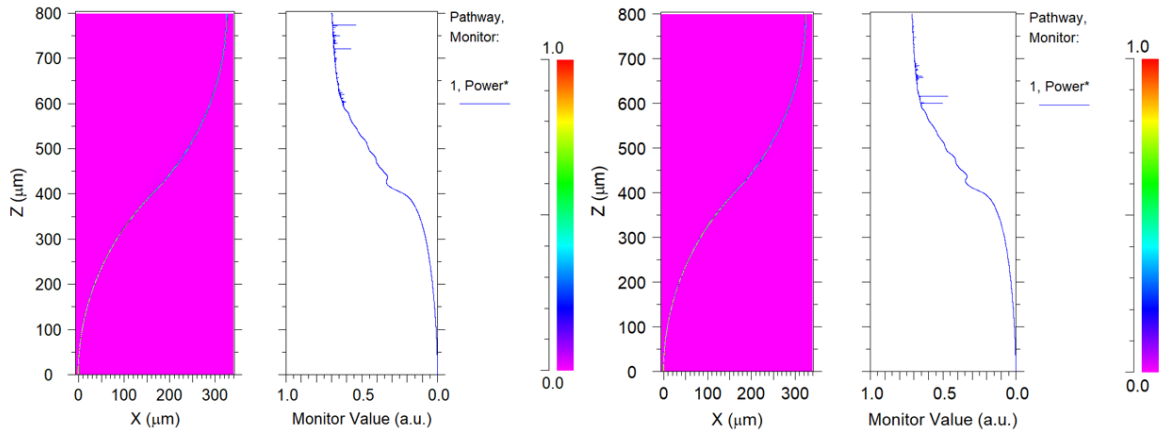


Fig. 4. 118 Comparison between simulation results for a ridge and deep ridge S-bend structure of 2-way Wilkinson power combiner.

In the 2x bow-tie and 1x separated bow-tie antenna-integrated UTC PDs 1x2MMI and one S-bend structure is utilized (Fig. 4. 119). Another S-bend structure is utilized in UTC PDs with adapted output in order to be coupled with external laser from the Fiwin5G project partners from UC3M. Structure and simulation results are presented in Fig. 4. 120 and Fig. 4. 121. Short summary of the S-bends parameters applied in the above-mentioned circuits design is presented in Fig. 4. 125.

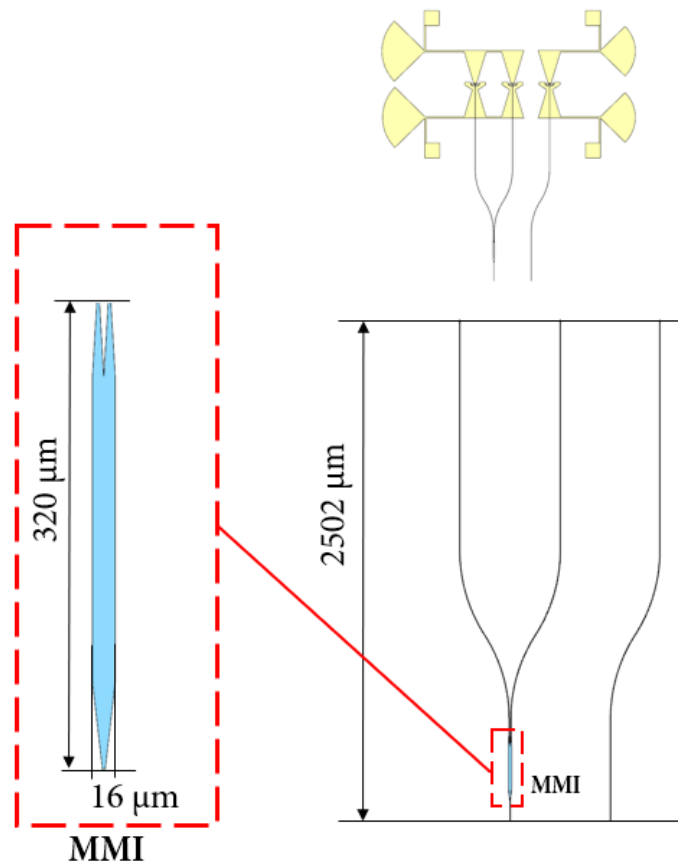


Fig. 4. 119 Overview of 2x bow-tie and separated 1x bow-tie antenna-integrated UTC PDs structures.

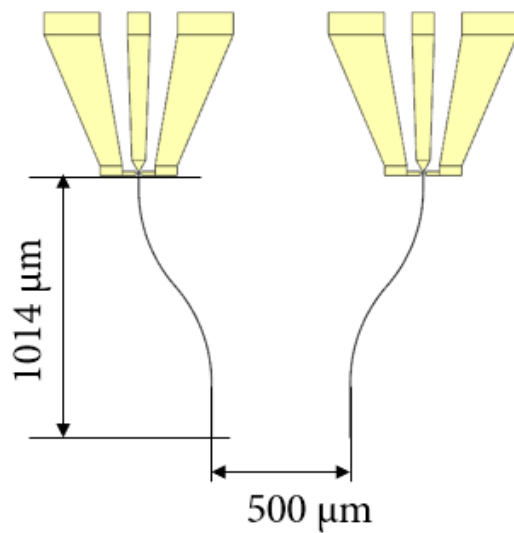


Fig. 4. 120 UTC PDs with adapted CPW output and S-bends.

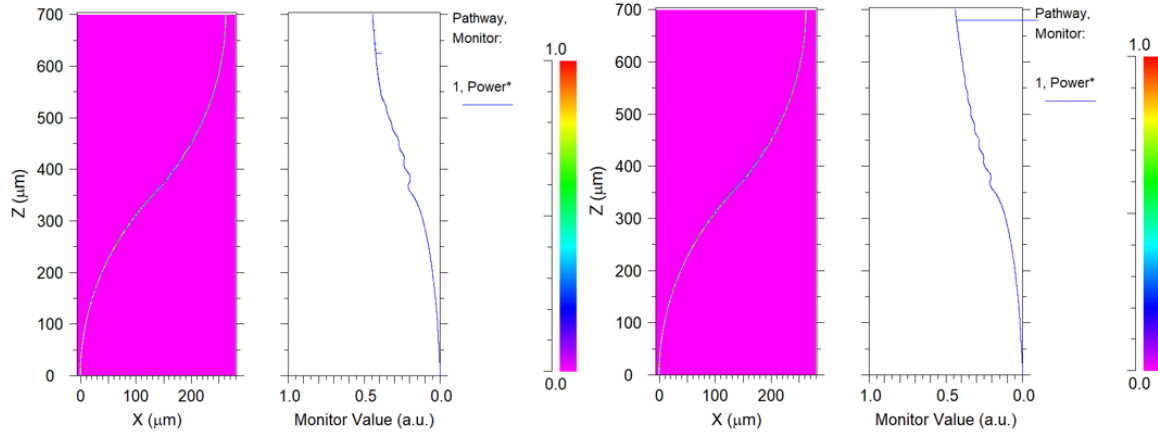


Fig. 4. 121 Comparison between simulation results for a ridge and deep ridge S-bend structure of the UTC PD with adapted output.

4.5.3 MMI - introduction

Multimode interference (MMI) device principle is based on the self-imaging effect [42] and it is used in integrated optics to perform splitting or combining functions. Schematic configuration of the single input and two outputs MMI (1 x 2 MMI) is presented in Fig. 4. 122, where the main part consists of a waveguide that supports large number of modes. This 3D structure can be reduced to 2D configuration and calculated by effective index method. The self-imaging characteristic can be confirmed by the Beam Propagation Method (BPM) simulation. By adapting device length and width, as well as, the number of inputs, different configuration of MMI device are possible. More details of the device physics can be found in [39].

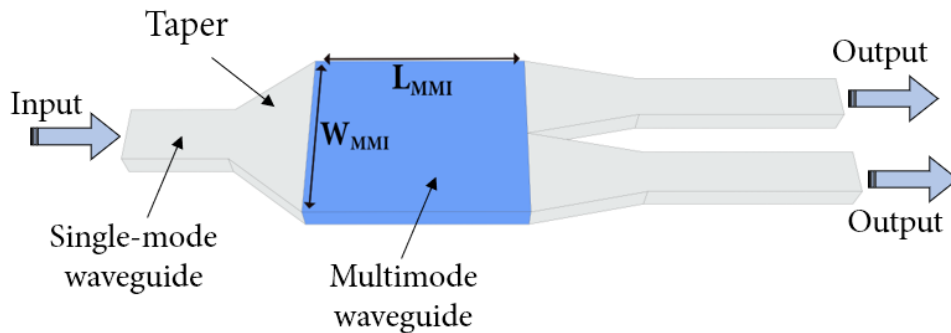


Fig. 4. 122 Schematic structure of a 1 x 2 MMI device.

4.5.4 MMIs – design and simulation results

In the previous subchapters, 1x3 and 1x2 MMI structures have been presented (Fig. 4. 112 and Fig. 4. 116). Commonly as in the optical waveguides design, FIMMWAVE and BeamPROP software has been utilized. Dimension of the both structures and contour plots of modes propagation are presented in Fig. 4. 123. Calculated values of the light division and losses for 1x2 MMI are similar for ridge and deep ridge design. For the 1x3 MMI, the deep ridge is less lossy.

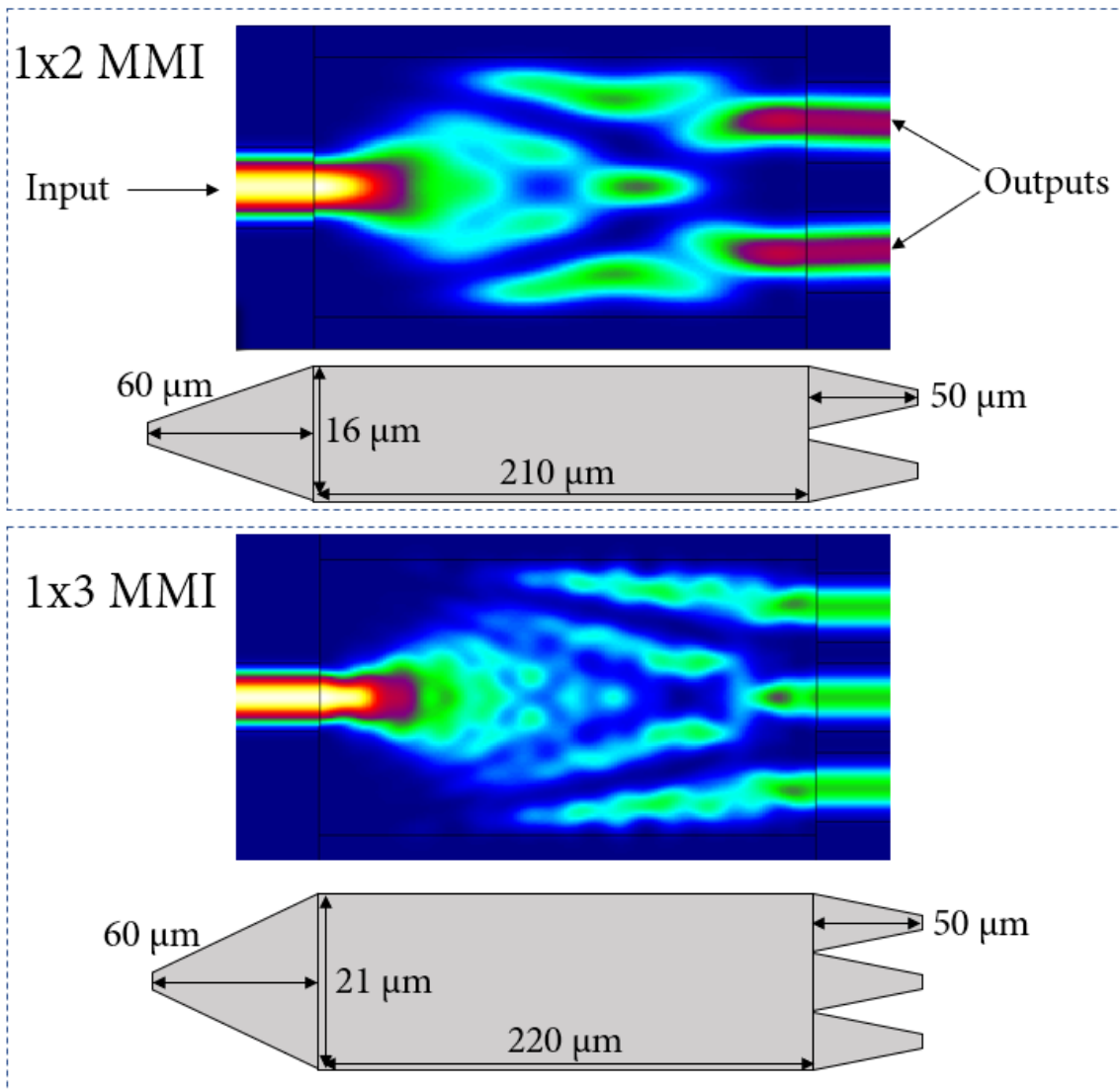


Fig. 4. 123 Contour plots and dimensions of 1x2 MMI (top) and 1x3 MMI (bottom) for ridge type structures.

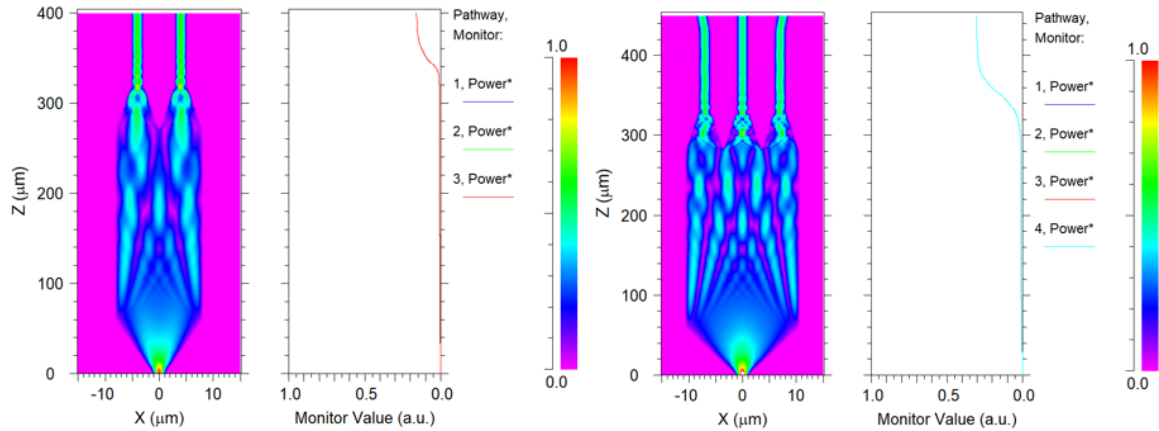


Fig. 4. 124 Modes propagation in 1x2 MMI (left) and 1x3 MMI (right) ridge type structures.

4.5.5 Optical design and simulations - summary

Summary of S-bends design parameters and MMI results are presented in Fig. 4. 125 and Fig. 4. 126, respectively. Based on the simulation results, InP-based ridge and deep ridge optical waveguides are in general lossy structures. Straight optical waveguides can be considered as much less lossy in comparison to S-bends. Even for a very long straight optical waveguide (2000 μm), obtained loss results are below 5 %. Moreover, S-bend simulations also reveal a critical angle of ca. 45° above which, the total loss of the transmission might reach almost 90 %. Another obstacle faced during the optical design is the area required for optical waveguides to be simulated, what in some cases might generate additional issues and requires very long simulation time. S-bend simulations also reveal that optical losses are in most cases around 45 %, and only with sharp angles these losses might be even higher. The MMI structures are much less lossy in comparison to S-bends. Based on the simulation results deep ridge type structure is more capable of low loss light propagation than ridge type. Nevertheless, for 1x2 MMI structures loss is similar. In conclusion, a considered amount (exceeding 70 %) of optical loss has to be taken into account in the long and sharp-angled S-bend optical waveguides.

S-bends					
	3x folded-dipole (side)	3x folded-dipole (middle)	3x bow-tie (side)	3x folded-dipole (middle)	2x bow-tie
Loss [%]	ca. 45	ca. 45	ca. 70	ca. 45	ca. 45
Arc radius [μm]	578	(3x S-bends) 1. 773 2. 480 3. 777	1162	(2x S-bends) 1. 1030 2. 955	760
Arc angle [°]	41	(3x S-bends) 1. 15 2. 41 3. 29	45	(2x S-bends) 1. 36 2. 37	33
	4-way Wilkinson (shorter)	4-way Wilkinson (longer)	2-way Wilkinson	UTC PD with adapted CPW output	
Loss [%]	ca. 20	ca. 25	ca. 70	ca. 45	
Arc radius [μm]	498	1144	573	532	
Arc angle [°]	37	34	44	41	

Fig. 4. 125 Data of simulated S-bend structures applied in the optical design of integrated circuits.

MMI				
	1x2 (ridge)	1x2 (deep ridge)	1x3 (ridge)	1x3 (deep ridge)
Loss [%]	ca. 8	ca. 8	ca. 12	ca. 6
Division per output [%]	1. 46 2. 46	1. 46 2. 46	1. 29 2. 30 3. 29	1. 31 2. 32 3. 31

Fig. 4. 126 Simulation results of 1x2 and 1x3 MMIs with ridge and deep ridge structure type.

To conclude:

- **Based on the simulations, the optical losses of the straight waveguides are expected to be below 5%, even for the structure above 2000 μm of length.**
- **The S-bend structures are much more challenging in terms of the design, as the top cladding thickness cannot be change and consequently optimized to be less lossy. Designed and simulated S-bends are generally lossy structures and the expected loss is above 50 % up to 70 %. Moreover, the limiting angle of the S-bend is about 45 %, above which the optical loss exceeds 70 %. Another challenge is the limitation of the simulation environment due to the big dimensions and also very long simulation time.**
- **The MMIs are much less lossy structures in comparison to S-bends. The 1x2 MMI and 1x3 MMI are very similar in terms of losses, expected to below 15 %.**
- **Total optical losses are expected to be high, exceeding 50 % up to 70 % for the Wilkinson power combiners as well as for the antenna-integrated structures.**

REFERENCES

- [1] www.ansys.com/products/electronics/ansys-hfss
- [2] www.photond.com/products/fimmwave.htm
- [3] www.synopsys.com/optical-solutions/rsoft/passive-device-beamprop.html
- [4] D. M. Pozar, *Microwave engineering*, 4th ed. Hoboken, NJ: Wiley, 2012.
- [5] K. Chang, *RF and microwave wireless systems*. New York: Wiley, 2010.
- [6] C. P. Wen, 'Coplanar Waveguide: A Surface Strip Transmission Line Suitable for Nonreciprocal Gyromagnetic Device Applications', *IEEE Transactions on Microwave Theory and Techniques*, vol. 17, no. 12, pp. 1087–1090, Dec. 1969.
- [7] R. N. Simons, *Coplanar Waveguide Circuits, Components, and Systems*. New York, USA: John Wiley & Sons, Inc., 2001.
- [8] W. H. Haydl, 'Resonance phenomena and power loss in conductor-backed coplanar structures', *IEEE Microwave and Guided Wave Letters*, vol. 10, no. 12, pp. 514–516, Dec. 2000.
- [9] I. Wolff, *Coplanar microwave integrated circuits*. Hoboken, N.J: Wiley-Interscience, 2006.
- [10] R. E. Collin, *Foundations for microwave engineering*, 2nd ed. New York: McGraw-Hill, 1992.
- [11] R. M. Fano, 'Theoretical limitations on the broadband matching of arbitrary impedances', *Journal of the Franklin Institute*, vol. 249, no. 1, pp. 57–83, Jan. 1950.
- [12] M. Natrella et al., 'Accurate equivalent circuit model for millimetre-wave UTC photodiodes', *Optics Express*, vol. 24, no. 5, p. 4698, Mar. 2016.
- [13] M. Natrella et al., 'Modelling and measurement of the absolute level of power radiated by antenna integrated THz UTC photodiodes', *Optics Express*, vol. 24, no. 11, p. 11793, May 2016.
- [14] L. N. Alyabyeva, E. S. Zhukova, M. A. Belkin, and B. P. Gorshunov, 'Dielectric properties of semi-insulating Fe-doped InP in the terahertz spectral region', *Sci Rep*, vol. 7, no. 1, p. 7360, Dec. 2017.
- [15] E. J. Wilkinson, 'An N-Way Hybrid Power Divider', *IEEE Transactions on Microwave Theory and Techniques*, vol. 8, no. 1, pp. 116–118, Jan. 1960.
- [16] R. Sorrentino and G. Bianchi, *Microwave and RF engineering*. Chichester, West Sussex, U.K. ; Hoboken, N.J: Wiley, 2010.
- [17] C. A. Balanis, *Antenna theory: analysis and design*, Fourth edition. Hoboken, New Jersey: Wiley, 2016.
- [18] J. D. Kraus, R. J. Marhefka, and A. Khan, *Antennas and wave propagation*. New Delhi: Tata McGraw Hill Education, 2011.
- [19] W. L. Stutzman and G. A. Thiele, *Antenna theory and design*, 3. ed. Hoboken, NJ: Wiley, 2013.

- [20] R. DuHamel and D. Isbell, 'Broadband logarithmically periodic antenna structures', in IRE International Convention Record, New York, NY, USA, 1957, vol. 5, pp. 119–128.
- [21] G. H. Brown and O. M. Woodward Jr., "Experimentally determined radiation characteristics of conical and triangular antennas," RCA Rev., vol 13, pp. 425452, Dec. 1952.
- [22] M. Hoefle, K. Haehnsen, I. Oprea, O. Cojocari, A. Penrice, and R. Jakoby, 'Compact and Sensitive Millimetre Wave Detectors Based on Low Barrier Schottky Diodes on Impedance Matched Planar Antennas', J Infrared Milli Terahz Waves, vol. 35, no. 11, pp. 891–908, Nov. 2014.
- [23] I. A. Glover, S. R. Pennock, and P. R. Shepherd, Eds., Microwave Devices, Circuits and Subsystems for Communications Engineering. Chichester, UK: John Wiley & Sons, Ltd, 2005.
- [24] G. Ghione and M. Pirola, Microwave electronics. Cambridge, United Kingdom ; New York, NY: Cambridge University Press, 2018.
- [25] J.-S. Hong, Microstrip filters for RF/microwave applications, 2nd ed. Hoboken, N.J: Wiley, 2011.
- [26] www.pasternack.com/0.05-mhz-50-ghz-2.4mm-bias-tee-150-ma-25-volts-dc-pe1610-p.aspx
- [27] F. Giannini, R. Sorrentino, and J. Vrba, 'Planar Circuit Analysis of Microstrip Radial Stub', in MTT-S International Microwave Symposium Digest, San Francisco, CA, USA, 1984, vol. 84, pp. 124–125.
- [28] M. F. Ismail, M. K. A. Rahim, and H. A. Majid, 'The Investigation of PIN diode switch on reconfigurable antenna', in 2011 IEEE International RF & Microwave Conference, Seremban, Negeri Sembilan, Malaysia, 2011, pp. 234–237.
- [29] Y. Huo, G. W. Taylor, and R. Bansal, 'Planar Log-Periodic Antennas on Extended Hemishperical Silicon Lenses for Millimeter/Submillimeter Wave Detection Applications', International Journal of Infrared and Millimeter Waves, vol. 23, no. 6, pp. 819–839, Jun. 2002.
- [30] S. Preu, G. H. Döhler, S. Malzer, L. J. Wang, and A. C. Gossard, 'Tunable, continuous-wave Terahertz photomixer sources and applications', Journal of Applied Physics, vol. 109, no. 6, p. 061301, Mar. 2011.
- [31] R. Rotman, M. Tur, and L. Yaron, 'True Time Delay in Phased Arrays', Proc. IEEE, vol. 104, no. 3, pp. 504–518, Mar. 2016.
- [32] A. Capozzoli, C. Curcio, and G. D'Elia, 'The design of an optical time steered antenna based on a new integrated true time delay unit', PIER, vol. 140, pp. 681–717, 2013.
- [33] I. Aldaya, G. Campuzano, G. Castañón, and A. Aragón-Zavala, 'A Tutorial on Optical Feeding of Millimeter-Wave Phased Array Antennas for Communication Applications', International Journal of Antennas and Propagation, vol. 2015, pp. 1–22, 2015.
- [34] Rohde and Schwarz White Paper 'Millimeter-Wave Beamforming: Antenna Array Design Choices & Characterization', 2016.

- [35] H. Li, T. Huang, C. Ke, S. Fu, P. P. Shum, and D. Liu, 'Photonic Generation of Frequency-Quadrupled Microwave Signal with Tunable Phase Shift', *IEEE Photon. Technol. Lett.*, vol. 26, no. 3, pp. 220–223, Feb. 2014.
- [36] L. Morgan and H. Andersson, 'An efficient beamforming method using a combination of analog true time and digital delay', in *Proceedings of the 2002 IEEE Radar Conference (IEEE Cat. No.02CH37322)*, Long Beach, CA, USA, 2002, pp. 260–265.
- [37] G. Lifante, *Integrated Photonics: Fundamentals*. Chichester, UK: John Wiley & Sons, Ltd, 2003.
- [38] C.-L. Chen, *Foundations for guided-wave optics*. Hoboken, N.J: Wiley-Interscience, 2007.
- [39] K. Okamoto, *Fundamentals of optical waveguides*, 2nd ed. Amsterdam ; Boston: Elsevier, 2006.
- [40] J. E. Goell, 'A Circular-Harmonic Computer Analysis of Rectangular Dielectric Waveguides', *Bell System Technical Journal*, vol. 48, no. 7, pp. 2133–2160, Sep. 1969.
- [41] E. A. J. Marcatili, 'Dielectric Rectangular Waveguide and Directional Coupler for Integrated Optics', *Bell System Technical Journal*, vol. 48, no. 7, pp. 2071–2102, Sep. 1969.
- [42] L. B. Soldano and E. C. M. Pennings, 'Optical multi-mode interference devices based on self-imaging: principles and applications', *Journal of Lightwave Technology*, vol. 13, no. 4, pp. 615–627, Apr. 1995.
- [43] Y. Chung and N. Dagli, 'An assessment of finite difference beam propagation method', *IEEE Journal of Quantum Electronics*, vol. 26, no. 8, pp. 1335–1339, Aug. 1990.
- [44] K. A. Williams et al., 'InP photonic circuits using generic integration [Invited]', *Photon. Res.*, vol. 3, no. 5, p. B60, Oct. 2015.

CHAPTER 5

PIC FABRICATION

The objective of this chapter is to present the overall fabrication process performed in the III-V Lab facilities to produce the designed structures.. In Fig. 5. 1 layout overview of the final 2” InP wafer is depicted. It can be seen that devices are divided into groups. It is done to secure the continuity of the process in case of substrate breakage, as well as, to optimize available surface to process on the wafer. It can be also noticed that, antenna-integrated devices require considerable amount of space in comparison to other structures placed on the chip. Due to complexity of the process flow, 12 level of photolithography masks are designed and needed for the fabrication. Moreover, additional test substrates are used to test specific process steps, but only one substrate with appropriate layer stack was available for the final chip processing. A brief description of the processing steps employed in the fabrication is presented in the following subchapter.

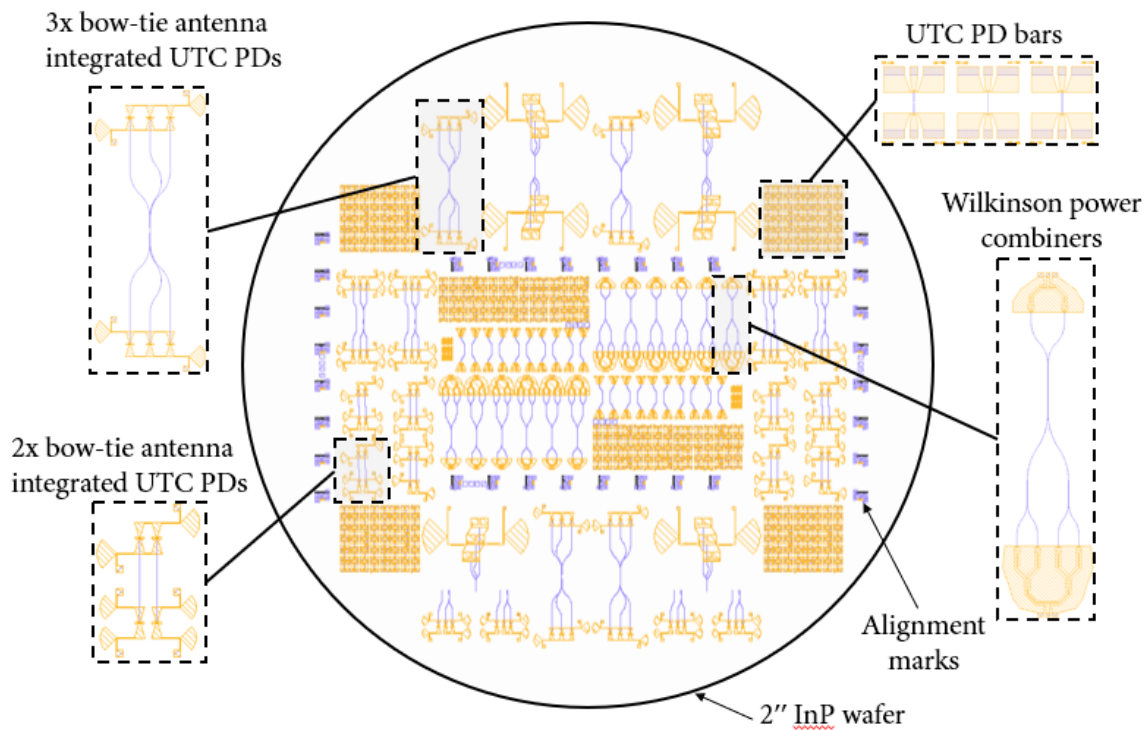


Fig. 5. 1 Final chip layout overview.

5.1 CLEANROOM PROCESSING - STEPS

The epitaxial layer stack of the InP semi-insulating substrate available for the cleanroom fabrication is presented in Fig. 5. 2. The optical waveguide core is composed of 300 nm of InGaAsP and an additional epitaxial re-growth of thick InP ridge layer is performed, and act as a top cladding. This layer stack was originally designed to be integrated with other optical components, including semiconductor optical amplifiers and DFB lasers. The UTC PD absorber layer is composed of a 120 nm thick gradually-doped InGaAs layer, with spacer layers between the 300 nm thick InP collector layer.

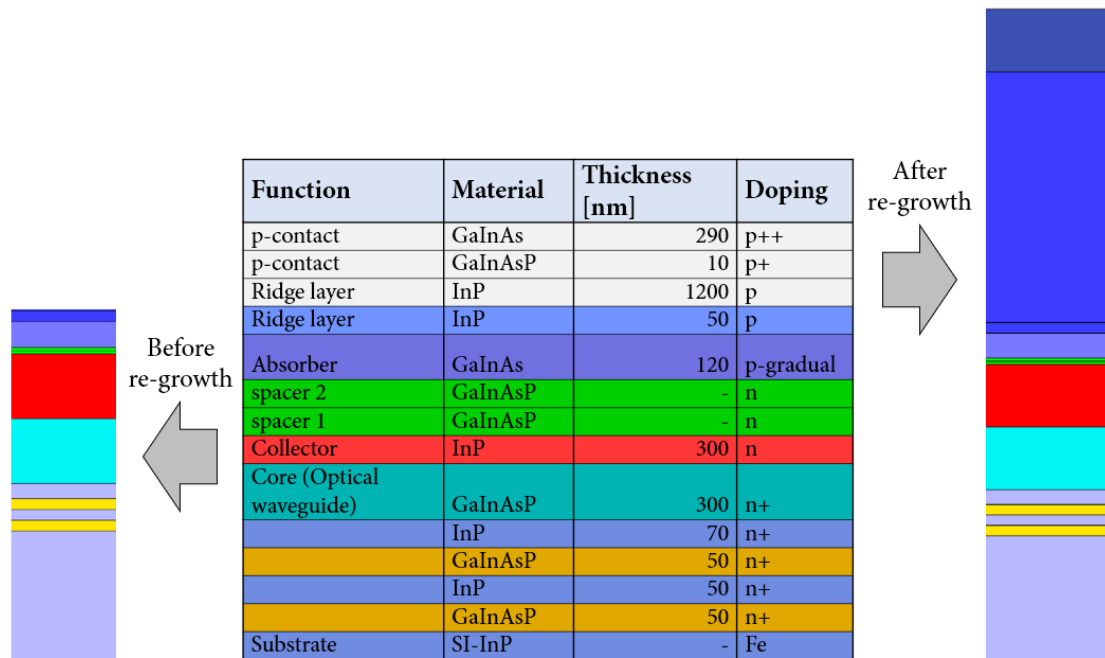


Fig. 5. 2 Substrate layer stack layout before and after epitaxial re-growth. (SI: semi-insulating).

Fabrication process can be divided into the following steps:

1. Mesa etching to separate UTC PD and optical waveguide layers.

Prior to this step, first alignment marks are etched on the substrate by ICP (Inductively coupled Plasma) Reactive Ion Etching (RIE) technique.

The SiO₂ mask is deposited by PECVD (Plasma-enhanced Chemical Vapor Deposition) on the substrate and mask patterns are etched by RIE (Reactive Ion Etching) technique. Afterwards, ICP-RIE is used to etch the mesa structure. A chemical restoration process and wet etch is also performed before Gas Source MBE re-growth.

In Fig. 5. 2 a simplified schematic overview of the mesa etching step is presented. From the front view it can be seen that ICP etching is performed until the collector layer that acts as etch stop layer. As the process is finalized with the chemical restoration, the collector layer is slightly etched as well. Measured mesa height after the processing revealed that around 100 nm of the collector layer is etched additionally.

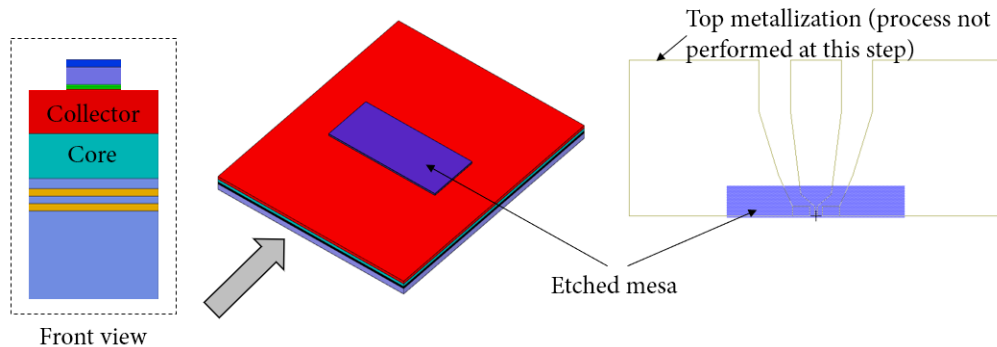


Fig. 5. 3 Simplified diagram of the mesa etching step to separate UTC PD and optical waveguide layers.

2. Epitaxial re-growth.

GS-MBE (Gas Source Molecular Beam Epitaxy) machine is used for the epitaxial re-growth of the ridge and p-contact layers, as presented in Fig. 5. 2. The total thickness of the layers regrown is ca. 1500 nm. In Fig. 5. 4 it is worth to note, that after the re-growth, there is a 300 nm difference in height between the UTC PD layers and optical waveguide layers.

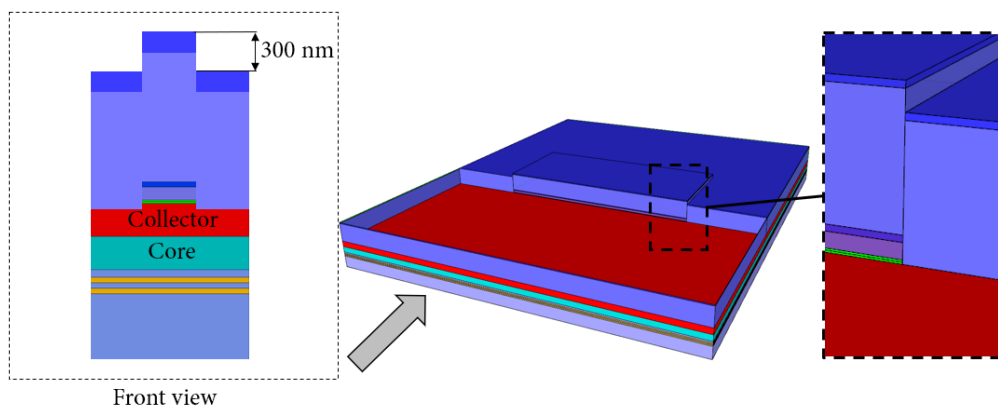


Fig. 5. 4 Simplified schematic of the epitaxial re-growth.

3. Alignment marks.

During this step, ca. 100 nm thick Pt layer is deposited by Ion Beam deposition technique on the substrate and is used as a mask for new alignment marks after the re-growth process. Platinum will also allow the fabrication of ohmic contacts (p-contact of UTC PD and CPW output contacts) on the top level of the architecture. Alignment marks are etched into the platinum by a dry IBE (Ion Beam Etching) etching technique.

4. Proton implantation

Proton implantation is introduced in the process to electrically insulate selected areas i.e. contact pads for CPW output. This step is outsourced in one of the III-V Lab contractors.

5. Photodiode and optical waveguides etching.

This step defines the UTC PDs and optical waveguides (including S-bends and MMIs) dimensions. The SiO_2 mask is used and mask pattern is etched by RIE. Moreover, IBE and ICP are employed to etch the platinum and semiconductor layers, respectively. As can be seen in Fig. 5. 5, ridge optical waveguide is formed and n-contact layers are reached.

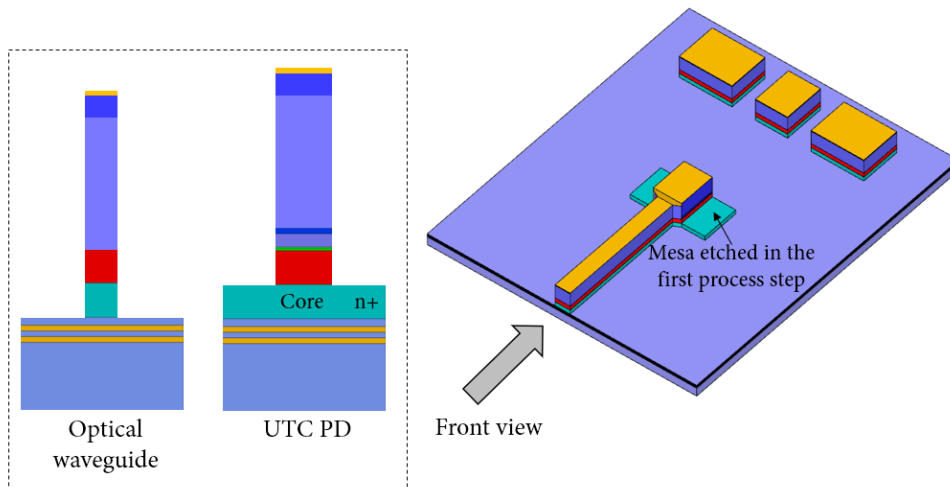


Fig. 5. 5 Simplified diagram of the UTC PD and optical waveguide etching.

6. Platinum removal.

The aim of this step is to remove Pt layer from the top of the optical waveguides and MMIs. It is necessary, as the metal layer on the top of optical structures could greatly increase the light propagation losses. Platinum is removed by IBE and a

selective wet etch is subsequently used to remove the highly p-doped InGaAs contact layer.

7. Etching till SI-InP substrate.

Dry and wet etching are used to reach the semi-insulating InP substrate on the areas as presented in Fig. 5. 6a. This step is finalized with a chemical restoration procedure. Moreover, an RTA (Rapid Thermal Annealing) process is also performed to establish ohmic contacts on the top surface of the photodiode.

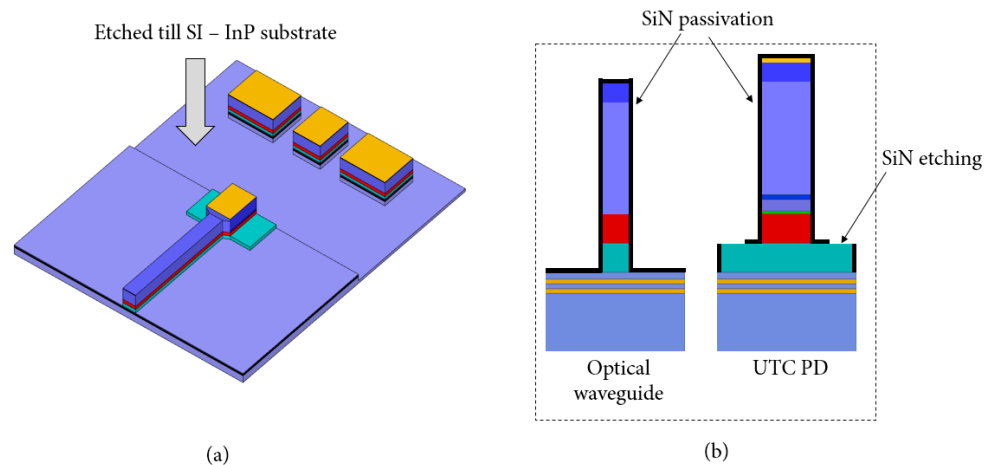


Fig. 5. 6 Simplified diagram of (a) the etching step till SI-InP and (b) passivation process.

8. Passivation and n-contact openings.

Structures are passivated with a 50 nm thick Si_3N_4 layer deposited by ICPCVD as presented in Fig. 5. 6b. Following the deposition, the N-contact openings for the future metallization are etched by a fluorine based RIE process.

9. Nickel/Chrome (NiCr) resistors.

In this step, NiCr resistors are required for the design of Wilkinson power combiners. A specific thickness of NiCr layer is deposited by sputtering and lift-off process to establish the wanted value of resistance. In Fig. 5. 7, the position of NiCr resistors for the 2-way Wilkinson power combiner is presented (as depicted in Fig. 4. 23 and Fig. 4. 24 with more details). In order to form the 50Ω resistor (made of two squares), value of the resistance per square is measured on the additional test substrate with four-point prober to adapt the NiCr layer thickness. Measured value is equal to ca. 28Ω per square which is ca. 3Ω above the ideal 25Ω per square value.

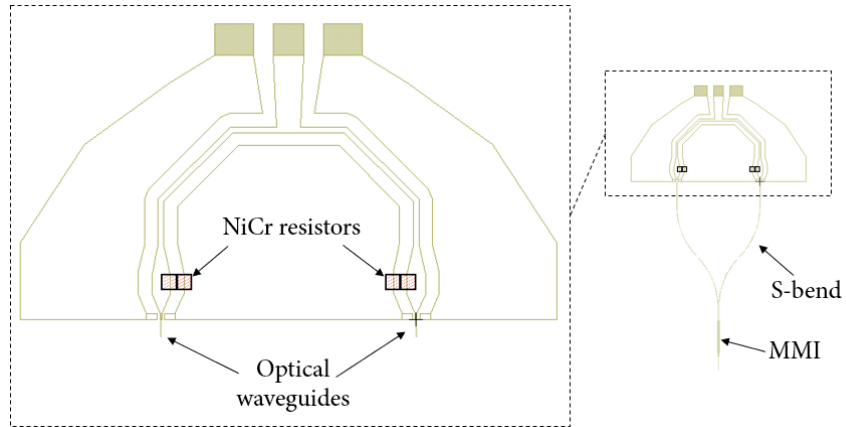


Fig. 5. 7 Schematic overview of the 2-way Wilkinson power combiner and the position of the NiCr resistors.

10. N-contacts metallization.

Deposition of Ti/Pt/Au is performed during this step to establish the n-contacts. Metal connections with the under-bridges and the NiCr resistors mandatory for the overall device performance are depicted in Fig. 5. 8 and Fig. 5. 9.

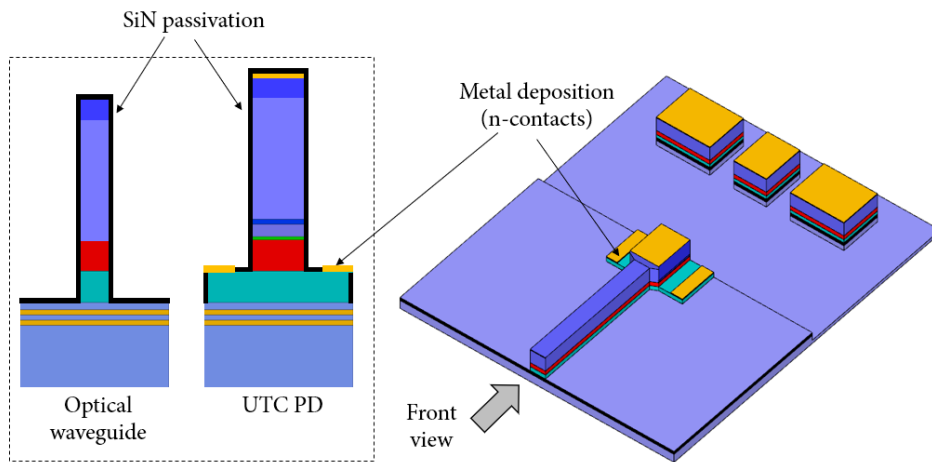


Fig. 5. 8 Simplified diagram of the n-contact deposition.

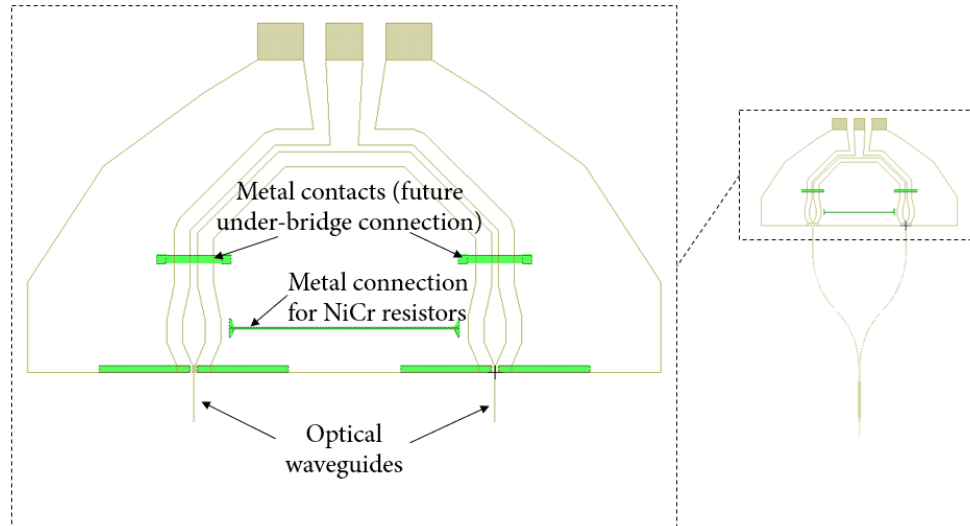


Fig. 5. 9 Schematic overview of the bottom side of the 2-way Wilkinson power combiner with the n-contacts and metal connections position.

11. BCB planarization and etching.

BCB-based polymer (Benzocyclobutene) is used in the planarization process as depicted in Fig. 5. 10. After the curing procedure, the BCB is etched/planarized by a fluorine-based RIE process until the top metal on the UTC PD. The SiN layer from the top of the p-contact of UTC PD is removed by RIE. Then a subsequent photolithography step is needed to define the openings where the BCB is etched to reach the bottom n-contacts of the devices.

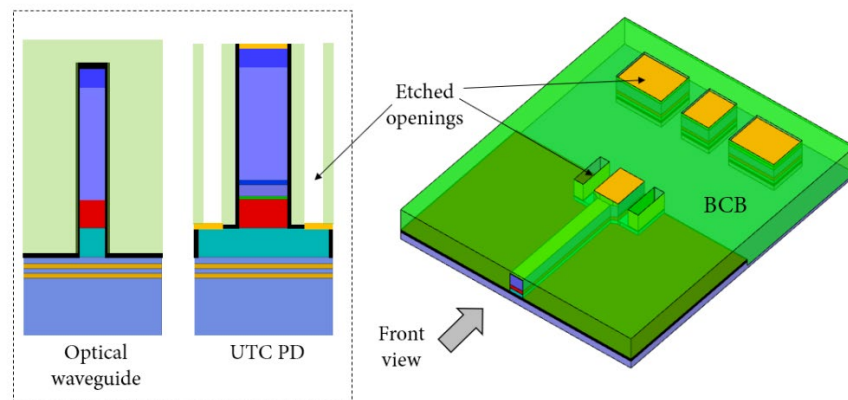


Fig. 5. 10 Simplified diagram of the BCB planarization and etching step.

12. Top metallization.

The top metallization of Ti/Pt/Au layers is performed in two steps. Firstly, the Ti/Pt/Au layers are deposited in a standard deposition process. In the second step, the substrate is tilted at an angle of 45° during the deposition of an additional layer of Au. The latter step is introduced to guaranty that the under-bridge connections and metal connections for the resistors are well established with the top metallization.

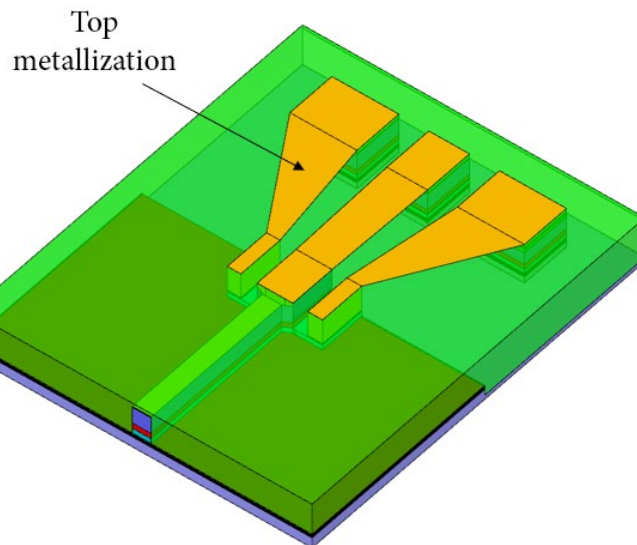


Fig. 5. 11 Simplified diagram of the top metallization step.

13. Wafer thinning and cleaving.

Finally, the wafer is thinned to ca. $125\ \mu\text{m}$ and cleaved to separate different structures from the chip.

5.2 CLEANROOM PROCESSING – RESULTS AND SUMMARY

As mentioned in the introduction, due to complexity of the processing and reduced number of available substrates (only one with useful layer stack) fabrication of the designed structures was very challenging. It took more than 10 months to finalize the processing and performed first measurements. Unfortunately, during the platinum removal step, part of the substrate broke down as presented in Fig. 5. 12. The broken part was not further processed. Fortunately, processing was continued with the bigger part. Nevertheless, several antenna-integrated structures, as well as, UTC PDs were lost due to the breakage. Moreover, the

irregular shape of the processed chip also introduced additional complications such as the uniformity of the BCB planarization.

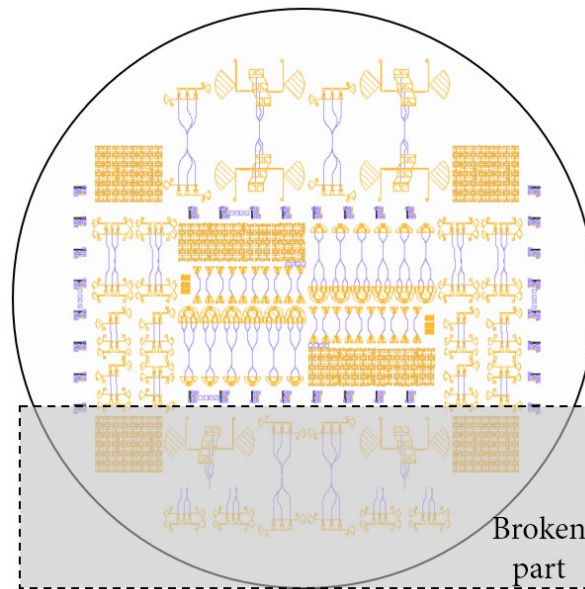


Fig. 5. 12 Broken part of the substrate during the processing.

In Fig. 5. 13 the fabricated UTC PDs are presented. Input optical waveguide and top metallization is clearly seen. The optical inspection from the top of the chip revealed, that structures are well defined. As can be seen, the substrate is cleaved into separated bars to facilitate the measurements and the fiber-to-chip coupling. Moreover, it can be also observed an edge of the metallization due to the second angled deposition. In Fig. 5. 14 the 2-way Wilkinson power combiner is presented with the optical part of the structure. Close-up views show the input CPW with and without isolation resistor, and the UTC PDs. Optical inspection of the under-bridge connections and connections to NiCr resistors does not reveal any issues with the structures.

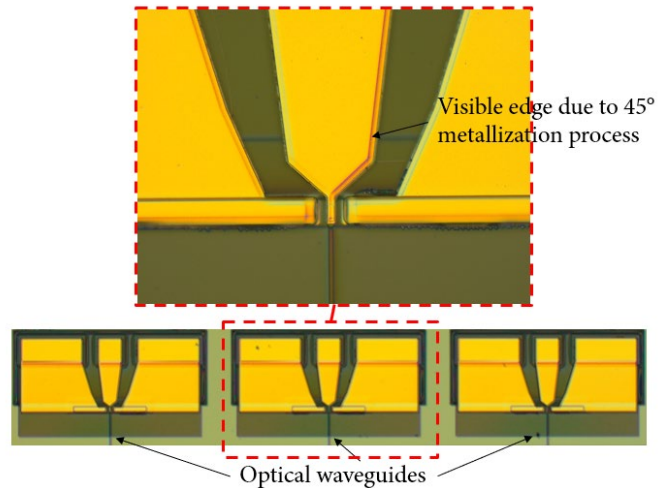


Fig. 5. 13 Optical microscope photograph of a UTC PDs after the fabrication process.

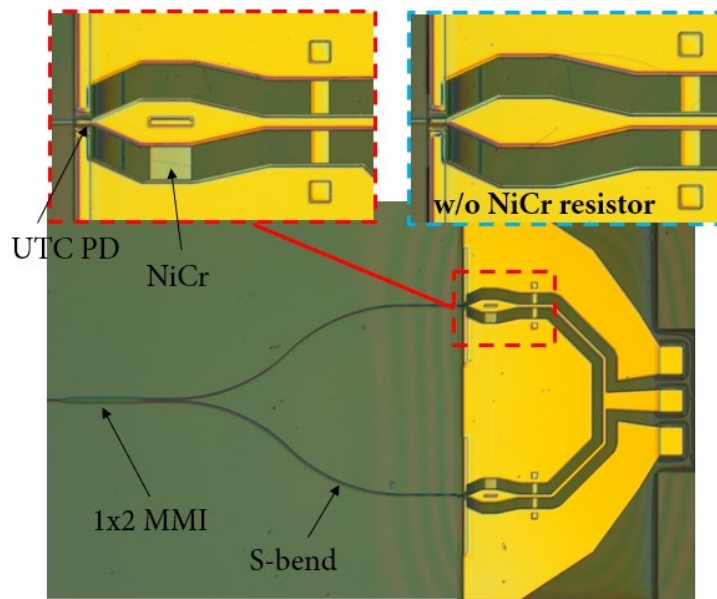


Fig. 5. 14 Optical microscope photograph of the fabricated 2-way Wilkinson power combiner with isolation resistors and a close-up on UTC PD and NiCr resistor.

In Fig. 5. 15 the 4-way Wilkinson power combiner (a) with and (b) without isolation resistors is presented. Optical inspection of the under-bridge connections does not reveal issues (Fig. 5. 16). The optical waveguides for both type of Wilkinson combiners are presented in Fig. 5. 17, with input waveguides and MMIs.

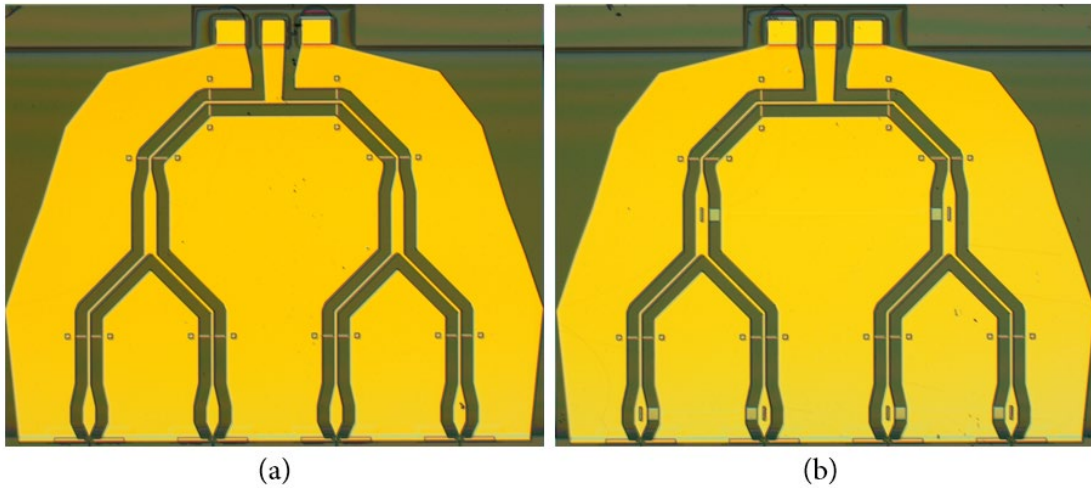


Fig. 5. 15 Optical microscope photograph of the fabricated 4-way Wilkinson power combiner (a) without isolation resistors and (b) with isolation resistors.

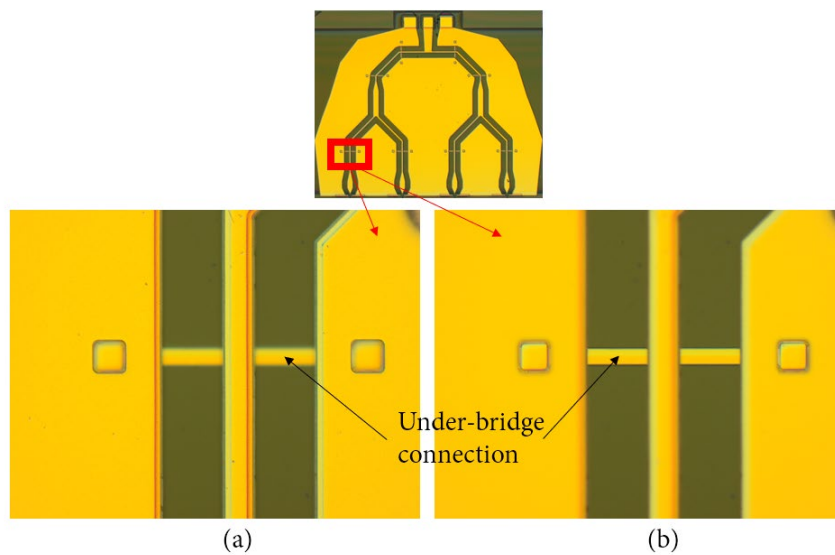


Fig. 5. 16 Optical microscope photograph of the under-bridge connection of the 4-way Wilkinson power combiner with the optical focus on the (a) top metal layer and (b) bottom metal layer.

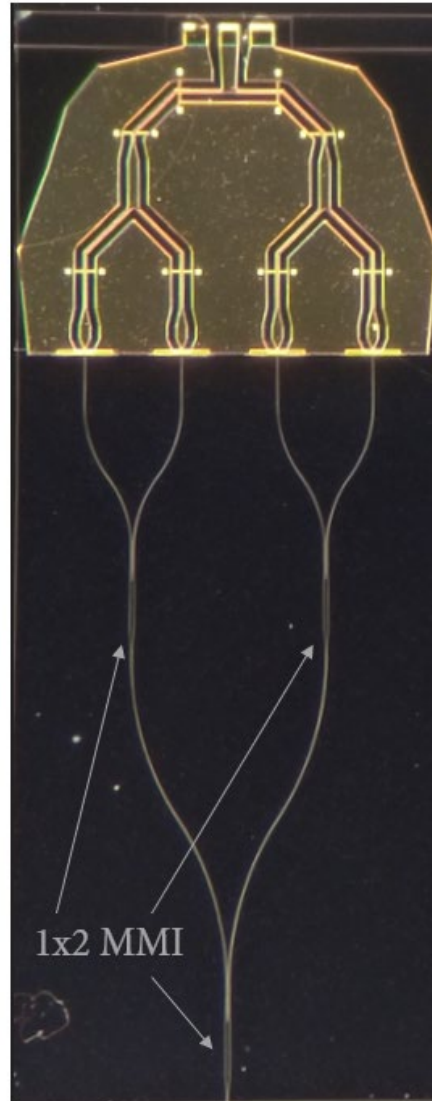
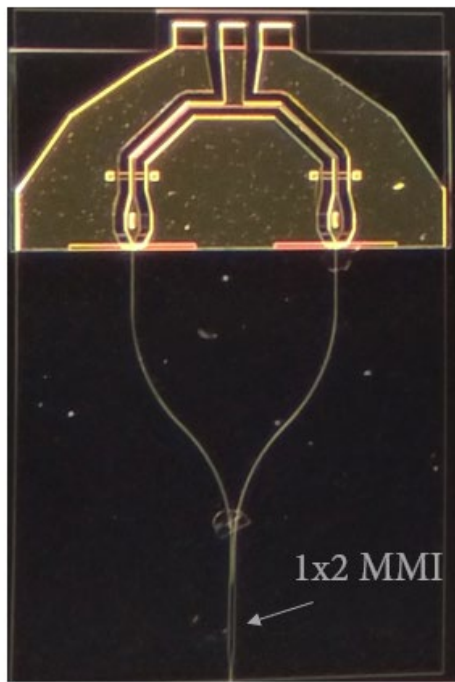


Fig. 5. 17 Optical waveguides and MMIs of the 2-way and 4-way Wilkinson power combiner after chip cleaving.

The folded-dipole antenna-integrated UTC PD structure is presented in Fig. 5. 18. Part of the optical waveguides can be seen, but due to the large structure dimensions and the camera reflections a sharp photograph cannot be obtained. The optical inspection from the top of the chip does not reveal fabrication defaults. Similarly, for the 3x bow-tie antenna-integrated structure and other configurations with bow-tie antenna structures presented in Fig. 5. 19, Fig. 5. 20 and Fig. 5. 21.

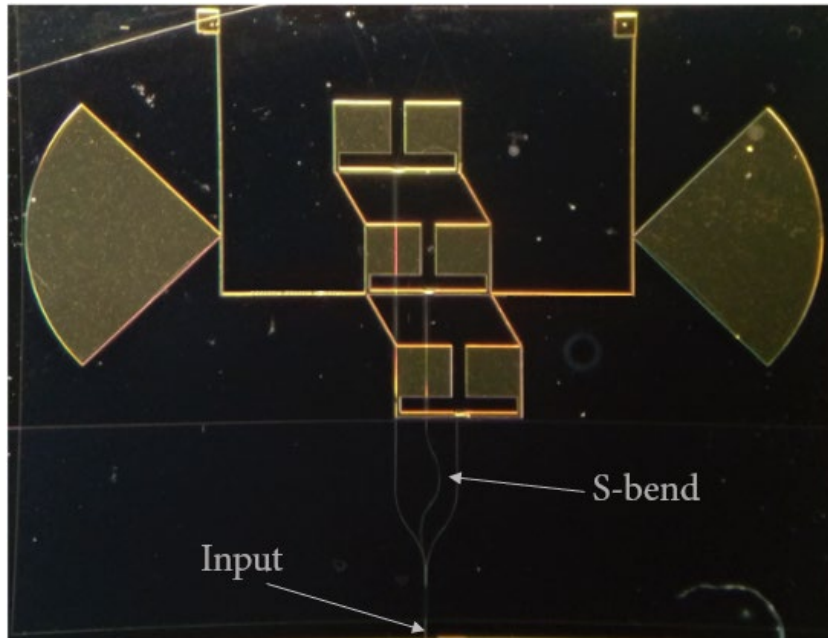


Fig. 5. 18 Folded-dipole antenna-integrated UTC PD structure with optical waveguides after fabrication and cleaving.

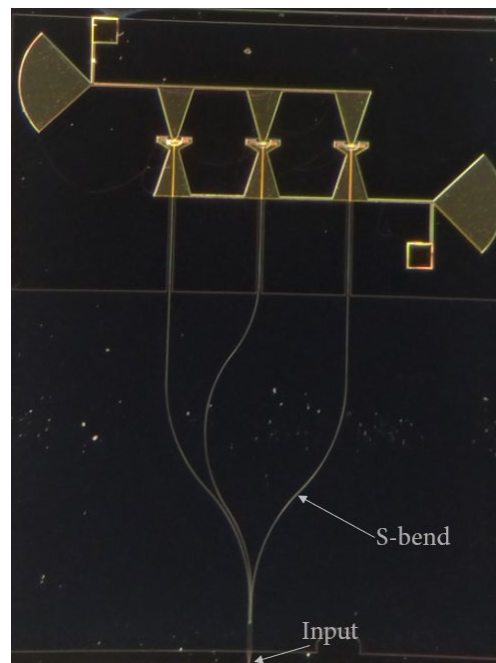


Fig. 5. 19 3x bow-tie antenna-integrated UTC PD structure with optical waveguides after fabrication and cleaving.

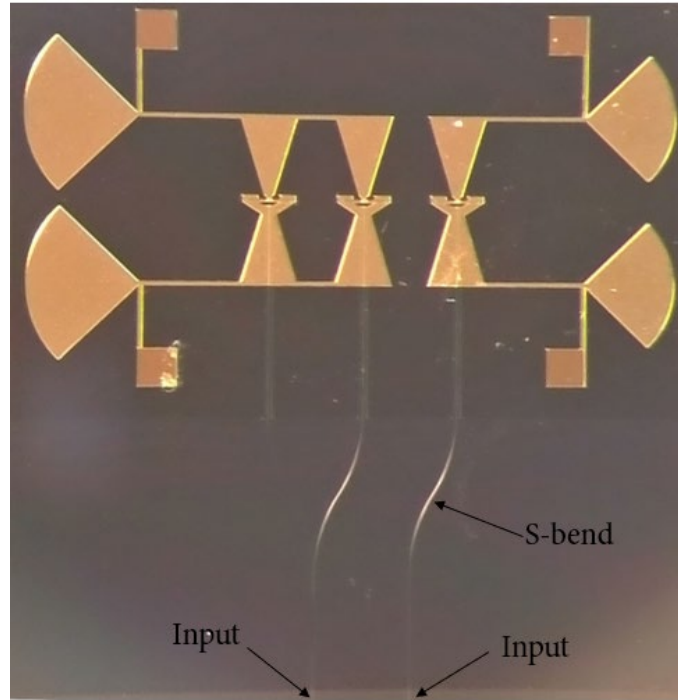


Fig. 5. 20 2x bow-tie and 1x bow-tie separated antenna-integrated UTC PD structure with optical waveguides after fabrication and cleaving.

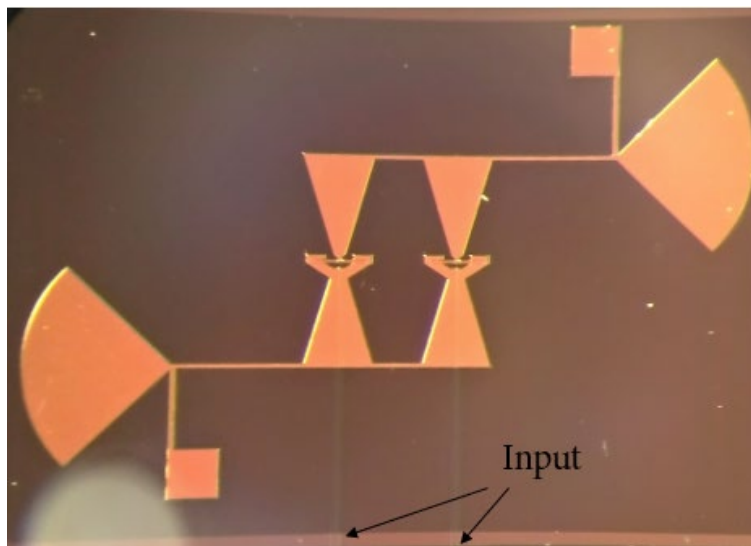


Fig. 5. 21 Connected 2x bow-tie antenna-integrated UTC PD structure with optical waveguides after fabrication and cleaving.

In summary, during this complex fabrication process, 12 levels of lithography masks were designed and additional tests to finalize processing steps were performed. Moreover, due to only one substrate available for the final process some of the steps could not have been tested with a dummy substrate before. That also greatly increased the breakage risk of the substrate. Nevertheless, process was finalized with the bigger part of the substrate. Optical inspection did not reveal serious fabrication issues, although problem with uniformity was observed.

To conclude:

- **Process was very complex and 12 lithography masks and epitaxial re-growth were required.**
- **Additional test substrates were utilized during the processing to established new fabrication steps (i.e. NiCr resistors).**
- **Unfortunately, only one substrate was available for the final process, and it broke down during one of the fabrication steps, what greatly complicated further processing, and part of the devices were lost.**
- **Process was completed with the bigger part of the broken substrate, but it suffered due to additional problems with uniformity.**

CHAPTER 6

MEASUREMENTS AND RESULTS

This chapter presents measurement results and experimental setups used for the optical and electrical characterization of single UTC PDs, Wilkinson power combiners and antenna-integrated UTC PDs. As described in Chapter 6, fabrication process encountered problems with the uniformity and unfortunate substrate breakage. What is more, the I-V characteristics of the fabricated devices revealed additional issues. Measured values of series resistance (R_s) greatly exceed 50Ω and in certain cases reaches up to ca. 6000Ω for a single UTC PDs. The antenna-integrated devices suffer from even higher values of series resistance, reaching up to ca. $60 \text{ k}\Omega$. These values are much above of any previously assumed series resistance values in the simulations. Further investigation of the cause is required due to the complexity of the fabrication process. Moreover, measured different series resistance values also indicates that uniformity issues faced during the fabrication process greatly impacted the devices. As a consequence, very weak performance of the designed devices' is inevitable, what also reduced the number of measurement experiments that could have been performed. Nevertheless, the bandwidth and compression point measurement were possible to be implemented at lower frequencies for single UTC PDs. The devices with Wilkinson power combiners and the antenna-integrated devices were characterized at lower frequencies as well. This also additionally impacted the performance, as the designed devices dimensions are optimized for different target frequencies.

Additional measurements of single UTC PDs and antenna-integrated devices, fabricated during different processing runs without fabrication issues, but never characterized, are presented in this chapter as well. Furthermore, experimental results of optoelectronic comb generation and cross-injection locking of photonic integrated circuit from previous fabrication run are also demonstrated. Obtained results are published in [7].

6.1 MEASURED DEVICES - DESCRIPTION

An overview of the devices fabricated within the Fiwin5G project are presented in Fig. 6. 1. As mentioned in the introduction, devices fabricated before this PhD thesis within iPHOS project are characterized as well, and an overview is presented in Fig. 6. 2.


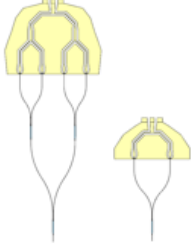
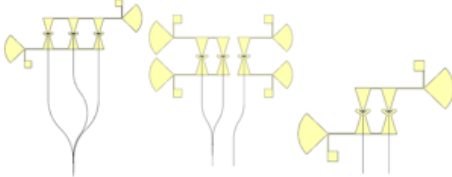
Fiwin5G		
Device	Measurement	Chapter
UTC PDs 	<ul style="list-style-type: none"> Electrical parameters: <ul style="list-style-type: none"> ✓ I-V characteristics ✓ Dark current characteristics Bandwith up to 40 GHz 1-dB compression point at 20 GHz Propagation losses of optical waveguides 	6.2 6.3 6.3 6.3.1
Wilkinson power combiners with 	<ul style="list-style-type: none"> Electrical parameters: <ul style="list-style-type: none"> ✓ I-V characteristics Bandwidth up to 40 GHz 1-dB compression point at 20 GHz S-parameters with VNA up to 65 GHz Propagation losses of optical waveguides 	6.2 6.3 6.3 6.2.2 6.3.1
Antenna-integrated UTC PDs 	<ul style="list-style-type: none"> Electrical parameters: <ul style="list-style-type: none"> ✓ I-V characteristics Frequency response at 50 GHz 	6.2 6.3.3

Fig. 6. 1 An overview of characterized devices fabricated within the Fiwin5G project.





iPHOS		
Device	Measurement	Chapter
UTC PDs 	<ul style="list-style-type: none"> Electrical parameters: <ul style="list-style-type: none"> ✓ I-V characteristics ✓ Dark current characteristics 1-dB compression point at 20 GHz Bandwidth from 77 GHz – 110 GHz 	6.2.1 6.3 6.3.2
Antenna-integrated UTC PDs 	<ul style="list-style-type: none"> Bandwidth from 77 GHz – 110 GHz 	6.3.4
Antenna-integrated UTC PD with Mode-locked laser 	<ul style="list-style-type: none"> Frequency response from 77 GHz – 110 GHz 	6.4
Photonic integrated circuit 	<ul style="list-style-type: none"> Optoelectronic comb generation and cross-injection locking 	6.5

Fig. 6. 2 An overview of characterized devices fabricated within the iPHOS project.

6.2 ELECTRICAL PARAMETERS – FIWIN5G – MEASUREMENTS AND DISCUSSION

In this chapter electrical parameters of measured devices are presented. The dark current characteristics versus bias voltage are depicted in Fig. 6. 3. Values of the dark current are in the range 10^{-8} – 10^{-7} A at -4 V of bias. Values are very similar between different photodiodes dimensions. The biggest scaling impact on the dark current values is recorded for the smallest photodiodes group L1W1 – L1W4, as presented in Fig. 6. 4. It might be connected with the surface leakage current and damage caused during fabrication. Nevertheless, this tendency is not observed for other dimensions.

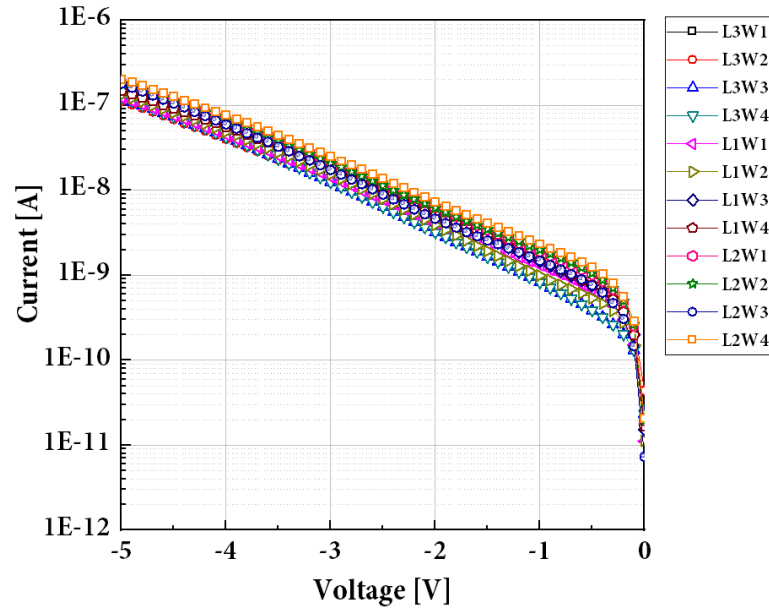


Fig. 6. 3 Dark current versus bias voltage for single UTC PDs for all of the dimensions.

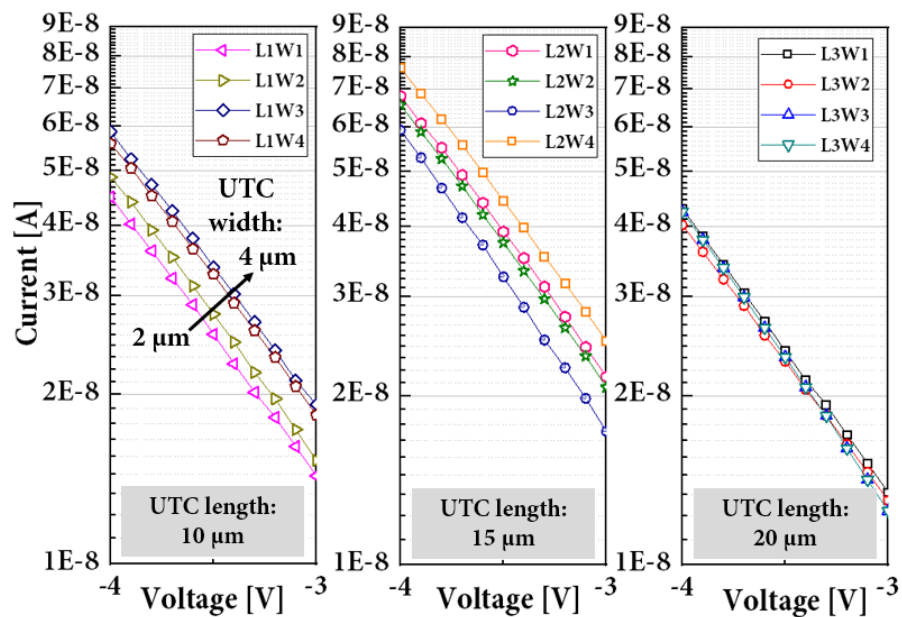


Fig. 6. 4 Dark current versus bias voltage for single UTC PDs for different dimensions group.

The I-V characteristics of UTC PDs in the forward direction are presented in Fig. 6. 5. As can be observed values of series resistance estimated from the curves are in the range of 1.5 k Ω up to 6 k Ω . The highest series resistance is recorded for the shortest photodiodes with 10 μm of length. Comparison results are presented in Fig. 6. 6.

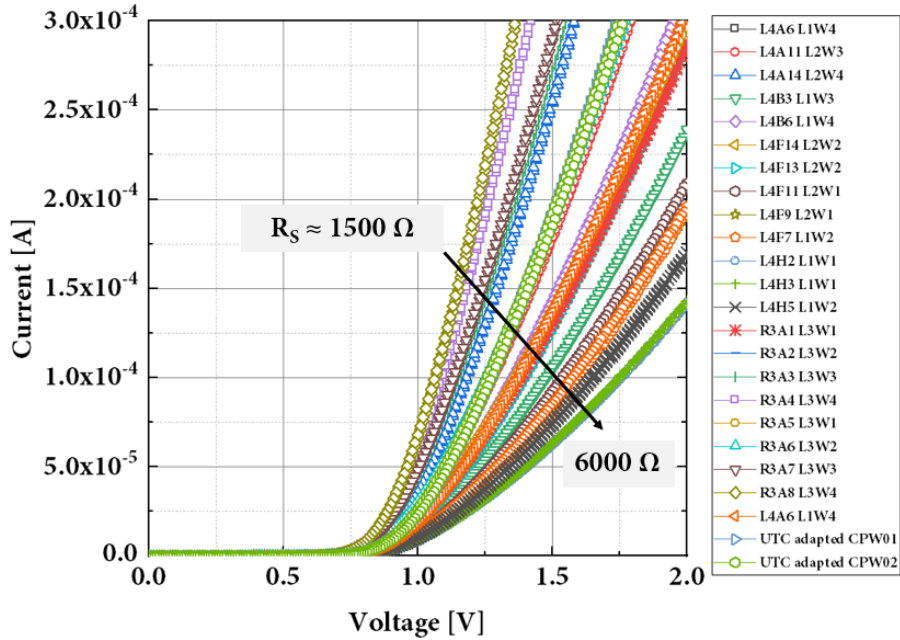


Fig. 6. 5 The I-V characteristics of single UTC PDs for all of dimensions.

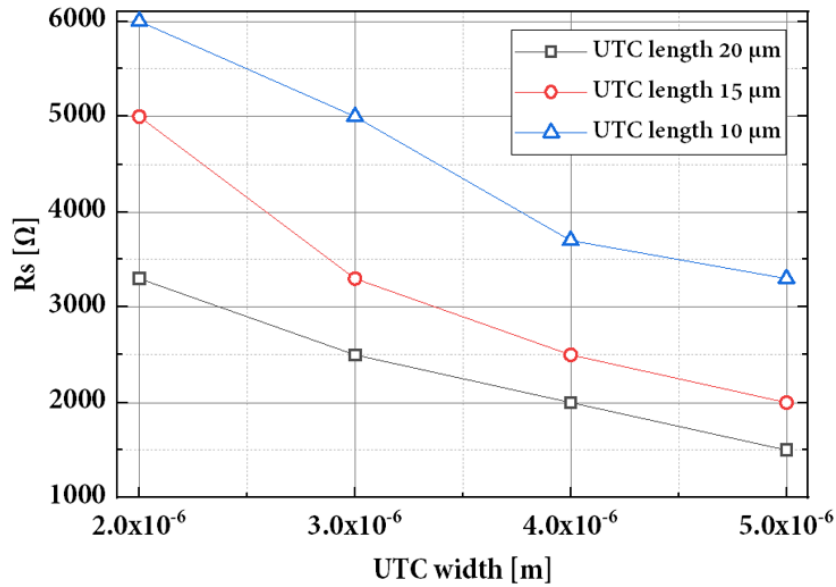


Fig. 6. 6 Comparison of the series resistance values between different dimensions of the UTC PDs.

Current densities for all the UTC dimensions are presented in Fig. 6. 7. The highest value is obtained for the biggest photodiode L3W4 (5 μm x 20 μm). As can be observed, current

density for majority of the structures varies in the range from 0.05 A/cm^2 up to 0.08 A/cm^2 . The lowest value is recorded for the smallest photodiode L1W1.

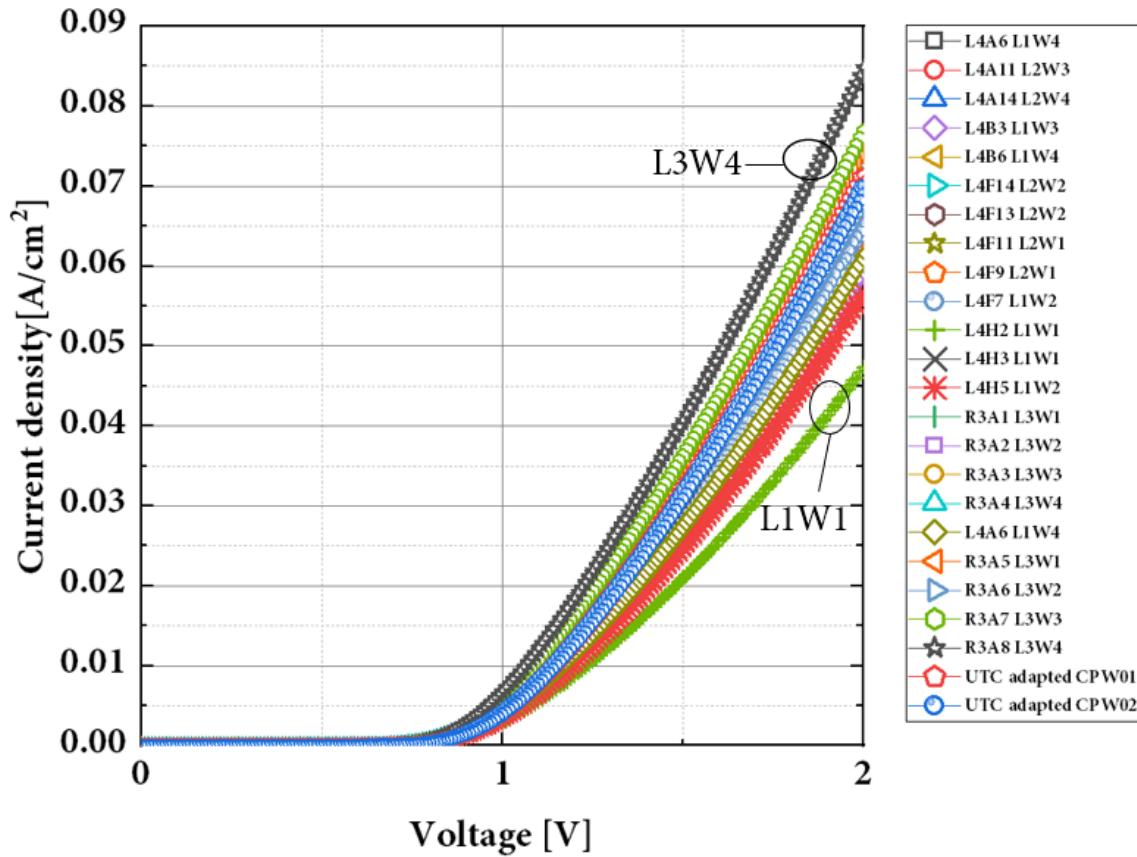


Fig. 6. 7 The current density characteristics of single UTC PDs for all dimensions.

The I-V characteristics are also measured for the Wilkinson power combiners and antenna-integrated devices. Based on the results, values of series resistance for a parallel connected UTC PDs in the Wilkinson power combiners are ca. $2 \text{ k}\Omega$. In the antenna integrated devices, single UTC PDs are also in a parallel connection. The R_s for a 3x folded-dipole antenna is about ca. $3 \text{ k}\Omega$. The highest R_s values are estimated for bow-tie antenna structures, what also shows how substrate uniformity problems affects the devices. In the single bow-tie antenna structure, value of R_s is ca. $25 \text{ k}\Omega$, but for the 3x bow-tie antenna structure it reaches ca. $60 \text{ k}\Omega$. The reason of extremely high values of series resistance due to complexity of the fabrication process is not easily explainable. This can be caused due to unexpected doping level problems, possible contamination during processing or epitaxial re-growth or, as well, can be connected with metal contacts deposition.

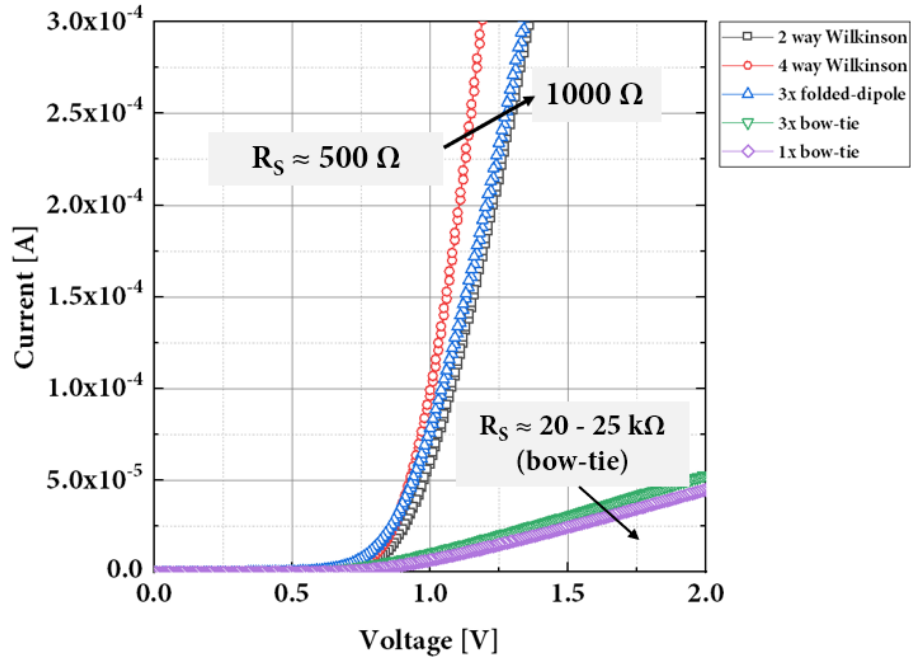


Fig. 6. 8 I-V characteristics of Wilkinson power combiners and antenna-integrated devices.

	Series resistance, R_S (for single UTC PD)
UTC PDs	1.5 k Ω – 6 k Ω
2-way Wilkinson	2 k Ω
4-way Wilkinson	2 k Ω
3x folded-dipole antenna	3 k Ω
3x bow-tie antenna	60 k Ω
2x bow-tie antenna	4 k Ω
1x bow-tie antenna	25 k Ω

Fig. 6. 9 Comparison of the R_S values between different devices based on I-V characteristics.

Additional electrical measurements to check the under-bridge connections in the Wilkinson power combiner structures were performed. The same approach, as during the I-V measurements was applied. In Fig. 6. 10 an example of the procedure employed for 2-way Wilkinson power combiner is presented. Similar approach is applied to the 4-way Wilkinson power combiner.

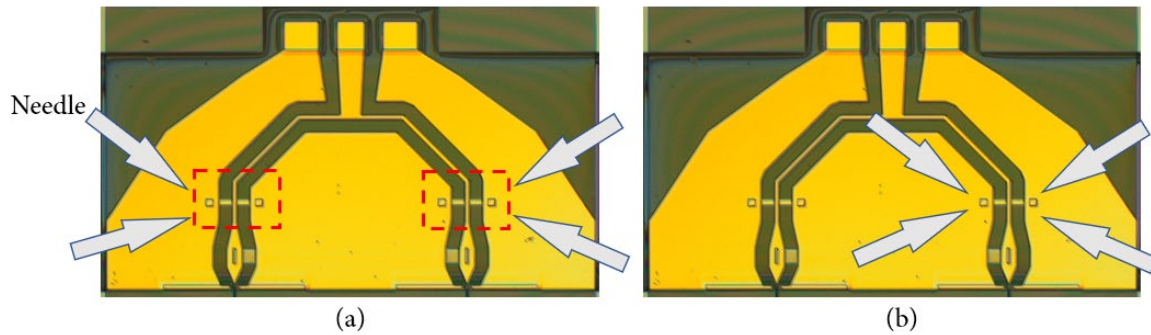


Fig. 6. 10 Electrical inspection of the under-bridge connection (a) from side-to-side and (b) side-to-middle of 2-way Wilkinson power combiner.

Based on the measurements, the under-bridge connection resistance is about 7Ω from side-to-side, and 3.5Ω for a side-to-middle. In the 4-way Wilkinson power combiner, the side-to-side value is about 9Ω . Values of single connections are more difficult to be estimated as the 4-way Wilkinson device contains 8 under-bridges, as depicted in Fig. 5. 15. This electrical inspection proves that, under-bridges are well established and applied fabrication process was successful.

	Series resistance, R_s (under-bridge connection)	
	Theoretical	Estimated
2-way Wilkinson (Length: $147 \mu\text{m}$; width: $17 \mu\text{m}$)	0.63Ω	$< 3.5 \Omega$
4-way Wilkinson (Length: $155 \mu\text{m}$; width: $7 \mu\text{m}$)	1.62Ω	$< 2 \Omega$

$\rho_{\text{Gold}} = 2.2 \times 10^{-8} [\Omega \times \text{m}]$
Gold thickness ca. 300 nm

Fig. 6. 11 Estimated values of R_s for under-bridge connections in the 2-way and 4-way Wilkinson power combiner structure in comparison to theoretical values.

To conclude:

- **Measured dark current values are in the range of $10^{-8} - 10^{-7}$ A at -4 V of bias.**
- **Unfortunately, due to fabrication processing problems extremely high series resistance values are measured. For the UTC PDs R_s values varies from 1.5 k Ω up to ca. 6 k Ω . The antenna-integrated devices also suffer from very high R_s values, reaching 60 k Ω in the most extreme case for 3x bow-tie antenna structure. For the Wilkinson power combiners, the R_s values are ca. 2 k Ω .**
- **The I-V measurement of the under-bridge connections, as presented in Fig. 6. 10, proved that the fabrication process was successful and the established connections and corresponding R_s values are close to the theoretical estimations.**

6.2.1 Electrical parameters – previous fabrication run (iPHOS)

This chapter presents electrical parameters of the devices characterized during this PhD thesis, but fabricated in the previous fabrication run. The dark current characteristics versus bias voltage are depicted in Fig. 6. 12. Measured UTC PDs are 15 μm long with the widths of 2 μm , 3 μm and 4 μm , respectively. Values of the dark current are in the range $10^{-8} - 10^{-6}$ A at -4 V of bias, and only one UTC PD is above this range (D2x15). The forward I-V characteristics are presented in Fig. 6. 13.

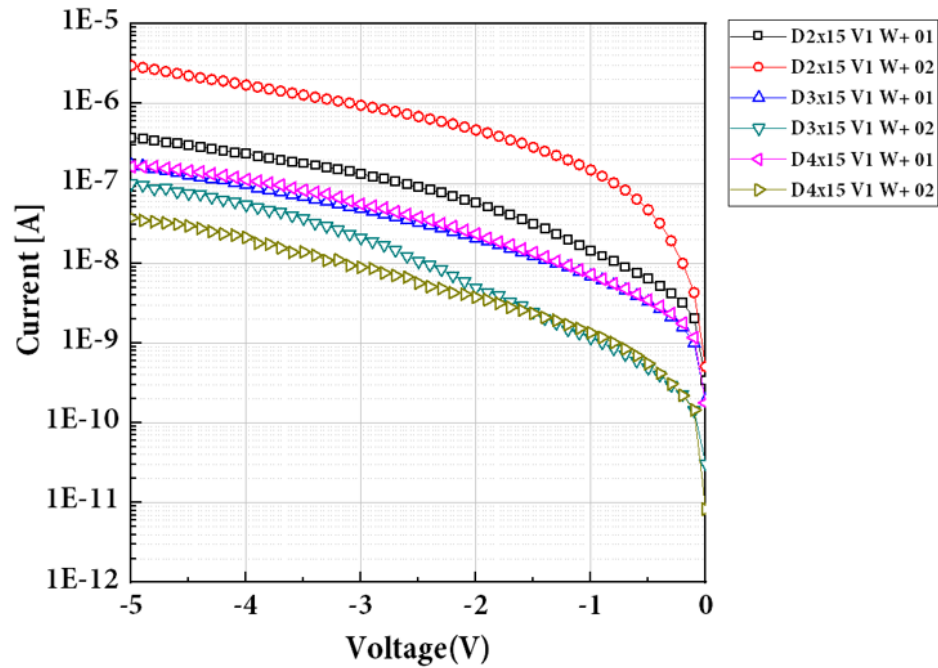


Fig. 6. 12 Dark current versus bias voltage for single UTC PDs from iPHOS fabrication run.

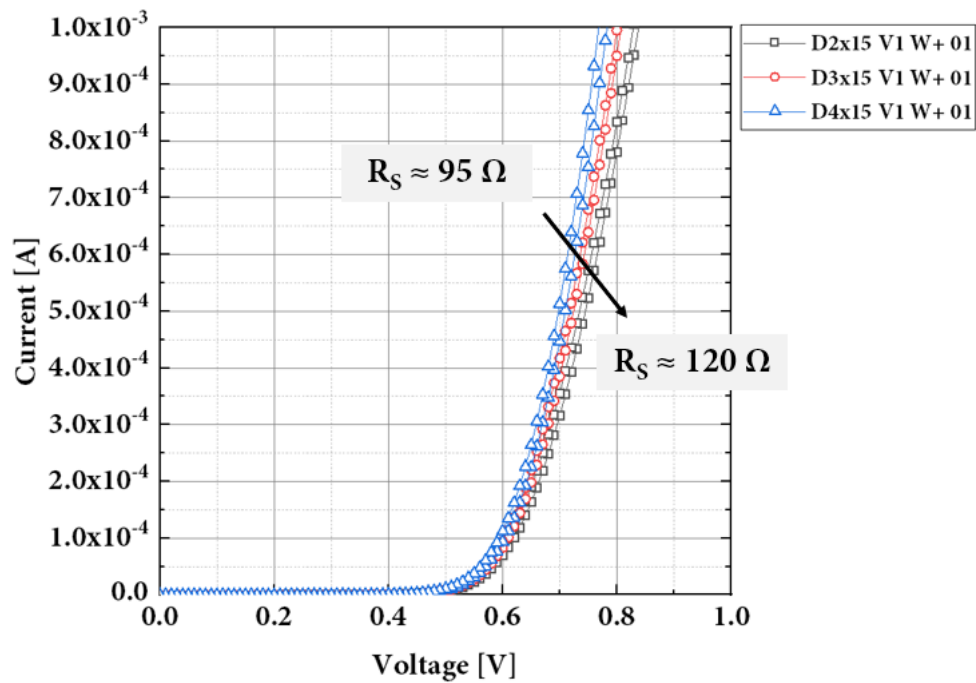


Fig. 6. 13 The I-V characteristics of single UTC PDs from iPHOS fabrication run.

As expected from this fabrication run, values of the R_s are much lower, and they vary from 95Ω up to ca. 120Ω . It also shows that this particular fabrication run also experienced some fabrication issues. Nevertheless, the outcome results of series resistance are much better and do not influence the device performance in such extent as in the case of Fiwin5G run.

	Series resistance, R_s (for single UTC PD)
UTC 2x15	120Ω
UTC 3x15	100Ω
UTC 4x15	95Ω

Fig. 6. 14 Comparison of the R_s values between iPHOS UTC PDs based on I-V characteristics.

To conclude:

- **Measured dark current values are in the range of $10^{-8} - 10^{-6} \text{ A}$ at -4 V of bias.**
- **The series resistance values are in the range of 90Ω to 120Ω , and therefore better performance of the devices from iPHOS fabrication run in terms of output power levels and 3-dB bandwidth is expected.**

6.2.2 Wilkinson power combiners – measurements with VNA up to 65 GHz

In this subchapter measurement setup and results of passive characterization of the Wilkinson power combiners are presented (Fig. 6. 15). In order to measure the s-parameters, the VNA (Anritsu 37397C) and two GSG probes are utilized (Cascade ACP 65-A) with 150 μm pitch. One GSG probe, with 100 μm of pitch, is terminated with 50 Ω load resistor. Measurement setup allows to characterize the circuit up to 65 GHz. Prior the measurement, calibration with SOLT (Short, Open, Load, Thru) calibration kit (Cascade) is performed. Furthermore, it is important to note that, the designed Wilkinson power combiner structures are not fully adapted for the s-parameter measurements. The GSG probes are placed on the 50 Ω transmission lines of the Wilkinson circuit but only the output dimensions are designed for the GSG probing, as presented in Fig. 6. 16. Two test configurations are employed during the s-parameters measurement experiment and are depicted in Fig. 6. 17. Configuration number 1. corresponds to the signal transmission between the input and the output, when only one input is available. For the second configuration, the isolation between the two input transmission lines can be measured. For these configurations, three active GSG probes would have been more accurate to characterize the circuit, but due to setup limitation the third probe is terminated with 50 Ω resistor. Moreover, additional difficulties are faced during the measurements, as the space for placing two GSG probes is very limited (Fig. 6. 16).

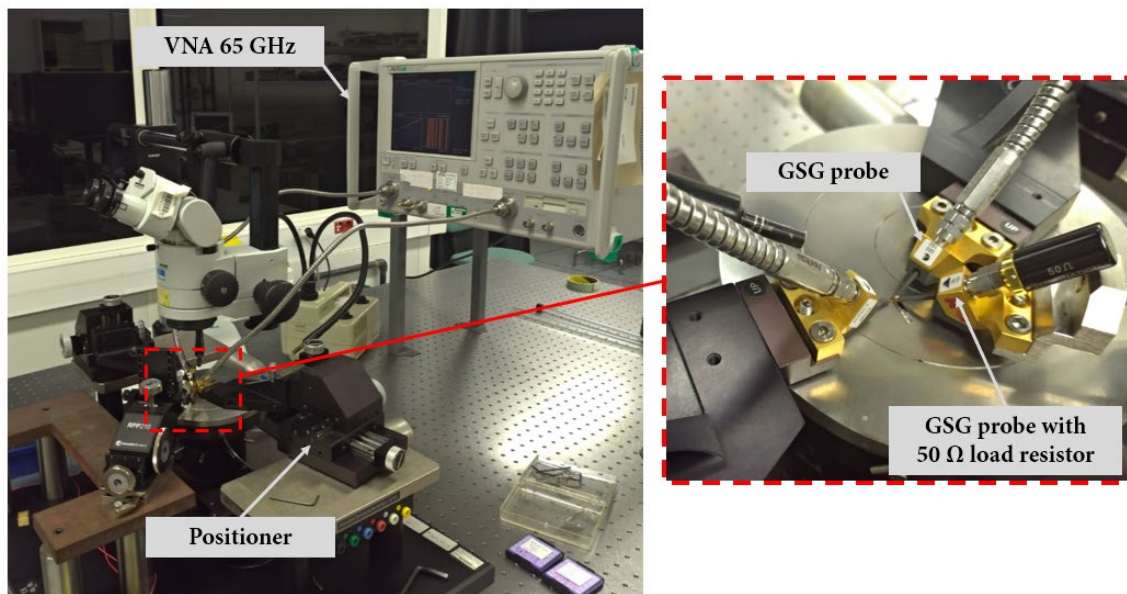


Fig. 6. 15 Measurement setup used for s-parameters measurements of the 2-way and 4-way Wilkinson power combiners with UTC PDs.

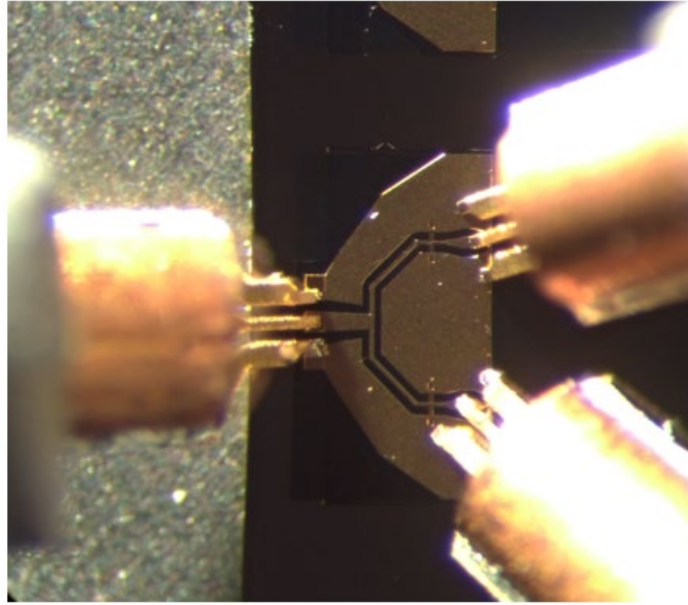


Fig. 6. 16 The 2-way Wilkinson power combiner with GSG probes used for the s-parameters measurements.

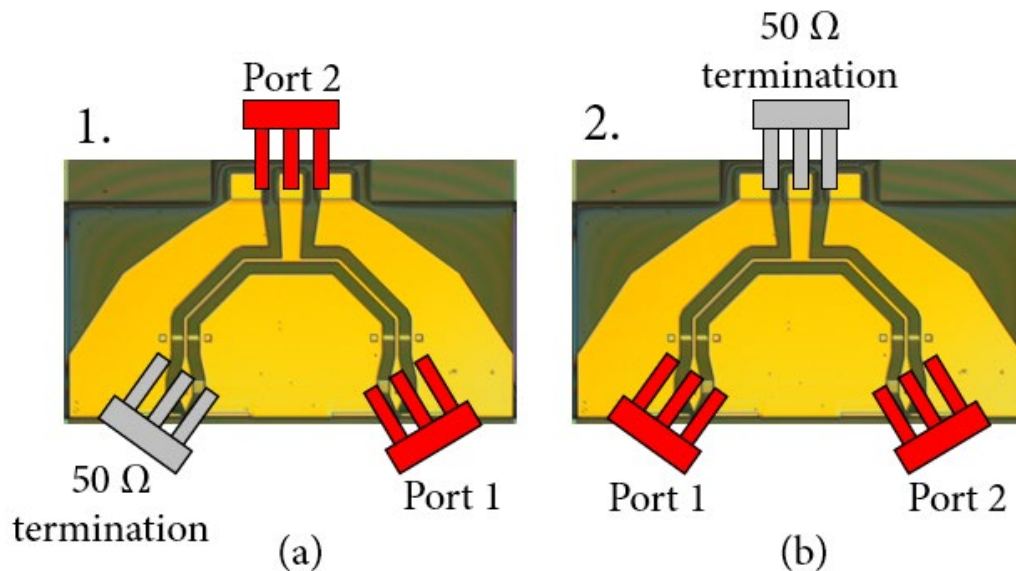


Fig. 6. 17 Schematic of the GSG probes position in a configuration (a) for a transmission (no. 1) and (b) for the isolation (no. 2) measurements of the s-parameters of the 2-way Wilkinson power combiner. The same configurations are used in the HFSS simulations.

In Fig. 6. 18, measurement results of the s-parameters for the configuration of the transmission between the input and output (no. 1) are presented. As can be observed, results differ between the 2-way Wilkinson power combiner with (Fig. 6. 18) and without isolation

resistors (Fig. 6. 19). Transmission losses (s_{12}/s_{21}), as expected from the HFSS simulations, are smaller for the circuit without isolation resistors. The s_{11} reflections are high for both types of combiners, but it is the result of not adapted transmission lines for the GSG probing, as shown in Fig. 6. 16. These configurations are also simulated with HFSS software and presented in Fig. 6. 18 and Fig. 6. 19. Good agreement between measured and simulated circuits proves that the simulation model behaviour is very similar to the real devices.

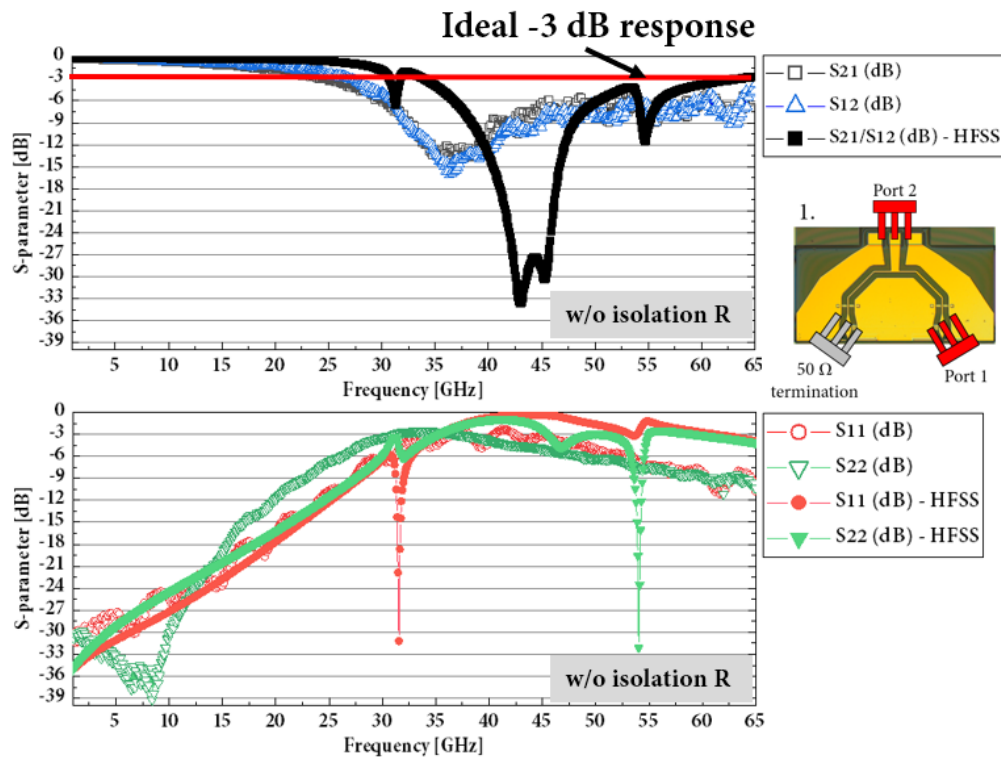


Fig. 6. 18 Transmission measurement and HFSS simulation of the s-parameters of the 2-way Wilkinson power combiner without isolation resistor (configuration no. 1).

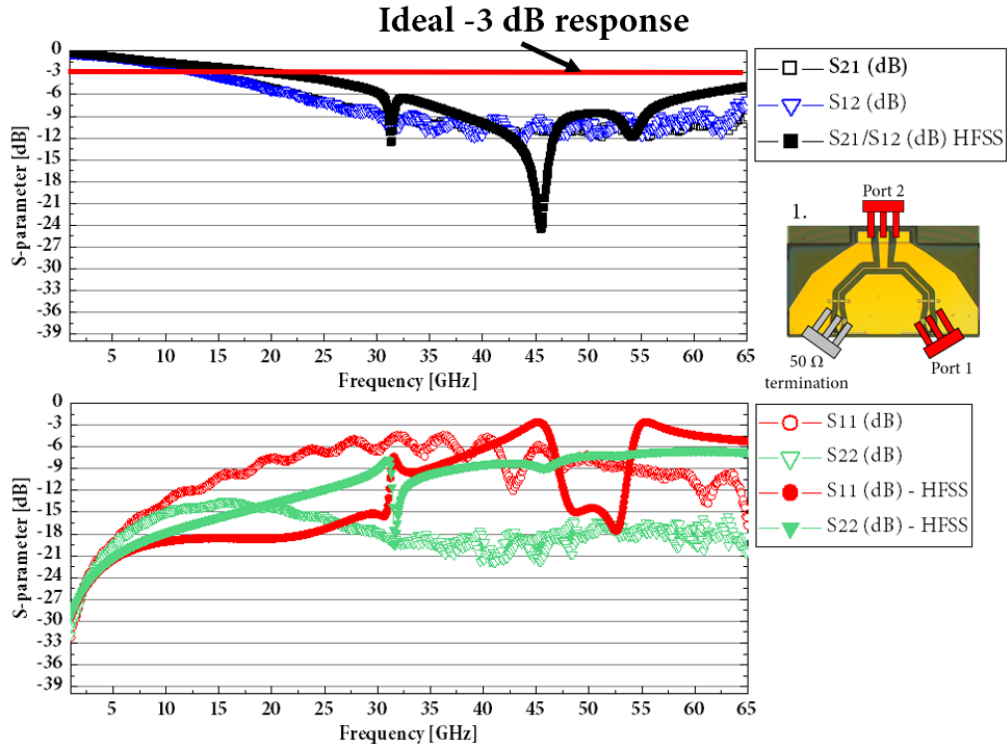


Fig. 6. 19 Transmission measurement and HFSS simulation of the s-parameters of the 2-way Wilkinson power combiner (configuration no. 1).

In Fig. 6. 20 and Fig. 6. 21 the measurement and simulation results of the isolation between the inputs are depicted. Differences between s_{11} and s_{22} signals show the influence of the probe positions on the transmission lines. Due to the GSG probe dimensions, placing them in the exactly same positions at the $50\ \Omega$ transmission lines is not possible, as presented in Fig. 6. 16. This configuration is also simulated with HFSS software and presented in Fig. 6. 20 and Fig. 6. 21. Presented results are considerably different between the simulations and the measurements. Much lower input reflections are obtained with HFSS simulations in comparison to the measured circuit. It also shows the difficulty in simulating the positions of the GSG probes during the measurement experiment and as a consequence it is not possible to reproduce the results with high precision.

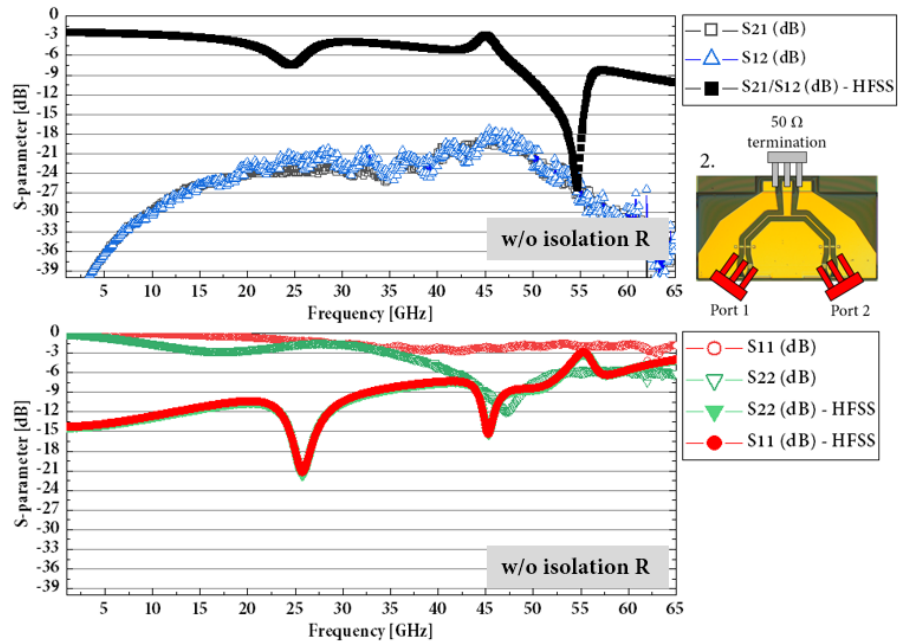


Fig. 6. 20 Isolation measurement and HFSS simulation of the s-parameters of the 2-way Wilkinson power combiner without isolation resistors (configuration no. 2).

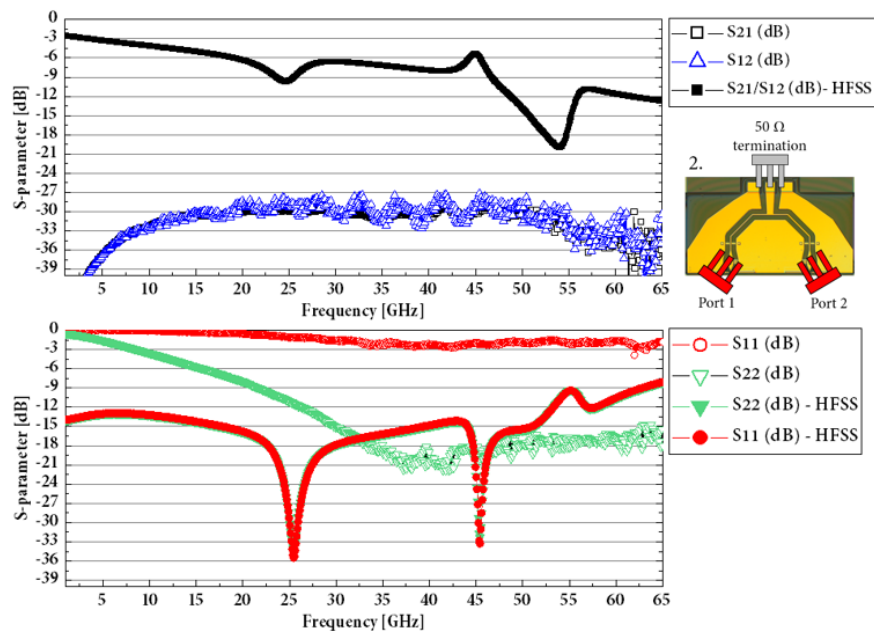


Fig. 6. 21 Isolation measurement and HFSS simulation of the s-parameters of the 2-way Wilkinson power combiner (configuration no. 2).

The 4-way Wilkinson structures are characterized in the same manner as the 2-way Wilkinson combiners. Example of the probe positions on the sample is presented in Fig. 6. 22 and measurement configurations in Fig. 6. 23.

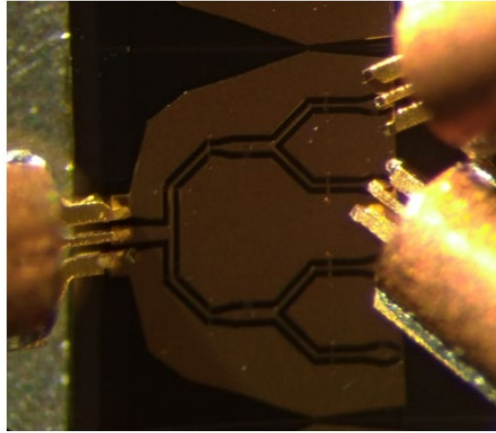


Fig. 6. 22 The 4-way Wilkinson power combiner with GSG probes used for the s-parameters measurements.

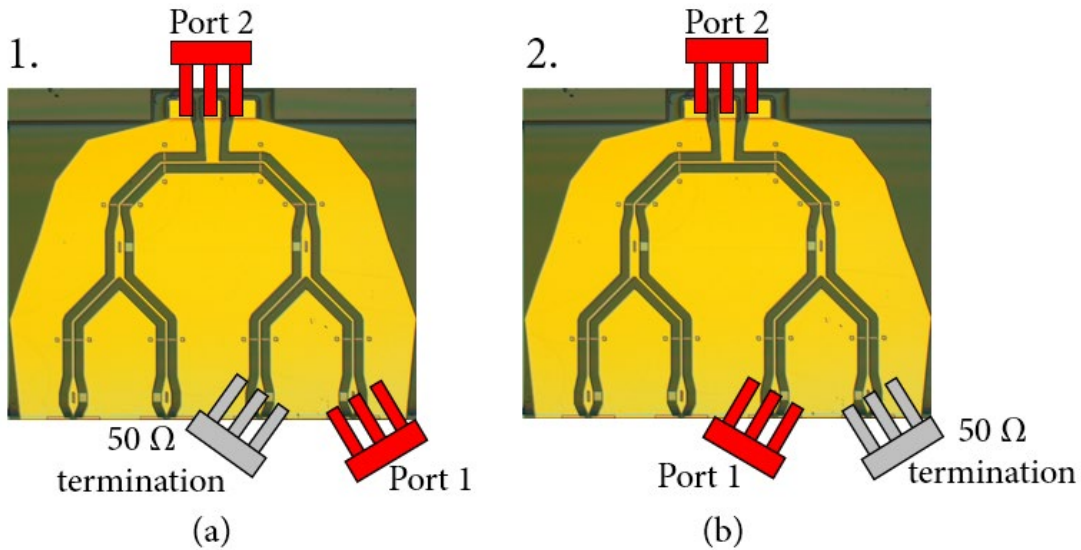


Fig. 6. 23 Schematic of the GSG probes position in configuration for a transmission measurements (a) no. 1 and (b) no. 2 of the s-parameters of the 4-way Wilkinson power combiner. The same configurations are used in the HFSS simulations.

In Fig. 6. 24 and Fig. 6. 25 measurement and simulation results for the transmission configuration no. 1 for the 4-way Wilkinson power combiner with and without isolation resistors are presented. Results for the second configuration (no. 2) of the transmission are depicted in Fig. 6. 26 and Fig. 6. 27. Similarly, to the 2-way Wilkinson combiner measurements, the transmitted signal losses are lower for the designs without isolation resistors. Moreover, high s_{11} reflections are caused by not adapted for GSG probing transmission line losses. Measured configurations were also simulated with HFSS software, and good agreements are

obtained. This also proves that the simulated models are accurate to reproduce the results of the measurements.

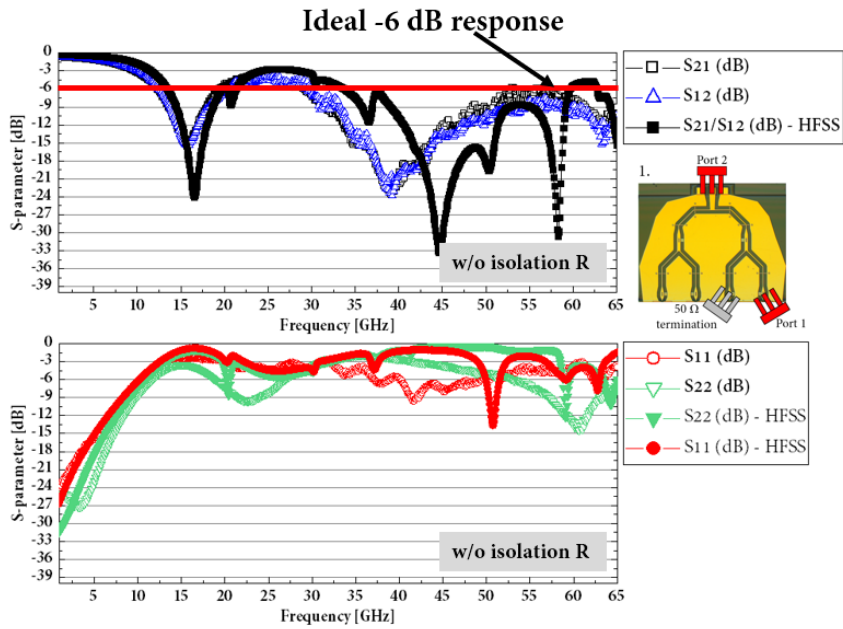


Fig. 6. 24 Transmission measurement and HFSS simulation of the s-parameters of the 4-way Wilkinson power combiner without isolation resistors (configuration no. 1).

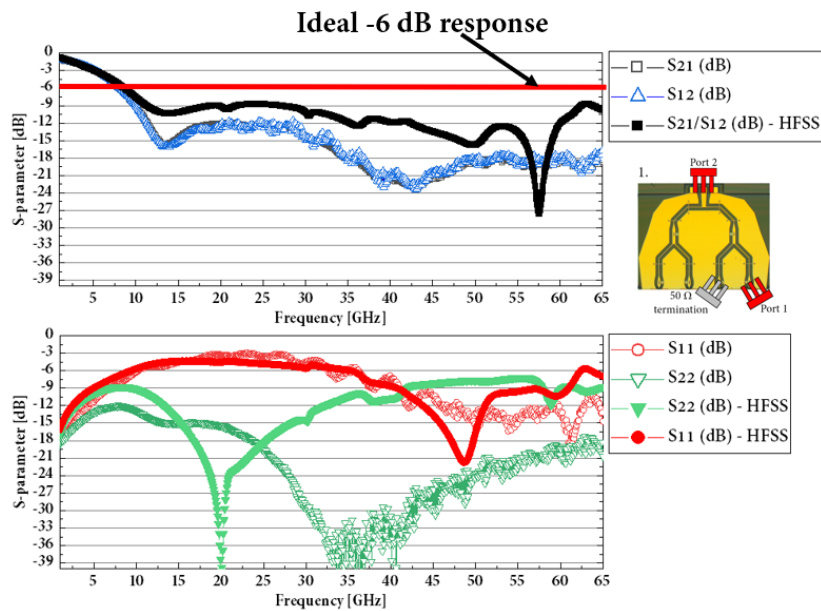


Fig. 6. 25 Transmission measurement and HFSS simulation of the s-parameters of the 4-way Wilkinson power combiner (configuration no. 1).

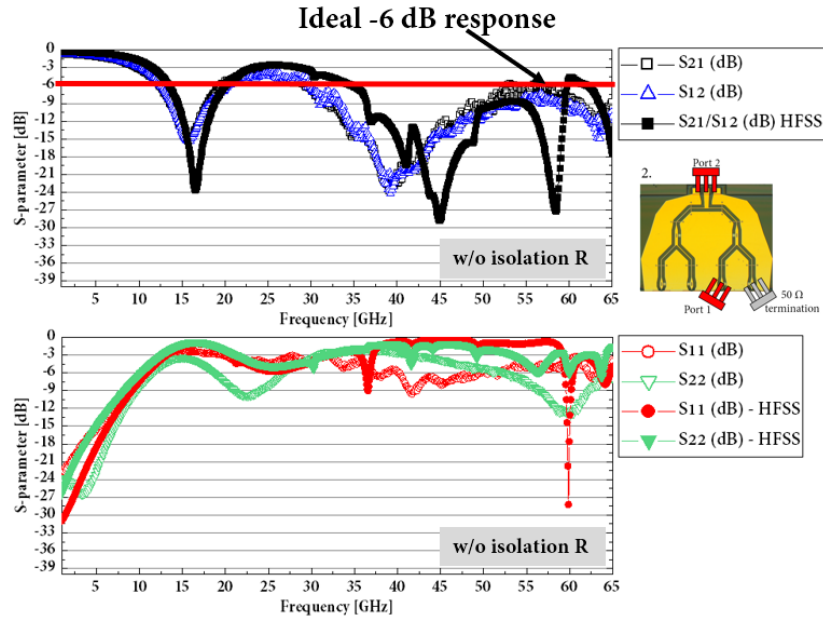


Fig. 6. 26 Transmission measurement and HFSS simulation of the s-parameters of the 4-way Wilkinson power combiner without isolation resistors (configuration no. 2).

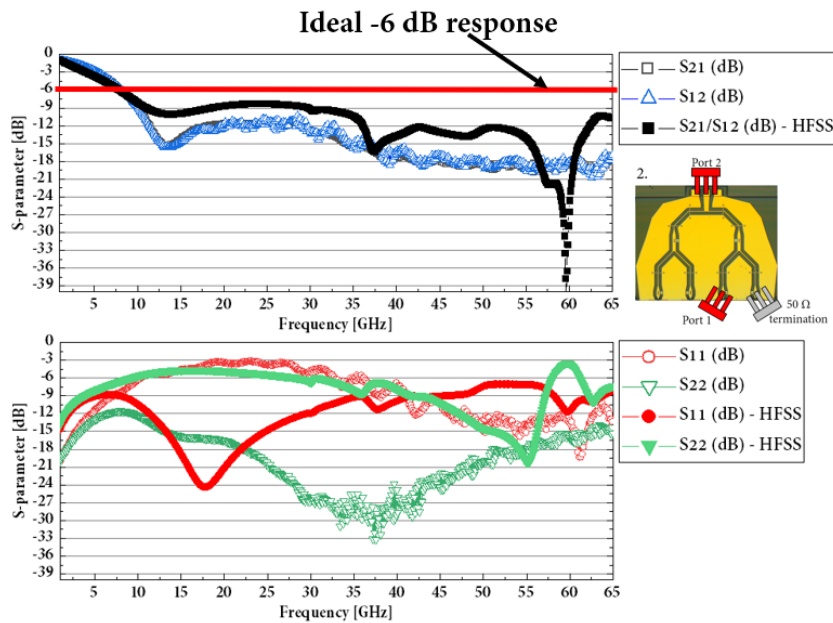


Fig. 6. 27 Transmission measurement and HFSS simulation of the s-parameters of the 4-way Wilkinson power combiner (configuration no. 2).

Measurements and HFSS simulations of the signal isolation between two inputs are performed as well. Two tested measurement configurations are presented in Fig. 6. 28. Similarly, to the 2-way Wilkinson power combiner, the position of the GSG probes on the transmission lines is not the same due to space limitations. It can be clearly observed from the measurement and simulation results in Fig. 6. 29 and Fig. 6. 30 for configuration no. 3, and from Fig. 6. 31 and Fig. 6. 32 for configuration no. 4. The values of the signals are not fully comparable with the HFSS simulations due the same difficulties with GSG probes positioning for both of the 4-way Wilkinson combiner configuration. It as well shows the difficulties to reproduce the results of measurements in the simulation environment with high precision.

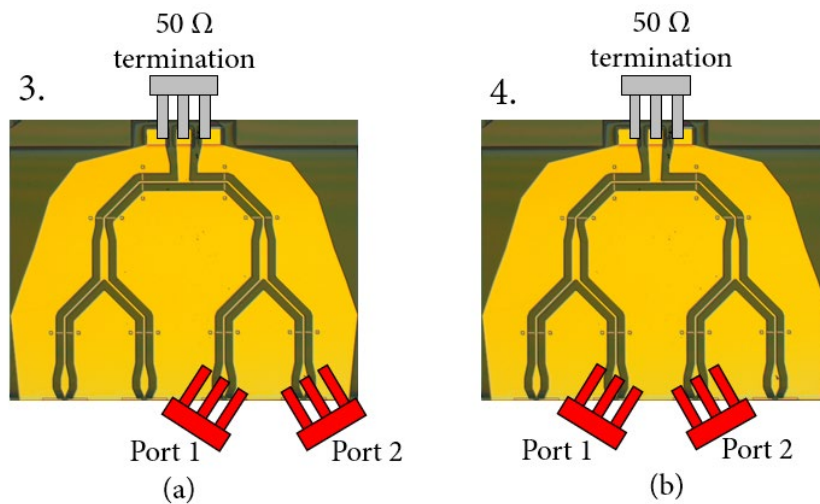


Fig. 6. 28 Schematic of the GSG probes position in configuration for an isolation measurement in configuration (a) no. 3 and (b) no. 4 of the s-parameters of the 4-way Wilkinson power combiner. The same configurations are used for the HFSS simulations.

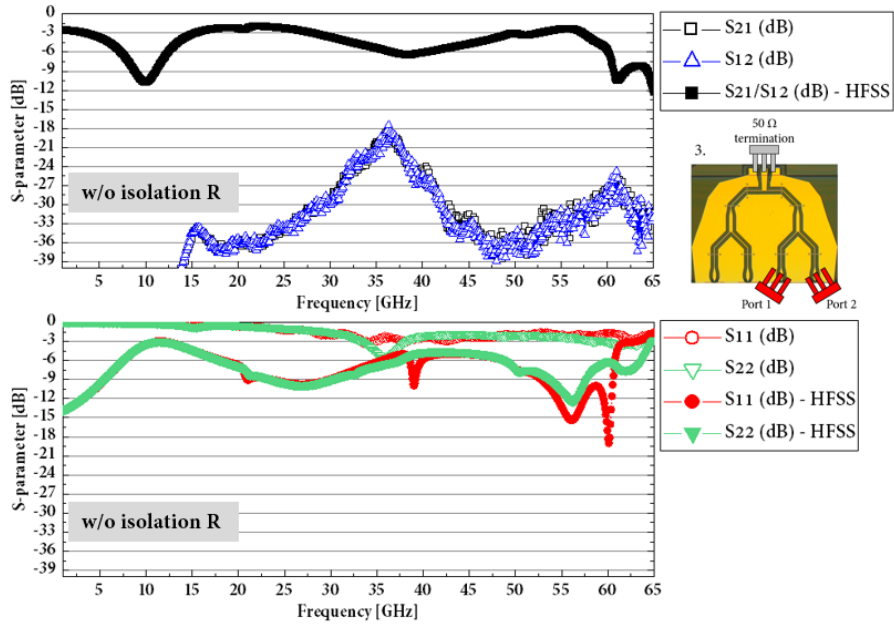


Fig. 6. 29 Isolation measurement and HFSS simulation of the s-parameters of the 4-way Wilkinson power combiner without isolation resistors (configuration no. 3).

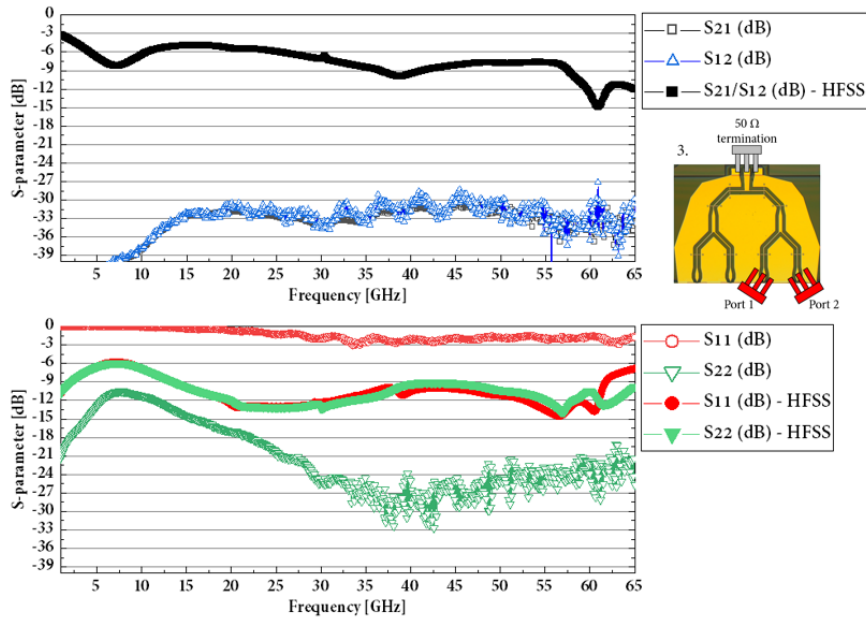


Fig. 6. 30 Isolation measurement and HFSS simulation of the s-parameters of the 4-way Wilkinson power combiner (configuration no. 3).

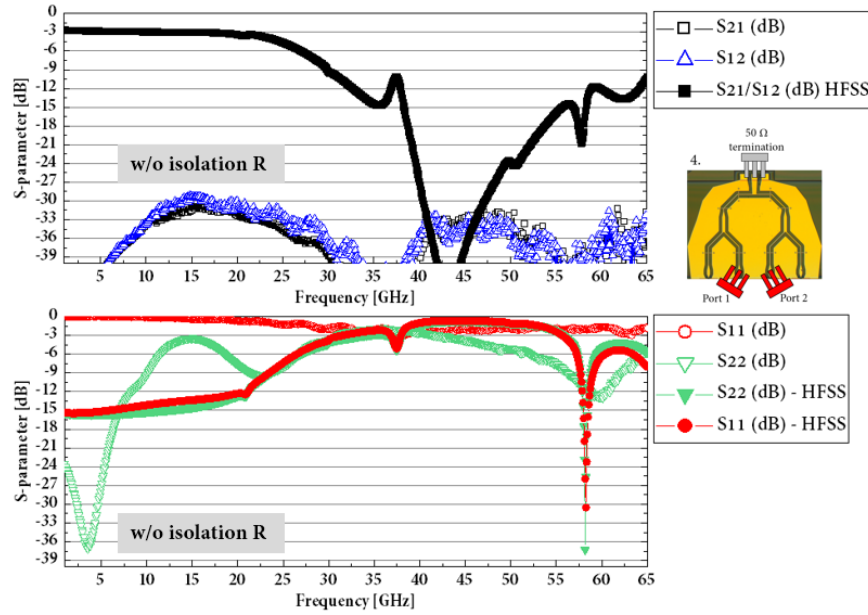


Fig. 6. 31 Isolation measurement and HFSS simulation of the s-parameters of the 4-way Wilkinson power combiner without isolation resistors (configuration no. 4).

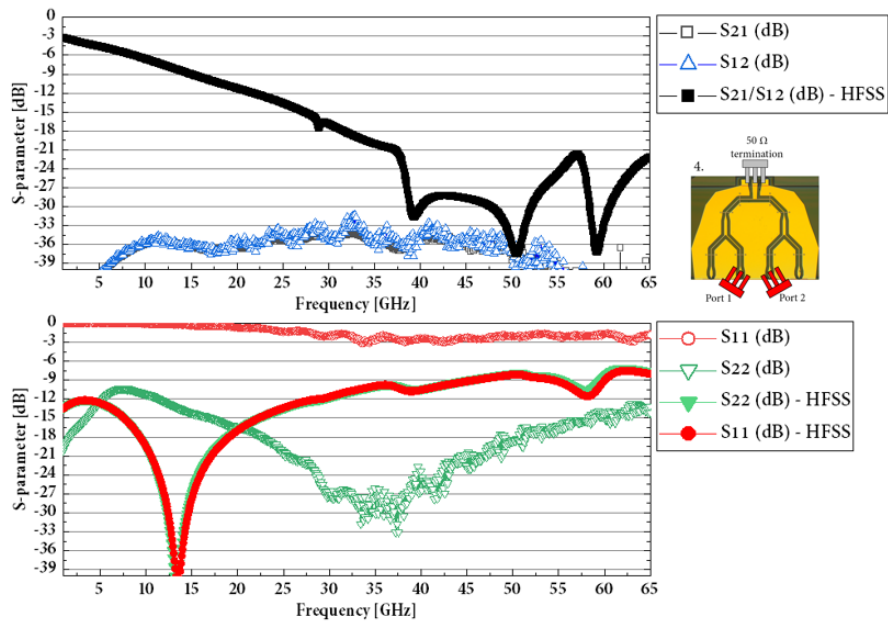


Fig. 6. 32 Isolation measurement and HFSS simulation of the s-parameters of the 4-way Wilkinson power combiner (configuration no. 4).

The comparison of measured s-parameters for the 2-way and 4-way Wilkinson power combiners are presented in Fig. 6. 33 and Fig. 6. 34 for the transmission (configuration no. 1) and isolation (configuration no. 2), respectively.

For configuration no. 1.	2-way Wilkinson	2-way Wilkinson without isolation resistors
Transmission (s_{21}/s_{12})	≤ -3 dB @ 1 - 8 GHz ≤ -10 dB @ 9 - 65 GHz	≤ -3 dB @ 1 - 25 GHz ≤ -15 dB @ 30 - 45 GHz ≤ -8 dB @ 45 - 65 GHz
Output match (s_{22})	≤ -15 dB @ 1 - 65 GHz	≤ -12 dB @ 1 - 20 GHz ≤ -10 dB @ 20 - 25 GHz ≤ -3 dB @ 25 - 42 GHz ≤ -3 dB @ 42 - 65 GHz
Input match (s_{11})	≤ -10 dB @ 1 - 20 GHz ≤ -7 dB @ 20 - 65 GHz	≤ -20 dB @ 1 - 20 GHz ≤ -10 dB @ 20 - 25 GHz ≤ -6 dB @ 25 - 32 GHz ≤ -3 dB @ 32 - 50 GHz ≤ -8 dB @ 50 - 65 GHz

Fig. 6. 33 Comparison of measured s-parameters for the 2-way Wilkinson power combiner in the transmission configuration (no. 1).

For configuration no. 1. and 2.	4-way Wilkinson	4-way Wilkinson without isolation resistors
Transmission (s_{21}/s_{12})	≤ -6 dB @ 1 - 12 GHz ≤ -6 dB @ 20 - 25 GHz ≤ -20 dB @ 30 - 50 GHz ≤ -10 dB @ 50 - 65 GHz	≤ -3 dB @ 1 - 8 GHz ≤ -18 dB @ 9 - 65 GHz
Output match (s_{22})	≤ -15 dB @ 1 - 65 GHz	≤ -10 dB @ 1 - 12 GHz ≤ -3 dB @ 12 - 20 GHz ≤ -6 dB @ 20 - 27 GHz ≤ -3 dB @ 27 - 55 GHz ≤ -9 dB @ 55 - 65 GHz
Input match (s_{11})	≤ -6 dB @ 1 - 20 GHz ≤ -3 dB @ 10 - 35 GHz ≤ -12 dB @ 35 - 65 GHz	≤ -10 dB @ 1 - 8 GHz ≤ -6 dB @ 8 - 10 GHz ≤ -3 dB @ 10 - 35 GHz ≤ -6 dB @ 35 - 65 GHz

Fig. 6. 34 Comparison of measured s-parameters for the 4-way Wilkinson power combiner in the transmission configuration (no.1 and no. 2).

To conclude:

- The s-parameters measurements of the 2-way and 4-way Wilkinson power combiners are performed on the not adapted coplanar waveguides. As a consequence, there is a considerable amount of additional loss that is influencing the measurements while probing the devices with the GSG active probes. Moreover, due to setup limitations only two active probes are used and the third one is terminated with a 50Ω resistor.
- The 2-way Wilkinson power combiner, despite the above-mentioned difficulties, shows good agreement with the HFSS simulation results of the transmitted signal between the input and CPW output, as presented in Fig. 6. 18 - Fig. 6. 19. Moreover, good agreement is achieved for both types of the design structures with and without isolation resistors. In the case of measurement of the isolation between the two inputs, the HFSS simulation results differs due to much higher reflections at the inputs, in comparison to the measurements. In addition, it is also difficult to mimic the position of the GSG probes on the transmission lines in the simulation environment. Furthermore, the s-parameters are measured up to 65 GHz, which is also below the target frequency of the 2-way Wilkinson power combiner.
- The 4-way Wilkinson power combiner measurements shows good agreement with the HFSS simulation results of the transmitted signal between the input and CPW output, as presented in Fig. 6. 24 - Fig. 6. 27. Good agreement is achieved for the both types of the design structures with and without isolation resistors. Similarly, to the 2-way Wilkinson design, the isolation measurement shows differences between the simulations and the measurements. It is as well caused by the much higher input reflections, in comparison to the simulated values, and due to difficulties to mimic the GSG probe positions in the simulation environment.

6.3 BANDWIDTH AND SATURATION MEASUREMENTS

The objective of this chapter is to present the frequency response measurements performed with the setup depicted in Fig. 6. 35. Two laser sources are employed, where Laser 1 is a high-power DFB laser (Alcatel 1905LMI) and Laser 2 is an EC-Laser diode (Thorlabs SFL1550P). Laser controllers LC1 and LC2 are responsible for controlling the injection current and the temperature. The frequency of Laser 1 is fixed near 1550 nm, whereas frequency of Laser 2 is tuneable over wide frequency range by controlling the temperature of the laser. An isolator is used for L1 as it is not included in the laser package. Furthermore, the two optical signals are then coupled via polarization-maintaining coupler and split into two arms. One arm is used to monitor the two optical tones on the OSA (Anritsu MS9740A) and the beat signal via high speed photodiode on the ESA (Rohde and Schwarz FSEK30). Two EDFAs are used to deliver high power at the optical output, up to ca. 25 dBm. A lens fiber is used to fiber-to-chip coupling with the DUT (Device Under Test). The GSG probe (Cascade ACP65-A-GSG-150) is used to probe the CPW output of the device. A bias tee is used to provide a DC bias via source meter (Keithley 2400). The RF signal was measured with a calibrated power meter (Anritsu ML2437A).

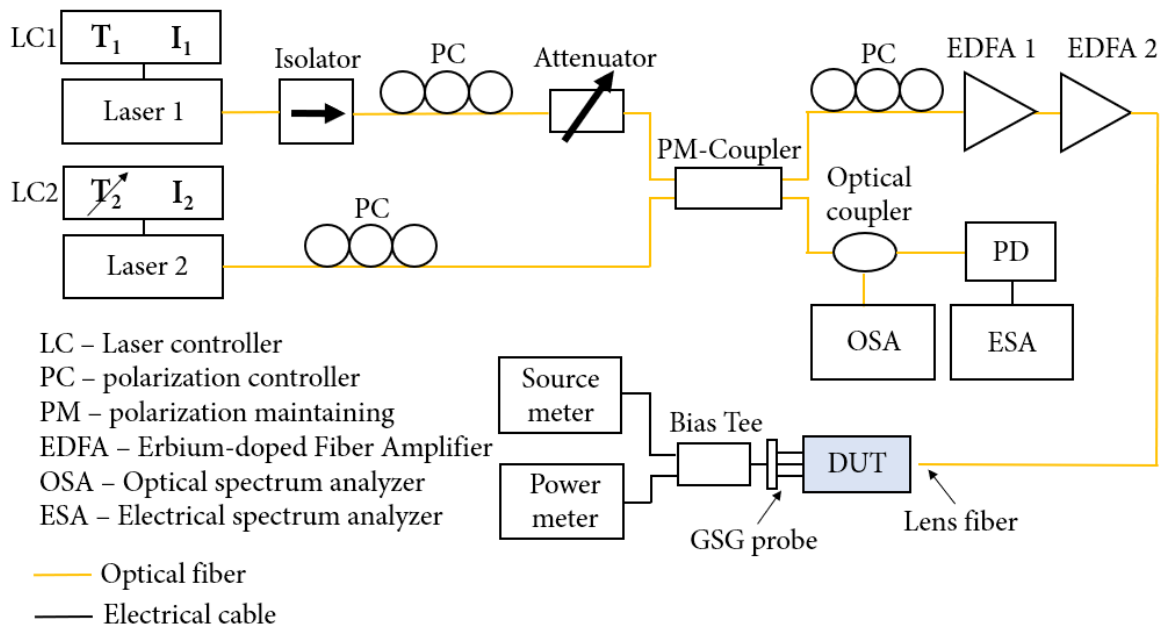


Fig. 6. 35 Optical heterodyne setup for the bandwidth measurement up to 40 GHz.

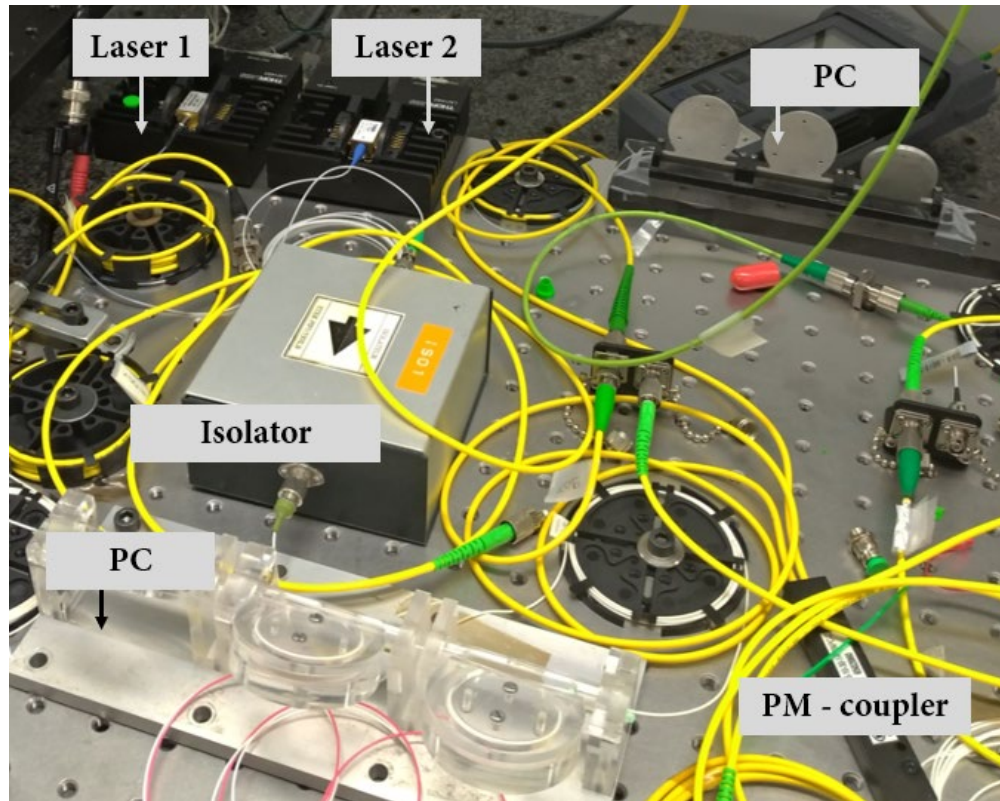


Fig. 6. 36 Optical part of the heterodyne setup used for the bandwidth and saturation current measurements; (OSA, PD, EDFs not shown).

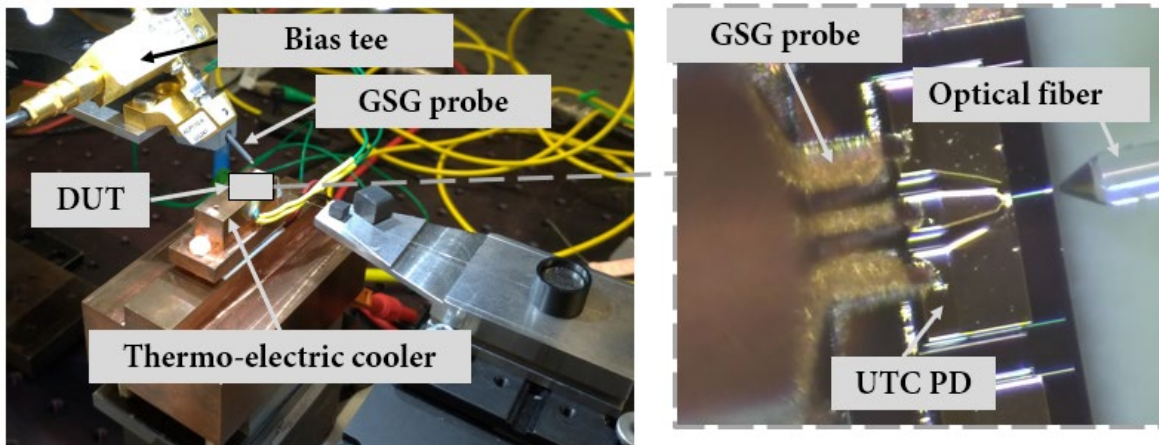


Fig. 6. 37 Fiber-to-chip coupling test bench used in the optical heterodyne setup.

The frequency response measurements up to 40 GHz are presented in Fig. 6. 38. The UTC PDs from previous fabrication run (iPHOS) delivers much higher output power levels at -4.7 V of bias in comparison to all of the measured devices. Moreover, it is also recorded that single UTC PDs deliver higher output power levels in comparison to 2-way and 4-way

Wilkinson power combiners. The reason is due to not only the considerable difference of series resistance between the structures but also due to the fact that target frequencies optimal for the power combiners are not at the 20 GHz range. For the 2-way Wilkinson power combiner (presented in Fig. 4. 26 - Fig. 4. 29 in chapter 4), frequencies around 70 GHz should be considered. For the 4-way Wilkinson (presented in Fig. 4. 37 - Fig. 4. 42 in chapter 4), frequencies nearby 43 GHz, 47 GHz and 63 GHz, with respect to the design, are the operating frequencies. Unfortunately, due to very small output power levels, measurements at higher frequencies were not possible to be performed and good comparison between both combiner types was not fully achieved.

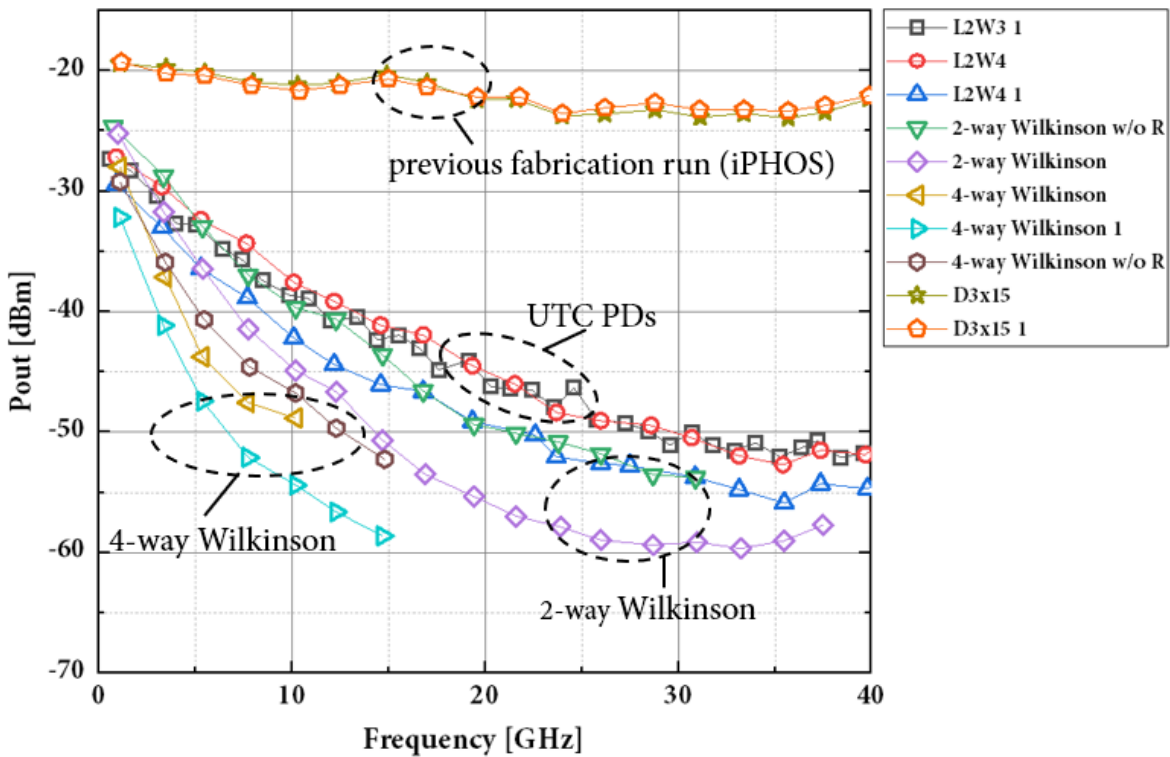


Fig. 6.38 Frequency response measurements up to 40 GHz with normalized output power to 1 mA of photocurrent.

Short summary of estimated 3-dB bandwidths for measured devices is presented in Fig. 6.39.

	3-dB bandwidth [GHz]
UTC PDs (Fiwin5G)	< 5
UTC PDs (iPHOS)	> 40
2-way Wilkinson	< 1
4-way Wilkinson	< 3

Fig. 6. 39 The 3-dB bandwidth based on the measurements results up to 40 GHz.

Additional HFSS simulations illustrate the impact of the R_s value on the device characteristics. In Fig. 6. 40 the s-parameters for the UTC PD L2W3 are presented. As can be observed, the transmission values (s_{12}/s_{21}) are below -9 dB or even lower when R_s is ca. 1.5 k Ω . For higher R_s values ca. 3 k Ω and ca. 6 k Ω , the transmission is below -11 dB and -14 dB respectively. Moreover, the input reflections are extremely high, and almost all signal power is reflected.

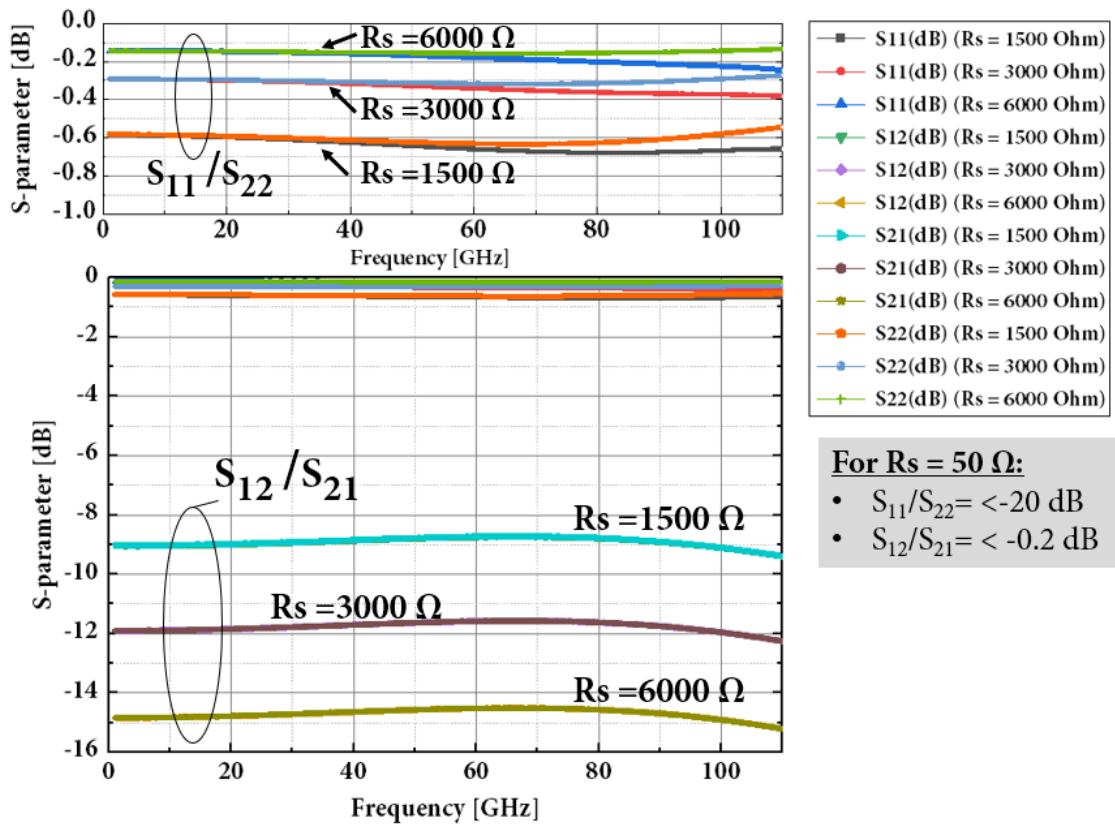


Fig. 6. 40 Simulated s-parameters of UTC PD L2W3 with R_s from 1.5 k Ω to 6 k Ω .

The s-parameters of the 2-way Wilkinson power combiner without isolation resistor with $R_s = 2000 \Omega$, are presented in Fig. 6. 41. The loss of the transmission is high, below -7 dB and it rises with the frequency. Furthermore, the input reflections are as well very high, and majority of the signal power is reflected.

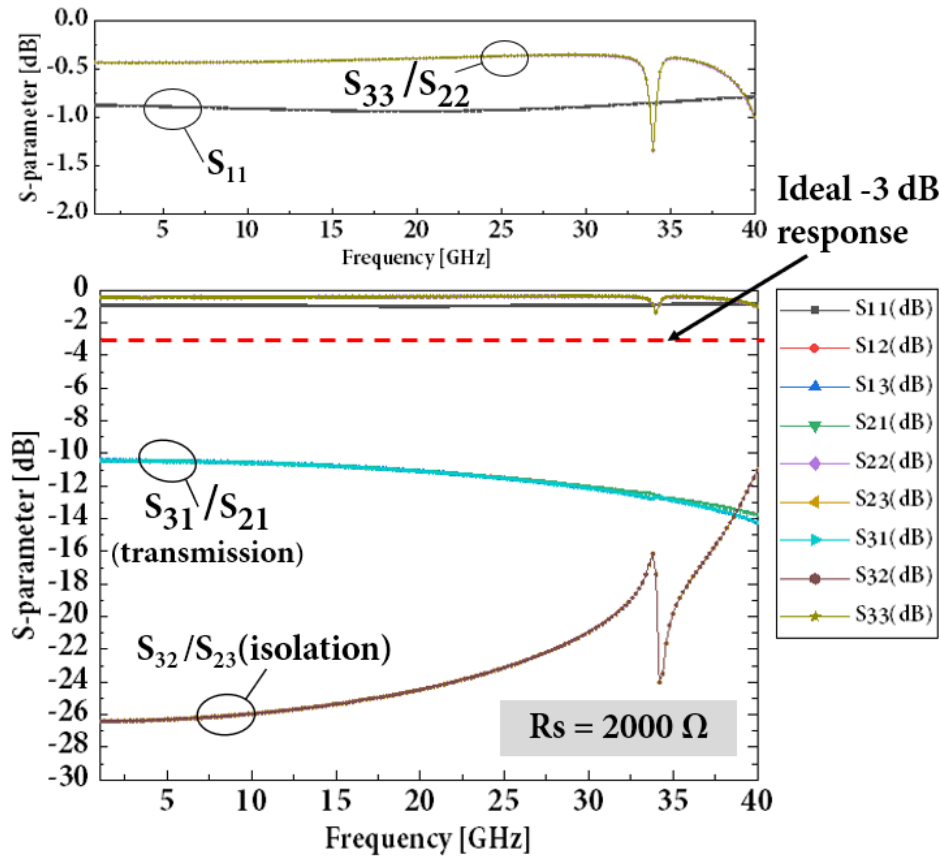


Fig. 6. 41 Simulated s-parameters of 2-way Wilkinson w/o isolation resistors with $R_s = 2000 \Omega$.

The 4-way Wilkinson power combiner with $R_s = 2 \text{ k}\Omega$ is simulated as well, with results depicted in Fig. 6. 42. The loss of the transmitted signal is more than -10 dB. The input reflections are very high and almost all signal power is reflected at the input. Moreover, the design is not adapted at the frequencies below 10 GHz due to very high input reflections. Simulation results for the $R_s = 50 \Omega$ are presented in chapter 4.3.4.

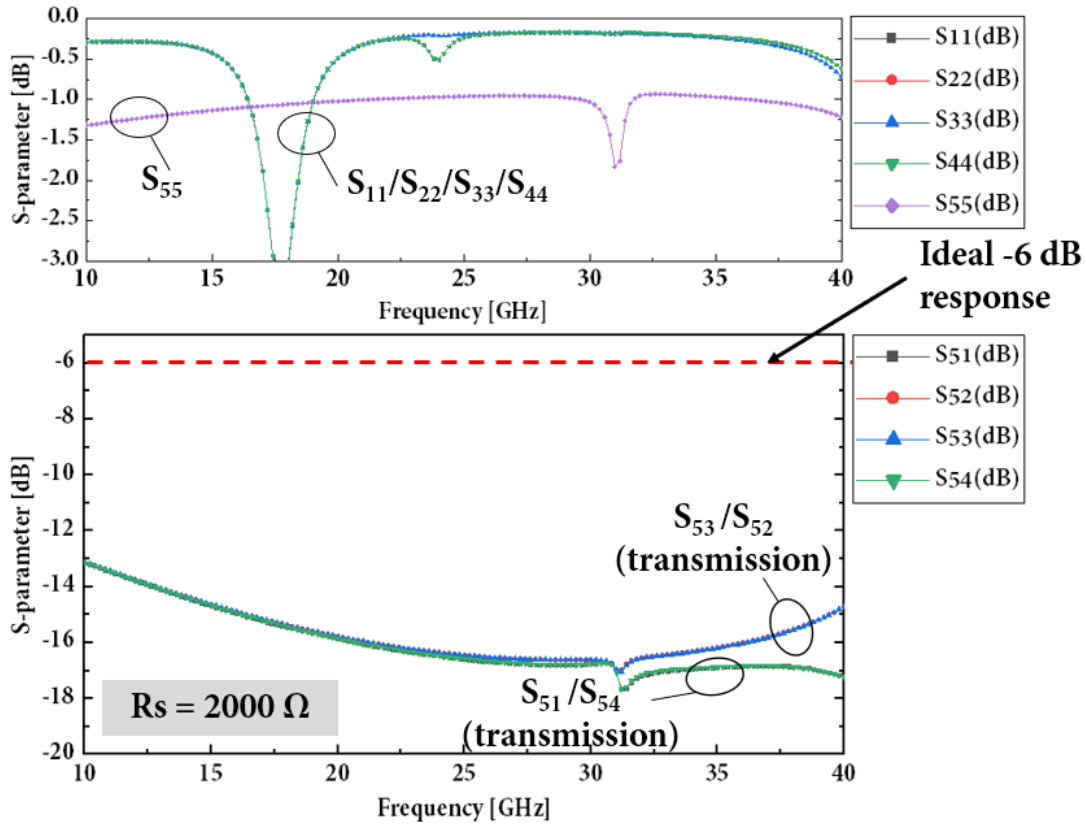


Fig. 6. 42 Simulated s-parameters of 4-way Wilkinson w/o isolation resistors with $R_s = 2000 \Omega$.

Setup presented in Fig. 6. 35 is also used for a 1-dB compression point measurements. For that measurements, frequency is fixed at 20 GHz and the output power is recorded along with the rising photocurrent until 1 dB compression is achieved. In order to investigate the saturation characteristics, the compression point measurements were performed at 20 GHz with -4.7 V of bias. Recorded results are presented in Fig. 6. 43. The difference between UTC PD from previous fabrication run (D3x15 V1 W+) is clearly seen. This photodiode achieves much higher saturation current, reaching 13 mA. The UTC PD L2W3 saturates at only 1.7 mA. In case of the 2-way and 4-way Wilkinson power combiners, the -1-dB compression point were not reached due to optical limitations of the measurement setup (maximum output is 25 dBm). The 2-way Wilkinson power combiner reached 7.5 mA of the photocurrent. In the case of the 4-way Wilkinson power combiner, 5 mA of the photocurrent was recorded. Furthermore, power dissipation is also presented in Fig. 6. 43. Dissipated power levels were calculated with correspondence to the series resistance values estimated from I-V characteristic (Fig. 6. 7, Fig. 6. 8, Fig. 6. 13). The thermal limitations are considered as one of the causes of the saturation of the photodiodes, by comparing the dissipated power at which compression appears, it is a good way to evaluate the high-power generation capabilities of the device. As can be observed the

highest level of dissipated power is obtained for the 2-way and 4-way Wilkinson power combiners, reaching 17.5 dBm and 14 dBm, respectively.

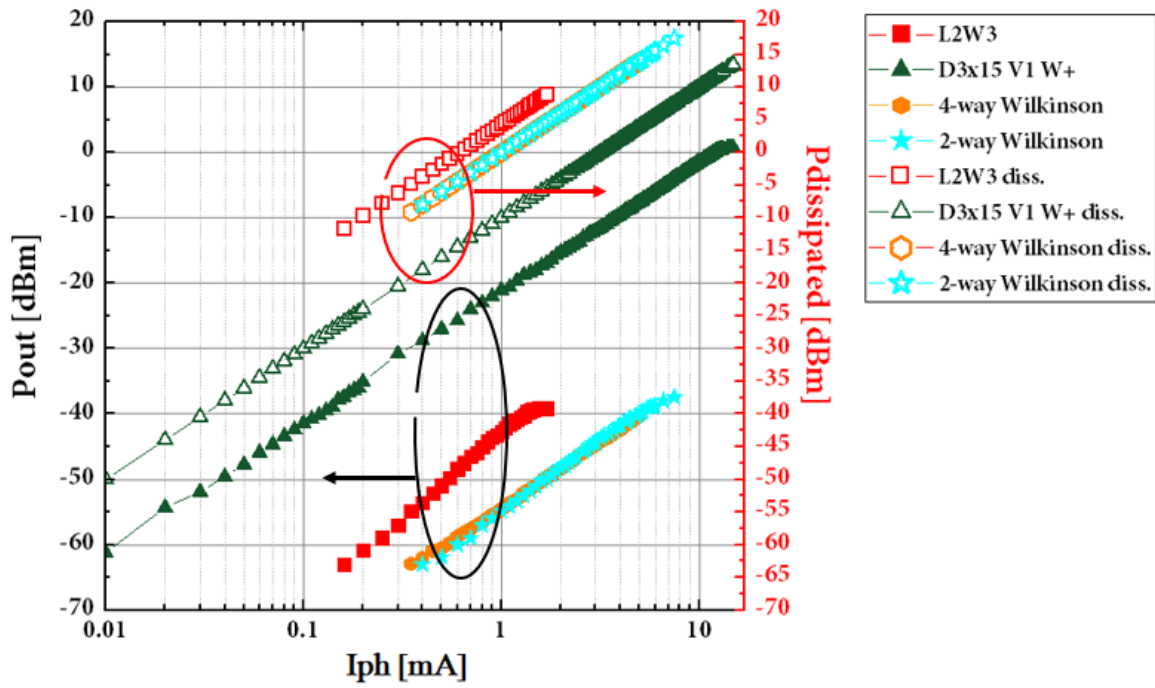


Fig. 6. 43 The -1-dB compression point measurement at 20 GHz and -4.7 V bias.

Short summary of the measured output powers and dissipated powers is presented in Fig. 6. 44.

	Pout [dBm]	Pdissipated [dBm]
L2W3	-40	9
D3x15	0.75	13
2-way Wilkinson	-40	14
4-way Wilkinson	-37	17.5

Fig. 6. 44 Output power and power dissipation based on 1-dB compression point measurements.

To conclude:

- Due to very high values of series resistance, the overall performance of the devices from Fiwin5G fabrication run is very reduced. Measured 3-dB bandwidth for the UTC photodiodes reveals that the bandwidth is very narrow and should not exceed 5 GHz (Fig. 6. 39). Even narrower 3-dB bandwidth is estimated for the Wilkinson power combiners ca. 1 GHz.
- Based on the 1-dB compression point measurements, the UTC PDs reached -40 dBm at 1.7 mA of photocurrent. The Wilkinson power combiners due to setup limitation (maximum power of optical output is 25 dBm), do not reached the 1-dB compression point.
- Based on the measurement results an immediate difference between the devices from iPHOS fabrication run is observed in comparison to FiWiN5G run. The series resistance values are around 90 Ω to 120 Ω , and therefore better performance of the devices is clearly measured.
- The 3-dB bandwidth of the UTC photodiodes should exceed 40 GHz. The 1-dB compression point is achieved at 13 mA of photocurrent and 0.75 dBm of output power.
- Based on the measured values of series resistance for the UTC PDs and Wilkinson power combiner from the FiWiN5G fabrication run, the dissipated power is about 9 dBm and 17.5 dBm, respectively. These calculations show that application of multiple devices in the design improves power dissipation and consequently higher output power levels could be achieved.

6.3.1 Propagation losses of optical waveguides

The aim of this subchapter is to present the propagation losses of optical waveguides fabricated during this PhD thesis. In order to estimate the propagation losses the same setup presented in Fig. 6. 35 is used, but with only one EDFA. The optical output power is set to 15 dBm. Measured devices are bias at -5 V. Recorded results are presented in Fig. 6. 45 for different devices. As can be observed, the photocurrent drops along with the increasing optical path. For

the UTC PD with a 100 μm of optical waveguide length, the photocurrent is the highest, ca. 0.7 mA. The estimated propagation losses are ca. 3.31 dB/cm, which is good agreement with published values for InP passive optical waveguides in [1]. Additional losses due to fabrication and corresponding roughness (etching process) should also be taken into account.

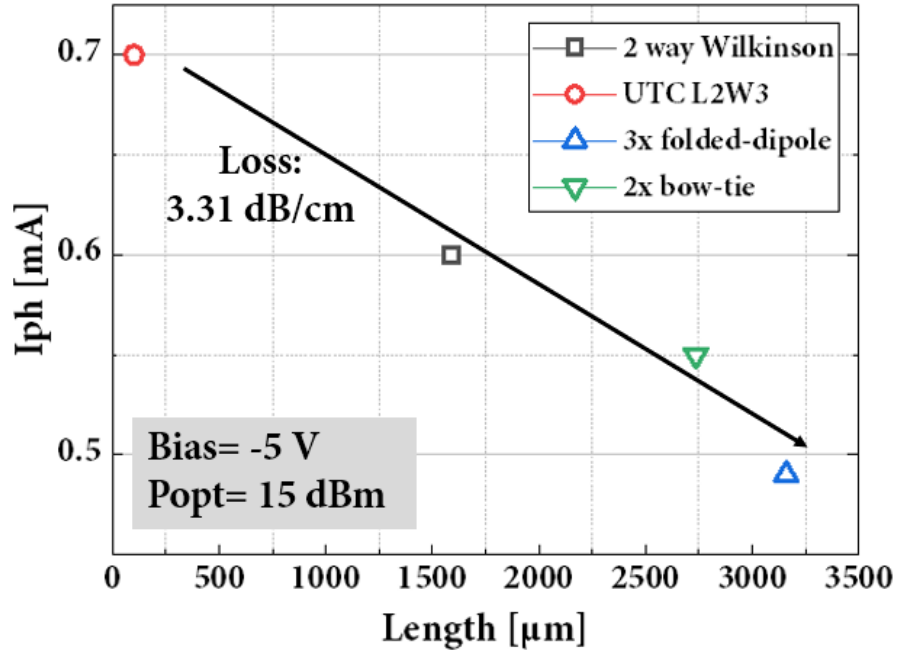


Fig. 6. 45 Measured photocurrent values vs. the optical length for a different structure from Fiwin5G fabrication run.

6.3.2 Bandwidth measurements – iPHOS fabrication run

The objective of this subchapter is to present the frequency bandwidth measurements from 77 GHz up to 110 GHz of the devices from the previous fabrication run. with setup presented in Fig. 6. 46. In this setup only one EDFA is used. The optical output power is set to ca. 8 dBm. The UTC photocurrent is kept at 1 mA with -5 V of bias voltage, and for all frequency points of the recorded spectra with ESA (Rohde and Schwarz FSU67GHz). The RBW (Resolution Bandwidth) and VBW (Video Bandwidth) are set to 3 MHz. The GSG probe (Cascade ACP110A) and harmonic mixer (Rohde and Schwarz FS-Z110) are used to extract the RF signal.

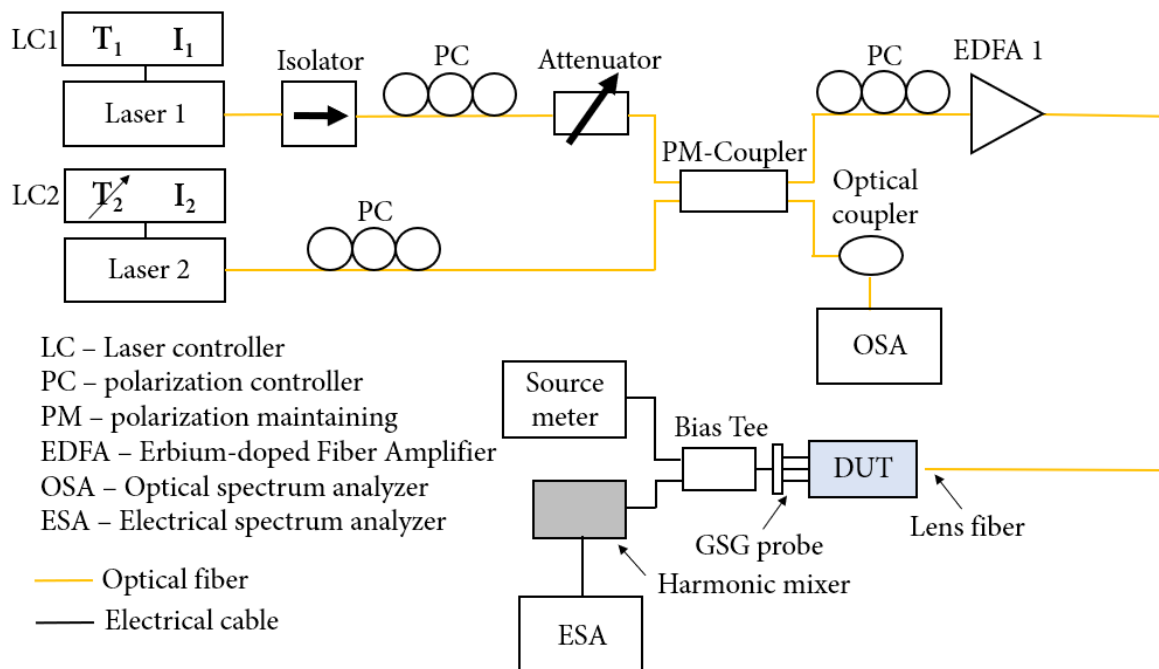


Fig. 6. 46 Optical heterodyne setup for the bandwidth measurement from 77 GHz – 110 GHz of the UTC PDs from iPHOS fabrication run.

The family of recorded frequency characteristics are presented from Fig. 6. 47 - Fig. 6. 52. Several photodiodes are characterized with the dimensions that correspond to the UTC PDs designed within Fiwin5G project. Based on the measurement results, the highest output power levels are recorded for the D4x15 with ca. -28 dBm of output power up to 93 GHz. Above 95 GHz, the output power levels drops down to ca. -33 dBm. For all other dimensions of UTC PD, the output power levels are generally below -30 dBm down to ca. -38 dBm. Short summary of the output power values is presented in Fig. 6. 53.

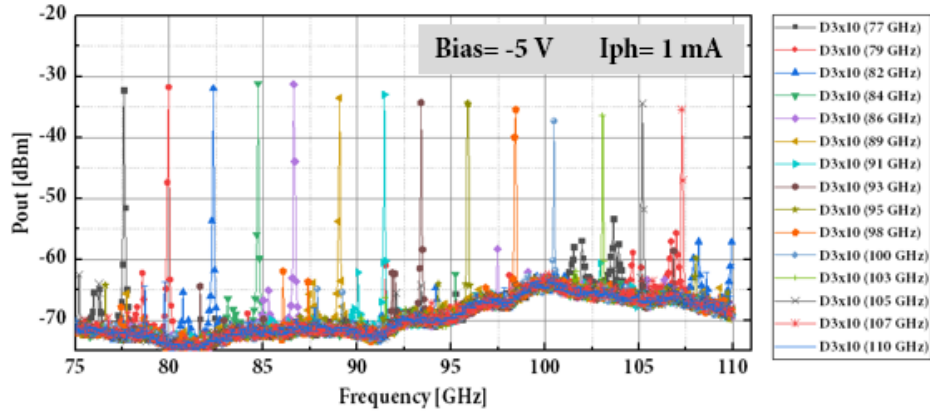


Fig. 6.47 Frequency response measurements from 77 GHz to 110 GHz for UTC PD D3x10.

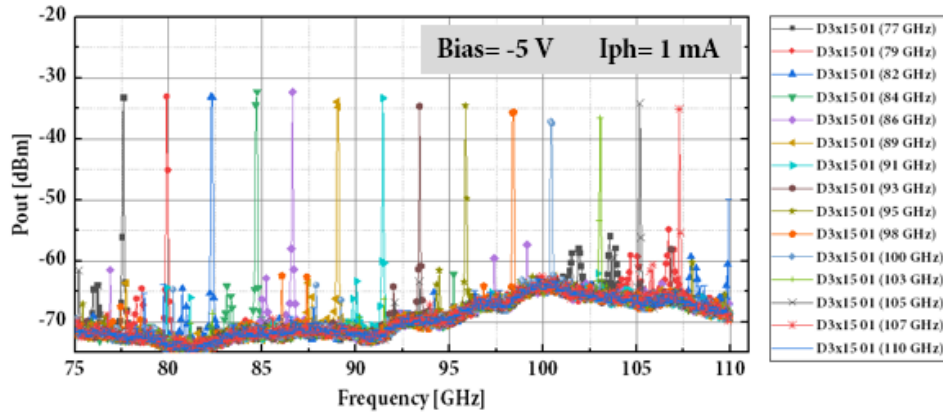


Fig. 6.48 Frequency response measurements from 77 GHz to 110 GHz for UTC PD D3x15 01.

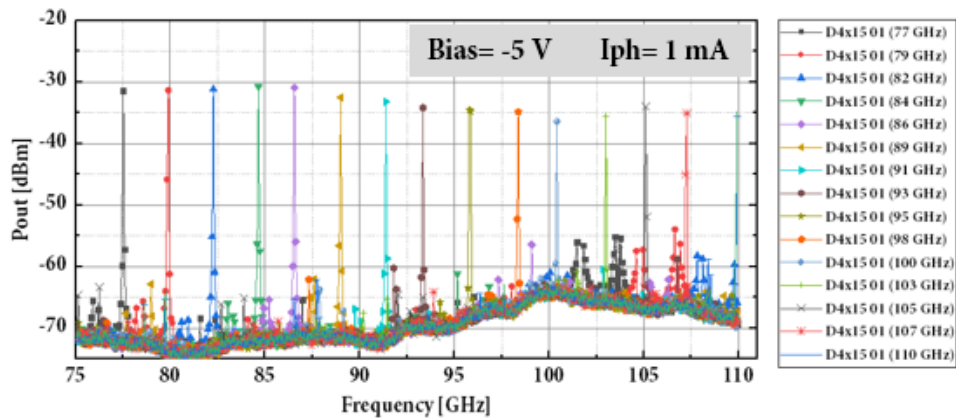


Fig. 6.49 Frequency response measurements from 77 GHz to 110 GHz for UTC PD D4x15 01.

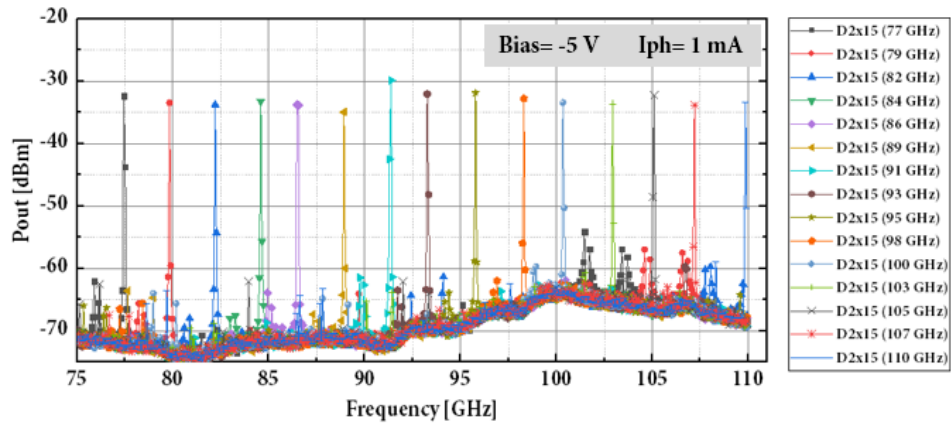


Fig. 6. 50 Frequency response measurements from 77 GHz to 110 GHz for UTC PD D2x15.

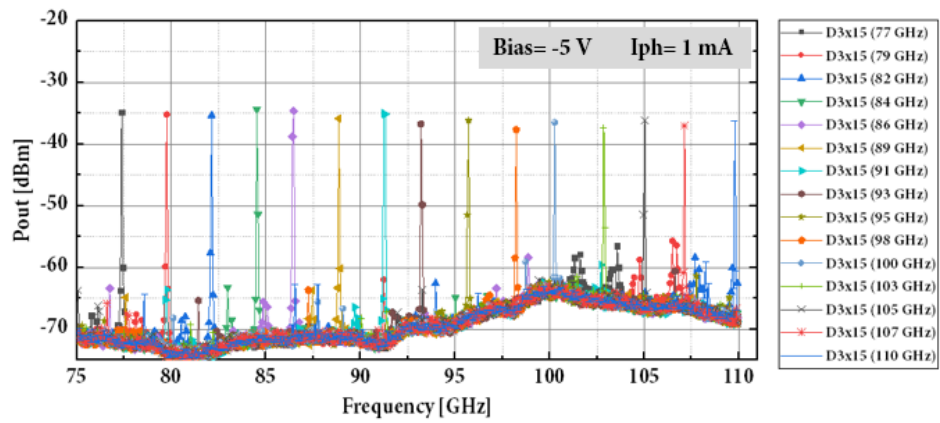


Fig. 6. 51 Frequency response measurements from 77 GHz to 110 GHz for UTC PD D3x15.

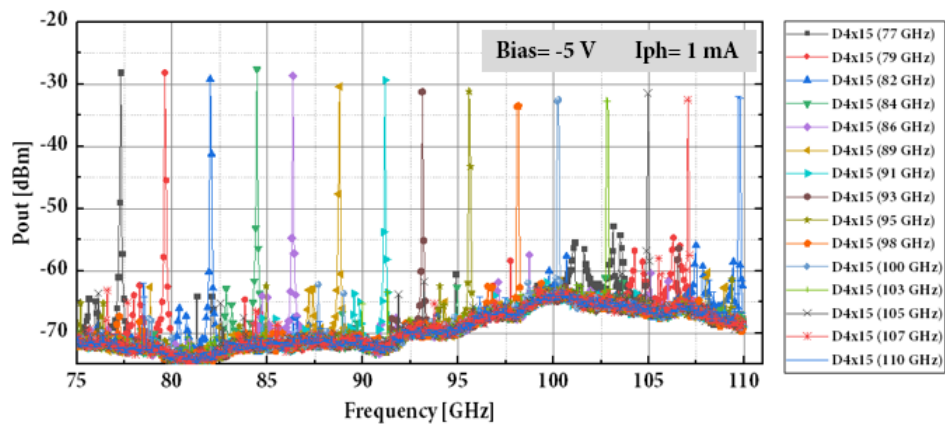


Fig. 6. 52 Frequency response measurements from 77 GHz to 110 GHz for UTC PD D4x15.

UTC PD [width x length]	Pout [dBm]
[3x10]	-31 @ 77 GHz -36 @ 107 GHz
[2x15]	-32 @ 77 GHz -34 @ 107 GHz
[3x15]	-32 @ 77 GHz -35 @ 107 GHz
[4x15]	-31 @ 77 GHz -35 @ 107 GHz

Fig. 6. 53 Comparison of UTC PD output power from 77 GHz – 110 GHz from iPHOS fabrication run.

To conclude:

- **As already mentioned in the previous subchapter much lower levels of the series resistance result in better performance of the UTC PDs from iPHOS fabrication run.**
- **Measured output power levels from 77 GHz up to 110 GHz are very comparable among the UTC PDs with different dimensions. The highest output power level is recorded at 84 GHz with -28 dBm of power measured with ESA for UTC D4x15 (Fig. 6. 52).**

6.3.3 Bandwidth measurements - antenna-integrated devices

This subchapter presents the results of antenna-integrated UTC PDs characterized at 50 GHz with the setup presented in Fig. 6. 55. In this setup high-resistive (HR) collimating lens (Batop CSL-20) is used. Signal is gathered with a horn antenna positioned at 0° (please see Fig. 6. 63). It is then down-converted with harmonic mixer (Agilent 11970V) operating from 50 up to 75 GHz, with conversion losses at 50 GHz of 34.9 dB at 14th harmonic and LO power between 14 to 16 dBm. The generator (Wiltron 69169A) used in the setup is fixed at ca. 5 GHz (F_{gen}) with 15 dBm of output power. Additional signal amplification is applied to measure the output RF spectra. The 500 MHz low-noise amplifier (Miteq AU1291) with ± 63 dB of gain is utilized, with operating point set at 10th harmonic. Generated frequency can be then estimated as (Fig. 6. 54):

$$F_{gen} \times 10^{th} \text{harmonic} \pm \text{ESA signal [MHz]} \quad (6.1)$$

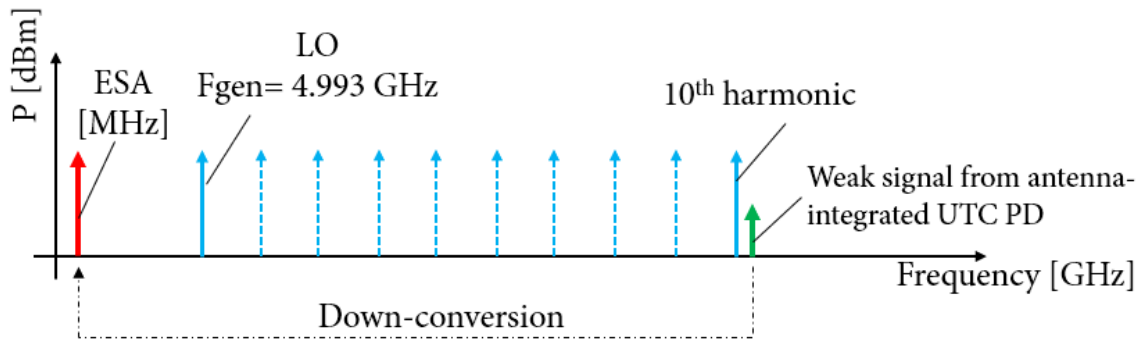


Fig. 6. 54 Down-conversion principle used in the measurement setup.

Signals spectra are obtained with ESA (Rohde and Schwarz FSEK30). The RBW is set to 30 kHz and VBW 300 kHz. In Fig. 6. 56 a photograph of a measurement setup is presented, with fiber-to-chip coupling positioner, HR Si lens, horn antenna and harmonic mixer. The optical output power is set to ca. 25 dBm. Antenna-integrated structures, as already mentioned, suffered from very high values of R_s , what greatly influenced measured characteristics. Signal from the 3x folded-dipole antenna structure is not measurable, even with the usage of low-noise amplifier. Nevertheless, it is possible to detect signal from bow-tie antenna-integrated UTC PDs in various configurations. Devices with two optical inputs are characterized only with the usage one of the inputs due to measurement setup limitations. Recorded characteristics are presented from Fig. 6. 57 to Fig. 6. 60. Measured output power for the 3x bow-tie antenna device at 50 GHz is ca. -45 dBm. Bias voltage is set to -5V. Recorded photocurrent is about 3.7 mA. Frequency of the generator is set to 4.993 GHz. The 2x bow-tie antenna integrated device (Fig. 6. 58) deliver almost the same output power level at slightly higher frequency of ca. 50.432 GHz. The highest value of output power is recorded for the

connected 2x bow-tie antenna-integrated UTC PDs (Fig. 6. 59), it reaches -37 dBm at 50.432 GHz, with 4.6 mA of photocurrent.

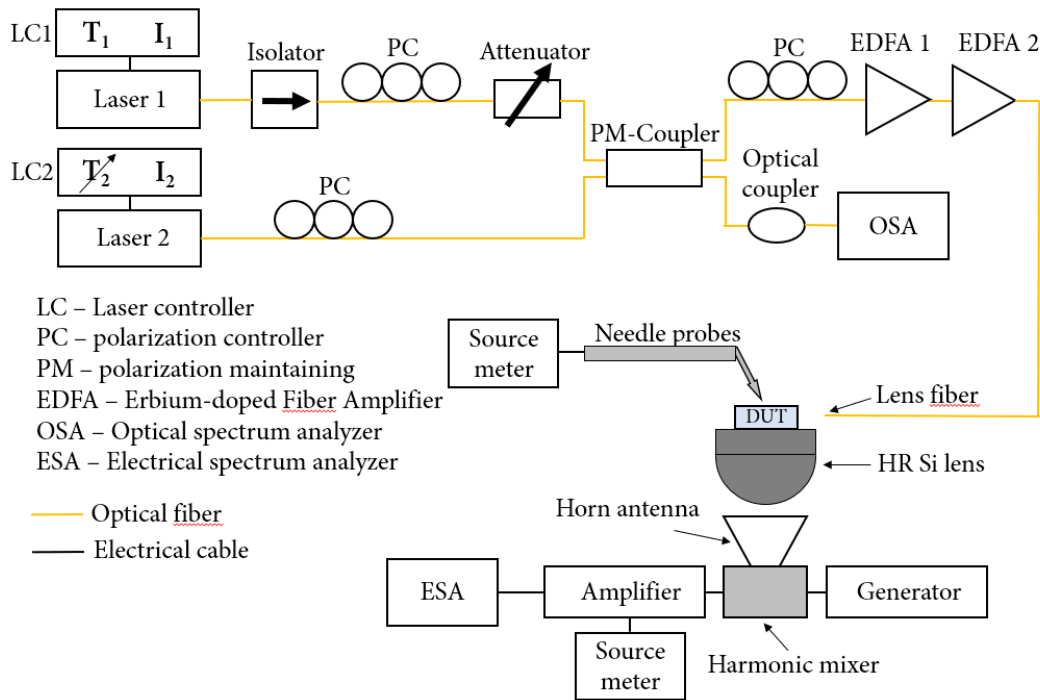


Fig. 6. 55 Measurement setup for characterization of the antenna-integrated devices at 50 GHz.

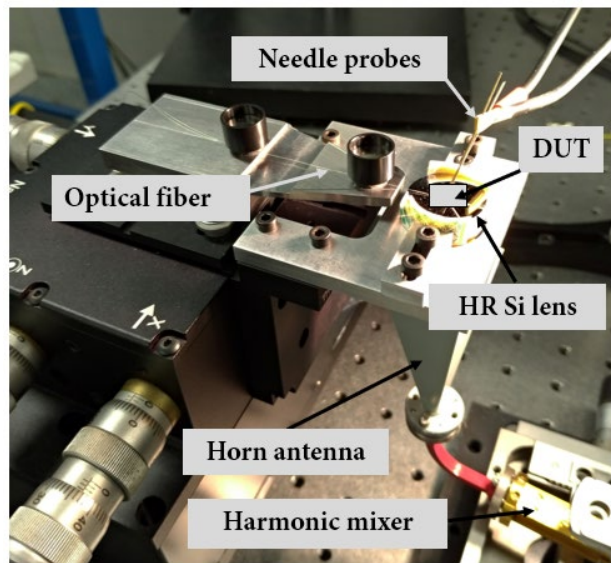


Fig. 6. 56 Part of the measurement setup with HR Si lens used in the antenna-integrated devices characterization.

Measured devices are not comparable in terms of output power levels due to different values of R_s , varying from 60 k Ω (for the 3x bow-tie antenna) to 4 k Ω (2x bow-tie antenna), as

presented in Fig. 6. 9. Moreover, with such a high level of series resistance, majority of the input power is reflected. What is more, similarly as to the case of Wilkinson power combiners, the target frequencies of the antenna design are higher than used for the measurements. The corresponding s-parameters are not in good matching condition at 50 GHz.

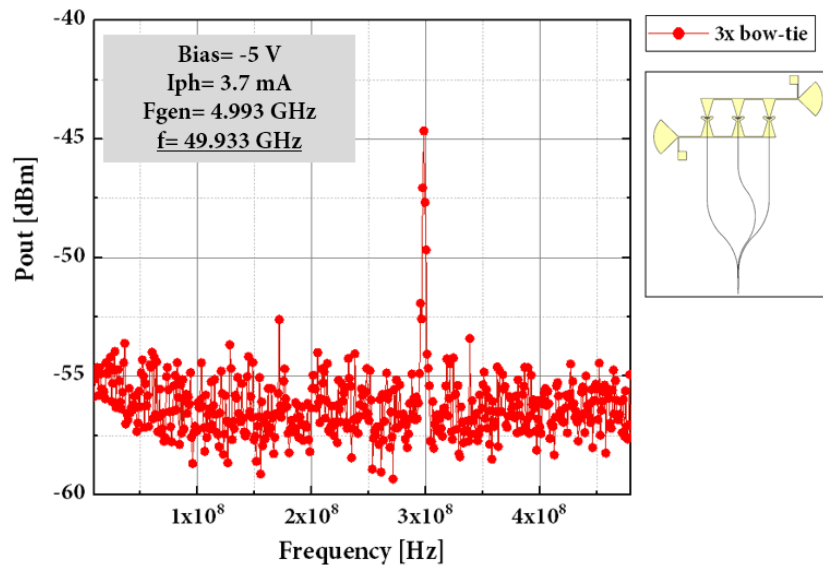


Fig. 6. 57 Frequency response measurements of 3x bow-tie antenna integrated UTC PDs at 50 GHz.

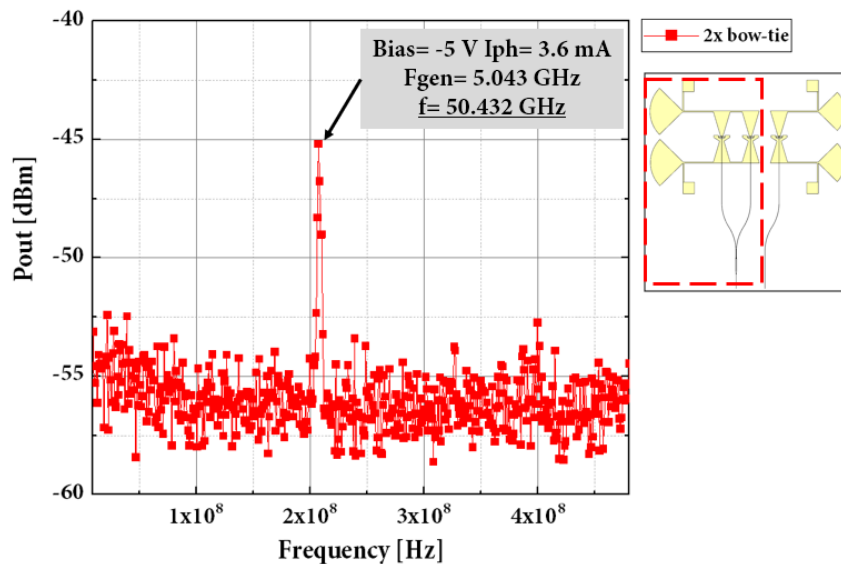


Fig. 6. 58 Frequency response measurements of 2x bow-tie and separated 1x bow-tie antenna-integrated UTC PD at 50 GHz (results for 2x bow-tie only).

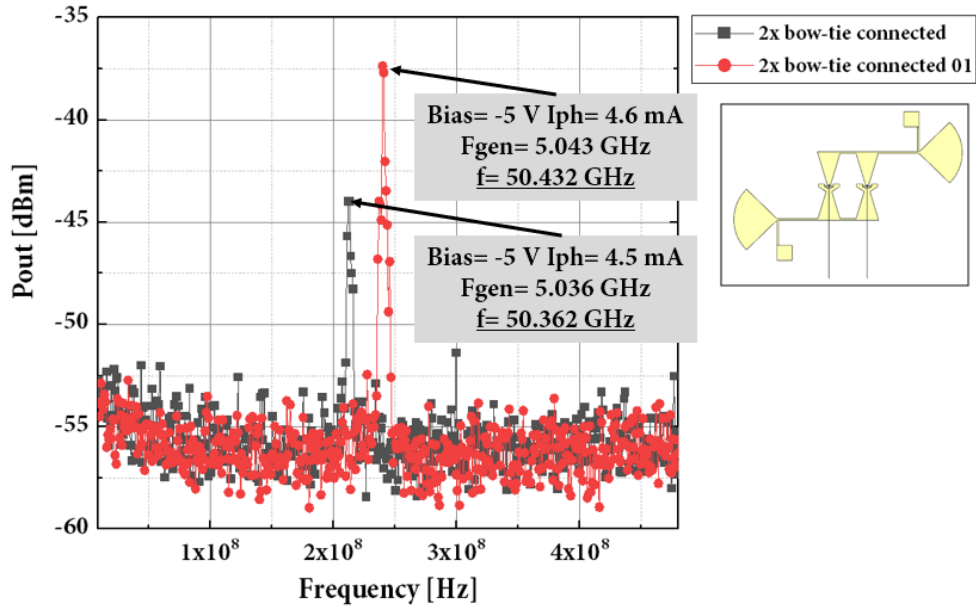


Fig. 6. 59 Frequency response measurements of connected 2x bow-tie antenna integrated UTC PDs at 50 GHz.

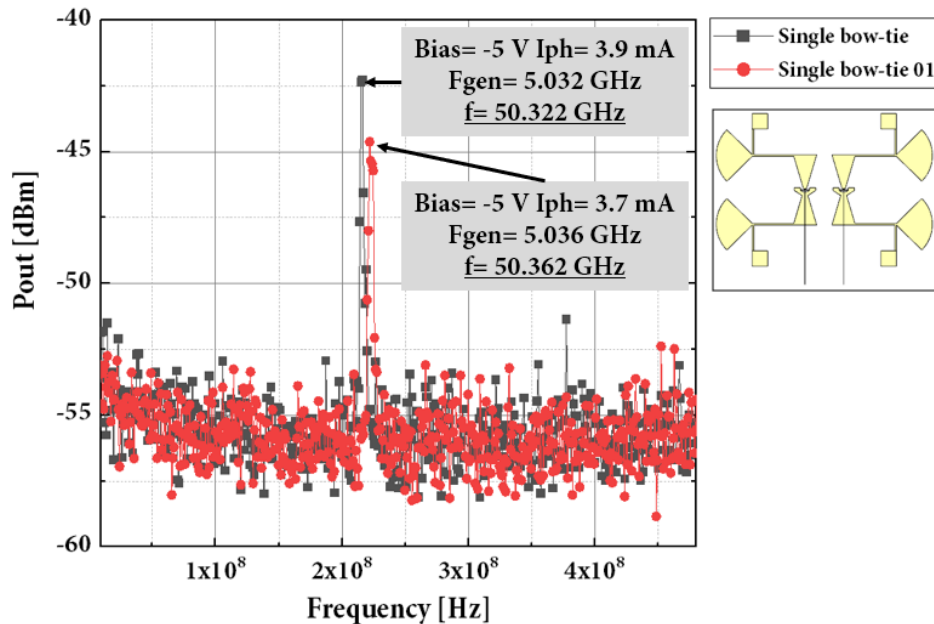


Fig. 6. 60 Frequency response measurements of separated 2x bow-tie antenna integrated UTC PDs at 50 GHz.

In Fig. 6. 61 a short comparison of RF output power levels for measured devices is presented. Based on the conversion losses data (cable losses are not included) the output power levels should reach ca. -80 dBm at 50 GHz.

Bias= -5 V Optical power (fiber output)= 25 dBm LNA gain= \pm 63 dB		Pout with LNA
3x folded-dipole antenna		Not detected
3x bow-tie antenna		-44 dBm @ 49.933 GHz
Connected 2x bow-tie antenna (with 2 optical inputs but only 1 used)		-37 dBm @ 50.432 GHz
2x bow-tie antenna (with 1 optical input)		-45 dBm 50.432 GHz
1x bow-tie antenna		-42 dBm @ 50.322 GHz

Fig. 6. 61 Comparison of the RF output power at 50 GHz between bow-tie antenna integrated UTC PD devices.

To conclude:

- Based on the measurement results of the 3x folded-dipole antenna integrated devices at 50 GHz with LNA the signal cannot be detected. It is as well due to the fact that the target frequency range is around 100 GHz.
- The signal from the bow-tie antenna-integrated structures is detectable at 50 GHz and the estimated output power levels are very comparable, reaching -80 dBm (without cable losses). Although the output power levels are very comparable it is important to note that the series resistance values are considerably different, as presented in Fig. 6. 9.
- To the best of author knowledge presented results are the first demonstration of the antenna-integrated UTC PDs array with single optical input, monolithically integrated on the same substrate.

6.3.4 Bandwidth measurements - antenna-integrated devices – previous fabrication run (iPHOS)

The objective of this subchapter is to present measurements of antenna-integrated devices from previous fabrication run. Measurement setup is presented in Fig. 6. 62. Devices were measured in the frequency band from 75 GHz up to 110 GHz. This setup is similar to the measurement setup used for the UTC PDs characterization in the same frequency range (Fig. 6. 46). Similarly, only one EDFA is used, but with optical output power set to 10 dBm. Bow-tie and LPT (Log-periodic toothed) antenna structure are characterized, at -5 V of bias and with the photocurrent kept at 1 mA. In this setup high-resistive (HR) collimating lens (Batop CSL-20) is used. Signal is detected with a horn antenna and harmonic mixer (Rohde and Schwarz FS-Z110). The RF spectra are recorded with ESA (Rohde and Schwarz FSU67GHz). The RBW (Resolution Bandwidth) and VBW (Video Bandwidth) are set to 3 MHz. Moreover, measurements are performed with the horn antenna fixed at two positions at 0° and 90°, as presented in Fig. 6. 63.

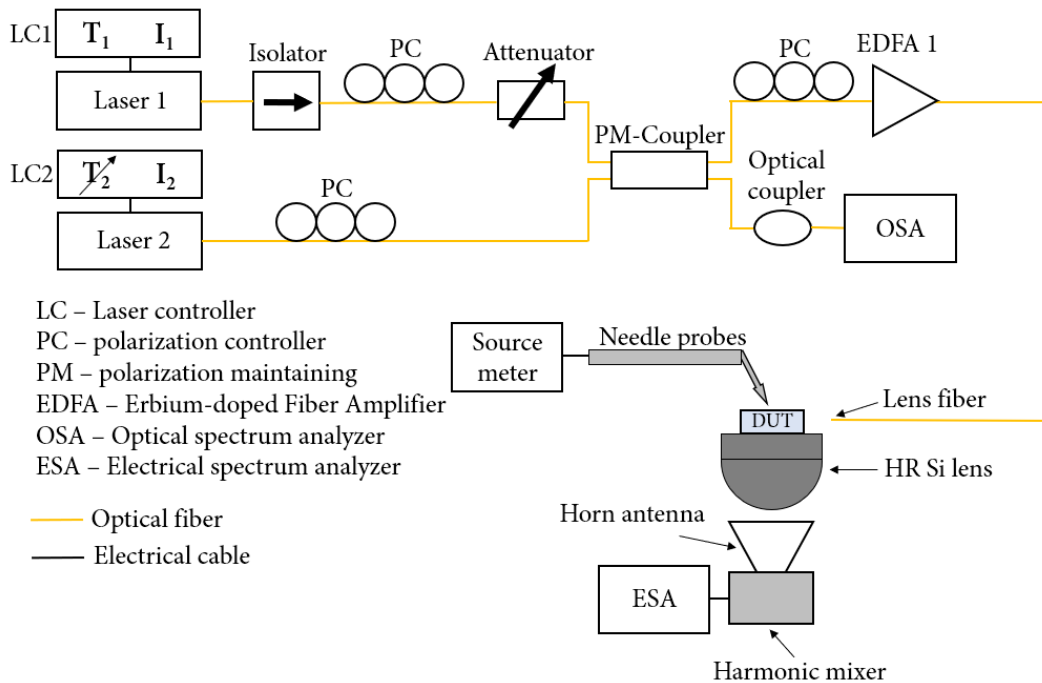


Fig. 6. 62 Measurement setup for characterization of the antenna-integrated devices from 77 GHz – 110 GHz.

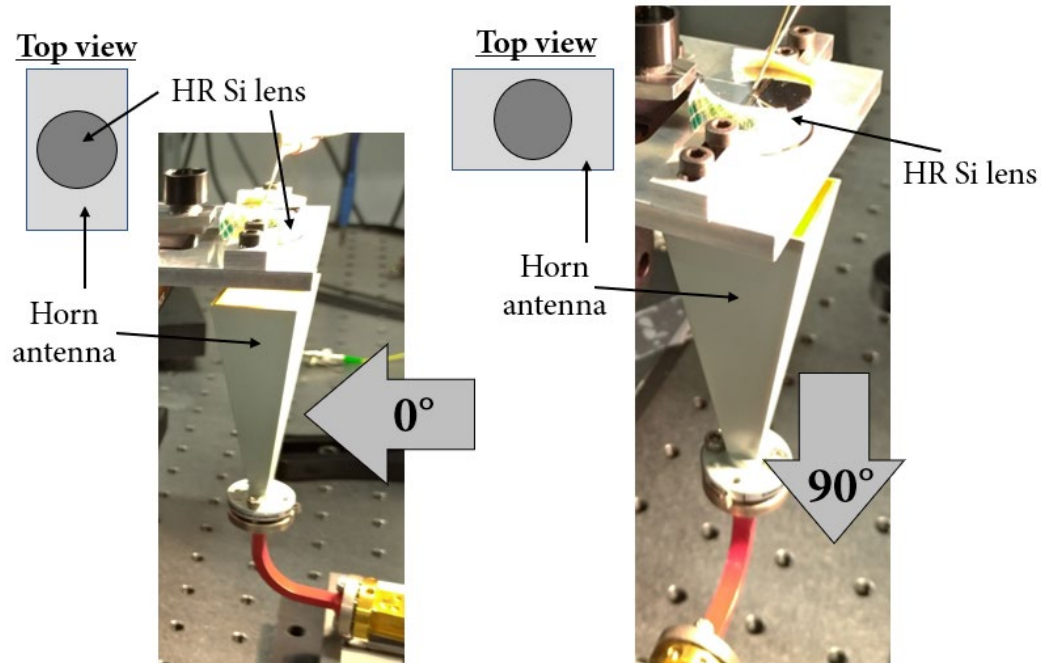


Fig. 6. 63 Position of the horn antennas in the measurement setup for antenna-integrated devices characterization from 77 GHz – 110 GHz.

The top views of bow-tie and LPT antenna-integrated UTC PD measured from 75 GHz – 110 GHz with corresponding dimensions are presented in Fig. 6. 64. Both type of structure employed a photodiode that correspond to dimensions L_2W_2 ($3 \mu\text{m} \times 15 \mu\text{m}$).

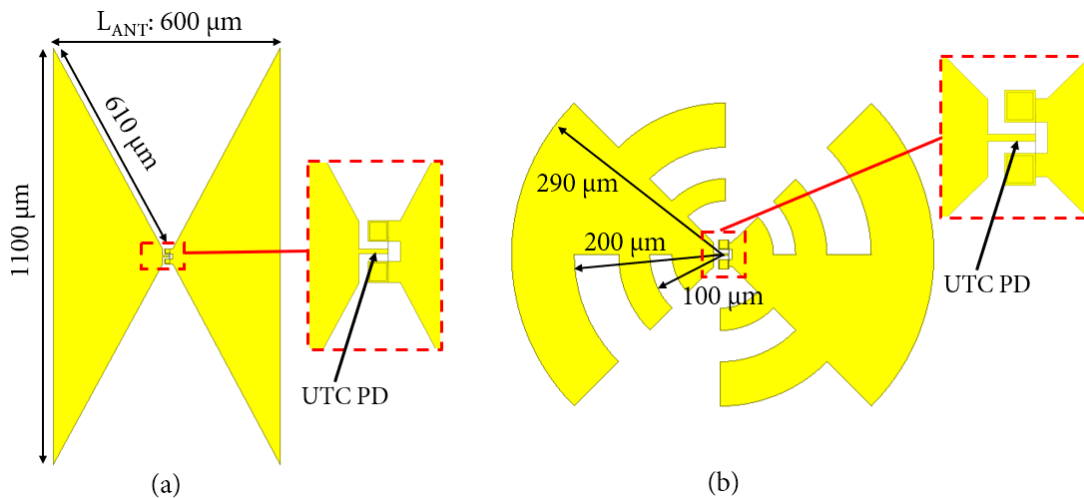


Fig. 6. 64 Top view of (a) bow-tie and (b) LPT antenna-integrated UTC PD structure from previous fabrication run with dimensions.

The family of characteristics for bow-tie antenna device is presented in Fig. 6. 65 at 0° and 90° of horn antenna position. As can be observed value of output power levels are up to 10 dBm higher for a 0° position in comparison to 90°. The highest output power level is recorded at 77 GHz and it is around -34 dBm, which is a very good result as the output power levels are measured with ESA and the same RF power is recorded for the UTC PD with CPW output at 80 GHz in [2].

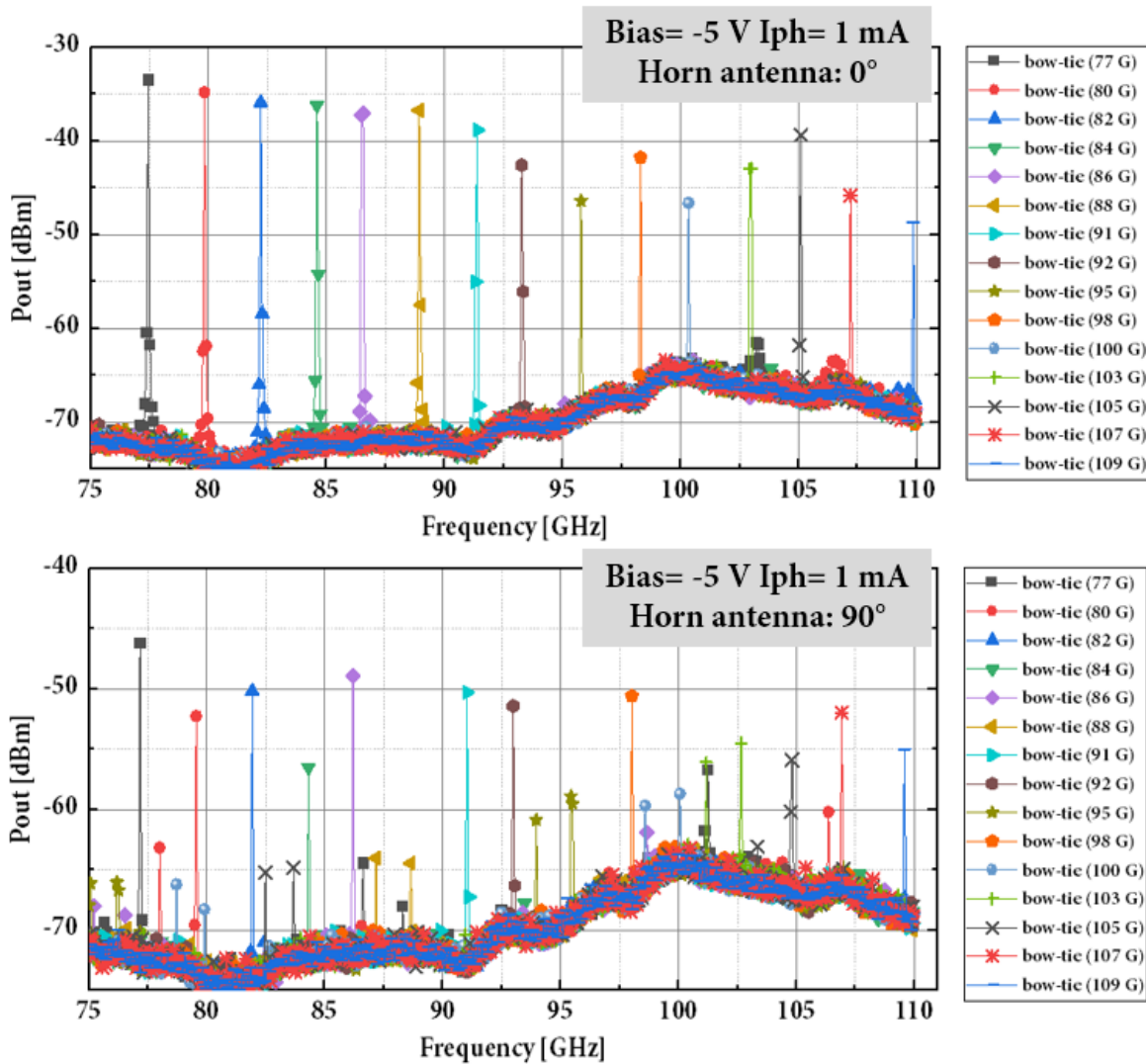


Fig. 6. 65 Frequency response measurements from 77 GHz – 110 GHz for bow-tie antenna-integrated UTC PD from previous fabrication run at 0° and 90° position of horn antenna.

The family of characteristics for bow-tie antenna device is presented in at 0° and 90° of horn antenna position. Based on the measurement results the influence on the antenna position impacted less LPT antenna structure as expected. The highest output power level is recorded at 79 GHz and 98 GHz, reaching -47 dBm. In comparison to bow-tie antenna structure, the LPT antenna delivers lower output power.

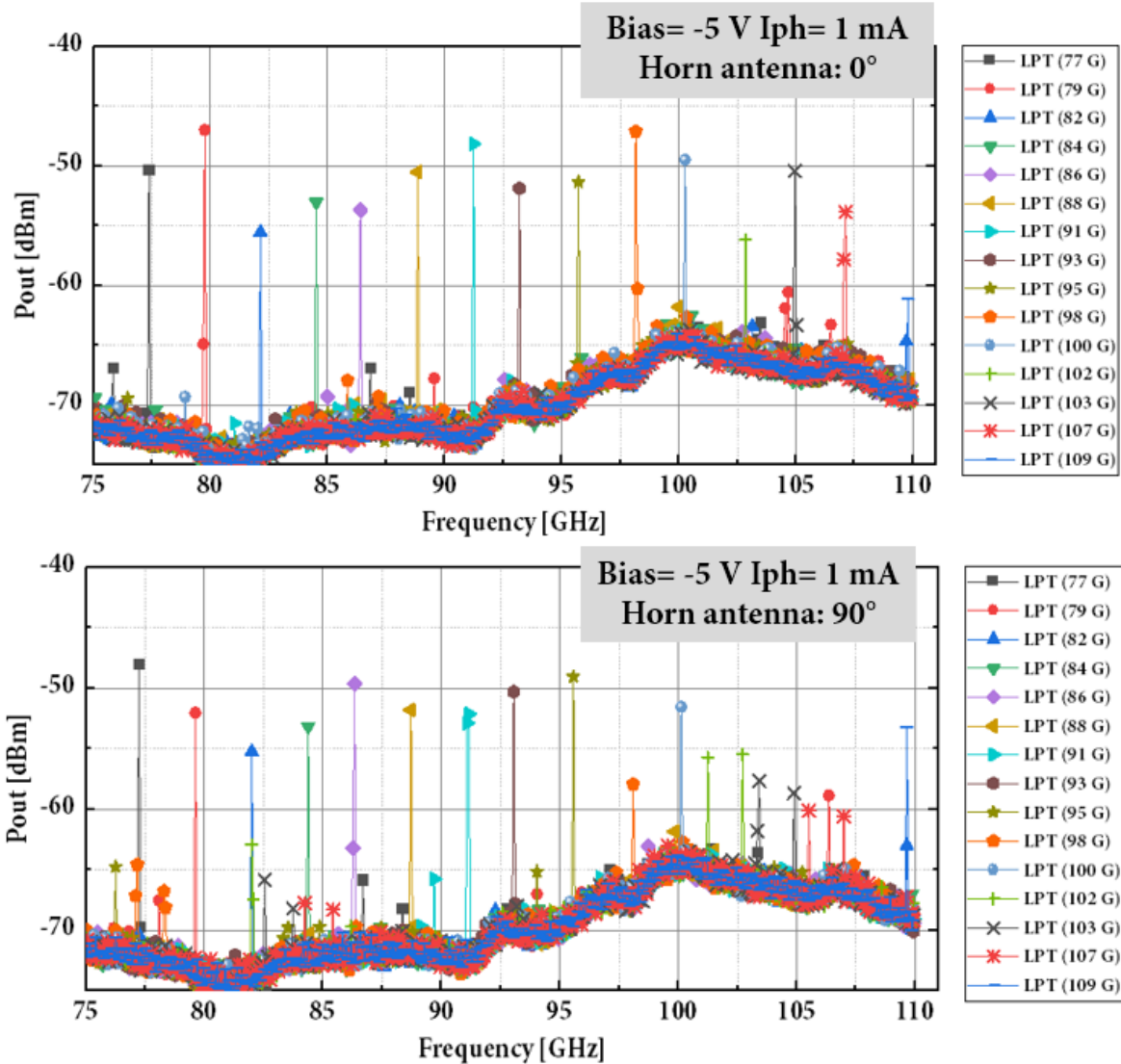


Fig. 6. 66 Frequency response measurements from 77 GHz – 110 GHz for LPT antenna-integrated UTC PD from previous fabrication run at 0° and 90° position of horn antenna.

In order to understand the differences between the two types of antenna structures, additional HFSS simulations are performed up to 300 GHz and are presented in Fig. 6. 67 and Fig. 6. 68. Two R_s values are simulated to compare the influence on the antenna bandwidth. As can be observed, the s_{11} input reflections are lower for the bow-tie antenna structure. It is also confirmed by the measurements for this type of antenna to deliver higher output power levels in comparison to log periodic toothed antenna.

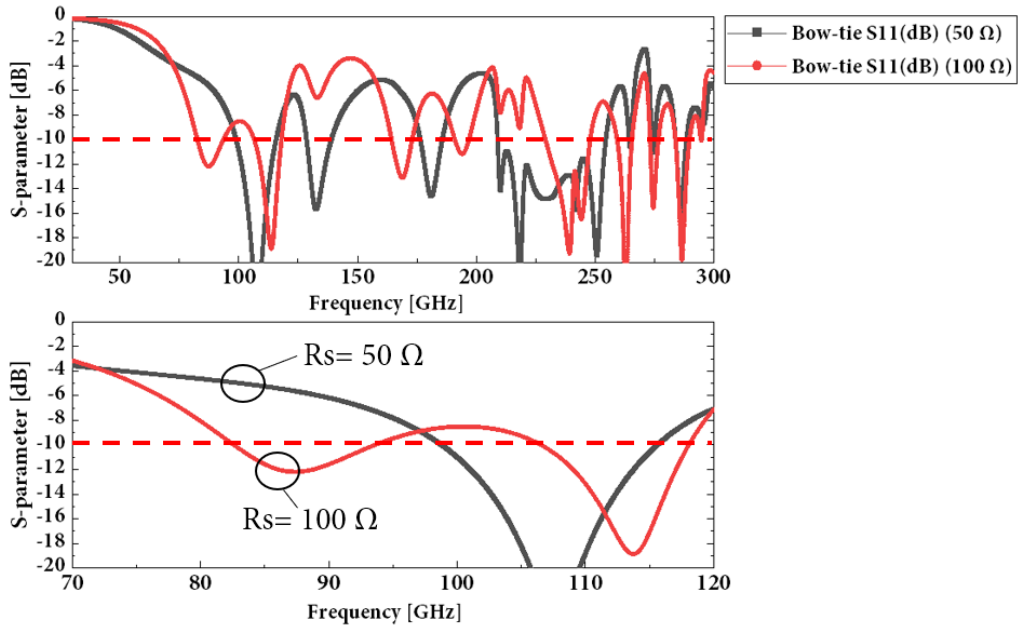


Fig. 6. 67 Simulation results of the s-parameter for the bow-tie antenna-integrated UTC PD structure from previous fabrication run. Source (port) impedance was set to 50 Ω and 100 Ω .

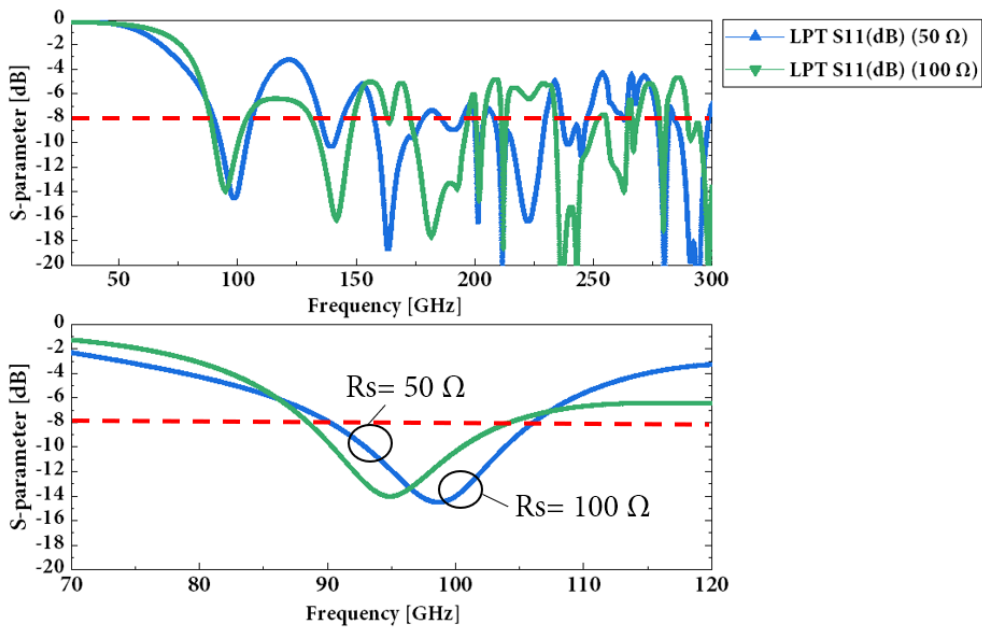


Fig. 6. 68 Simulation results of the s-parameter for the LPT antenna-integrated UTC PD structure from previous fabrication run. Source (port) impedance was set to 50 Ω and 100 Ω .

Short summary of the output power values is presented in Fig. 6. 69.

Bias= -5 V Optical power (fiber output)= 10 dBm	Pout [dBm]
Bow-tie antenna (horn antenna at 0°)	-34 @ 77 GHz -45 @ 107 GHz
Bow-tie antenna (horn antenna at 90°)	-46 @ 77 GHz -52 @ 107 GHz
LPT antenna (horn antenna at 0°)	-50 @ 77 GHz -54 @ 110 GHz
LPT antenna (horn antenna at 90°)	-48 @ 77 GHz -60 @ 110 GHz

Fig. 6. 69 Comparison between the bow-tie and LPT antenna-integrated UTC PD output power from 77 GHz – 110 GHz.

To conclude:

- **Based on the measurement results for the bow-tie antenna-integrated UTC PDs, there is a strong influence of the antenna position on the output power levels what clearly prove polarization dependency (Fig. 6. 65). The highest output power level is recorded at 77 GHz with -34 dBm of power which is the same as for the UTC PD with CPW output [2]. Recorded values are measured with ESA, not the power meter, and therefore higher output power level is expected.**
- **Based on the measurement results for the LPT antenna-integrated UTC PDs, the antenna position influence is weaker on the output power levels what clearly prove less polarization dependant properties. The output power levels of the LPT antenna structures are lower in comparison to bow-tie antennas. The highest output power levels are recorded at 79 GHz with -47 dBm.**

6.4 LPT ANTENNA-INTEGRATED UTC PD – MEASUREMENTS WITH MODE-LOCKED LASER

One of the solutions to increase the maximum RF power from a photodiode with a given amount of optical power is to use an optical frequency comb (please see chapter 2.6.2 and Fig. 2. 27 for more details). This method is used with one the LPT antenna-integrated photodiode from previous fabrication (iPHOS). Measurement setup used is presented in Fig. 6. 70. The laser source is a Quantum-Dash Mode-locked laser (QD MLL) fabricated at III-V Lab. Used RF electrical generator is fixed at 10.66 GHz with 23 dBm of output power in order to electrically injection lock the QD MLL laser and copy the phase noise of the generator to the phase noise of the beat note of the QD MLL laser. The QD MLL laser is supplied with 800 mA from source meter. In this setup only one EDFA is used and the optical output power is set to 10 dBm. The LPT antenna structure are characterized, at -5 V of bias and with the photocurrent kept at 1 mA. In this setup high-resistive (HR) collimating lens (Batop CSL-20) is used. Signal is detected with a horn antenna and harmonic mixer (Rohde and Schwarz FS-Z110). The RF spectra are recorded with ESA (Rohde and Schwarz FSU67GHz). The RBW (Resolution Bandwidth) and VBW (Video Bandwidth) are set to 100 kHz.

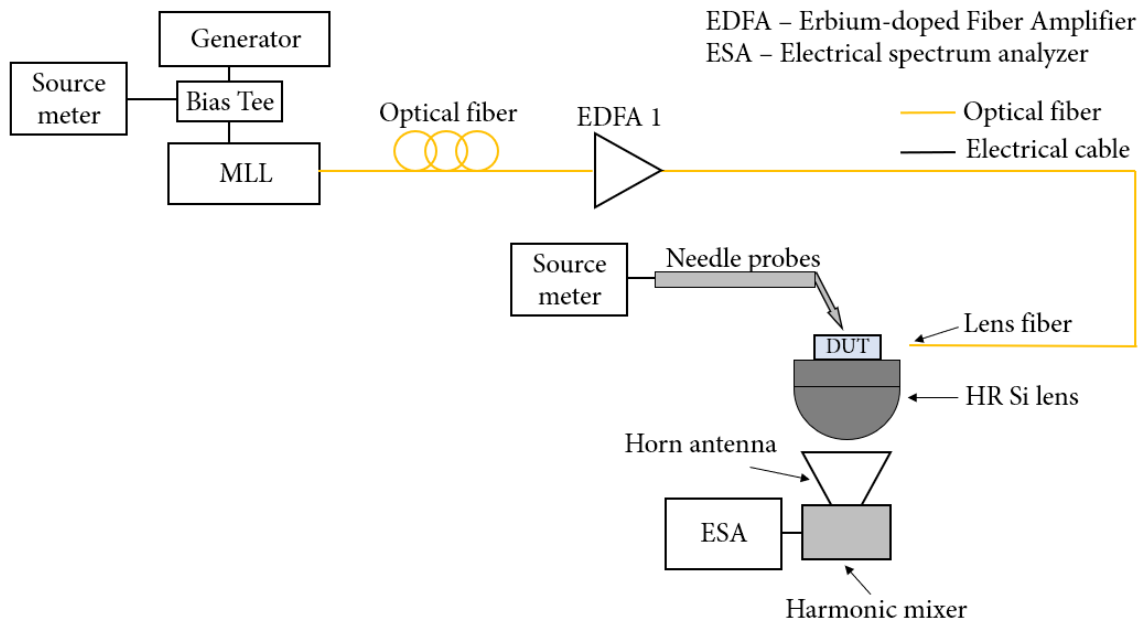


Fig. 6. 70 Measurement setup for characterization of the antenna-integrated devices from 77 GHz – 110 GHz with Mode-locked laser.

QD MLL source requires an adjusted length of single-mode optical fiber to use the dispersion in order to compensate for the group delay of the laser. More details about the

source and corresponding results can be found in [3]. Moreover, as presented in chapter 2.6.3 and described in [4], application multi-wavelength source to generate mm-wave signals can increase the output power levels up to 6 dB compared with a more usual two-tone optical source. In Fig. 6. 71 an example of the optical spectra of the frequency combs of QD MLL laser at different current supply values are presented.

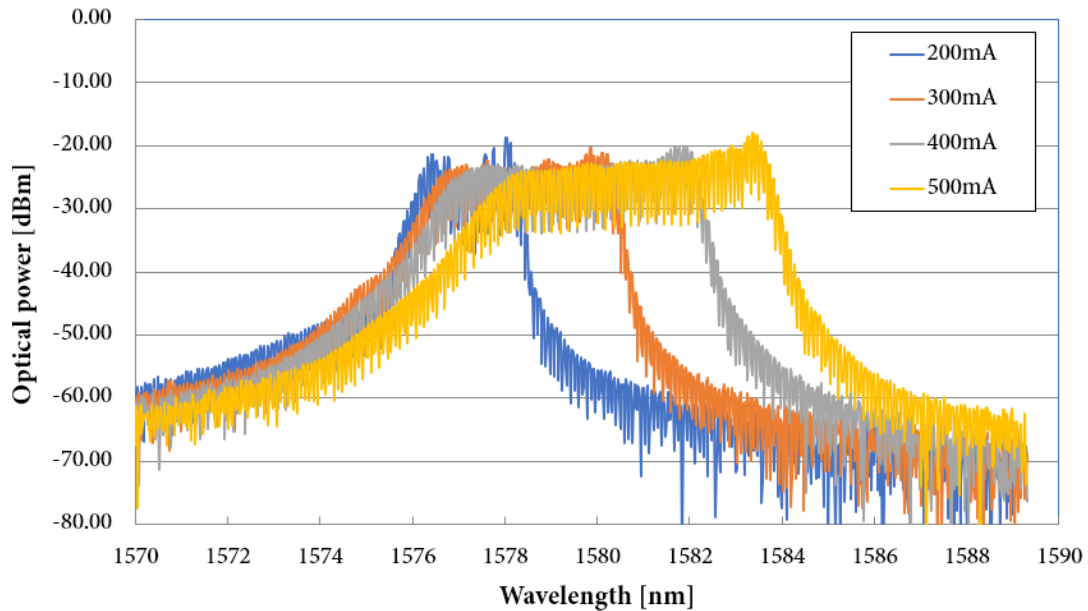


Fig. 6. 71 Example of the optical frequency comb of QD MLL laser at different current supply points.

In order to estimate the necessary length of optical fiber in the measurement setup, several distances are tested and recorded results are presented in Fig. 6. 72. For the LPT antenna-integrated structure at 80 GHz, output power level reaches ca. -22 dBm at 650 m of optical fiber length. This length is used for the experiment with the same device at 85 GHz, 96 GHz and 107 GHz, as presented in Fig. 6. 72. These frequencies correspond to the 8th, 9th and 10th harmonics of the fundamental repetition rate of 10.66 GHz. Furthermore, as can be noticed output power levels are higher in comparison to standard setup presented in chapter 6.3.3 in Fig. 6. 62. It is important to note that output power levels are not measured with a power meter.

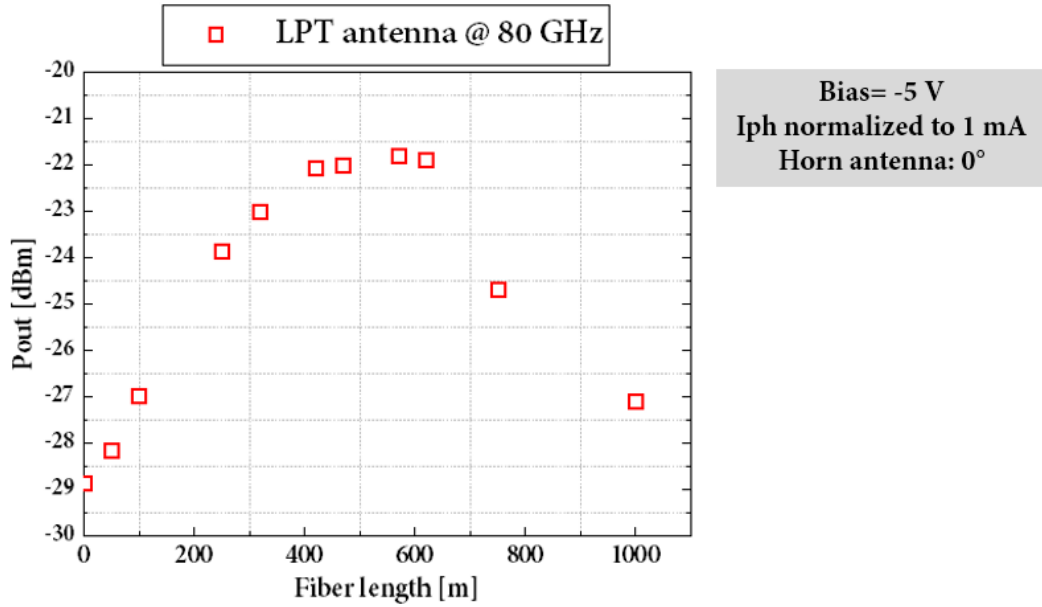


Fig. 6.72 Measurement of the LPT antenna-integrated UTC PD at 80 GHz vs. the optical fiber length.

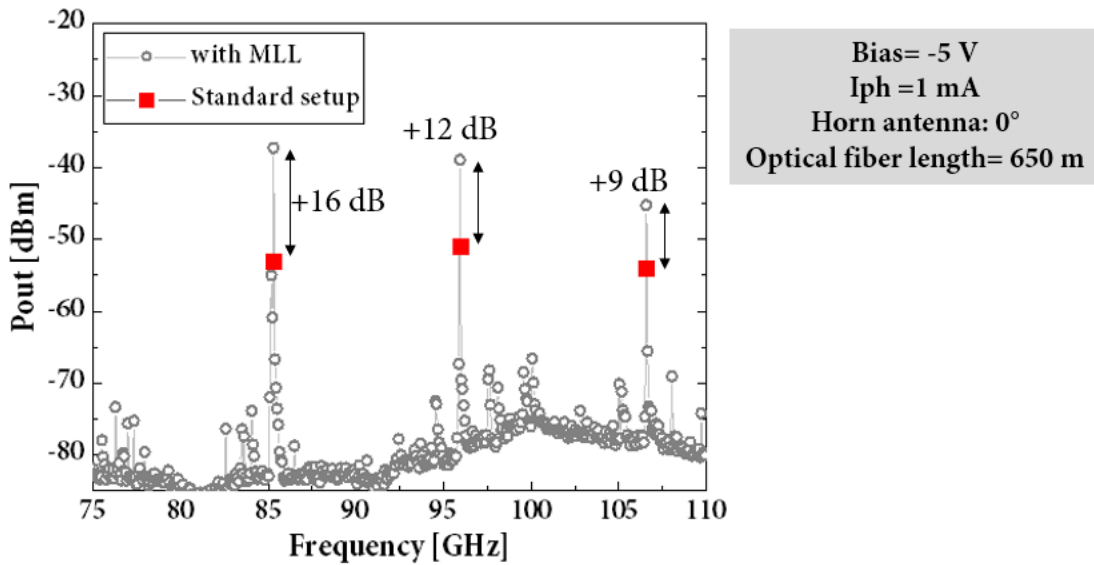


Fig. 6.73 Measurement of the LPT antenna-integrated UTC PD at 85 GHz, 96 GHz and 107 GHz output power in comparison to standard heterodyne setup.

To conclude:

- **Based on the measurement results and as reported in [4], output power improvement is recorded with the setup using frequency comb instead of standard two-tone source (Fig. 6. 70).**
- **The output power increase is recorded at 85 GHz, 96 GHz and 107 GHz, with 9 dB up to 16 dB higher output power levels in comparison to standard heterodyne setup (Fig. 6. 73). It is important to note, that the recorded output power values are measured with ESA, not power meter.**

6.5 PHOTONIC INTEGRATED CIRCUIT – MEASUREMENTS

In the previous sections some of the solutions to increase the output power levels from the photodetectors with application of photonic integrated circuits technology have been presented. In this subchapter, the phase noise reduction technique based on the photonic integrated circuit is described. The PIC presented in Fig. 6. 69 is used in the experiment for optoelectronic comb generation and cross-injection locking to generate mm-wave signal. Utilized PIC was fabricated in the previous fabrication run (iPHOS). Recorded results are published in [7]. The PIC is composed of two 1.1 mm-long DFB lasers operating at around 1550 nm wavelength. The MMI coupler is used to combine the laser beams and semiconductor optical amplifiers (SOAs) are utilized to amplify and adjust the signal levels at different positions of the circuit. The UTC photodiode receives optical beat-note which passes through the two SOAs and through one of the modulators (EAM). Modulators are inserted before the photodiode to modulate the beat-note, which is used as a frequency carrier. The UTC photodiode converts the received signal into an RF signal. The RF output frequency corresponds to the difference between the two optical frequencies and, after connecting mm-wave antenna to the photodiode output. This PIC can be utilized for free space data transmission, as presented in [2] . An optical access to the DFB lasers is provided on the other side of the chip (left-hand side in Fig. 6. 74). The dimensions of the device are 4.4 mm of length and 0.7 mm of widths. The DFBs wavelengths are adjusted and tuned thermally by the driving current. A continuous tuning from 5 GHz up to 110 GHz is demonstrated in [2], what also confirms continuous tunability of the beat-note and high frequency response of integrated UTC photodiode.

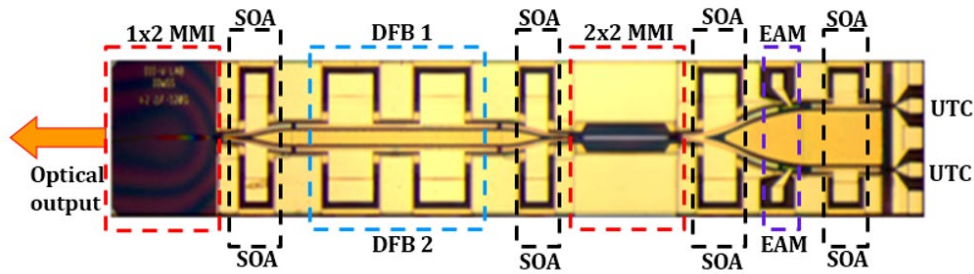


Fig. 6. 74 Microscope view of the integrated photonic chip.

The measurement setup is presented in Fig. 6. 75 and Fig. 6. 76. Chip is placed on the AlN submount with contact pads that are used for wire bonding connections. The DC bias is delivered to different sections of the chip (i.e. DFBs, SOAs) through multicontact DC probe controlled by the computer with dedicated software. The GSG probes (Cascade ACP65-A-GSG-150) are utilized to probe the UTC PD output and the modulator contact pads. The DC bias to UTC PD is provided by the source meter (Keithley 2400) via the bias tee. The optical signal tones are recorded on the other side of the chip with the OSA (Apex AP2043B). The PIC temperature for cross-injection locking and for optical frequency comb generation is maintained at 25 °C with thermoelectric cooler.

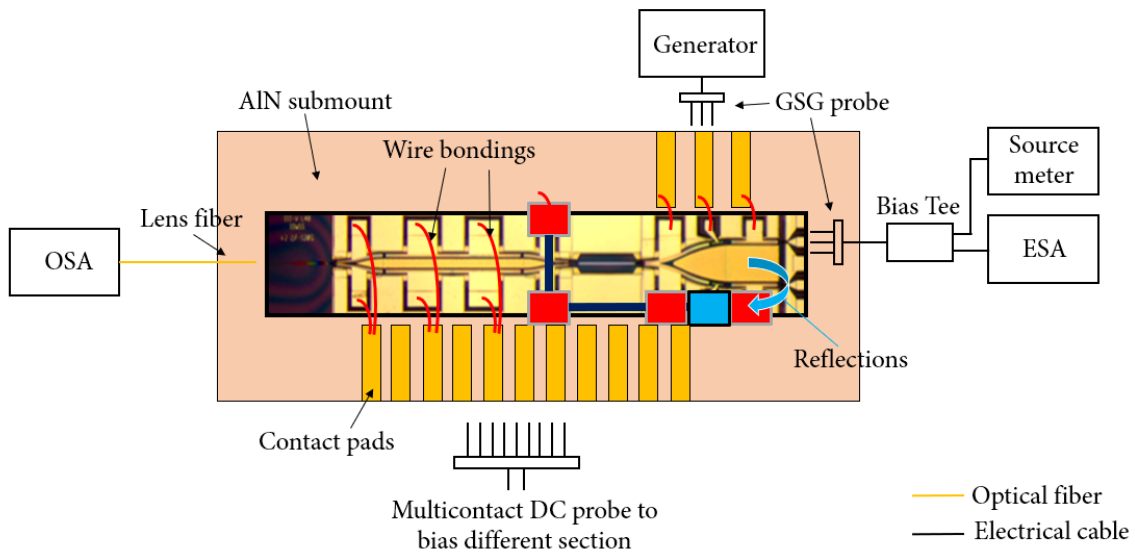


Fig. 6. 75 Measurement setup used for PIC characterization and with configuration for optical frequency comb generation (red and blue squares).

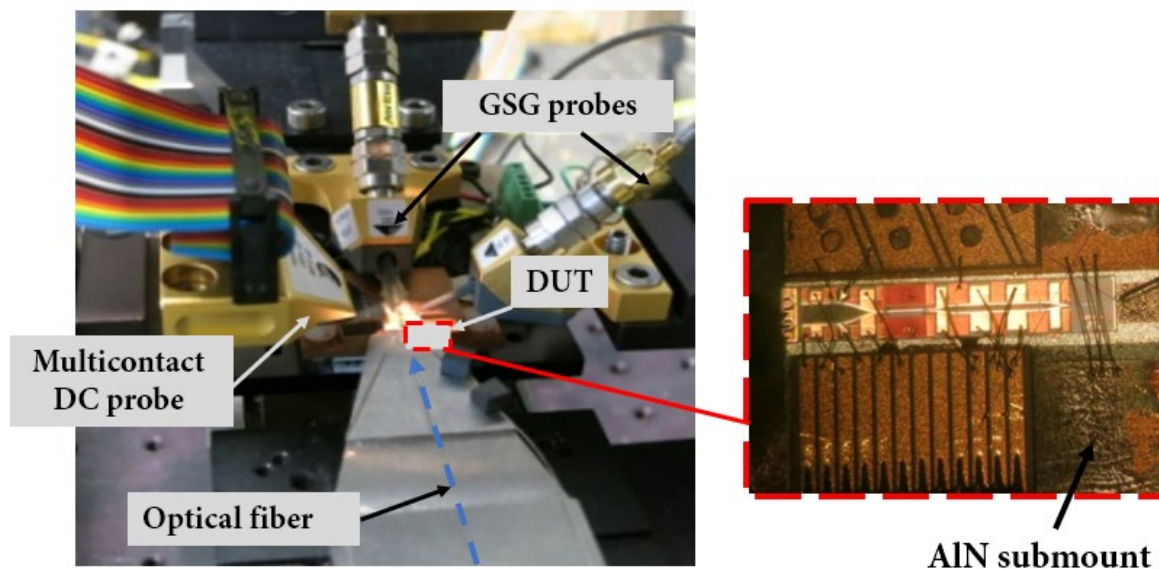


Fig. 6.76 Part of the measurement setup with close up view on the PIC on AlN submount.

In order to generate optical frequency combs, only one DFB laser is used. The DFB output signal is modulated twice, before and after reflection on the back of the photodiode as depicted in Fig. 6.75. This causes generation of sidebands, which form an optical frequency comb [5]. The modulator is driven with 20 dBm RF signal. The SOAs bias current values are tuned from 5 mA up to 200 mA, and the synthesizer frequency is fixed successively at 1 GHz, 2 GHz and at 10 GHz. Examples of the optical combs at 1 GHz and 2 GHz are presented in Fig. 6.77. Comparison of optical combs for 200 mA of bias current is depicted in Fig. 6.78. From these measurements it is clearly seen that the use of amplitude modulation assisted by integrated SOAs is an efficient way to generate an optical frequency comb. This is attributed to a combination of contribution from four wave mixing in SOAs and four wave mixing in the self-injected DFB laser. Increasing the bias current increases the optical power being self-injected in the laser and SOAs, and as a consequence, increase the span of the comb as can clearly be seen on the figures. The highest number of harmonics is measured at 200 mA bias current at 1 GHz. For the 2 GHz RF signal, the generated optical frequency comb is less wide with lower number of harmonics. The narrowest optical frequency comb is observed at 10 GHz RF signal with as well the lowest number of harmonics. It is caused due to the limited modulation bandwidth of the integrated modulator which is below 2 GHz.

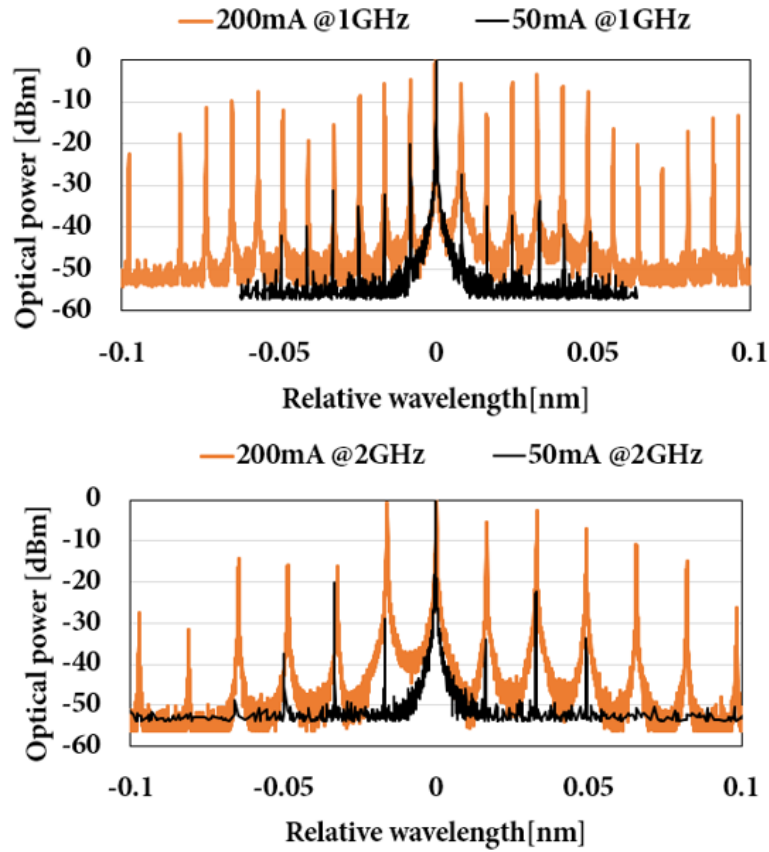


Fig. 6. 77 Optical frequency comb at different bias condition of SOAs at 1 GHz (top) and 2 GHz (bottom) for generator signal.

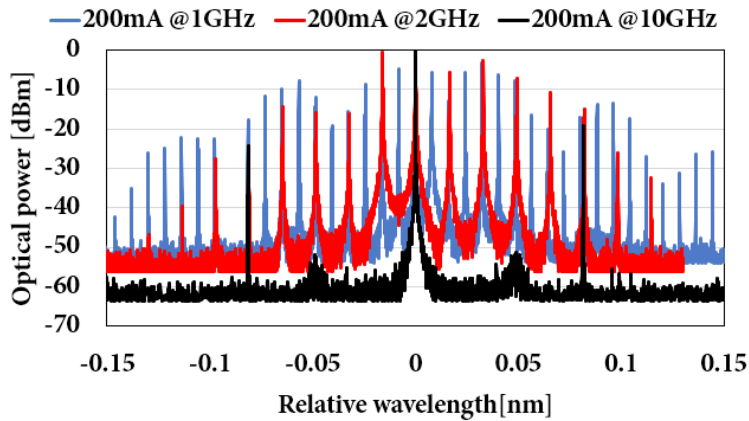


Fig. 6. 78 Comparison of optical frequency combs at different frequencies for 200 mA of bias current.

A solution to use optical injection locking (OIL) assisted by sub-harmonic injection locking with a synthesizer is reported in [5]. Injecting a slave laser (SL) with low-phase-noise master laser (ML) forces the SL to work at the same wavelength with the phase noise similar to ML. This condition is satisfied when the wavelengths of the two lasers are close enough and injected optical power is optimized. When the ML is a comb of optical tones, the SL can lock to the nearest tone, as it has been successfully tested on one of the III-V Lab PIC [6]. This solution requires an additional stable laser to generate the comb. To overcome this limitation, a generation of frequency comb around each DFB line and optical reinjection of this dual-comb into the PIC is applied. For the experiment presented here an integrated EAMs and residual reflection on the back of the highspeed photodetectors are utilized. The beat note frequency delivered by the PIC is tuned to 33.5 GHz. In Fig. 6. 79 optical and electrical spectra measured with OSA and ESA are presented with and without RF modulation. The modulator is driven at 4.8 GHz what corresponds to the 7th sub-harmonic of the generated signal. Thanks to fine adjustment of the modulation frequency, a narrow linewidth of the beat-note can be established.

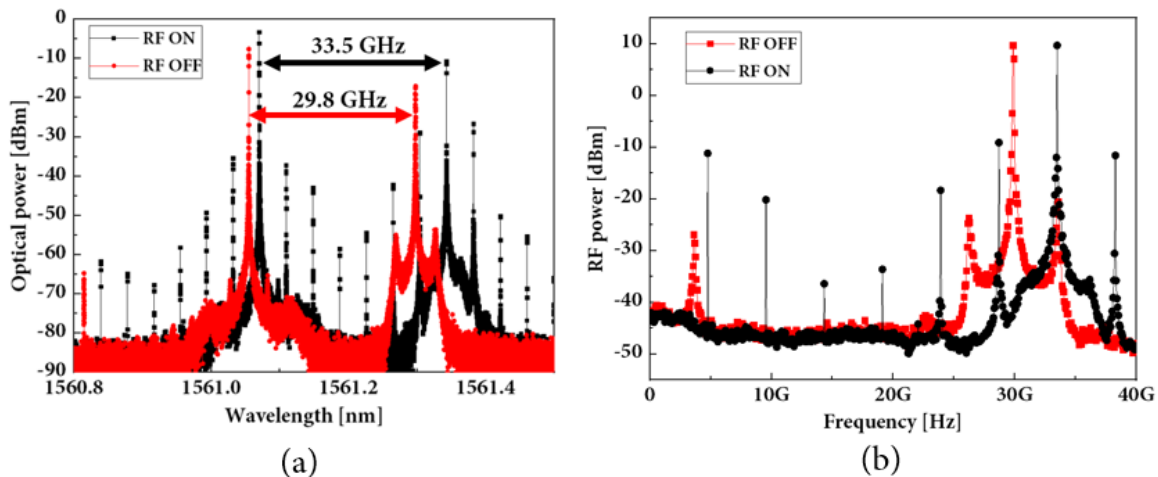


Fig. 6. 79 Optical (a) and (b) electrical spectrum for cross injection locking with sub-harmonic injection locked with 20 dBm of electrical injection.

In Fig. 6. 80 the beat-note of generated signal at 33.5 GHz for different injected frequencies at the optimum adjustment and around it, presenting efficient injection locking (the measurement for effective injection locking is represented by curve p4). The phase noise of the self-injected beat-note is measured using ESA (Fig. 6. 81). For comparison, the phase noise spectral density of the synthesizer is presented as well. Measured phase noise level of the self-injected beat note is below -90 dBc/Hz at 10 kHz frequency offset.

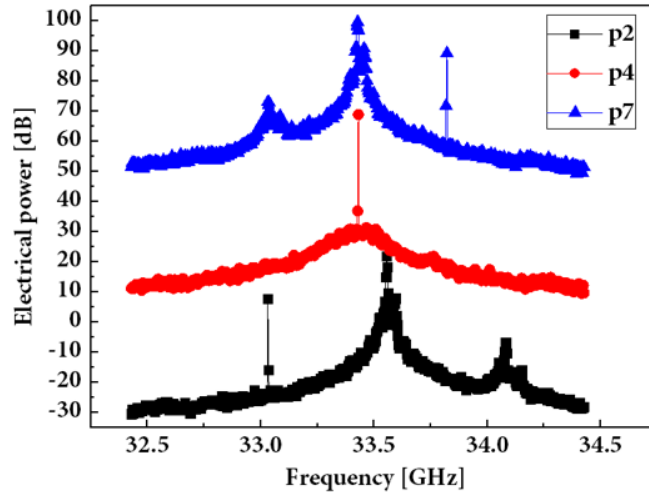


Fig. 6. 80 Electrical spectrum of the beat-note for lock-in condition at 33.5 GHz.

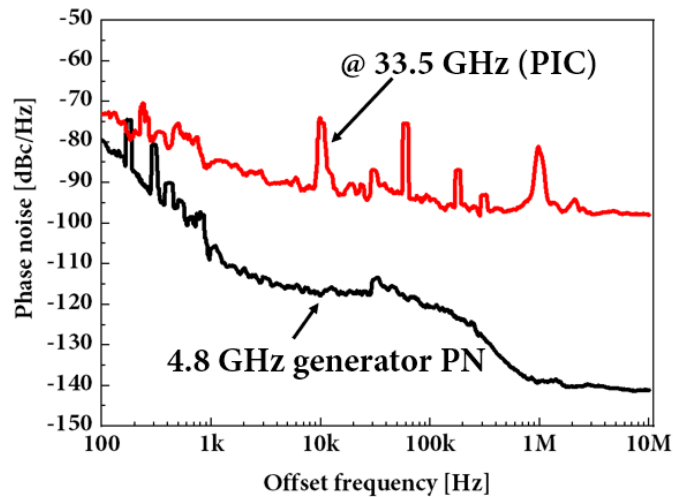


Fig. 6. 81 Comparison between the synthesizer and the self-injected beat-note phase noise.

To conclude:

- In the above described experiment, the optical frequency comb generation from a monolithically integrated heterodyne source is successfully tested and presented in Fig. 6. 77 - Fig. 6. 78.
- With the application of the generated optical frequency comb, the cross-injection locking up to 33.5 GHz is demonstrated by external

modulation up to 7th sub-harmonic, as presented in Fig. 6. 79 - Fig. 6. 80.

- **Based on this technique a low phase noise signal generation is achieved with -90 dBc/Hz at 10 kHz of frequency offset, without any external optoelectronic device.**

6.6 MEASUREMENTS AND RESULTS - SUMMARY

To briefly summarized previously presented results of the devices fabricated during the FiWiN5G and iPHOS fabrication run and characterized during this PhD thesis:

- Due to unexpected problems during the cleanroom processing, the impedance of the devices from the FiWiN5G fabrication run is very high, reaching up to ca. 6 k Ω for the single UTC PD, ca. 2 k Ω for the devices with Wilkinson power combiners and up to ca. 60 k Ω for the antenna-integrated devices.
- In the 2-way and 4-way Wilkinson power combiners the under-bridge connections are successfully established and the estimated values of the series resistance of the connections are in good theoretical agreement.
- The s-parameters measurements of the 2-way and 4-way Wilkinson power combiners with the VNA up to 65 GHz, reveal good agreement between the simulations and the measurements of the transmitted signals.
- Despite the high impedance mismatch, the UTC PDs and devices with Wilkinson power combiners are characterized up to 40 GHz. Based on the results of the -1-dB compression point measurement, a considerable improvement in power dissipation is expected when the multiple devices are applied in the design and consequently higher output power levels could be achieved.
- Estimation of the optical propagation losses of the InP passive optical waveguides are in good agreement with the published results.
- Antenna-integrated devices from the FiWiN5G run are characterized at 50 GHz, measured values of the output powers are ca. -80 dBm (without cable losses), but it is important to note that the series resistance values are different between the antenna structures.
- The UTC PDs and antenna-integrated devices from the iPHOS fabrication run show how strongly the device impedance influence the performance. The output power levels are much higher as well as the 3-dB bandwidths when the impedance value are below 100 Ω .

- The LPT and bow-tie antenna structures from iPHOS fabrication run are characterized from 77 GHz up to 110 GHz. Based on the results, the bow-tie antenna-integrated UTC PD device achieve higher output power levels up to -34 dBm @ 77 GHz (measured with ESA).
- Application of optical frequency combs can greatly improve the output power levels in comparison to standard two-tone sources, as presented in the experiment with LPT antenna-integrated UTC PD.
- Based on the results presented in the experiment with the photonic integrated circuit, the low-phase noise signal can be achieved with the optical frequency combs and cross-injection locking without any external optoelectronic device.

REFERENCES

- [1] D. D'Agostino et al., 'Low-loss passive waveguides in a generic InP foundry process via local diffusion of zinc', *Opt. Express*, vol. 23, no. 19, p. 25143, Sep. 2015.
- [2] F. van Dijk et al., "Integrated InP Heterodyne Millimeter Wave Transmitter," in *IEEE Photonics Technology Letters*, vol. 26, no. 10, pp. 965-968, May15, 2014.
- [3] M. Faugeron et al., 'High Peak Power, Narrow RF Linewidth Asymmetrical Cladding Quantum-Dash Mode-Locked Lasers', *IEEE J. Select. Topics Quantum Electron.*, vol. 19, no. 4, pp. 1101008–1101008, Jul. 2013.
- [4] F.-M. Kuo et al., 'Spectral Power Enhancement in a 100 GHz Photonic Millimeter-Wave Generator Enabled by Spectral Line-by-Line Pulse Shaping', *IEEE Photonics Journal*, vol. 2, no. 5, pp. 719–727, Oct. 2010.
- [5] F. Van Dijk et al., "Electrical injection locking of a fully integrated photonic integrated circuit based heterodyne source," in *Optical Fiber Communication Conference, OSA Technical Digest (online) (Optical Society of America, 2016)*, paper M2B.2.
- [6] K. Balakier, "Optical injection locking of monolithically integrated photonic source for generation of high purity signals above 100 GHz," *Opt. Express* 22, 29404-29412 (2014).
- [7] A. Jankowski, G. Kervella, M. Chtioui, M. Lamponi and F. v. Dijk, "Optoelectronic comb generation and cross-injection locking of photonic integrated circuit for millimetre-wave generation," *ECOC 2016; 42nd European Conference on Optical Communication*, Dusseldorf, Germany, 2016, pp. 1-3.

GENERAL CONCLUSIONS

During this PhD thesis a new generation of the 2-way and 4-way Wilkinson power combiners with UTC photodiodes are designed, fabricated and characterized. Moreover, antenna-integrated structures based on folded-dipole and bow-tie topologies, designed to operate as well in the mm-wave frequency band are developed and fabricated. These compact photonic integrated circuits are of great interest in the modern telecommunication systems, where photonic-based solutions find several applications.

In the first two chapters, general introduction to mm-wave electronics-based solutions and fundamental operating principles are given. The most common diode-based and transistor-based mm-wave circuits are presented and discussed. Furthermore, photonics-based solutions are also presented and both technologies are compared in terms of output powers and phase noise levels in the mm-wave frequency range. More detailed description of the main limiting factors for high-power signal generation based on photonics is included in the third chapter. It also presents existing and most promising solutions to generate high-power mm-wave signals. Based on literature study and reported results, Wilkinson power combiners and array of antenna-integrated UTC PDs are chosen for the final design of the new photonic integrated circuits.

Design and simulation procedures employed to develop and to design structures with Wilkinson power combiners and antenna-integrated devices are presented in chapter four. Simulations revealed additional information about the limitations and difficulties to design wideband circuits. Perfect symmetry and circuit geometry optimization play a crucial role in the design. What is more, simulations and design process of the optical elements such as passive optical waveguide, S-bends, and MMIs are also described and presented. It also shows that the additional optical losses have to be taken into account due to material composition of the design devices.

Complex processing steps that are applied to produce the design circuits in the III-V Lab cleanroom facilities are described in chapter 5. Unfortunately, due to unexpected chip breakage, additional fabrication issues have to be faced. This includes not only the partial loss of the devices from the broken part of the chip, but also uniformity problems. Measurements presented in chapter 6 revealed additional issues with very high series resistance values, varying from 1.5 k Ω up to 6 k Ω . As a consequence, the final performance of the designed devices is dramatically reduced. Measured responsivities of the UTC PDs are about 0.02 A/W, with 3-dB bandwidth <5 GHz. Structures with Wilkinson power combiners due to more complex topologies are even more influenced by very high series resistance values. The target frequency

ranges are above 60 GHz, but due to very low output power levels, characterization at frequencies above 40 GHz is not possible. Nevertheless, calculation of theoretical power dissipation revealed that Wilkinson power combiners outperformed single UTC photodiodes. Moreover, the saturation current measurements also show that Wilkinson power combiners should achieve higher output power levels in comparison to single UTC photodiodes. The -1 dB point is not reached for the devices with Wilkinson power combiner due to setup limitations. Furthermore, additional passive measurements of the s-parameters with the VNA on the Wilkinson power combiners are performed, despite the fact that the characterized circuit is not fully adapted for this type of measurement. Recorded results are in good agreement with the simulated circuits for the signal transmission between the input and the output. Measurements and comparison of the isolation between the two inputs are more challenging due to very high input reflections. The antenna-integrated devices, are as well strongly influenced by high series resistance values. Measurements at 50 GHz, which is not the target frequency of the designed antennas, are possible with an LNA. Measurements at higher frequencies are not feasible due to very low output power levels. In addition to characterization and measurements of the devices fabricated within Fiwin5G, measurements of previously fabricated devices from iPHOS project are presented as well. The 3-dB bandwidth for UTC PDs is above 40 GHz. Antenna-integrated structures and single UTC photodiodes are characterized additionally at 77 – 110 GHz. Measurements with the MLL and LPT antenna-integrated UTC PD shows that the output power levels can be increased by introduction of multiwavelength sources in the setup. In addition, the optoelectronic comb generation and cross-injection locking experiments were performed showing that these techniques can be used to generate low-phase noise signals at mm-wave frequencies.

Based on the results obtained during this PhD thesis, despite fabrication issues and very high series resistance values, it is shown that Wilkinson power combiners integrated with UTC photodiodes and antenna-integrated devices are a very promising solution to increase the output power levels. Nevertheless, several improvements can be applied in the next generation of components such as:

- Fabrication process simplification:
 - Reduced number of fabrication steps.
 - Additional wafers available for the fabrication.
- New layer stack with optimized thickness for passive optical waveguides.
- Flip-chip mounting on the high thermal conductivity material i.e. diamond.
- Wilkinson power combiners:
 - Optimized symmetry of the 4-way Wilkinson.
- Antenna-integrated devices:

- The bias circuitry area reduction and/or use of the external substrate for this electrical circuit.
- Use of external passive optical circuits for optical power splitting that are more compact.
- Some designs that have been proposed during this PhD thesis could not be validated in terms of the beam steering capabilities and the far-field measurements and require further evaluation.

ANNEX 1

The aim of this annex is to present briefly the principles of ANSYS HFSS simulations performed during this PhD thesis.

Several steps can be defined in order to perform the simulations:

1. Define the 3D model of the simulated structure with the dimensions that correspond to the dimensions of the real structure.
2. Assign material parameters by using material library from HFSS or manually, if the material is not included.

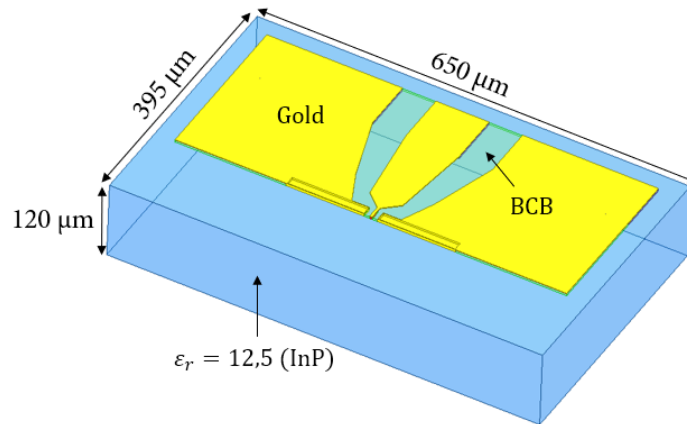


Figure 1. The 3D model of UTC PD used in the HFSS simulations.

3. Add port excitations in order to simulate the S-parameters. Excitation port such as lumped port has to touch perfect electric boundary. Define the port impedance according to the required value.

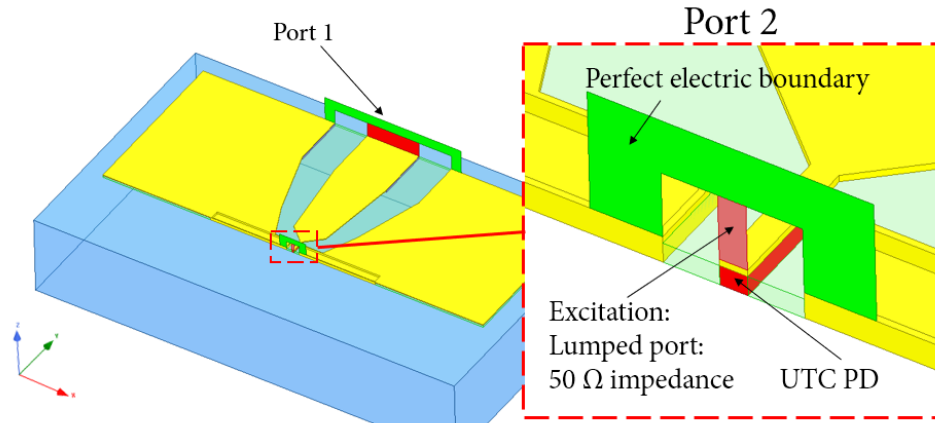


Figure 2. Port assignment in HFSS simulations.

4. Structure has to be surrounded by “air box” in order to define the simulation boundaries, as well as, the radiation boundaries for the antenna simulations. It is required to keep the minimum distance of $\lambda/4$ (λ corresponds to simulation frequency) between the structure and the boundary.

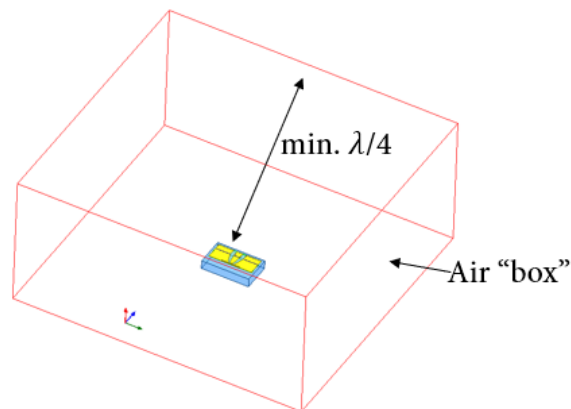


Figure 3. “Air box” used in HFSS simulations as a boundary.

5. For the UTC PD simulation metallic ground layer (perfect electric boundary) is defined on the bottom of the “air box”. It is included to simulate the influence of the measurement setup where the sample is placed on the alumina platform.

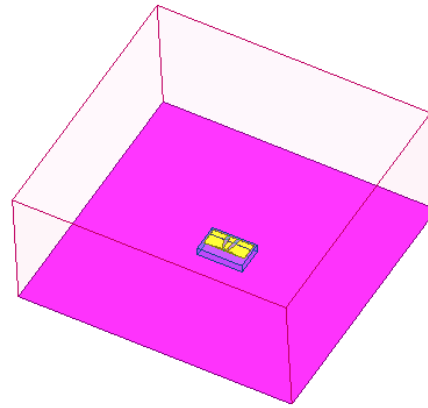


Figure 4. Ground layer used in the HFSS simulations.

6. The UTC PD structure is simulated as a simplified lumped element model, where R, C and L values can be defined. In the HFSS simulations the R value was set to 50Ω (or higher, as stated in the simulations). The value of C corresponds to the theoretical capacitance that depends on the UTC dimensions.